

UC Irvine

UC Irvine Electronic Theses and Dissertations

Title

Optical Absorption for Continuously Monitoring Sulfur Oxides and Sulfuric Acid in Flue Gas Conditions

Permalink

<https://escholarship.org/uc/item/6qr9d9s8>

Author

Biasioli, Andrea

Publication Date

2021

Copyright Information

This work is made available under the terms of a Creative Commons Attribution License, available at <https://creativecommons.org/licenses/by/4.0/>

Peer reviewed|Thesis/dissertation

UNIVERSITY OF CALIFORNIA,
IRVINE

Optical Absorption for Continuously Monitoring Sulfur Oxides and Sulfuric Acid in Flue
Gas Conditions

DISSERTATION

submitted in partial satisfaction of the requirements
for the degree of

DOCTOR OF PHILOSOPHY

in Mechanical and Aerospace Engineering

by

Andrea Biasioli

Dissertation Committee:

Professor Emeritus Derek Dunn-Rankin, PhD, Advisor, Chair

Professor Bihter Padak, PhD, Committee Member

Professor Barbara Finlayson-Pitts, PhD, Committee Member

Dr. Yu-Chien Chien, PhD, Co-advisor, Committee Member

TABLE OF CONTENTS

	Page
LIST OF FIGURES	v
LIST OF TABLES	x
ACKNOWLEDGMENTS	xii
CURRICULUM VITAE	xiii
ABSTRACT OF THE DISSERTATION	xiv
1 Introduction	1
1.1 Worldwide coal use outlook	3
1.2 Sources of sulfur oxides in coal-fired power plants	4
1.3 Sulfuric acid (H_2SO_4) formation	5
1.4 Flexible operations of coal-fired power plants	8
1.5 Pulverized coal and circulating fluidized bed technologies	10
1.6 Ammonium bisulfate (ABS) formation	11
1.7 Practical considerations for SO_3 and H_2SO_4 continuous measurements	13
1.8 Motivations and objectives	14
2 Experimental methods	17
2.1 Industry-standard methods to measure sulfur species concentration	17
2.2 Differential Optical Absorption Spectroscopy (DOAS)	22
2.2.1 Differential absorption cross-sections for SO_2	24
2.2.2 Differential absorption cross-sections for SO_3	26
2.3 External Cavity Quantum Cascade Laser (ECQCL)	29
2.3.1 Mid-infrared transitions for SO_2	30
2.3.2 Mid-infrared transitions for SO_3	32
2.3.3 Mid-infrared transitions for H_2SO_4	35
2.3.4 Mid-infrared transitions for other flue gas species	36
2.4 Controlled condensation method: EPA Method 8A	37
3 Experimental facility design and setup	40
3.1 In-lab SO_3 generation design strategy review and challenges	40
3.2 Design parameters	43

3.3	First design iteration	44
3.4	Second design iteration	50
3.4.1	Schematics and flow control	53
3.5	Root of sum of squares (RSS) uncertainty analysis for SO_x generation	64
4	Numerical methods	68
4.1	Chemkin Model	69
4.1.1	Define the experimental conditions and species interest	69
4.1.2	Gather an appropriate chemical mechanism	69
4.2	Fluent model	73
4.2.1	Model and mesh	74
4.2.2	Boundary conditions	79
4.2.3	Solver settings	82
5	Numerical results	88
5.1	Chemical equilibrium analysis using Chemkin	90
5.2	Identification of key aspects in the reaction paths for experiment conditions	91
5.2.1	SO_2 formation from SO_3 thermal dissociation	92
5.2.2	Simulated H_2SO_4 and SO_3 are fundamentally at equilibrium	94
5.3	Fluent simulation results	98
5.3.1	Reference case	100
5.3.2	Corner case 1 and corner case 2 comparison	104
5.3.3	Corner case 2 and corner case 3 comparison	108
5.3.4	Temperature and concentrations profiles along the core of the measurement cell	112
5.3.5	Sulfuric acid concentrations adjacent to the windows	117
5.3.6	Thermal boundary layer and thermocouples location	122
5.4	Simulated effect of axial temperature non-uniformity on spectroscopic measurements	125
5.4.1	Effect of temperature changes on the absorbance spectrum	125
5.4.2	Effect of temperature uncertainties on the measured absorbance spectrum	129
5.4.3	Effect of simultaneous temperature and concentration change	131
5.4.4	Effect of pressure variations	134
5.5	Conclusions	136
6	Experimental results	139
6.1	Differential Optical Absorption Spectroscopy	140
6.1.1	Sulfur dioxide (dry tests)	140
6.1.2	Sulfur trioxide (dry tests)	141
6.2	External Cavity Quantum Cascade Laser (ECQCL)	145
6.2.1	Experiment test structure	146
6.2.2	Experiment matrix	156
6.2.3	Raw data set overview for an ECQCL 7 experiment	157
6.2.4	Raw data set overview for an ECQCL 8 experiment	169

6.2.5	The role of H ₂ SO ₄ damage on optical windows	176
6.2.6	Spectral libraries	180
6.2.7	Ion chromatography measurement uncertainty	192
6.2.8	Step 1 experiment results analysis	194
6.2.9	Summary of Step 1 results	215
6.2.10	Step 2 experiment results	216
7	Summary	241
7.1	Conclusions	242
7.2	Recommendations and future work	243
	Bibliography	246
A	ECQCL experiment log	257
A.1	Step 1	258
A.2	Step 2	261

LIST OF FIGURES

	Page
1.1 Simplified schematic of a coal-fired power plant.	5
1.2 Notion of chemical equilibrium between sulfur compounds [38].	8
1.3 SCR inlet temperature as function of the load [45]	9
1.4 Simplified power plant schematics with relevant temperatures	14
2.1 The basic principle of absorption-based spectroscopic trace gas detection [65]	22
2.2 Principle of DOAS: I_0 and σ are separated by an adequate filtering procedure into a narrow (D' and σ') and broad band part (I'_0 and σ_b) [65].	23
2.3 Absorption cross-sections database for SO ₂ at room temperature (165-240 nm) [71].	25
2.4 Absorption cross-sections database for SO ₂ at room temperature (240-340 nm) [71].	26
2.5 Absorption cross-sections database for SO ₃ [71].	28
2.6 Absorption spectra of SO ₃ and SO ₂ at 400 C [73].	28
2.7 Predicted mid-IR spectra of SO ₂ and H ₂ O at 300K in a 1 m path, modeled with SpectralCalc Gas-Cell Simulator tool using HITRAN2016 database [84].	31
2.8 Predicted mid-IR spectra of SO ₂ and H ₂ O at 700K in a 1 m path, modeled with SpectralCalc Gas-Cell Simulator tool using HITRAN2016 database [84].	32
2.9 Central region of the ν_3 band of SO ₃ at 0.002 cm ⁻¹ resolution at 298K with pressure 9.4 Pa [86].	34
2.10 Measured absorption spectrum of 119 ppm SO ₃ (at 200 °C, blue), 100 ppm SO ₃ (at 400 °C, red), and 238 ppm SO ₂ (at 200 °C, magenta) in a 50 cm cell at ambient pressure [89].	34
2.11 Vapor-phase IR spectrum of H ₂ SO ₄ in the range of 500-1550 cm ⁻¹ . The spectrum was recorded at 150 °C with a path length of 100 cm [69].	36
2.12 Predicted mid-IR spectra of 20% CO ₂ , 2000ppm SO ₂ , 2000ppm NO ₂ , 500ppm NO, 500ppm CO, and 10ppm NH ₃ at 700K in a 1 m path cell at 1atm, modeled with SpectraPlot Gas cell simulator tool using HITRAN2012 database [91]. .	37
2.13 Schematics for the sampling system of EPA Method 8A (from [63]).	38
2.14 Dew point temperature of H ₂ SO ₄ , with respect to SO ₃ and H ₂ O concentration.	39
3.1 Schematics for the first design iteration.	46
3.2 Temperature measurements for the first design iteration.	48
3.3 The catalyst bed reactor is located inside a heating oven.	49
3.4 Overview of the complete system, with Unisearch DOAS.	49

3.5	Schematics for the second design.	55
3.6	Simplified-logic schematic for the second design.	56
3.7	Temperature measurement locations for the second design, with color-coded heating zones.	57
3.8	Overview of the bare system, with thermocouples installed and a temporary catalyst bed reactor, before the installation of water evaporator and main flow valve.	59
3.9	System ready to operate with OKSI ECQCL7, before the installation of water evaporator and main flow valve.	60
3.10	Gold plated mirrors of the Herriott cell in 44-pass configuration.	60
3.11	Mirrors of the Herriott cell in 16-pass configuration.	61
3.12	Visualization of the beam path with a visible red diode laser.	61
3.13	Closeup of the water evaporation system.	62
3.14	Full experimental setup undergoing maintenance.	63
3.15	Closeup of the upstream window. The purging nitrogen line is not connected. A cloudy white BaSO ₄ layer is visible on the window.	64
3.16	RSS uncertainty analysis on the generation of different SO _x levels with 5 slm overall flow rate.	67
4.1	Rendering from ANSYS Solidworks measurement cell model.	74
4.2	Trimetric view of the SpaceClaim measurement cell model. Shared topologies are highlighted in green.	76
4.3	Side view of the SpaceClaim measurement cell model, with the definition of the origin.	76
4.4	Mosaic mesh for the measurement cell. Fluid is represented in lilac color.	78
4.5	Detail of the mosaic mesh in close proximity to the gas inlet and the upstream window.	78
4.6	Representation of mesh zones, each one tied to a correspondent boundary conditions. Dashed arrows are related to surfaces not directly visible.	80
4.7	Settings for Fluent viscous model.	83
4.8	Settings for Fluent species model.	83
4.9	Settings for Fluent species model mixture properties	85
4.10	Settings for Fluent residual monitor.	86
4.11	Settings for Fluent additional convergence conditions for SO ₃ and H ₂ SO ₄	86
5.1	Normalized equilibrium curve for sulfur species as a function of gas temperature for two different water concentrations 12% (solid) and 3% (dash).	91
5.2	Normalized PSR simulated-experiment conditions results using the <i>combined-mech1</i> (solid) compared to ER equilibrium conditions (dash)	93
5.3	Formation of SO ₂ from SO ₃ thermal dissociation as a function of reaction time for different gas temperature.	94
5.4	PSR simulated-experiment conditions for the <i>combined-mech1</i> model (solid) compared to the <i>combined-mech2</i> model (dash).	95

5.5	Difference in prediction of H_2SO_4 formation between <i>combined-mech1</i> and <i>combined-mech2</i> models as a function of temperature for different water vapor content.	96
5.6	Formation of H_2SO_4 predicted from <i>combined-mech1</i> mechanism as a function of residence time for different gas temperatures.	97
5.7	Formation of H_2SO_4 predicted from <i>combined-mech2</i> mechanism as a function of residence time for different gas temperature.	97
5.8	Fluent simulations corner cases.	99
5.9	Temperature contour plots for the <i>reference case</i> . Temperature values are in Kelvin.	101
5.10	H_2SO_4 concentration contour plots for the <i>reference case</i> . Concentration values are in parts per million volume.	102
5.11	SO_3 concentration contour plots for the <i>reference case</i> . Concentration values are in parts per million volume.	103
5.12	Temperature contour plots on zx plane ($y = 0$) for the reference case (top) compared to the high-temperature high-flow ($700\text{K}, 1.25\text{slm}$) nitrogen purging flow (bottom). Temperature values are in Kelvin.	105
5.13	Temperature contour plots on yx plane ($z = 0$) for the reference case (top) compared to the high-temperature high-flow ($700\text{K}, 1.25\text{slm}$) nitrogen purging flow (bottom). Temperature values are in Kelvin.	106
5.14	H_2SO_4 contour plots on zx plane ($y = 0$) for the reference case (top) compared to high-temperature high-flow ($700\text{K}, 1.25\text{slm}$) nitrogen purging case. Concentration values are in ppmv.	107
5.15	H_2SO_4 contour plots on yx plane ($z = 0$) for the reference case (top) compared to high-temperature high-flow ($700\text{K}, 1.25\text{slm}$) nitrogen purging case. Concentration values are in ppmv.	108
5.16	Temperature contour plots on zx plane ($y = 0$) for the high-temperature high-flow ($700\text{K}, 1.25\text{slm}$) case compared to the low-temperature high-flow ($400\text{K}, 1.25\text{slm}$) nitrogen purging case. Temperature values are in Kelvin.	109
5.17	Temperature contour plots on yx plane ($z = 0$) for the high-temperature high-flow ($700\text{K}, 1.25\text{slm}$) case compared to low-temperature high-flow ($400\text{K}, 1.25\text{slm}$) nitrogen purging case. Temperature values are in Kelvin.	110
5.18	H_2SO_4 contour plots on zx plane ($y = 0$) for the high-temperature high-flow ($700\text{K}, 1.25\text{slm}$) case compared to low-temperature high-flow ($400\text{K}, 1.25\text{slm}$) nitrogen purging case. Concentration values are in ppmv.	111
5.19	H_2SO_4 contour plots on yx plane ($z = 0$) for the high-temperature high-flow ($700\text{K}, 1.25\text{slm}$) v. low-temperature high-flow ($400\text{K}, 1.25\text{slm}$) nitrogen purging flow. Concentration values are in ppmv.	112
5.20	Definition of the core surfaces along the x-axis. The blue surfaces are parallel to the zy plane, while the red surfaces transition from parallel to each window to parallel to the zy plane.	113
5.21	Temperature, H_2SO_4 and SO_3 concentrations, along the x-axis for different nitrogen purging flow rates and for two different nitrogen temperatures.	115
5.22	Gas volume monitored (green) adjacent to the window (gray).	118

5.23	Window 1 and Window 2 temperatures as a function of purging nitrogen flow rate and for different nitrogen temperatures.	119
5.24	Window 1 and Window 2 H ₂ SO ₄ concentrations as a function of purging nitrogen flow rate and for different nitrogen temperatures.	119
5.25	Ratio between H ₂ SO ₄ concentration from numerical simulation results and H ₂ SO ₄ concentration estimated from the diluted flow at chemical equilibrium.	121
5.26	Stream traces for Corner Case 1 (Reference case, left) and Corner Case 2 (High-flow high-temperature case, right).	122
5.27	Cross section of the measurement cell highlighting the definition of 15 consecutive surfaces along the radial coordinate z at thermocouple 1 longitudinal location.	123
5.28	Temperature distribution along the measurement cell radial axis for three different thermocouple longitudinal locations.	124
5.29	Simulated absorbance for 300ppm of SO ₂ in two gas volumes at different temperatures.	128
5.30	Simulated absorbance for 300ppm of SO ₂ in three gas volumes at different temperatures.	129
5.31	Simulated absorbance A_R and A_E resulting from a 50K temperature measurement error.	131
5.32	Simulated absorbance A_{1+2+3} and A_E for gas sections with different temperature and concentration.	134
5.33	Experimental pressure change in the measurement cell as function of main inlet flow rate at ambient temperature.	135
5.34	Simulated absorbance for different measurement cell pressure values.	136
6.1	UV spectrum of 54ppmv SO ₂ at 400 °C and 1atm pressure with 1m path length	140
6.2	Estimated conversion efficiency of the catalyst reactor for different flow rates and initial SO ₂ concentrations based on SO ₂ disappearance rather than by direct measure of SO ₃	141
6.3	Subtraction of the SO ₂ spectrum from the spectrum of SO ₃ collected by direct injection of SO ₃	143
6.4	Experimental Schumann-Runge bands resulting from flowing air with a nitrogen background	144
6.5	SO ₂ and SO ₃ concentrations in the Step 1 ECQCL 7 07/14/2020 $T = 350C$ experiment timeline.	158
6.6	H ₂ SO ₄ concentration in the Step 1 ECQCL 8 07/14/2020 $T = 350C$ experiment timeline.	170
6.7	Spectral absorbance of BaSO ₄ evaluated by comparison of two <i>Air</i> conditions, before and after H ₂ SO ₄ damage respectively.	178
6.8	Absorbance spectrum of BaSO ₄ from different sources in comparison to the UCI ECQCL 8 measured signal through the damaged windows.	179
6.9	Absorbance spectrum of CaSO ₄ from NIST [115]	180
6.10	Library spectrum for SO ₂ at different temperatures.	182
6.11	Library spectrum for SO ₂ at different temperatures for ECQCL 7.	183
6.12	Library spectrum for H ₂ O at different temperatures for ECQCL 7.	184

6.13	Saturated detector and correspondent water absorbance spectrum.	185
6.14	Water libraries for small concentrations/oscillations, at different temperatures for ECQCL 7.	185
6.15	Library spectrum for H ₂ O at different temperatures for ECQCL 8.	186
6.16	Library spectrum for SO ₂ at different temperatures for ECQCL 8.	187
6.17	Library spectrum for BaSO ₄ at different temperatures for ECQCL 8	188
6.18	Library spectrum for H ₂ SO ₄ at different temperatures for ECQCL 8.	191
6.19	Library spectrum to correct for laser drift at different temperatures for ECQCL 8	192
6.20	SO ₂ measurements in <i>Bypass 100ppm</i> test conditions.	197
6.21	SO ₂ estimation error in <i>Bypass 100ppm</i> test conditions with respect to the nominal expected SO ₂ concentration.	198
6.22	SO ₂ measurements in <i>Water only + Bypass 81ppm</i> test conditions.	199
6.23	SO ₂ estimation error in <i>Water only + Bypass 81ppm</i> test conditions with respect to the nominal expected SO ₂ concentration.	199
6.24	SO ₂ measurements in <i>Regular</i> test conditions.	200
6.25	SO ₂ ratio between <i>Equalized</i> and <i>Regular</i> test conditions readings.	201
6.26	SO ₂ ECQCL7 measurements and EPA Method 8A measurements for <i>Regular</i> test conditions.	202
6.27	Error between SO ₂ ECQCL7 measurements and EPA Method 8A measurements for <i>Regular</i> test conditions.	203
6.28	SO ₃ measurements in <i>Regular</i> test conditions.	204
6.29	Complete timeline for SO ₃ and SO ₂ measurements in <i>Regular</i> test conditions for ECQCL 7 Step 1 tests.	205
6.30	Error between the measured concentration of SO ₂ + SO ₃ with respect to the inlet variable SO_x , in <i>Regular</i> test conditions for ECQCL 7 Step 1 tests.	206
6.31	SO ₃ ECQCL7 measurements and EPA Method 8A measurements for <i>Regular</i> test conditions.	207
6.32	Error between SO ₃ ECQCL7 measurements and EPA Method 8A measurements for <i>Regular</i> test conditions.	208
6.33	SO ₃ ratio between <i>Equalized Decay</i> and <i>Regular</i> test conditions readings.	209
6.34	SO ₃ and H ₂ SO ₄ normalized theoretical equilibrium at 3% water vapor as a function of temperature, with ECQCL7-measured SO ₃ fraction.	211
6.35	Measured H ₂ SO ₄ concentrations (ECQCL8, circles) and H ₂ SO ₄ concentrations estimated from the EPA Method 8A measurements under the assumption of chemical equilibrium.	213
6.36	Estimated H ₂ SO ₄ measurement error of ECQCL 8 with respect to the H ₂ SO ₄ concentrations estimated from the EPA Method 8A measurements under the assumption of chemical equilibrium.	214
6.37	SO ₂ and SO ₃ concentrations in the Step 2 ECQCL 7 08/13/2020 $T = 350C$ experiment timeline.	217
6.38	SO ₂ and H ₂ SO ₄ concentrations for Step 2 ECQCL 8 08/13/2020 $T = 350C$ experiment timeline.	228
6.39	SO ₂ and SO ₃ concentrations in the Step 2 ECQCL 8 08/11/2020 $T = 250C$ experiment timeline	239

LIST OF TABLES

	Page
2.1 Current state-of-the-art in optical techniques to measure the concentration of SO ₃ , SO ₂ , and H ₂ SO ₄	19
2.2 Current techniques to measure the concentration of SO ₃ , SO ₂ , and H ₂ SO ₄ not relying on optical measurements.	21
3.1 Design parameters	44
3.2 Temperature measurement points for the first design iteration.	48
3.3 Temperature measurement locations.	58
3.4 Color-coded heating zones with heat cable characteristic parameters.	58
4.1 Possible hydration models for SO ₃ and respective reaction rates.	72
4.2 Average and maximum skewness of the mesh in the different cell zones.	77
4.3 Fluid and solid heat transfer-related parameters.	80
4.4 Boundary conditions for the fluid regions.	81
4.5 Boundary conditions for the solid regions.	82
5.1 Boundary conditions for the fluid regions in the <i>reference case</i>	100
6.1 Explanation of different test conditions	152
6.2 Test conditions as a function of the test variables	155
6.3 Step 1 experiments	156
6.4 Step 2 experiments	156
6.5 Description, raw detector signal, and absorbance for each test condition, for Step 1 ECQCL 7 07/14/2020 $T = 350C$ experiment, represented in temporal order.	168
6.6 Description, raw detector signal, and absorbance for each test condition, for Step 1 ECQCL 8 07/14/2020 $T = 350C$ experiment, represented in temporal order.	175
6.7 Time, raw detector signal, and absorbance in <i>Step 2, Water Add</i> test conditions with respect to <i>Water Only (8%)</i> background condition for Step 2 ECQCL 8 08/11/2020 $T = 300C$ test.	177
6.8 Ion chromatography measurement uncertainty	193
6.9 Experiment sets used in Step 1 ECQCL 7 analysis.	196

6.10	Description, raw detector signal, and absorbance for each test condition, for Step 2 ECQCL 7 08/13/2020 $T = 350C$ experiment, represented in temporal order.	225
6.11	Description, raw detector signal, and absorbance for each test condition, for Step 2 ECQCL 8 08/13/2020 $T = 350C$ experiment, represented in temporal order.	236
A.1	Step 1 Experiment runs	260
A.2	Step 2 ECQCL7 Experiment runs	261
A.3	Step 2 ECQCL8 Experiment runs	262

ACKNOWLEDGMENTS

I would like to thank the Electric Power Research Institute (EPRI) in the person of Richard Himes and the Department of Energy (DOE) for financial support, together with the partners for this project Opto-Knowledge Systems, Inc. (OKSI) and Fossil Energy Research Corporation (FERCo), especially Jason Kriesel, Ilya Dunayevskiy, and Camille Makarem at OKSI, and Lawrence Muzio and Jin Dang at FERCo.

This work has been possible thanks to the constant and unconditional support from my advisor Professor Dunn-Rankin. Dr. Yu-Chien Chien, together with current and past Lasers, Flames, and Aerosols laboratory researchers, including exchange and undergraduate students, played an important role as well. I would like to extend my gratitude to Professor Gamero-Castaño for the Teaching Assistantship support.

Finally, I would like to deeply thank my family.

CURRICULUM VITAE

Andrea Biasioli

EDUCATION

Doctor of Philosophy in Mechanical and Aerospace Engineering	2021
University of California, Irvine	<i>Irvine, CA</i>
Master of Science in Aeronautical Engineering	2015
Politecnico di Milano	<i>Milan, Italy</i>
Bachelor of Science in Aerospace Engineering	2012
Politecnico di Milano	<i>Milan, Italy</i>

CONFERENCE PUBLICATIONS

Exploring Continuous Monitoring Methods for SO₃ and H₂SO₄ in Flue Gas Condition	Mar 2019
11th US National Combustion Meeting	
Exploring Continuous Monitoring Methods for SO₃ in Flue Gas Conditions	Oct 2017
WSSCI 2017 Fall Meeting	

ABSTRACT OF THE DISSERTATION

Optical Absorption for Continuously Monitoring Sulfur Oxides and Sulfuric Acid in Flue Gas Conditions

By

Andrea Biasioli

Doctor of Philosophy in Mechanical and Aerospace Engineering

University of California, Irvine, 2021

Professor Emeritus Derek Dunn-Rankin, PhD, Advisor, Chair

Atmospheric emission of sulfuric acid (H_2SO_4) and its precursors, sulfate oxides SO_2 and SO_3 , are generated by burning fuels such as coal, oil, and gas for energy production or in the metallurgical industry. While sulfuric acid is important in many industrial applications, in the atmosphere it is one of the culprits for acid rain formation. Steps have been taken to reduce the sulfur content of fuels (for example, the migration to low sulfur fuel in the marine industry), but sulfur emissions are still a significant problem, especially for coal-fired power-plants. In the atmosphere, sulfate constitutes a large fraction of particulate matter air pollutants with aerodynamic diameter <2.5 microns (PM 2.5), which has been found responsible for adverse health effects. Although the use of coal is sharply declining in the United States, it is still on the rise in China and in Southeast Asia.

In coal-fired power-plants, most of the fuel sulfur content is oxidized to sulfur dioxide, while a small percentage can be further oxidized to sulfur trioxide (SO_3) in the boiler and across the NO_x reduction catalyst. In the presence of water, sulfur trioxide reacts at low temperatures to form sulfuric acid. The $\text{SO}_3/\text{H}_2\text{SO}_4$ emissions can be reduced by injecting neutralizing sorbents, entailing an additional operating cost. With continuous monitoring, a closed-loop control for sorbent injection could be developed, reducing sulfate emissions, and improving the operational performance of power plants. Therefore, the continuous

monitoring of SO_3 , H_2SO_4 , and SO_2 is a primary need for the coal industry.

The goal of this dissertation is to evaluate the feasibility of continuous measurements in flue gas conditions using optical absorption methods, including providing a high temperature spectral database of SO_2 , SO_3 , and H_2SO_4 . A further goal is the experimental investigation of the relationship between SO_3 and H_2SO_4 , often assumed to be at chemical equilibrium. The equilibrium has been hypothesized and relied on in many measurement techniques, however a direct experimental verification has not been accomplished.

Specifically, this work examines the performance of Differential Optical Absorption Spectroscopy (DOAS) and External Cavity Quantum Cascade Laser (EC-QCL) as potential methods for continuous measurement. The results are validated using the Environmental Protection Agency (EPA) Method 8A, the current industry standard for the measurement of sulfur species. The experimental setup includes a unique high-temperature multi-pass optical cell and a flow system able to replicate appropriate levels of flue gas species. The gas temperature and spatial distribution of sulfur species in the measurement cell was also investigated using numerical simulations.

The DOAS technique performed well for SO_2 measurements in the UV, while SO_3 and H_2SO_4 could not be evaluated with accuracy. The DOAS technique was found unsuitable for continuous sulfur species monitoring in flue gas conditions.

The mid-IR ECQCL technique could successfully detect SO_2 in flue gas conditions, in the spectral ranges near both $7\mu\text{m}$ and $8\mu\text{m}$, and for the first time, high-temperature mid-IR spectral libraries for SO_3 and H_2SO_4 were recorded. The equilibrium between SO_3 and H_2SO_4 was verified through direct optical measurements at 3% water vapor concentration within $\pm 12\%$ uncertainty.

At $7\mu\text{m}$, while SO_3 measurements are successful, the strong absorbance of SO_2 limits measurements only to low-sulfur coals (with SO_2 concentrations $< 500\text{ppm}$) in the current multi-pass configuration. Sulfuric acid does not absorb at $7\mu\text{m}$.

At $8\mu\text{m}$, SO_2 is a weak absorber, hence high-sulfur coal emission monitoring is feasible.

Sulfuric acid is a strong absorber and can be measured even at low levels, while SO_3 does not absorb at $8\mu\text{m}$ and needs to be calculated from equilibrium. Unfortunately, however, sulfuric acid reacts with the windows material (BaF_2) to form a layer of BaSO_4 , and at this wavelength, the layer formation causes a significant performance degradation, as BaSO_4 absorbs strongly. As the BaSO_4 layer thickens, it prevents the laser light from reaching the detector, and this poses a significant engineering challenge and limits the measurement to short time frames (10 to 30 minutes).

Chapter 1

Introduction

The generation of sulfur compounds is inherent during the combustion of coal in power plants because all coals contain sulfur that is incorporated into their carbonaceous matrix during formation. While the amount of sulfur in coal depends on its geochemistry [1], sulfur content ranges from just below 1% in low-sulfur coals to above 3% in high sulfur coals. It is also generally impractical to remove the sulfur from coal before it is burned [2]. Hence, sulfur control and mitigation relies on flue gas treatment. Most of the fuel sulfur content is oxidized to sulfur dioxide (SO_2), while a small percentage is further oxidized to sulfur trioxide (SO_3) in the boiler, and across the selective catalytic reduction (SCR) catalyst for NO_x reduction used in coal-fired power plants [3]. In wet flue gas, SO_3 can react to form H_2SO_4 , which is a misty acid that is difficult to capture due to the small size of the acid droplets. H_2SO_4 has adverse effects on both plant operation and the surrounding environment, including corrosion of ductwork surfaces [4], flyash contamination [5], formation of visible plumes [6], powdered activated carbon (PAC) poisoning [3], formation of ammonium bisulfate (ABS) due to ammonia slip from selective catalytic reduction (SCR) or selective non-catalytic reduction (SNCR) processes [7], and formation of particulate level PM 2.5, a known health hazard [8]. Ambient air particulate matter PM 2.5 have been associated with negative health effects (such as ischemic heart disease, lower birth weight, and respiratory hospital admissions) [9–

12]. While sulfate constitutes a large fraction of the mass of PM 2.5 pollutants [13], the exact role of sulfate on PM 2.5 toxicity is still unclear [12, 13]. Sulfate might play an indirect role by influencing the bioavailability of metallic species [13], whose presence in PM 2.5 has been linked with increased IHD mortality and cardiovascular and respiratory hospital admissions [11, 12].

Challenges in relation to the reactivity of sulfur species have prevented any reliable method to date for continuously monitoring SO_3 and H_2SO_4 concentration in coal-fired power plant flue gas. Flue-gas desulfurization typically involves the use of alkali sorbents to neutralize SO_3 and H_2SO_4 . The amount of sorbent could be optimized if a suitable continuous measurement of SO_3 and H_2SO_4 was available, especially under the increasingly common flexible operations condition. In flexible operations condition (flex-ops), coal-fired power plants are required to balance power grids by compensating for the variable electricity supply from renewable energy sources, with frequent start-ups together with major and rapid load changes [14]. The pollutant emission profiles can vary substantially with the load. Real-time sorbent tuning would decrease the operating costs of the power plant as well as extend the lifespan of components downstream of the boiler. Hence, the objective of this dissertation is to examine the continuous monitoring of these reactive sulfur species.

This introduction begins by describing the continued demand for coal into the future (1.1). It provides background knowledge to date concerning the fate of the sulfur in coal, with the details of the key oxidation reactions and where they occur in a coal power plant (1.2). A description on how and why sulfur oxides convert rapidly into sulfuric acid and ammonium bisulfate under power plant operation conditions is then provided (1.3, 1.6). The potential and challenges for continuously monitoring of sulfur species based on location and temperature is considered (1.7) which leads to the motivations and goals of the dissertation research (1.8).

1.1 Worldwide coal use outlook

The increasing sensitivity to anthropogenic sources of greenhouse gases like carbon dioxide from combustion has had a major impact on coal use in developed countries. Nevertheless, the global outlook for coal combustion shows continued high demand, and if methods for CO₂ sequestration (or "clean coal technology") become viable then coal use could see a further resurgence. The International Energy Agency (IEA) December 2020 Coal report provides summary and figures on the recent status of coal use worldwide, together with a five-year outlook [15]. In 2019 the power generation from coal declined 3% (it constituted 38.5% of the share of the global power mix in 2018), driven by low prices for natural gas – especially for the USA and Europe. In India, in 2019 coal-fired power plant generation decreased for the first time in forty years. Only China and Southeast Asia countries saw an increase in coal power generation.

The electricity demand in year 2020 has significantly dropped in the first half of the year, due to COVID-19. However, the decline in global coal demand in 2020 has been lower than forecasted, since China (where more than half of global coal is consumed) experienced a robust economic recovery.

A rebound in global coal demand is predicted for year 2021, driven by the prospect of a global economic recovery that would increase electricity demand. For coal, the demand is predicted to be largely driven by China, India, and Southeast Asia. In Europe and in the USA, coal consumption is expected to grow for the first time in a decade due to an increase in electricity demand and natural gas prices; however, the EU and the USA together account for only around 10% of the global coal use. In the US, coal accounted for about 20% of the total electric sector power generation in 2020 [16]. China's pledge of carbon neutrality before 2060 can affect its future energy share mix, but its coal demand has been stable at a plateau in recent years, and carbon sequestration approaches could affect fuel choice as well. India and other Southeast Asia countries are still in the process of adding new coal-fired capacity,

and they are expected to surpass the USA and the EU by 2025 in coal consumption.

Coal demand is expected to plateau by 2025, since coal-fired power plants have been rapidly retiring in the developed countries which at the same time are counterbalanced by the increasing demands in the developing countries. The increasing demand is particularly acute for countries in Southeast Asia, which mostly rely on coal for power generation.

It is clear that, even in the most optimistic clean energy future scenarios, the use of coal for power generation worldwide will continue along with the concomitant atmospheric emissions of pollutants. Therefore, it is important to provide tools for understanding the sulfur compounds created during coal combustion to aid in their control and damage mitigation.

1.2 Sources of sulfur oxides in coal-fired power plants

The presence of sulfur oxides (and sulfuric acid) in post-combustion gases of power plants is directly linked to the sulfur content of the fuel used, that is determined by the geological environments and the processes involved in coal formation [17]. As mentioned earlier, the sulfur content of raw coal is on the order of percent which is a significant pollutant load from the fuel alone. A typical 500 MW power plant (serving 250,000 people) will burn 200 metric tons of coal per hour. This means that even for low sulfur coal more than 2 metric tons/hour of sulfur must be dealt with.

During combustion in the boiler, the sulfur content of coal oxidizes to SO_2 , while a small fraction of it (approximately 0.1 to 1%, based on coal composition) is converted to SO_3 [18, 19] according to the reactions :



Under oxy-coal combustion, a promising technique to reduce NO_x and to capture CO_2 combustion emissions [20], SO_2 and SO_3 volumetric concentrations further increase, with SO_3 levels raising several fold [21].

After the combustion gases exit the boiler, the concentration of SO_3 will increase across the SCR catalyst. In fact, current deNO_xing SCR catalysts contain vanadia (V_2O_5), which is the typical sulfuric acid catalyst [22, 23] responsible for promoting the SO_2 oxidation reaction to form SO_3 .

In the next section, a background on the formation of sulfuric acid H_2SO_4 from SO_3 hydration process and its importance in coal-power plants are analyzed.

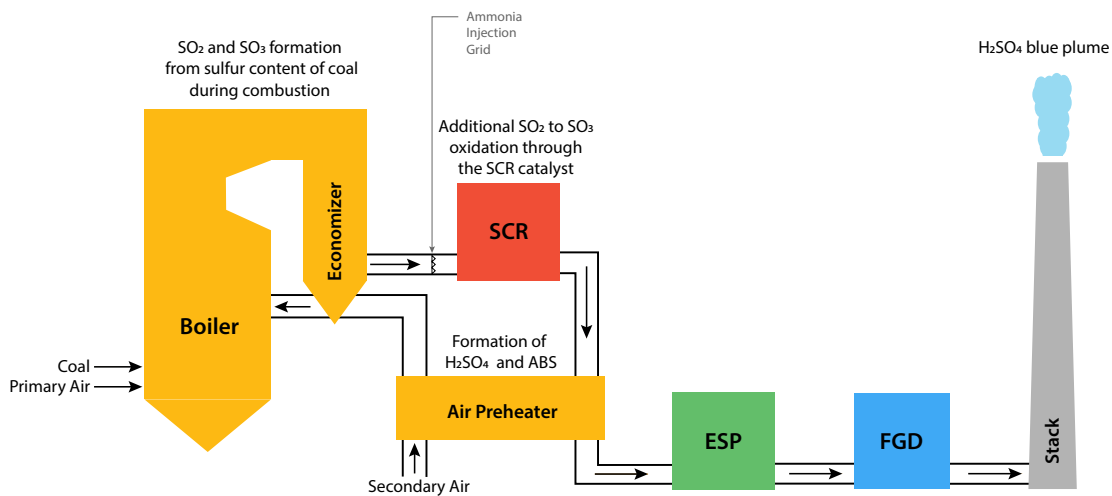


Figure 1.1: Simplified schematic of a coal-fired power plant.

1.3 Sulfuric acid (H_2SO_4) formation

Sulfur trioxide reacts rapidly [24–27] and exothermically [28] with water, to form sulfuric acid according to the reaction:



The hydration of SO_3 has been extensively studied in atmospheric chemistry [29], but studies in post-combustion conditions are lacking. Despite its prevalence and importance, the detailed steps in the conversion reaction from SO_3 to H_2SO_4 is not fully understood, as SO_3 and H_2SO_4 experimental measurements are complicated by surface reactions and other heterogeneous reactions. In fact, the reaction can proceed both as a homogeneous reaction (gas-phase) and as a heterogeneous reaction, such as reactions with adsorbed H_2O or SO_3 on reactor surfaces [30, 31] and condensation aerosols from binary homogeneous nucleation at high SO_3 and H_2O concentrations conditions [27, 30, 32].

Several experimental studies highlighted the extremely fast [24–27] and violent [28] character of the reaction, suggesting the absence of an energy barrier [24]. However that is in contrast to the notion that SO_3 and H_2O are two stable molecules [31]. Instead, the reaction might progress with the formation of an intermediate adduct $\text{SO}_3 \cdot \text{H}_2\text{O}$ [25], but the reaction through the adduct is still unlikely due to the high energy barrier between the adduct $\text{SO}_3 \cdot \text{H}_2\text{O}$ and H_2SO_4 . Any adduct with sufficient energy will in fact more likely dissociate back to its reactants [26, 33]. Additional studies highlighted that the reaction has second-order dependence on water vapor concentration and a strong negative temperature dependence. This once again suggests there is the formation of bound intermediates and a complex mechanism. Similarly to the above, the large activation energy barrier for the SO_3 adduct may prevent the reaction pathway [32]. This high energy barrier makes the process impossible without a relying on catalysts [34], and water clusters possibly have a role in promoting H_2SO_4 formation [26, 33]. Other studies confirmed that the reaction is second order in water vapor, with observed SO_3 consumption likely involving reaction with the water dimer $\text{SO}_3 + (\text{H}_2\text{O})_2 \longrightarrow \text{H}_2\text{SO}_4 + \text{H}_2\text{O}$, or a competing path $\text{SO}_3 + (\text{H}_2\text{O})_2 \longrightarrow \text{SO}_3 \cdot \text{H}_2\text{O} + \text{H}_2\text{O}$. However, it was unclear whether H_2SO_4 was also formed directly through the reaction of the adduct with water vapor $\text{SO}_3 \cdot \text{H}_2\text{O} + \text{H}_2\text{O} \longrightarrow \text{H}_2\text{SO}_4 + \text{H}_2\text{O}$ [27]. The energy barrier values obtained from $\text{SO}_3 + 2 \text{H}_2\text{O}$ reflected a considerable decrease, when compared to the reaction of SO_3 with one water molecule only. The relatively large energy barrier, not sup-

ported by experimental data, suggests that other reaction pathways are contributing to the formation of H_2SO_4 [35]. For example, the addition of a third and fourth water molecule that does not participate in proton transfer but acts as catalyst by stabilizing the reactant complex and products reduce significantly the energy barrier to almost zero [34, 35]. The reaction involving just one water molecule was shown to be too slow by about 23 orders of magnitude to account for the experimental behavior, while the reaction involving two water molecules agrees better but is still slower by three orders of magnitude [36]. An additional possible contributing factor is that H_2SO_4 can act as an auto-catalyst, and an increase in the rate constants between 5 times and 2 orders of magnitude for the H_2SO_4 -catalyzed SO_3 hydrolysis compared to the H_2O -catalyzed hydrolysis has been estimated [37].

Despite all of the uncertainty in the above described literature of potential reaction pathways, given the empirically observed fast character of the reaction, sulfuric acid is often assumed to be in chemical equilibrium with SO_3 at flue-gas conditions, which depends on temperature and water vapor concentration. According to the chemical equilibrium, increases in temperature shift the reaction towards SO_3 , while a decrease in temperature would shift it towards H_2SO_4 , as shown in Figure 1.2. The expectations of equilibrium (and the rate at which species achieve equilibrium) is particularly important for flexible-operations of coal power plants, where the temperature varies based on the load, as shown in Figure 1.3. Although the assumption of equilibrium is often made, the direct evidence for it under flue gas conditions has not been obtained. Providing such evidence is one of the objectives of the current work.

While there is no direct limit imposed by the Environmental Protection Agency (EPA) on the emissions of H_2SO_4 , sulfuric acid is responsible for the formation of a visible blue plume [6] that violates EPA rules on exhaust opacity.

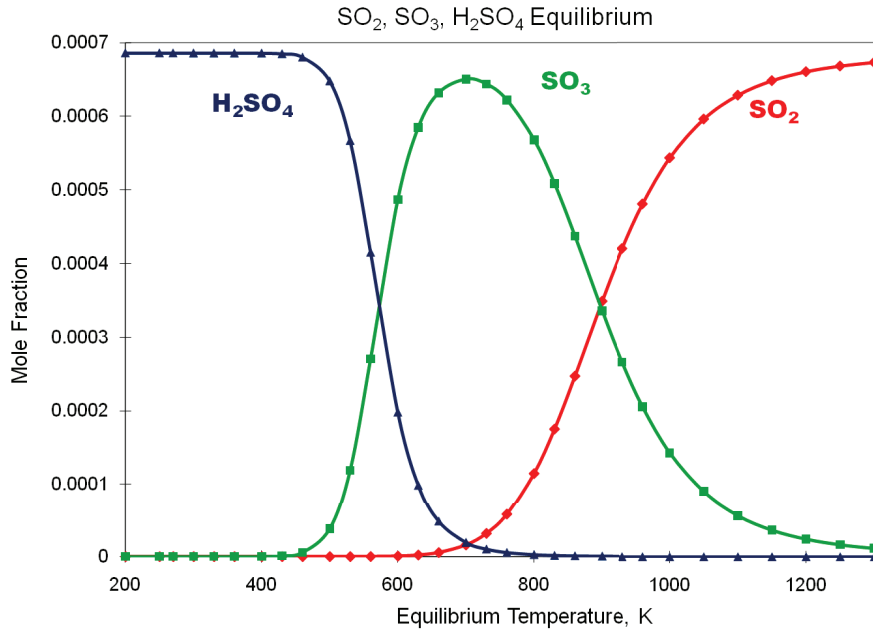


Figure 1.2: Notion of chemical equilibrium between sulfur compounds [38].

1.4 Flexible operations of coal-fired power plants

The recent preference towards the use of renewable energy sources over fossil energy sources like coal is expected to lead to major impacts on the operating patterns of coal-fired power plants [39]. With the increasing penetration of renewable energies the coal-fired power plants are required to adjust their output levels in a load-following mode to satisfy the grid demands and face an increase in the frequency of start-up and shut-down events to accommodate for the renewable power generation profile [40–43]. For example, the 2013 Western Wind and Solar Integration Study Phase 2 analyzed the simulated impact of 35% renewable energy on the Western Interconnection. The study predicted a marked increase in ramping requirements for operating fewer hours per each power plant start event and ramping daily instead of weekly as wind/solar penetration increases [44]. As most coal power plants were designed primarily for the purpose of baseload operation, they suffer from wear-and-tear damage from load cycling. Load cycling will lead to increased operations and maintenance costs accounting for more frequent repairs, reduced component life, more frequent forced outages, and in

turn a negative effect on the plant's marginal costs [44].

Figure 1.3 represents the temperature at the inlet of the SCR catalyst increasing from 500F to 675F (260C to 357C, 533 to 630K) with increasing power plant load. For the power plant of Figure 1.3, the nominal minimum load is 400MWg, with nominal minimum temperature of 550F (287C). The aforementioned temperature range is particularly important for this study, as the SCR inlet is one of the suggested locations for continuous measurement of sulfur species (addressed in Section 1.7). As previously seen in Figure 1.2, in that temperature range the $\text{SO}_3/\text{H}_2\text{SO}_4$ chemical equilibrium can completely shift from 100% H_2SO_4 at the lower end of the range to >80% SO_3 at the upper end. In summary, the expectation of chemical equilibrium plays the key role during flexible-operations, as the temperature of the flue gas varies based on the load. If SO_3 and H_2SO_4 are at equilibrium with each other, the measurement of only one of the two species together with the knowledge of temperature and water vapor content is enough to determine the value of the other. To date, there is no direct experimental verification of the chemical equilibrium between SO_3 and H_2SO_4 in flue gas conditions. One of the main goals of this dissertation is therefore focused on addressing this verification experimentally through spectroscopic measurements.

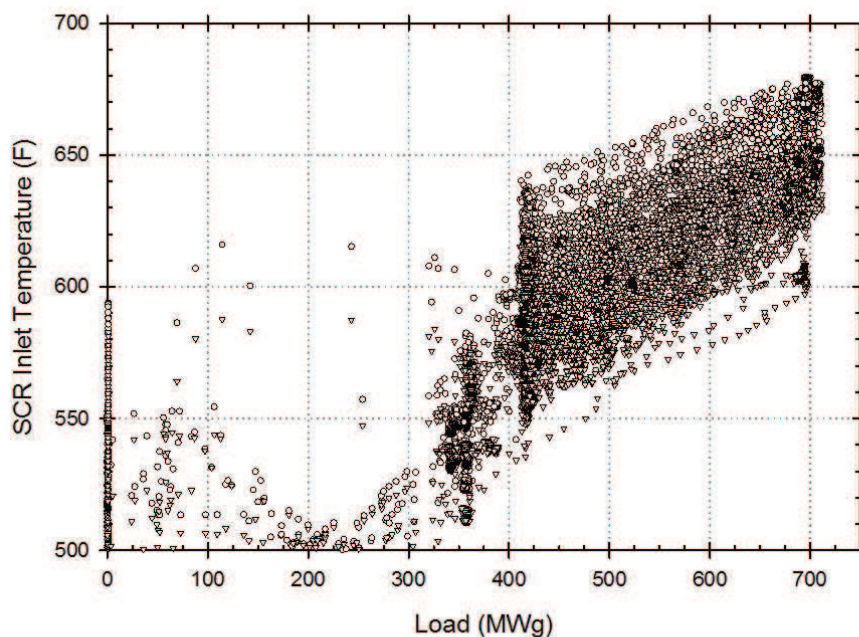


Figure 1.3: SCR inlet temperature as function of the load [45]

1.5 Pulverized coal and circulating fluidized bed technologies

Coal-fired power plants have historically relied on pulverized coal combustion (PC) for utility-scale power generation, though in recent years circulating fluidized bed combustion (CFB) has emerged as a possible alternative [20]. CFB offers a greater degree of fuel flexibility and the possibility of in-situ desulfurization through limestone injection directly in the boiler, but its adoption has been hindered by higher capital costs, smaller unit size preventing economy of scale, and high auxiliary power needed (leading to an overall lower efficiency) [20]. The in-situ desulfurization in the boiler is an appealing concept, with the possibility of capturing up to 90% of the sulfur dioxide output without the use of a separate flue gas desulfurization system and possibly decreasing operating costs [46, 47], but the process still presents major uncertainties [48].

An FGD system used with a PC boiler requires typically slightly above the stoichiometric amount of limestone for the capture of sulfur ($\text{Ca/S} < 1.1$), while limestone injection in fluidized bed boilers requires above 2 times the stoichiometric amount ($\text{Ca/S} > 2$) [46]. Therefore, CFB boilers have to use much larger amounts of sorbent with respect to FGD, but on the other hand FGD scrubbers take more space and consume much water [46]. A 90% reduction in SO_2 emissions with CFB technology could still be insufficient to comply with environmental regulations, as the typical emission control capability of a typical CFB boiler is $\sim 200 \text{ mg/Nm}^3$ for SO_2 [49]. For example, China requires all coal-fired power plants to meet the ultra-low emission standard (ULE) by 2020, with SO_2 emissions limited to 35 mg/Nm^3 [50]. The ULE requirements can drive the adoption of low-sulfur fuels, and a further increase in Ca/S ratio to decrease emissions. However, the increase of limestone in the boiler is bound to increase NO_x and a lower boiler efficiency [47]. The issue is particularly challenging for high-sulfur coals, which is a large part of China's coal resources [51] and for which the desulfurization in the CFB boiler have to be necessarily complemented by a FGD system

[47]. If a FGD system is added downstream from the CFB boiler to meet regulations, then the technology loses its economical emission control advantage and becomes less competitive than a PC boiler with FGD [49]. The decision between PC and CFB boilers for a new power plants is not trivial, and the desired degree of fuel flexibility and/or quality of the locally available coal can be the determining choice.

In the context of this work, another important factor is the requirement on load following capabilities (described in Section 1.4). The load following capability of CFB can be slightly inferior to that of PC, as the large mass of bed material carries considerable thermal inertia. The thermal inertia is particularly relevant for cold start-up events, as the ignition can require the consumption of large amounts of oil [20]. In addition, the dynamics of the boiler is strongly non-linear, resulting in the need of complex control systems to manage the coupling between the boiler's slow dynamics with the turbine's fast dynamics [52]. It is possible, however, to operate CFB boilers at lower loads with respect to PC boilers without the need of supporting fuel. Even if operations at low load and low circulation are possible, they can negatively impact the efficiency of the desulfurization process in the boiler [20].

While this study targets traditional PC boilers, it is clear that the presence of sulfur species (and related problems) is ubiquitous in coal-combustion processes and the possibility of continuous detection of sulfur species in flue gas remains a relevant problem. The difference between the two technologies in the context of this work is likely related to the levels of sulfur species present past the boiler at the measurement location, namely lower SO_2 and SO_3 expected levels in the CFB case.

1.6 Ammonium bisulfate (ABS) formation

After the flue-gas flows past the NO_x control system (SCR or SNCR), sulfur oxides and water can react with the ammonia slip from the SCR/SNCR to form ammonium bisulfate (ABS) and ammonium sulfate in correspondance of the air preheater, where temperatures

are below 500F (260C). ABS is known to cause corrosion and pluggage in the air preheater that can require unplanned outages and expensive cleaning [53, 54].

When coal-fired power plants operate at lower loads, the temperature of the gas entering the SCR catalyst will decrease, potentially resulting in the formation of ABS on the SCR catalyst itself, decreasing its activity and performance [55]. The issue can extend to natural gas combustion, albeit the level of sulfur of these fuels is usually reduced by hydrodesulfurization to meet regulations.

ABS formation can occur from a three-body reaction with ammonia, water, and sulfur trioxide, SO_3 , (Equation 1.5a), or from a two-body reaction between ammonia and sulfuric acid (Equation 1.5b). Equation 1.4a can act as an intermediary reaction for ammonium bisulfate formation [38].



The presence of SO_3 , H_2SO_4 , NH_3 , and ABS is also linked to the formation of ammonium sulfate, and both ammonium sulfate and ammonium bisulfate can act as initial precursors for the nucleation of aerosol particles [56]. Sulfate aerosols are responsible for the formation of PM2.5 [57]. Knowing the key sulfur compounds and their precursor species, along with the thermal conditions encouraging their formation, it is then possible to identify the segments of the power plant most appropriate for monitoring them. As can be seen from the discussion above, SO_3 is the key species from which the subsequent compounds form, and consequently the continuous monitoring of SO_3 is the highest priority.

1.7 Practical considerations for SO_3 and H_2SO_4 continuous measurements

Figure 1.4 represents a simplified schematic of a coal-fired power plants, together with the expected typical temperature conditions at every point. A simplified schematic of a typical coal-fired power plant was represented in Figure 1.1. Potential sampling locations for a SO_3 monitor demonstration are (1) the economizer outlet, which is the optimal location to evaluate and contrast ABS formation; (2) the SCR inlet, which provides similar advantages to the economizer outlet, although ammonia presence can negatively impact the measurement; and (3) the SCR outlet, where the highest concentration of SO_3 will be found, resulting from SO_2 oxidation in the SCR. Each of the options has respective advantages related to the flue gas desulfurization system adopted. For example, sorbent injection before the SCR catalyst would be better complemented by strategies (1) or (2), while a downstream FGD is likely better suited to operate in coordination with strategy (3). As sulfur trioxide concentration further increases across the SCR catalyst, strategy (3) is slightly more convenient for spectroscopic detection and measurements of SO_3 . However, especially for a demonstration on an existing plant or for a retrofit monitoring approach, the choice is often limited by the physical accessibility of the location and the presence of proper view-ports for each power plant. As a secondary consideration (for demonstration efforts particularly) the location should also offer good weather protection and reduced ambient temperature to minimize the operator's discomfort.

As seen in Figure 1.3, the gas temperature at the SCR outlet is highly dependent on the load, and its range (500 F to 680 F, correspondent to 260C to 360C) can significantly shift the chemical equilibrium from SO_3 to H_2SO_4 and vice versa (see Figure 1.2). This is particularly important, as seen in the temperature variations of Figure 1.3, for coal power plants operated in a flex-ops regime, with high load variability. Under such variability, it is evident that an accurate characterization of the equilibrium $\text{SO}_3/\text{H}_2\text{SO}_4$ is fundamental to

provide meaningful measurements and continuous monitoring.

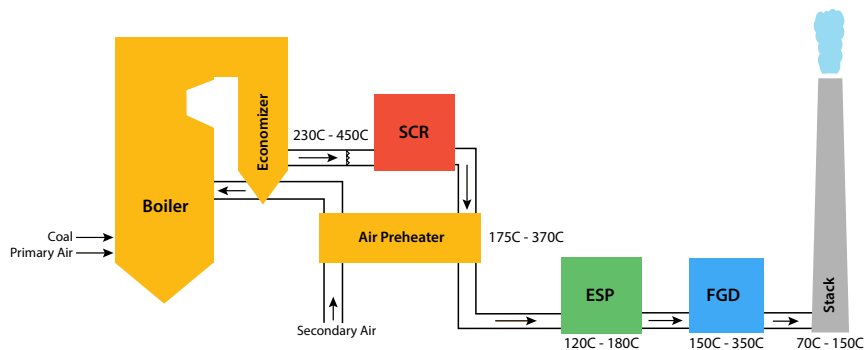


Figure 1.4: Simplified power plant schematics with relevant temperatures

1.8 Motivations and objectives

The presence of sulfur species in coal-fired power plants flue-gas can negatively impact the environment and power plant operations if the flue-gas is not properly treated. This is true independent of the type of coal power plant since the sulfur inherent in the coal fuel means that any combustion will produce high levels of sulfur oxides. Fuel desulfurization is currently too costly to implement and any mitigation strategy will involve treating the combustion or flue gases. Capturing sulfur from flue gas involves the use of a sorbent brought into contact with the sulfur containing gas, but the level of sorbent needed depends on the amount of sulfur in the exhaust and its form. Too little sorbent can lead to unlawful emissions and too much sorbent is an operational cost that can affect substantially the profitability of the power plant. In addition, the conditions of operation can affect the sulfur species conditions in the flue gas and so the first step in the mitigation strategy would ideally include continuous and direct measurements of sulfur species, in order to properly tune the amounts of sorbents needed for the desulfurization step. A closed-loop control of this kind would reduce both operating costs and environmental impact. To date, however, there are no continuous real-time sulfur-species measurement techniques able to fulfill the requirements needed for effective control. The reason that there is no commercial method

currently available is that the highly reactive sulfur species make the methods used for other more stable emissions ineffective. In addition, the division of reactive sulfur between sulfuric acid and sulfur trioxide varies with conditions, and both species need to be determined to be sure to capture the concentration accurately. There have been some techniques proposed that assume equilibrium conditions between SO_3 and H_2SO_4 and then measure only one of them. For example, the Breen approach condenses sulfuric acid onto a conductive probe to determine the acid dewpoint and from that information determines the gas composition. Another instrument, SICK MCSO3, captures a sample from the stack and then reheats it to the conditions of the sample location for an ex situ measurement using IR absorption with the assumption that the gas composition will have returned to its original state (more about the various techniques appear in Chapter 2). This continuous equilibrium view is an inviting concept but the chemical equilibrium between sulfuric acid H_2SO_4 and sulfur trioxide SO_3 has never been verified using direct experimental measurements in flue gas conditions.

Based on the need for verified continuous monitoring methods for sulfur species in flue gas conditions, this dissertation has the following three main elements:

1. Develop and build an experimental rig able to reliably generate simulated flue-gas conditions, in terms of temperature and chemical species for use in evaluating continuous monitoring methods for sulfur species
2. Analyze the feasibility of continuous measurements using two promising spectroscopic techniques, Differential Optical Absorption Spectroscopy (DOAS) in the UV and External Cavity Quantum Cascade Laser (ECQCL) in the Mid-IR
3. Investigate the chemical equilibrium between SO_3 and H_2SO_4 through direct spectroscopic measurements to determine if the common assumption is reasonable and can form the basis for monitoring only a single species.

This current work relies on optical absorption methods heavily which means that the spectral signature of the important species will be critical for the success of any technique. While

spectral information is generally accessible for sulfur dioxide SO_2 , it is largely unavailable for SO_3 and H_2SO_4 at the temperatures of interest (between 250C and 350C). A fundamental portion of this work is therefore aimed at defining spectral libraries for SO_2 , SO_3 , and H_2SO_4 at temperatures between 250C and 350C from direct experimental readings.

The remaining chapters of the dissertation cover an overview of the existing measurement techniques together with the ones used in this work (Chapter 2), a description of the experimental setup (Chapter 3), a complete numerical characterization of the newly designed high-temperature measurement cell (Chapter 4 and Chapter 5), and finally the experimental results (Chapter 6). The last chapter presents the closing remarks and conclusions, together with suggestions and future work recommendations (Chapter 7).

Chapter 2

Experimental methods

This chapter will first introduce the current state-of-the-art methods used in industry for the determination of sulfur species, and it will then cover the details and literature review of the specific methods of Differential Optical Absorption Spectroscopy (DOAS), External Cavity Quantum Cascade Laser (ECQCL), and Environmental Protection Agency (EPA) Method 8A that will be used experimentally in this research.

2.1 Industry-standard methods to measure sulfur species concentration

As described in the introduction, there is no technique capable of measuring the reactive sulfur species continuously and in real time. However, the desirability of such measurement has spawned a wide range of attempts with varying levels of success and precision. In order to provide the context for the work in this dissertation the current status of industry-oriented flue gas sulfur measurements is outlined. Current measurement techniques are summarized in Table 2.1 and Table 2.2. Since many of these methods are commercial, the references to them are company website information, primarily. There is no peer-reviewed literature that

critically evaluates their performance so the main information source comes from informal discussions at conference meetings associated with attempts by the Electric Power Research Institute (EPRI) to evaluate their accuracy and stability in pilot testing. There is not, therefore, any clear fundamental reason limiting their measurement ability but the practical experience is that aspects of each method contain unresolved problems. The primary proof that issues remain with the current techniques is that none of them (with the exception of EPA method 8A) are in regular use in the industry.

Company	Sampling Method	Measurement Method	Performance
GeoSyntec	Custom sampling line	FTIR	Not commercial. Unclear accuracy
SICK MCSO3 [58]	Heated sample line and cell (200C)	Broadband NDIR 1-16 μm wavelength range absorption	Can measure H_2SO_4 , SO_2 , and SO_3 . Questions on effect of line cooling on the accuracy of the measurements
ProCeas SO_2/SO_3 analyzer [59]	Low pressure sampling (100 mbar) and non- heated/modestly heated lines	IR laser cavity absorption, with broad spectral range	Given low pressure sampling, ques- tions on faithful representation of in- flow condition
ThermoFisher Arke SO_3 [60]	Dilution extractive heated probe with built-in SO_3 gener- ator and dust filter. Oxidizes SO_2 to SO_3 for the calibration	QC laser in high tempera- ture optical cell. Narrow QCL linewidth allows separa- tion from water and SO_2	Narrow sweep spectral range
PNNL OKSI [61]	Heated line	EC-QCL IR spectroscopy	Being tested at UCI in heated cell with windows
Unisearch DOAS [62]	Heated line	UV absorption	Being tested at UCI in heated cell with windows

Table 2.1: Current state-of-the-art in optical techniques to measure the concentration of SO_3 , SO_2 , and H_2SO_4 .

Name	Sampling Method	Measurement Method	Performance
EPA Method 8A [63]	Heated line with quartz filter	H ₂ SO ₄ condensation, SO ₂ reaction with H ₂ O ₂ , and sulfate ion analysis	Requires long sampling time if the concentration of SO ₃ is low. Assumption of full conversion and capture of SO ₃ to H ₂ SO ₄ . Results dependent on operator. Industry standard
EPA Method 8	Heated line	SO ₃ reaction with isopropanol, SO ₂ reaction with H ₂ O ₂ , and sulfate ion analysis	As for EPA Method 8A. Isopropanol captures also a part of the SO ₂ leading to overestimated SO ₃ values
Salt Method	Heated line	H ₂ SO ₄ reaction with NaCl	Has to operate in a regime where H ₂ SO ₄ is in the gaseous phase. Relies on notion of equilibrium SO ₃ / H ₂ SO ₄ . It does not provide SO ₂ concentration

Breen AbSensor SO ₃ [64]	In-situ probe	Acid Dew Point	Identifies the condensation temperature. Does not distinguish acids and depends on water conditions (analyzed theoretically to evaluate an accurate value for SO ₃). Assumption of equilibrium. Sampling not needed. It has shown good results for ABS condensation
-------------------------------------	---------------	----------------	---

Table 2.2: Current techniques to measure the concentration of SO₃, SO₂, and H₂SO₄ not relying on optical measurements.

2.2 Differential Optical Absorption Spectroscopy (DOAS)

As seen in the tables of techniques in the previous section, optical absorption methods have attracted substantial efforts, and DOAS is one of the promising in-situ optical measurement. The DOAS technique is already used for the measurement of several atmospheric trace gases [65], including sulfur dioxide [66]. In this section, a basic description is provided here only to highlight the aspects that are relevant to understand the current research. As with many spectroscopic measurements, the DOAS technique relies on Beer-Lambert's Law:

$$I(\lambda) = I_0(\lambda) \exp(-\sigma(\lambda) \cdot c \cdot L) \quad (2.1)$$

Where $I_0(\lambda)$ is the initial intensity emitted by a light source, $I(\lambda)$ is the intensity collected at the detector after the radiation has traveled through the media of length L . In the media, the concentration c of the absorber is considered uniform, and $\sigma(\lambda)$ represents the absorption cross-section as a function of the wavelength which is a characteristic property of the absorber species. The absorption cross-section can depend on temperature as well, since the population distribution among energy states changes with temperature.

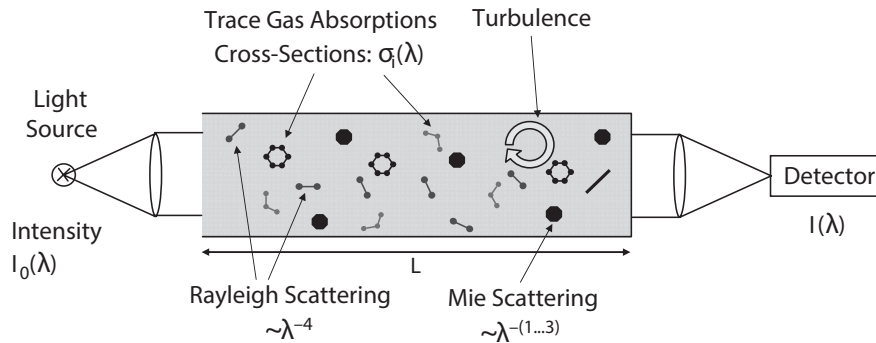


Figure 2.1: The basic principle of absorption-based spectroscopic trace gas detection [65]

In most cases, the unknown in Equation 2.1 is the concentration c , that can be expressed

as:

$$c = \frac{\ln\left(\frac{I_0(\lambda)}{I(\lambda)}\right)}{\sigma(\lambda) \cdot L} = \frac{D}{\sigma(\lambda) \cdot L} \quad (2.2)$$

where D represents the optical density of the media (also called the Napierian absorbance).

When the light travels through the media, its intensity is reduced also by the absorption of other gases, as well as from scattering by air molecules and aerosol particles. A DOAS technique takes advantage of the fact that aerosol extinction processes, the effect of turbulence, and trace gas absorption show broad or evenly smooth spectral characteristics, while the target gases of interest will exhibit narrowband absorption structures. By separating broad and narrowband spectral structures in an absorption spectrum, it is possible to isolate the narrow features given by individual gases and apply Beer-Lambert's Law to the narrowband absorption. Only to species with absorption structures significantly narrower than the typical measuring window of 15-40 nm can be measured with the DOAS technique [66].

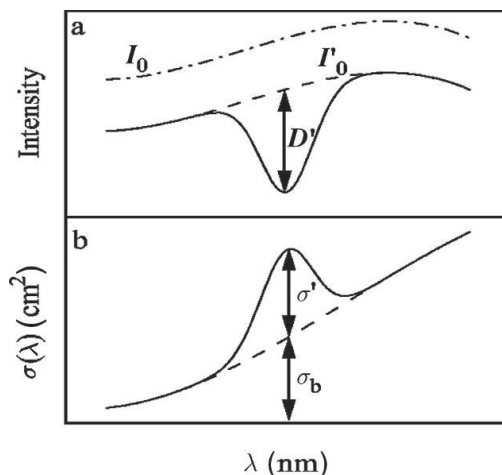


Figure 2.2: Principle of DOAS: I_0 and σ are separated by an adequate filtering procedure into a narrow (D' and σ') and broad band part (I'_0 and σ_b) [65].

At shorter wavelengths, the usable spectral range of DOAS is limited by rapidly increasing Rayleigh scattering and O_2 absorption features starting around 280 nm and below [67].

A significant issue related to DOAS in the context of this work is that experimental and

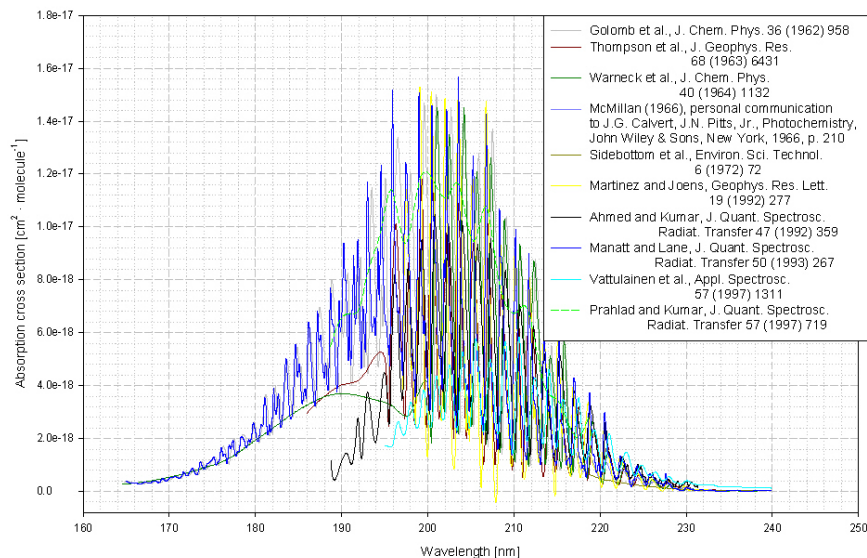
numerical studies did not identify any absorption that could be attributed to sulfuric acid. In fact, the first electronic transition for sulfuric acid is estimated to occur at 81800 cm^{-1} (or 122 nm) [68, 69], while the current study focuses on the lower energy $200 - 300\text{ nm}$ UV region for the detection of sulfur species using DOAS. While the simultaneous determination of SO_3 and H_2SO_4 to ascertain the chemical equilibrium notion is hence precluded, it can still be possible to investigate indirectly if equilibrium holds by analyzing the SO_3 concentration drop that occurs when H_2O vapor is introduced into a previously dry flow. By difference, the drop in SO_3 concentration directly corresponds to the formation of H_2SO_4 , as previously explained in Section 1.3. The following sections provide an overview of the absorption cross-sections for sulfur oxides species in the analyzed UV region.

2.2.1 Differential absorption cross-sections for SO_2

The most significant challenge in the determination of SO_2 and SO_3 with DOAS technique is that their absorption spectra in the UV overlap, and under realistic operating conditions the concentration of SO_2 is often more than an order of magnitude larger than that of SO_3 [70]. A high resolution absorption spectrum for both of these species is therefore fundamental to assure detection.

Sulfur dioxide spectral measurements in the UV are widely available, mostly deriving from studies that examine sulfur dioxide concentration and behavior in the atmosphere. Figure 2.3 and Figure 2.4 give an overview of the wide availability and high level of agreement between the SO_2 UV spectral measurements from different sources. The data in the figures represents the absorption cross-sections for SO_2 in the UV region at room temperature from all the different sources collected in *The MPI-Mainz UV/VIS Spectral Atlas of Gaseous Molecules of Atmospheric Interest* [71]. SO_2 shows two active UV spectral regions with visible narrowband structures, one between 200 and 230 nm (Figure 2.3), and a second between 290 and 310 nm (Figure 2.4). The differential absorption cross-section for SO_2 at those wavelengths is well known [72], and it is characterized even at temperatures well above

1500K. Unfortunately, the high-resolution SO_2 spectrum collected at conditions closest to the temperatures of this work (250C to 350C, 523K to 623K) is reported only at the significantly higher temperature of 800K (526C) [71]. A low-resolution SO_2 spectrum is however reported at 400C (673K) [73], and is represented in Figure 2.6.



Low- and medium resolution absorption cross sections of sulfur dioxide SO_2 at room temperature (165-240 nm)

Figure 2.3: Absorption cross-sections database for SO_2 at room temperature (165-240 nm) [71].

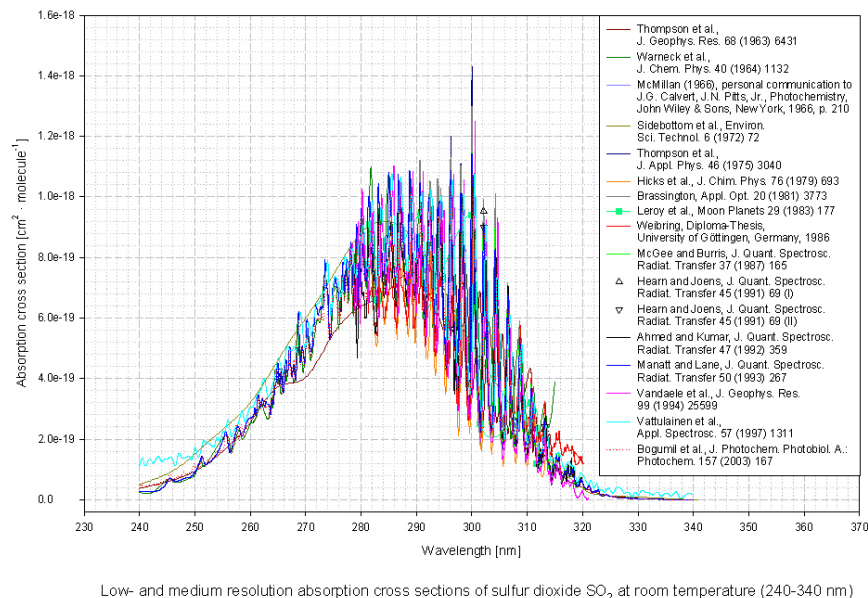


Figure 2.4: Absorption cross-sections database for SO₂ at room temperature (240-340 nm) [71].

Since the SO₂ UV spectrum has been extensively studied, also for temperatures relevant for flue-gases, the prospect of extending the DOAS technique for the experimental measurement of sulfur trioxide in this work is promising.

2.2.2 Differential absorption cross-sections for SO₃

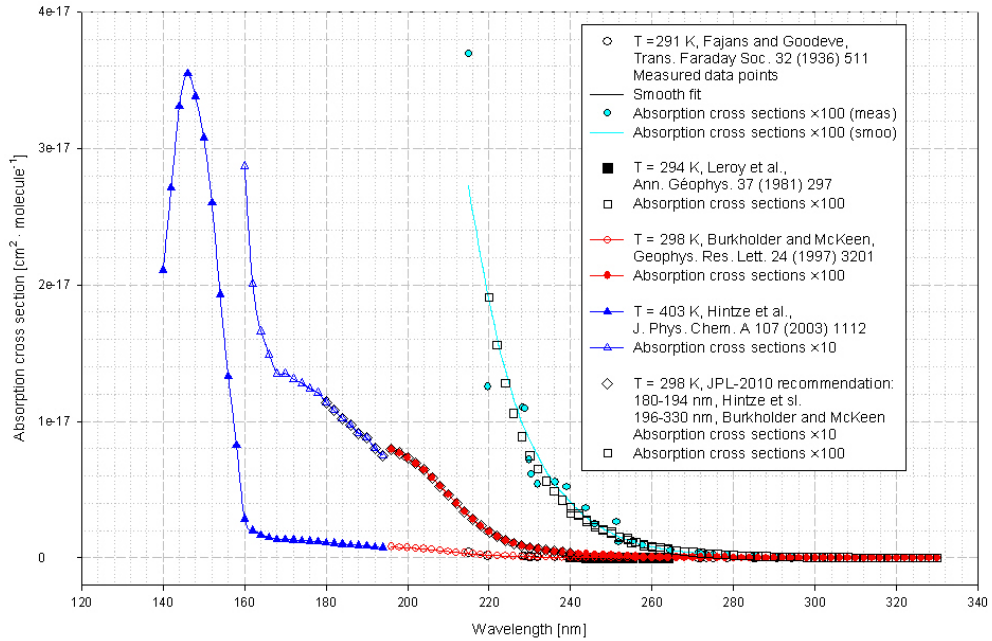
The absorption spectrum of SO₃ is continuous with a number of weak diffuse vibrational bands between 225 and 295 nm [70, 74], as seen in Figure 2.5, where the SO₃ spectra from different sources and collected in *The MPI-Mainz UV/VIS Spectral Atlas of Gaseous Molecules of Atmospheric Interest* [71], are represented. As seen from Figure 2.5, only a few sources of SO₃ spectral measurements in the UV region are available, unlike for SO₂. The maximum temperature at which the cross-section was recorded for Figure 2.5 was only 403K (129C), significantly lower than the temperatures relevant for flue-gas studies (250C to 350C).

The spectra of SO₃ in the UV are likely less available because the generation of a stable concentration of SO₃ at low temperatures – i.e., temperatures relevant to atmospheric studies

– presents a unique set of challenges. For example, handling of SO_3 poses important safety hazards, especially when it is generated using liquid SO_3 . Furthermore, if water vapor is present even at trace levels, it reacts with SO_3 to form H_2SO_4 . Sulfuric acid has low vapor pressure, so it will rapidly stick to surfaces and form a film on measurement cell windows altering the cell optical transmission [70]. Sulfuric acid formation can occur not only in homogeneous gas-phase reactions but also through heterogeneous reactions on surfaces and condensation aerosols, as mentioned in Section 1.3, complicating experimental efforts. Sulfuric acid is also very corrosive, and the minimization of H_2SO_4 formation is not trivial, especially at ambient temperature, where sulfuric acid formation is favored by its chemical equilibrium with SO_3 .

The absorption spectrum for SO_3 overlaps with the one for SO_2 in the region between 200 and 230 nm, as seen in Figure 2.6. At room temperature, the SO_2 cross sections are about 10 times larger in the 190 to 220 nm region, making the technique very sensitive to SO_2 presence [70]. The SO_2 and SO_3 spectra represented in Figure 2.6 results from experimental measurements of flue-gas at 400C, close to the flue-gas temperature conditions of this work (250C to 350C). However, the absorption spectrum of SO_3 is calculated by the subtraction of the SO_2 absorption spectrum contribution from the overall measured absorption spectrum, while the measurement in a condition were SO_3 is the only absorber species would be preferable, especially given their important overlap.

In flue-gas conditions, where the concentration levels of SO_2 are at least an order of magnitude larger than the levels of SO_3 , it will be very challenging to extract the SO_3 contribution from a measured absorption spectrum that is so strongly dominated by SO_2 absorption in the UV region. Hence, the accuracy of the spectral libraries is crucial, and the lack of high resolution SO_3 absorption information at flue gas temperatures complicates the potential for UV DOAS measurements of this species.



Absorption cross sections of sulfur trioxide SO₃

Figure 2.5: Absorption cross-sections database for SO₃ [71].

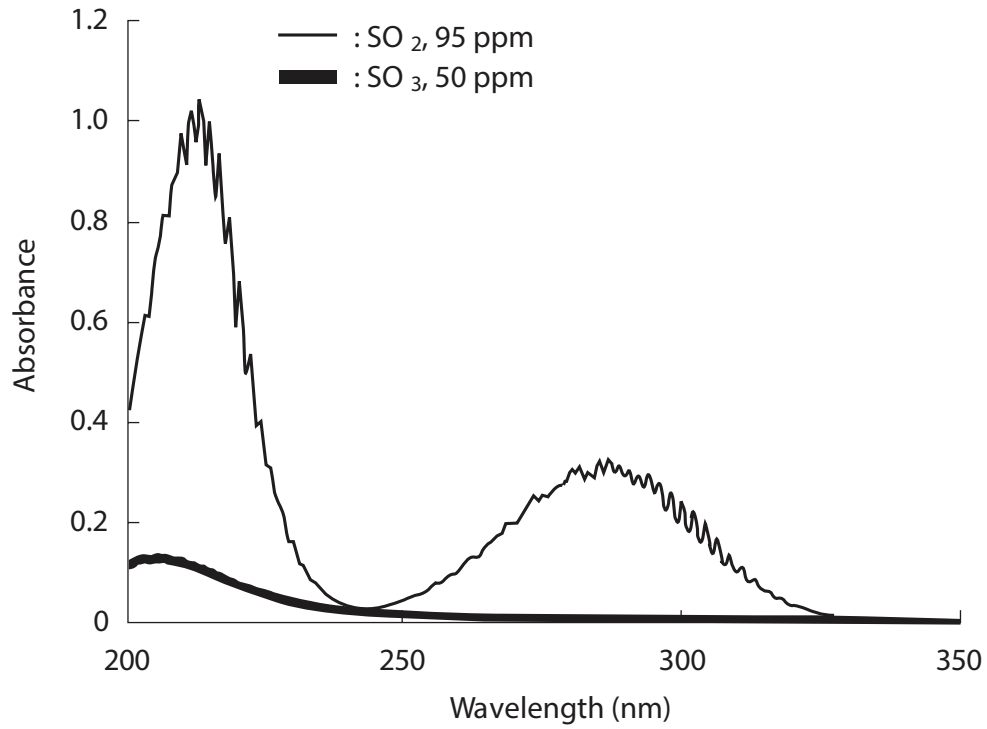


Figure 2.6: Absorption spectra of SO₃ and SO₂ at 400 C [73].

2.3 External Cavity Quantum Cascade Laser (ECQCL)

As described in the previous section, the DOAS technique in the UV region can present issues in the determination of the sulfur species, because of the lack of absorption features for sulfuric acid and the complete spectral overlap between the strong absorber SO_2 and the weak absorber SO_3 . In turn, this creates challenges in distinguishing low concentrations of SO_3 from an absorption spectrum largely dominated by high concentrations of SO_2 . While the DOAS technique typically uses a broadband light source with spectral separation relying on a spectrometer-based detector, a possible alternative technique is to use mid-IR detection of sulfur species using scanned narrowband light from an ECQCL. A brief introduction of the technique is here provided.

Diode lasers rely on lasing transitions occurring between the conduction band and the valence band, and this limits access to mid-infrared wavelengths, particularly in the molecular fingerprint region between 2 and $20\mu\text{m}$ [75, 76]. In a quantum cascade laser, the lasing transition occurs between energy levels that do not exist naturally in the constituent materials of the active region but are artificially created by structuring the active region in ultra-thin layers known as quantum wells [75]. This approach allows the production of lasers finely tuned on precise wavelengths. Using a grating-coupled external-cavity adds complexity but allows the extension of the tuning range [77]. External-cavity quantum cascade lasers (ECQCLs) are therefore considered excellent sources for mid-IR spectroscopy due to their high spectral brightness, narrow spectral linewidth, and broad wavelength coverage ($\Delta\lambda/\lambda > 10\%$) [78]. Available commercial ECQCL systems can achieve wide tuning range up to 250cm^{-1} at 100Hz scan rates, with 2cm^{-1} typical spectral linewidth, with the possibility of combining multiple modules to achieve a range of over 1100cm^{-1} [79]. Even with this performance potential, there are tradeoffs between the width of the tuning range, the velocity at which the range is scanned, and the spectral resolution. For real-time gas detection, as for this

study, a spectral acquisition rate faster than 1Hz is desired in order to detect rapid changes in concentrations. In terms of spectral resolution, the narrowest atmospheric pressure gases spectral features are typically $>0.1 \text{ cm}^{-1}$ wide [78], and a wide tuning range is needed to differentiate different chemical species whose spectra overlap [78]. Fourier transform infrared (FTIR) spectroscopy has similar spectral potential to the ECQCL approach but in FTIR the rate of scanning is lower, the spectral intensity of the source light is weaker, and the physical footprint of the instrument is larger [80]. While effective in steady laboratory conditions, all of these have made FTIR instruments undesirable for implementation in the field at power plants.

In this work, two ECQCL lasers from Opto-Knowledge Systems, Inc. (OKSI) are used. One is ECQCL7, scanning from 1470 cm^{-1} to 1265 cm^{-1} ($6.8 \mu\text{m}$ to $7.9 \mu\text{m}$) at 100Hz rate and 0.03 cm^{-1} spectral resolution. The other is ECQCL8, scanning from 1282 cm^{-1} to 1111 cm^{-1} ($7.8 \mu\text{m}$ to $9.0 \mu\text{m}$) at 100Hz rate and 0.04 cm^{-1} spectral resolution. Measuring concentrations of sulfur species using the ECQCL approach requires the knowledge of their mid-IR absorption spectra at conditions matching those of the expected measurement, and these spectra are described and investigated in the next sections.

2.3.1 Mid-infrared transitions for SO_2

The high-resolution transmission molecular absorption database (HITRAN) provides a suite of parameters (mixture of direct observations, theoretical calculations, and semi-empirical values) that are used as input to various modeling codes, for example high-resolution line-by-line codes, to model transmission and emission of light in the atmosphere in the presence of absorber molecules [81]. The HITRAN database is the recognized international standard for fundamental spectroscopy studies, particularly for species of atmospheric interest [82].

Figure 2.7 shows the HITRAN-modeled spectrum for SO_2 and H_2O at the same concentration of 1% in a 1m measurement cell at 300K (27C). While the estimation of water vapor concentrations is not the focus of this work, it is highlighted in Figure 2.7 and Figure 2.8

since it can significantly impact the measurement of SO_2 (and SO_3).

Sulfur dioxide has two QCL-accessible Mid-IR vibrational bands, from 1100 to 1400 cm^{-1} is an asymmetric stretch band (ν_3) centered near 1360 cm^{-1} (7.35 μm), and a weaker symmetric stretch band (ν_1) is centered near 1150 cm^{-1} (8.7 μm) [83]. As seen from Figure 2.7, the asymmetric stretch ν_3 has much stronger absorbance, which is promising to achieve the highest sensitivity. However, there are several water absorption features interfering with ν_3 , and the extent of the interference is very important at high temperatures, as seen in Figure 2.8 with the predicted absorbance for the same mixture at 700K. The weaker stretch ν_1 , on the other hand, shows little to no interference from H_2O , even at high temperatures.

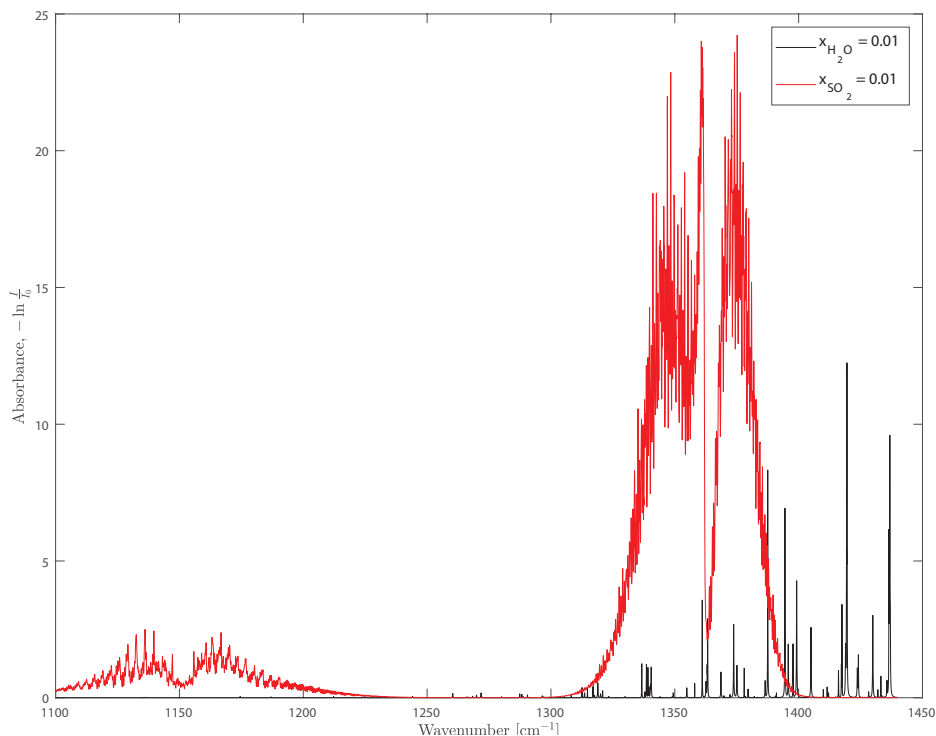


Figure 2.7: Predicted mid-IR spectra of SO_2 and H_2O at 300K in a 1 m path, modeled with SpectralCalc Gas-Cell Simulator tool using HITRAN2016 database [84].

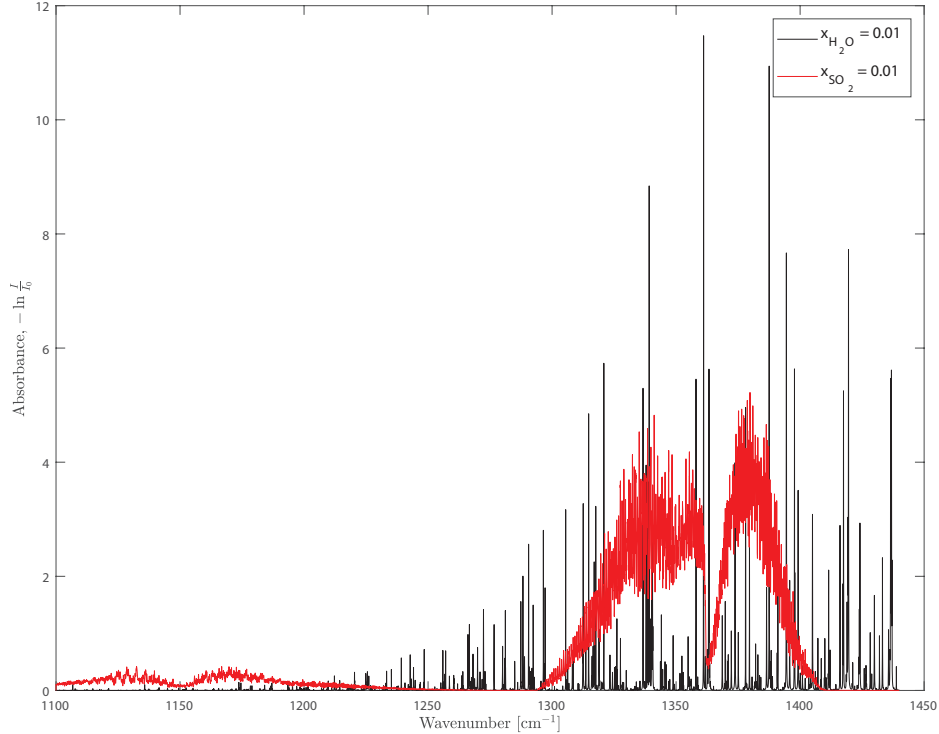


Figure 2.8: Predicted mid-IR spectra of SO₂ and H₂O at 700K in a 1 m path, modeled with SpectralCalc Gas-Cell Simulator tool using HITRAN2016 database [84].

2.3.2 Mid-infrared transitions for SO₃

Most of the literature available for the mid-IR spectrum of SO₃ only includes conditions of ambient temperature and reduced pressure. Only the ν_3 band centered at 1391.5 cm^{-1} ($7.18\text{ }\mu\text{m}$) is accessible to a QC laser, even if additional ν_2 and ν_4 bending bands are present in the infrared spectrum near 500 cm^{-1} [83]. The ν_3 band of SO₃ has been studied and reported, but with no line strength provided [85]. However, the peak absorbances lead to an estimation of the line strength comparable to those for SO₂ in the ν_3 stretch [83]. High resolution detailed FTIR absorption measurements were reported for SO₃ at low pressures and room temperature [86] and are represented in Figure 2.9, but these measurements do not give quantitative absorption strengths [87]. Hieta et al. used a narrowband QCL laser to access the high temperature (380C) and reduced pressure (60hPa) spectrum of SO₃ between 1396 and 1399cm^{-1} [88]. The approach is unsuited to ambient pressure studies, as the

rotational features of the spectrum widen and overlap to those of SO_2 and H_2O .

A recent study reported high-temperature measurement spectra of SO_3 together with SO_2 [89], and the SO_3 spectra are reported at 400C and 200C and represented in Figure 2.10, together with SO_2 absorbance spectrum at 200C. The SO_2 spectrum is reported as “artificially shifted”, but the reason and the details about the shift are not explained. In the work, SO_3 was generated by reacting SO_2 with ozone, and the resulting concentration of SO_3 was calculated from the laser-measured drop in SO_2 . Unfortunately, this approach has the risk of dismissing SO_3 losses along the flow path, especially since visible proof of H_2SO_4 formation and condensation on different surfaces was reported in the same work. The cross-sections provided in the report also did not match the absorbance data provided in the same report and here reported in Figure 2.10 for the given concentration values. As is well-known, it is very difficult to prevent sulfuric acid attachment to surfaces (and further, it is difficult to drive the sulfuric acid back off surfaces once there), and so any concentration based on difference will require independent confirmation of sulfur balance. This independent confirmation is included in the current work to appropriately bound uncertainty.

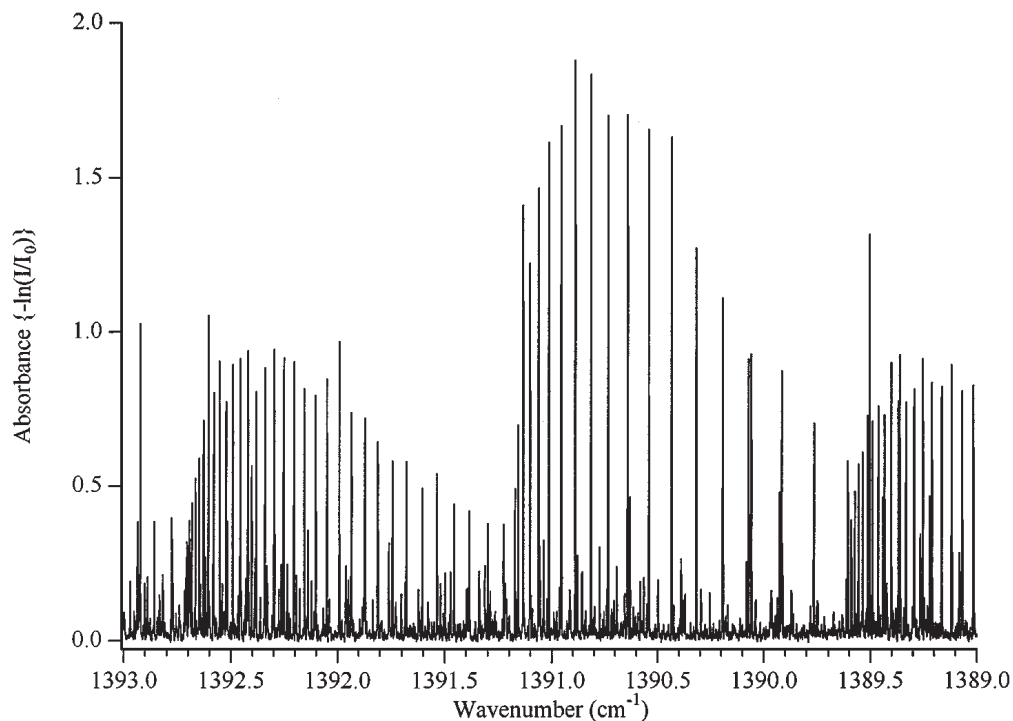


Figure 2.9: Central region of the ν_3 band of SO_3 at 0.002 cm^{-1} resolution at 298K with pressure 9.4 Pa [86].

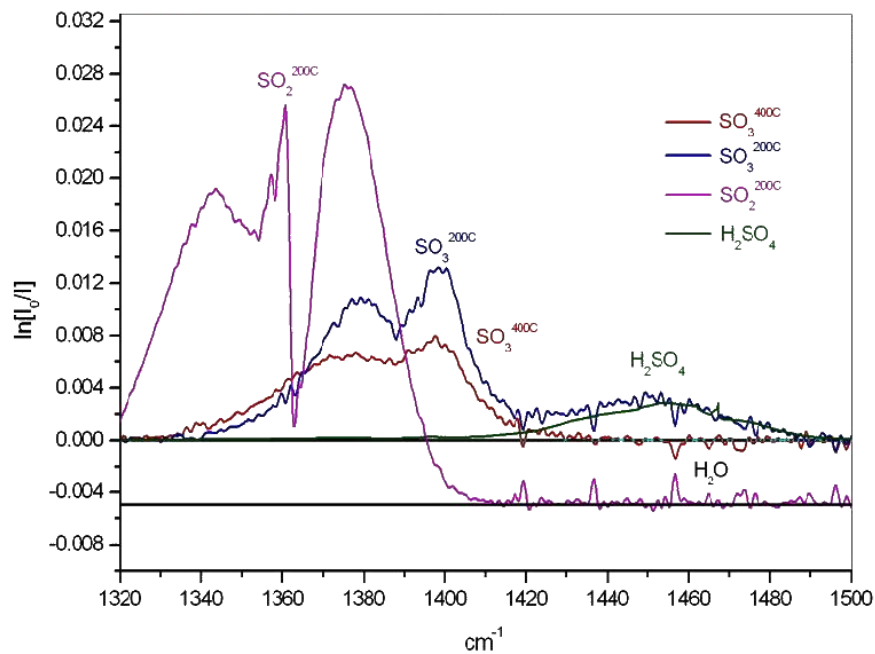


Figure 2.10: Measured absorption spectrum of 119 ppm SO_3 (at 200°C , blue), 100 ppm SO_3 (at 400°C , red), and 238 ppm SO_2 (at 200°C , magenta) in a 50 cm cell at ambient pressure [89].

The mid-IR spectrum of SO_3 has been the object of several studies, including cases at relevant temperature and pressure [89], but the precise characterization of the SO_3 spectrum at high-temperature is still lacking and the definition of high-temperature SO_3 spectral libraries in the current work can prove valuable for the scientific community.

2.3.3 Mid-infrared transitions for H_2SO_4

Vapor-phase sulfuric acid studies are subject to a different set of challenges with respect to SO_3 , such as aerosol formation [69] and sticking to surfaces [70], as reported previously in Section 2.2.2. There are several accessible bands for H_2SO_4 in the IR/NIR region, represented in Figure 2.11 [69]. The region between 1100 and 1300 cm^{-1} has been probed with FTIR at 185C (the pressure value is not reported) [90]. Because of the notion of chemical equilibrium between SO_3 and H_2SO_4 , and the expectation that sulfuric acid decomposes at high temperature, studies analyzing the spectra for H_2SO_4 have been limited to temperatures below 200 °C.

The measurements of H_2SO_4 at flue-gas conditions hence does not appear to be problematic for the current optical spectroscopy technologies. Rather, the main limitations lie in the low concentrations of H_2SO_4 present in the flue-gas at high temperature (as H_2SO_4 decomposes to SO_3) and in the practical challenges of operating with sulfuric acid, with possible formation of aerosols and sulfuric acid attack on surfaces.

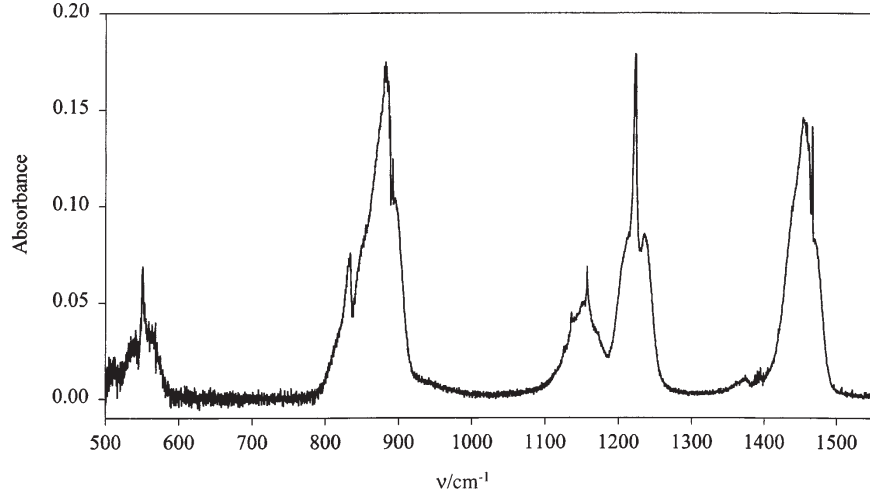


Figure 2.11: Vapor-phase IR spectrum of H_2SO_4 in the range of 500-1550 cm^{-1} . The spectrum was recorded at 150 °C with a path length of 100 cm [69].

Although the outlook for optical detection of gaseous sulfuric acid is very positive, other typical flue gas species, such as CO_2 and NO_x , can possibly influence the spectroscopic measurement, and their contribution has to be accounted for.

2.3.4 Mid-infrared transitions for other flue gas species

In flue gas several additional species are present at concentration levels larger than those of sulfur species. N_2 and O_2 are present at high concentration, but homonuclear diatomic molecules do not absorb in the mid-IR region. Figure 2.12 represents the contribution of different flue gas species at typical concentrations to the overall absorbance spectrum at 700K (425C), at a pressure of 1atm and 1m path length. The represented composition is 20% CO_2 , 2000ppm SO_2 , 2000ppm NO_2 , 500ppm NO , 500ppm CO , and 10ppm NH_3 . Ammonia presents several strong features below 1200 cm^{-1} , but it is present only at low concentrations after the SCR catalyst (ammonia slip) and therefore does not impact the measurement. CO_2 presents significant absorbance. However, it is situated at the margins of the operating region of ECQCL 8, and the overlap with SO_2 spectral features is minimal. It appears, therefore, that with the notable exception of water, the main gaseous species present in flue gas will not affect the optical measurement of SO_2 , SO_3 , and H_2SO_4 .

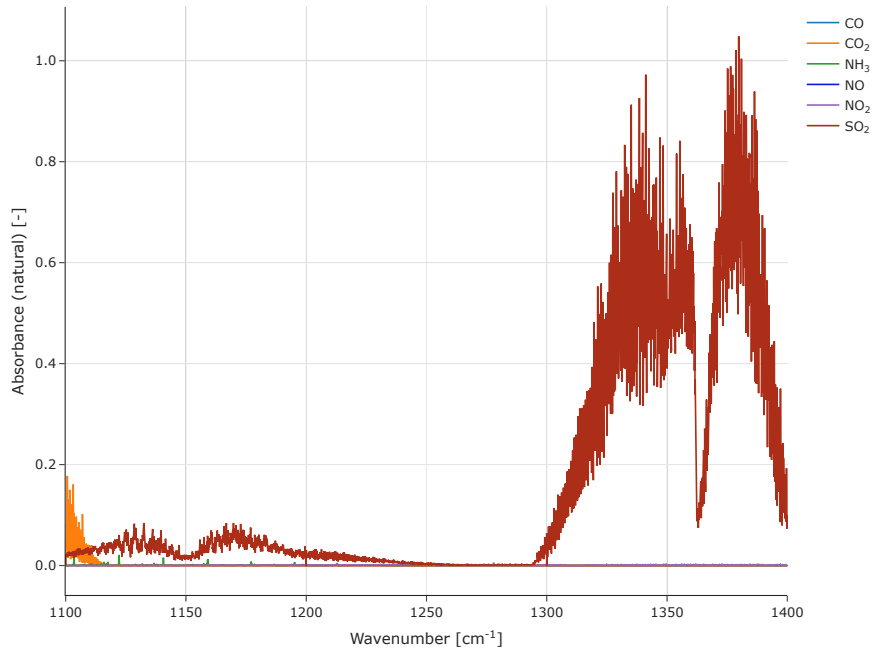


Figure 2.12: Predicted mid-IR spectra of 20% CO₂, 2000ppm SO₂, 2000ppm NO₂, 500ppm NO, 500ppm CO, and 10ppm NH₃ at 700K in a 1 m path cell at 1atm, modeled with SpectraPlot Gas cell simulator tool using HITRAN2012 database [91].

The spectroscopic measurements or the definition of spectroscopic libraries for chemical species require validation from other techniques in order to certify the process and the results. As noted earlier, this is particularly true when highly reactive species like sulfuric acid is involved. The following section will introduce the details of the current industry standard in sulfur oxides and sulfuric acid measurement in flue-gas conditions, and the EPA Method 8A will provide the independent verification needed to effectively bound the errors in the optical measurements presented.

2.4 Controlled condensation method: EPA Method

8A

The current industry-standard method for the determination of sulfur oxides and sulfuric acid measurement in flue-gas conditions is a sampling technique defined in EPA Method

8A [63], and it will be used in this work to validate the spectroscopy measurement. The schematics for the sampling system of EPA Method 8A [63] is shown in Figure 2.13. A sample of the gas is extracted and flows through a Modified Graham condenser, a coiled glass tubing of 200 cm length and 5-mm ID. The condenser is filled with water and the temperature is maintained between 75 °C and 85 °C (167 to 185F). The goal for the condenser is to operate below the dew-point temperature of H_2SO_4 and above the dew-point temperature of H_2O , in order to effectively collect only sulfuric acid. The condensation coil is followed by a train of three 500 mL impingers, two of which containing H_2O_2 in order to react and collect SO_2 . The samples from the condensation coil and from the impingers can later be analyzed with ion chromatography or titration (wet chemistry) to determine the sulfate concentration. This method is also referred to as “controlled condensation method”, given the presence of a condenser coil with controlled temperature. While it is the industry standard for measurement mandated by the EPA, Method 8A is known to suffer from relatively high variability associated with the wet-chemistry detection methods.

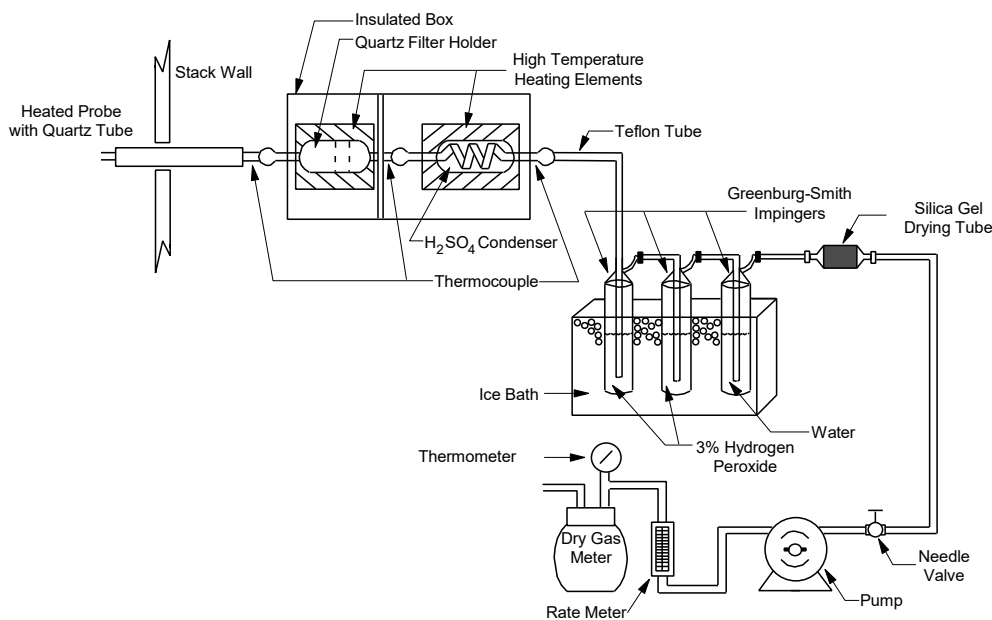


Figure 2.13: Schematics for the sampling system of EPA Method 8A (from [63]).

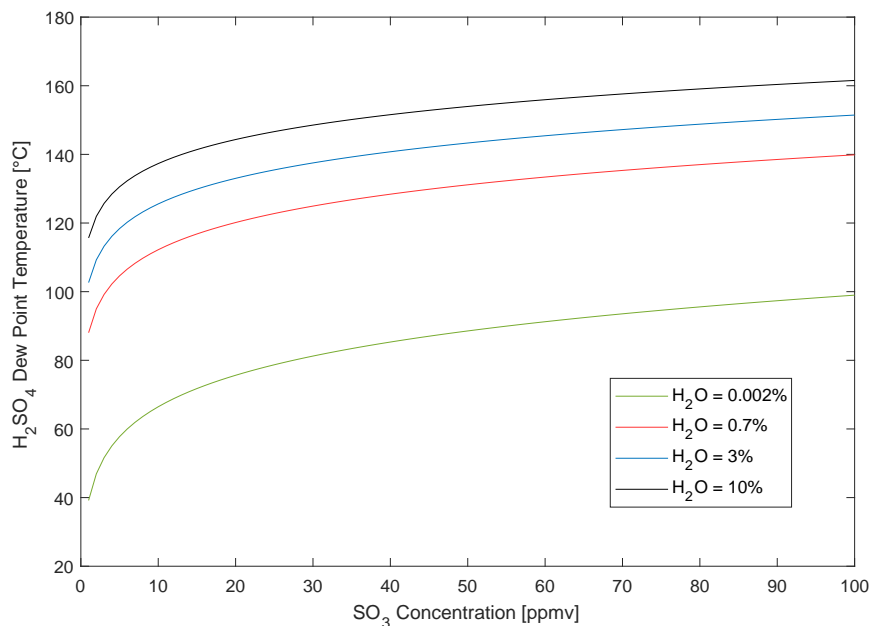


Figure 2.14: Dew point temperature of H₂SO₄, with respect to SO₃ and H₂O concentration.

With the above overview of experimental methods and the background on SO₂, SO₃, and H₂SO₄, the following chapter introduces numerical methods for the simulation of the conditions inside the experimental measurement cell. As a brief summary, this chapter has shown that the mid-IR spectral region is superior to that of the UV for detection of sulfur species. In addition, mid-IR spectral information for SO₂ is available while that for SO₃ and H₂SO₄ is not, and so the current research must provide it. Finally, the only standard technique for measuring sulfur species at flue gas conditions relies on batch sampling and wet-chemistry collection with its attendant uncertainties.

Chapter 3

Experimental facility design and setup

This chapter first reviews the existing designs for in-laboratory SO_3 generation systems (3.1) then it highlights the key parameters and design requirements and constraints for this research (3.2). Following this background, the chapter introduces the SO_3 generation system and the measurement cell for the DOAS measurements in the UV region (3.3). Based on lessons learned from this system, the chapter details a second iteration of the SO_3 generation system that was used for the mid-infrared optical measurements (3.4). A preliminary uncertainty analysis is made to demonstrate the gas flow dilution impact on measurement precision. This analysis is included as Section 3.5.

3.1 In-lab SO_3 generation design strategy review and challenges

Due to the high reactivity of the sulfur species, the generation of a stable, reproducible, and well characterized source of SO_3 presents several difficulties. From the literature, there are four general strategies for SO_3 generation, and one representative work is listed for each method:

1. A gaseous carrier gas is bubbled through liquid SO_3 to produce a saturated vapor condition that can be later mixed with other gases in controlled ratios [38]
2. SO_2 is oxidized with ozone [89]. This method simply oxidizes SO_2 with an O_3 reactor at 200C
3. Hydrocarbons are burned adding SO_2 so that the output from the firing furnace presents a mixture of SO_2 and SO_3 [19]
4. SO_2 is oxidized over a conversion catalyst in the presence of air. This class of catalytic SO_2 converters are commonly referred to as sulfuric acid catalysts, and they can have different performance, respond differently to water vapor addition, and have different operating temperatures, depending on their composition and size of catalyst material [92]. For example, the continuous operation range for Haldor Topsøe VK59 catalyst goes from 370C to 500C, but can extend up to 630C for the VK38 catalyst. The ignition temperature (also considered the minimum activation or light-off temperature) can vary as well, from 320C to 360C [93].

Strategy (1) has been used successfully, but liquid SO_3 is extremely dangerous to handle particularly considering its vapor's exothermic reaction with water vapor even in atmospheric air. In addition, liquid SO_3 requires a stabilizer to prevent its crystallization and the fittings must all be heated to prevent Joule-Thomson cooling from creating unfavorable solidification. Strategies (2) and (3) are not ideal for optical in-situ characterization of the SO_3 spectrum at high temperature, since the SO_3 features partially overlaps with the SO_2 spectrum, which has stronger absorption features in the UV [70] and SO_2 has much higher concentration at equilibrium levels [19]. It is also relatively difficult to assure an accurate SO_3 concentration following the conversion when SO_2 is also part of the product gas. After considering the advantages and disadvantages of each, the approach for this experimental setup relies on method (4), incorporating the use of a V_2O_5 catalyst optimized for sulfuric acid production (Haldor Topsøe VK48 and Haldor Topsøe VK59). To generate SO_3 using the catalyst, a gas

stream with variable concentration of SO_2 in air is fed to the catalyst bed (this research uses a chamber) through a heated line. As mentioned above, the catalyst bed requires heating to ignite and operate. While this approach normally involves the presence of SO_2 , it is possible to exploit the SO_3 adsorption-desorption mechanism typical of vanadia catalyst to temporarily operate the catalyst, after it has reached a stable conversion condition, on air alone (without SO_2) to produce a gas output consisting only of SO_3 and air [94].

While the use of a catalyst allows the measurement of an isolated SO_3 spectrum, SO_3 yield is in general not predictable with high accuracy, and it depends on several factors, such as the SO_2 inlet concentration and H_2O vapor presence. Furthermore, the catalyst requires a long conditioning time. The conditioning time is defined as the time needed for the catalyst to achieve steady-state SO_3 generation after a change in operating conditions, most commonly a change in SO_2 feed concentration. The conditioning time is associated with catalyst surface sulfate species buildup and consequent transient SO_3 output, and it can last up to 70 hours of operation [94, 95].

in this dissertation, there were two SO_3 experimental systems designed and built. Both of the designs are heating a catalyst for SO_3 generation. The second design overcomes the shortcomings of the first iteration. These shortcomings are described thoroughly in the section providing details of the second design but, briefly, included improved heating uniformity throughout the test cell, proper crushing and volume of catalyst material, and creation of a flow manifold that permits more control of the gases bypassing the measurement cell when needed. Despite its shortcomings, the first design was sufficient to permit the evaluation of the DOAS UV approach to SO_3 measurement. The second iteration system was used exclusively with Opto-Knowledge Inc. ECQCL lasers for mid-IR absorption measurements.

3.2 Design parameters

In this section, the design parameters considered in the design phase are described, with a summary appearing in Table 3.2. The catalyst operating temperature and the space velocity are bound by the specifications provided by the catalyst vendor, Haldor Topsøe [93]. The requirement on space velocity is directly linked to the dimensions of the catalyst chamber, and the volumetric flow rate through the catalyst. The maximum flow through the catalyst that ensures the satisfaction of the space velocity requirement is 8.5 slm. However, additional gas can be injected in the cell after the catalyst, and the maximum volumetric flow rate is determined by the range of the flow controllers used. The minimum volumetric flow rate is the flow that would assure reasonable temperature uniformity in the cell. The SO_2 upper limit is imposed by the maximum realistic flue-gas concentration in coal-fired power plants, while the minimum represents conditions where no SO_2 is present in the measurement cell. SO_2 concentration values can be imposed spanning the 0 to 2500ppm range. The maximum concentration level for SO_3 (and for H_2SO_4 , since the two species are related) is set to a target that is marginally larger than the 60ppm level expected in coal-fired power plants. The concentrations possible for SO_3 from the current facility are likely higher, as they depend on the SO_2 inlet concentration (up to 2500ppm) and the catalyst conversion efficiency ($\leq 30\%$). Such extreme levels are not useful for the current study, however. The water vapor concentration range extends past the maximum expected in air-firing power plants (12%). The water vapor delivery limit is not high enough to reach the 36% level representative of wet recycling in oxy-fuel combustion [96], but oxy-fuel conditions are not part of the current study.

	Symbol	Value	Unit
Volumetric flow rate	\dot{V}	$4 < \dot{V} < 12$	slm
Measurement Cell Temperature	T_{cell}	$T_{amb} < T_{cell} < 450$	°C
SO ₂ Concentration	c_{SO_2}	$0 < c_{SO_2} < 2500$	ppmv
SO ₃ Concentration	c_{SO_3}	$0 < c_{SO_3} < 100$	ppmv
H ₂ O Vapor Concentration	c_{H_2O}	$0 < c_{H_2O} < 15$	% v/v
Catalyst Activation Temperature	T_{act}	360	°C
Catalyst Operating Temperature	T_{ops}	480	°C
Catalyst Recommended Space Velocity	SV	< 1200	h ⁻¹

Table 3.1: Design parameters

3.3 First design iteration

The schematic for the first design using a heated oven is represented in Figure 3.1. The first design was to satisfy higher requirements of volumetric flow rate (around 30 slm, later adjusted to 10 slm). It used 3/8" 316L stainless steel tubing, since it is resistant to corrosion from sulfur species and can sustain temperatures above 200C. An appropriate mixture of SO₂, air, and N₂ is composed using mass flow controllers and rotameters. The mixture flows downstream to the catalyst bed reactor (CBR), located in the heating oven. Preheating of the gas mixture is ensured by flowing the gas into a stainless steel coiled tube (42-ft long, 30 revolutions, 25 in length, 5 in coil ID, 3/8" tube OD), designed using appropriate correlations [97–99]. The CBR is a 2.5" diameter, 12" long 316L stainless steel tube with CF Flanges, and it is sealed using gold plated gaskets. After the CBR, all the tubing sections are heated to the desired temperature using heating cables driven by PID controllers implemented in NI Labview. The tubing sections are thermally insulated using ultra-high-temperature mineral wool. A bypass line allows the injection of SO₂ into the measurement cell without its first passing through the oxidation catalyst, and a septum-sealed injection port allows the injection of liquid SO₃ or H₂SO₄ into the heated line leading to the measurement cell. The direct injection of these species creates extremely high concentrations of SO₃ that can provide a clear and strong signal, avoiding other species interferences, for evaluating the feasibility of SO₃ measurements with DOAS. Water vapor is injected into the heated line

right before the measurement cell.

The measurement cell is a 1 m long stainless steel tube, with ceramic heating. Two view ports with SiO₂ windows are installed at either end, and a Unisearch DOAS Gas Analyzer single-pass system operating between 195 nm and 450 nm utilizes the optical access provided by the view ports. After the measurement cell, the gas is bubbled through a basic solution scrubber (water and sodium bicarbonate) to neutralize SO₃ and H₂SO₄. Alternatively, the flow can be diverted to a controlled condensation system (EPA Method 8A).

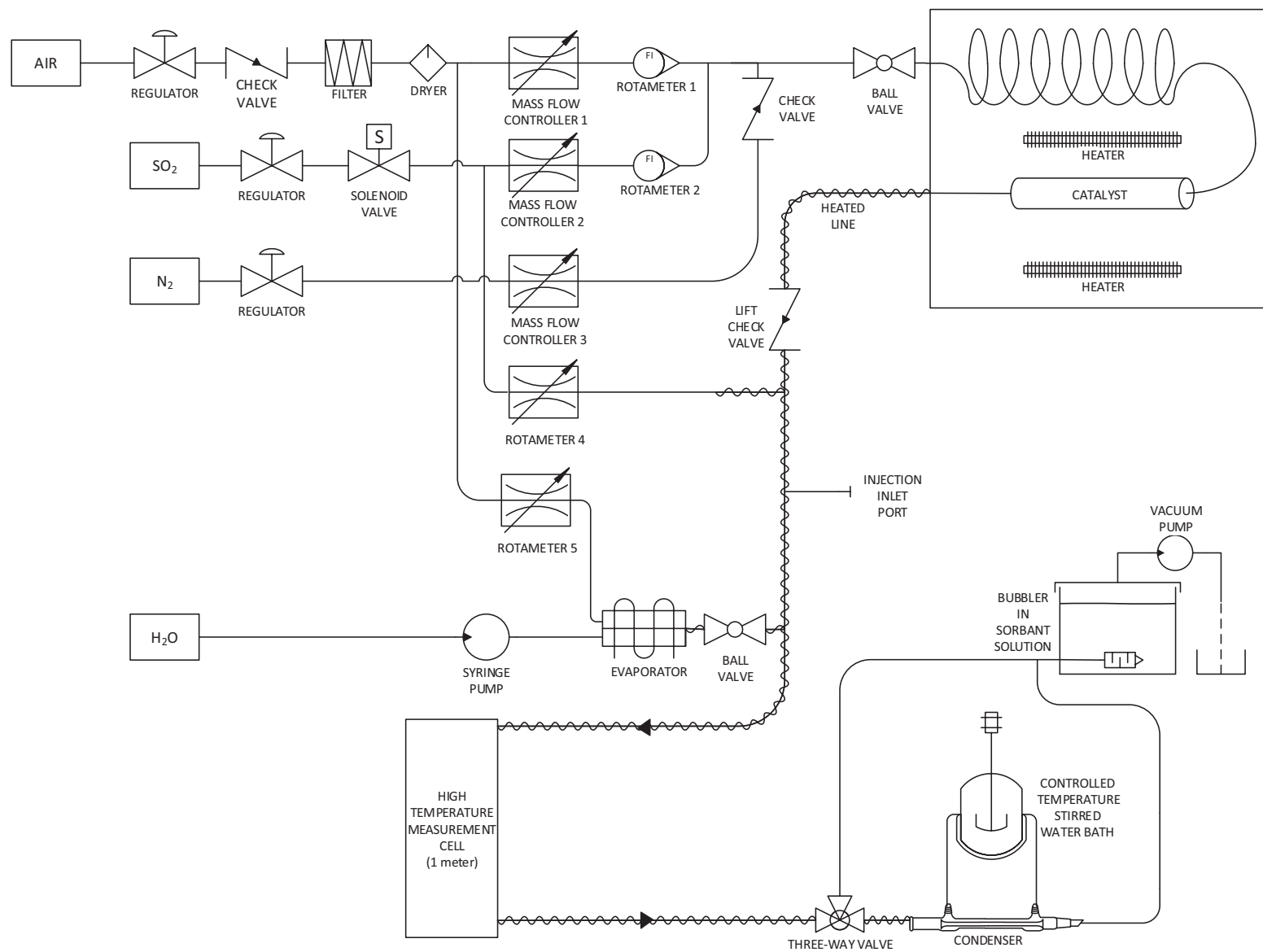


Figure 3.1: Schematics for the first design iteration.

Figure 3.2 represents the locations where temperatures are monitored along the flow path, in a simplified-logic schematics. The gas mixture at room temperature enters the heated oven and warms up as it flows through the coiled tubing. At the end of that section, the temperature of the gas T1 is measured. The temperature of the gas is measured again at the outlet of the catalyst chamber (T4). The temperature inside the oven is measured at two different locations, represented by T2 and T3, to determine if there is good thermal distribution. The temperature of the gas mixture is measured twice along the way to the measurement cell (T5 and T6) to provide feedback for the PID heating control of the tubing. The gas temperature is also measured at the outlet of the cell (T7). The measurement cell is provided with a standalone temperature control, set to 400C, using only one temperature measurement input. The related thermocouple was installed in contact with the stainless steel main body of the cell, enclosed by a ceramic fiber heater shell. The thermocouple was hence not immersed in the gas flow, but was installed externally. The presence of temperature measurements at the inlet and the outlet of the cell (T6 and T7 respectively) helped determine the thermal uniformity of the cell, as any difference between the two temperatures would result from undesirable gas cooling, or heating, inside the measurement cell. The thermocouple measurement locations are summarized in Table 3.2.

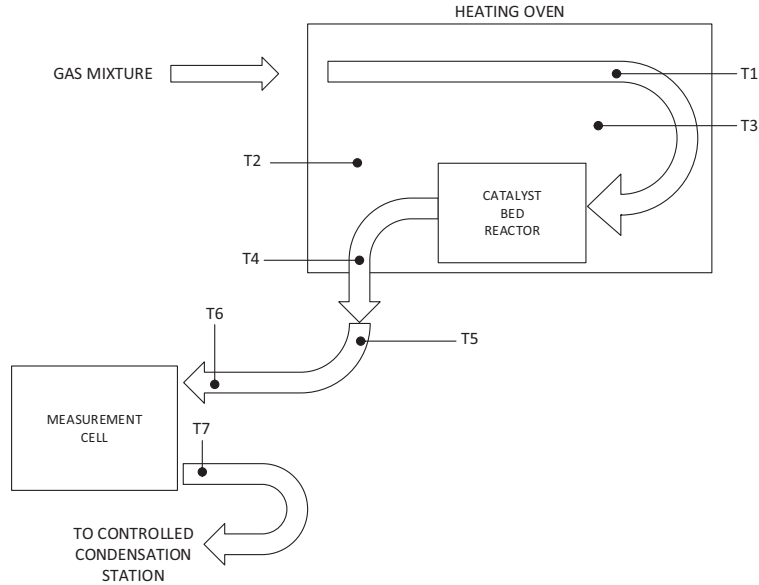


Figure 3.2: Temperature measurements for the first design iteration.

Location	
T1	Temperature of the mixture past the heating coil
T2	Temperature of the heating oven
T3	Temperature on the heater rod surface
T4	Temperature of the mixture after the CBR
T5	Temperature of the mixture midway to the measurement cell
T6	Gas mixture inlet temperature
T7	Gas mixture outlet temperature

Table 3.2: Temperature measurement points for the first design iteration.

Figure 3.3 is a photo of the heating oven, with labels describing components and flow directions. The ambient temperature gas mixture enters the oven (inlet), warms up in the coil, and enters the catalyst bed reactor. The gas then exits the oven and proceeds towards the measurement cell. Figure 3.4 shows the remaining flow path, with the outlet from Figure 3.3, labeled as outlet as well in Figure 3.4, proceeding to the 1m heated cell. The DOAS instrument is visible in Figure 3.4, with the lamp installed on the right-hand side and the

detector on the opposite end of the measurement cell. The data acquisition system was installed above the measurement cell.

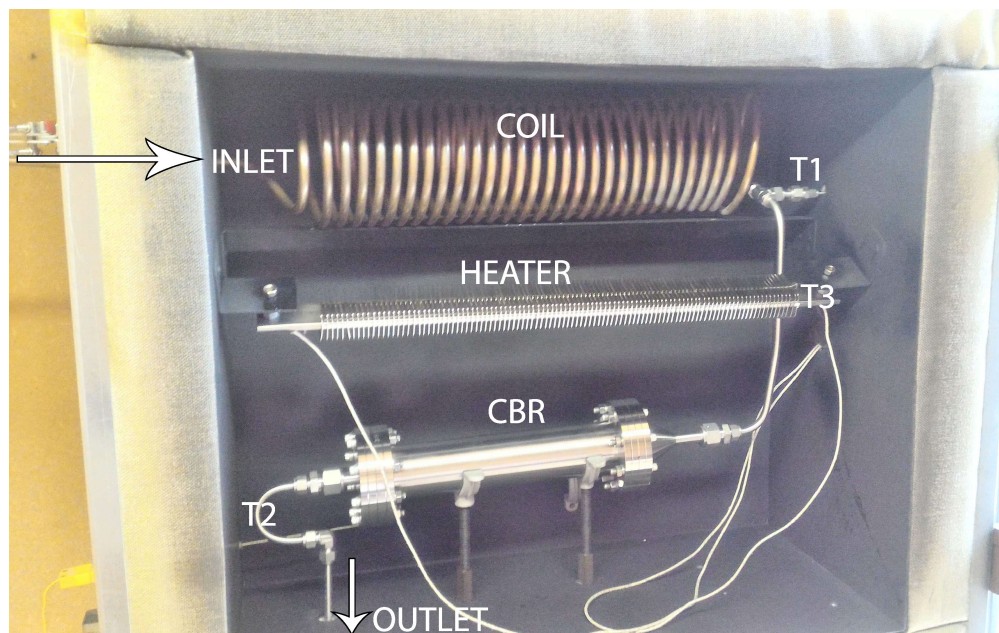


Figure 3.3: The catalyst bed reactor is located inside a heating oven.

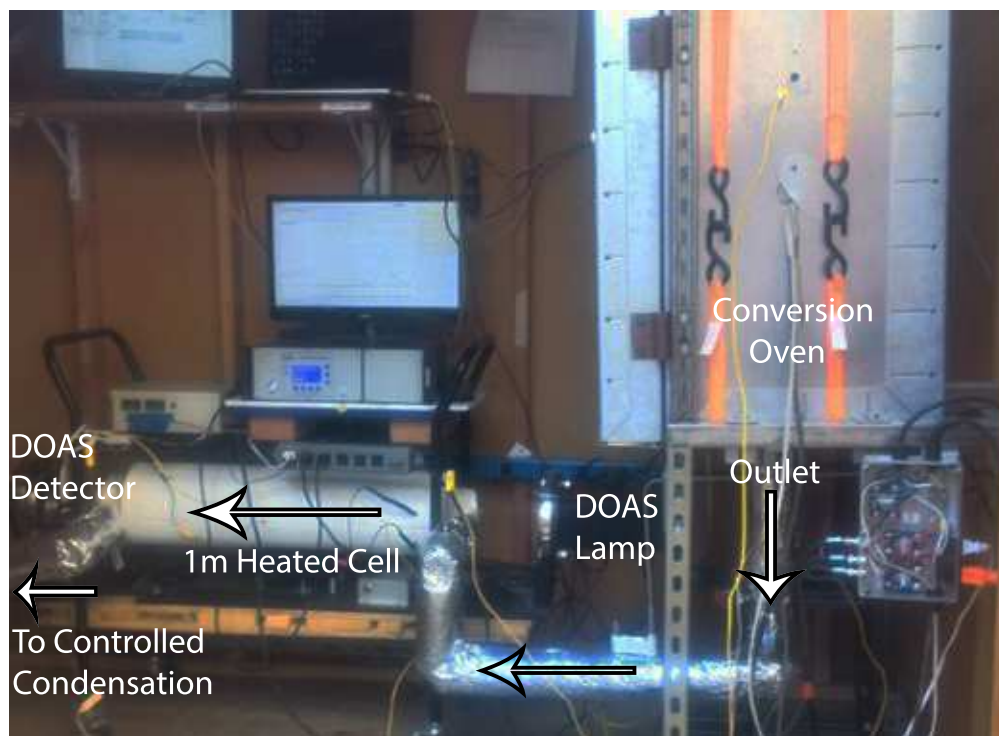


Figure 3.4: Overview of the complete system, with Unisearch DOAS.

3.4 Second design iteration

The second design addresses the lessons learned from the first design iteration. These lessons are described as part of the results section from the DOAS measurements but generally resulted from the bulky nature of the system. The changes in the design were focused on providing a cleaner and more controlled environment for mid-IR optical measurements, including the potential for a multi-pass optical pathway. The modifications included:

1. Improved catalyst performance by operating at a lower volumetric flow rate (5 to 10 slm). The reduction of the flow rate derived from space limitations for the catalyst chamber and the measurement cell
2. Minimizing the distance from the CBR to the measurement cell to reduce sulfur losses as the gas flows through pipes and valves
3. Minimizing temperature gradients along the optical path to achieve a homogeneous temperature distribution
4. Offering the option of nitrogen purging of the windows through heated lines to reduce window damage occurring when sulfuric acid comes in contact with the windows
5. Adding the option of running the catalyst continuously by diverting its outlet flow directly to the scrubber. The goal is to avoid the presence of reactive species (SO_3 and H_2SO_4) in the measurement cell, since sulfuric acid aggressively damages the windows. This option can hence decouple the need of long catalyst conditioning time with the need of extending the windows lifespan by flowing the reactive species into the cell only when needed for measurement. This improvement was added in the latter stages of the experimental campaign.

The design goals were met by building a more compact system that could sit entirely on an optical table that served as a stable platform for all components. The system is located in a

laboratory room, under a ventilation hood and is enclosed within plexiglass (four sides) to reduce dust and to minimize exposure risks if leaks occur.

A new optical measurement cell was designed and built to correct the issues faced with the 1 meter cell used in the first design. The most important of these issues were the significant temperature drop between the inlet and the outlet of the cell at the experimental flow rates (5 to 10 slm), the lack of temperature readings along the cell length, and the insufficient path length. The new cell is physically shorter (about 14" window-to-window length) but provides longer path length through its compatibility with multi-pass mirror arrangements. It has three temperature sensors along the cell longitudinal axis, and a two-zone separated heating control, to reduce the non-uniformity of the temperature along the optical path. This is particularly important given the role of this experiment, which is to provide a reliable spectral library for SO_2 , SO_3 , and H_2SO_4 under different conditions. The detailed components of the measurement cell design are described and shown in the model drawings in Section 4.2.1. CaF_2 and BaF_2 windows, 2" in diameter and 3mm thick, were used at the ends of the measurement cell to provide optical access. BaF_2 windows could be used for both $7\mu\text{m}$ and $8\mu\text{m}$ measurements, while CaF_2 use was limited to the $7\mu\text{m}$ measurements (as they have insufficient transmissivity at $8\mu\text{m}$). Standing offset a distance outside of the two windows of the cell are two gold plated mirrors for the purpose of multi-pass Herriot cell, reflecting laser beams for up to 44 passes (depending on the exact configuration). The general multi-pass design was accomplished by OKSI but in-place adjustments of the mirrors was needed to maintain the effective path length. There are two ECQCL lasers operating in different wavelength bands. One is ECQCL7, which ranges from 1470 cm^{-1} to 1265 cm^{-1} ($6.8\mu\text{m}$ to $7.9\mu\text{m}$) for detection of SO_3 and SO_2 . Another is ECQCL8, covering 1282 cm^{-1} to 1111 cm^{-1} ($7.8\mu\text{m}$ to $9.0\mu\text{m}$) for measuring H_2SO_4 and SO_2 .

The design of the cell was coupled with a simulation of the cell in the working conditions, and the radial location of the thermocouples tips was established according to the simulation results to assure representative bulk gas temperatures and to avoid temperatures readings in

the thermal boundary layer (see Section 5.3.6 for the numerical results) [100]. The distance from the CBR outlet to the measurement cell is about 8" (while it was ~9 feet in the first design).

All the components in contact with the flows (tubing, measurement cell, catalyst bed reactor) are 316L stainless steel coated with Silcotek Silconert2000 to minimize corrosion and sulfur losses at the surfaces. As seen in Figure 3.5, a mixture of SO₂, air, and N₂ at desired gas compositions were controlled by mass flow controllers and flowed into the catalyst bed reactor (CBR) situated in a shell-clamp style quartz-tube furnace. Preheating the gas mixture is achieved by a line heated using electric heating cables. The CBR is a 2.5" diameter, 12" long 316L stainless steel tube with CF Flanges, sealed using gold plated gaskets. An inert quartz liner in the catalyst bed reactor prevents the direct contact of the V₂O₅ catalyst with bare metal. Similar to the experience with the first design for maintaining the gas lines warm throughout, all the tubing sections are heated to the desired temperature using heating cables, and the tubing sections are thermally insulated using ultra-high-temperature mineral wool insulation tubes. The 8" long tubing section connecting the catalyst reactor to the measurement cell is maintained at a temperature between 400C (when the desired measurement cell temperature is 350C) and 330C (when the desired measurement cell temperature is 250C). The intent is to minimize sulfuric acid formation and its possible condensation along the tubing walls, while not exceeding temperatures at which SO₃ starts to thermally dissociate to SO₂ (above ~800C, see Section 5.2.1 for more details). The temperature is higher than the desired measurement cell temperature to counteract the gas temperature drop at the cell inlet due to the decreased convective heating and increased heat loss near the upstream viewport. A bypass line allows SO₂ injection directly in the measurement cell without first passing through the oxidation catalyst.

The water vapor generation system consists of a Bronkhorst Controlled Evaporator Mixer (CEM), with a carrier flow of air provided through a mass flow controller and liquid water provided through a Bronkhorst Coriflow mass flow meter. The liquid water is supplied to the

flow meter from a nitrogen-pressurized water tank. The three-way valve, shown in Figure 3.5 as the *H₂O location valve*, past the CEM allows redirection of the water vapor flow either before or after the measurement cell. The capability of adding water vapor after the measurement cell is useful for running the industry-standard EPA Method 8A even when the gas flow in the measurement cell is dry. After the measurement cell the gas is bubbled through a basic solution scrubber (water and sodium bicarbonate) to desulfurize the stream. Alternatively, the flow can be diverted by a valve (*CC valve* in Figure 3.5) to a controlled condensation system, designed according to the guidelines of EPA Method 8A [63].

3.4.1 Schematics and flow control

The full experimental schematics is shown in Figure 3.5, while a simplified-logic schematics is represented in Figure 3.6. In the latter, the controlled condensation system is represented in green, the different exhaust lines are in red, and general purpose flow lines are in blue. The numbered items on the simplified-logic schematics represent different major control points where the desired flow conditions are set. They are described in detail as follows:

1. **Air and SO₂ main inlet**: a mixture of air and sulfur dioxide is generated and flows into the catalyst bed reactor, where SO₂ partially oxidizes to SO₃. The main inlet provides mixtures of SO₂ and SO₃ to be analyzed in the measurement cell. Air and SO₂ flows are controlled by two separate flow controllers.
2. **Main flow valve** (if present): this valve can divert the gas flow exiting the catalyst either towards the measurement cell or directly to the exhaust. The valve was not present in all experiment sets, as it was added in the latter stages of the experimentation. The valve allows the catalyst to reach steady state oxidizing conditions (conditioning of the catalyst) while avoiding corrosive SO₃ and H₂SO₄ gases in the measurement cell, thereby reducing window damage by diverting the catalyst output flow directly to the exhaust except during active measurements. The main flow valve

and its exhaust system are highlighted in blue in Figure 3.5.

3. **Air and SO₂ bypass:** a mixture of air and sulfur dioxide can be introduced directly in the measurement cell, avoiding the oxidation catalyst. This bypass line is used to introduce SO₂ directly into the measurement cell. The bypass flow can also be used during the measurement cell warm-up phase, to provide a clean air background measurement, or to provide a known concentration of SO₂ in air. Air and SO₂ flows are controlled by separate flow controllers.
4. **H₂O location valve:** a mixture of air and water vapor at high temperature (200C) is generated. The mixture can be injected either before the measurement cell (defined as PRE- configuration) or after the measurement cell (defined as POST- configuration). In PRE- configuration, this valve is used to add water vapor into the measurement cell to allow the measurement of water vapor and/or sulfuric acid. In the POST-configuration, it offers the opportunity to run the controlled condensation system even if only dry gas is present in the measurement cell. Air and H₂O flows are controlled by separate flow controllers.
5. **Nitrogen windows-purging flow:** nitrogen can be added in front of the optical windows to decrease the local concentration of H₂SO₄ (a significant factor in the degradation of window performance). The flow is equally distributed at the two windows, and it is controlled by a flow controller and one needle valve.
6. **Controlled Condensation valve:** the flow from the measurement cell can be directed to the scrubber and the exhaust, or it can be analyzed with the controlled condensation system.

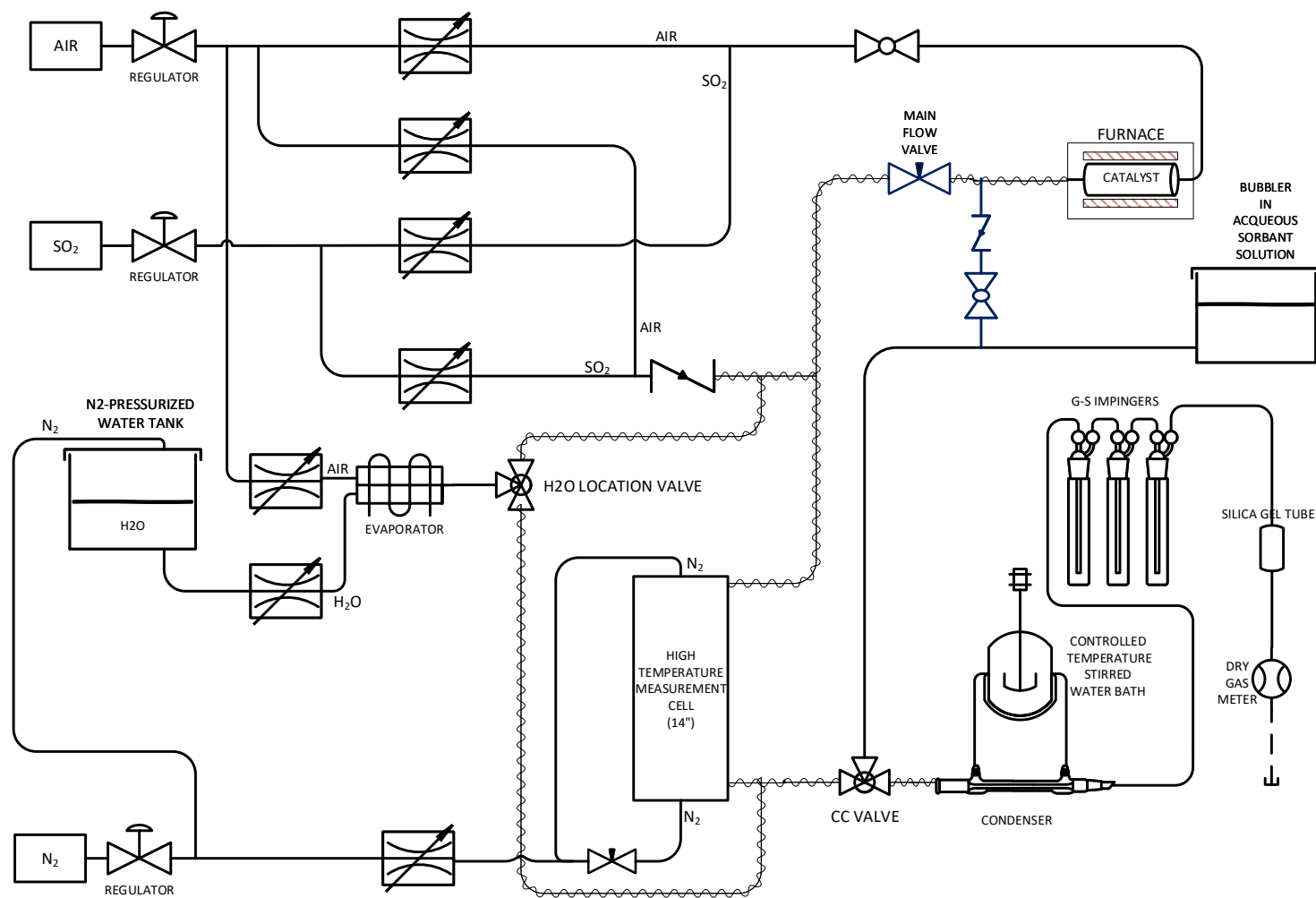


Figure 3.5: Schematics for the second design.

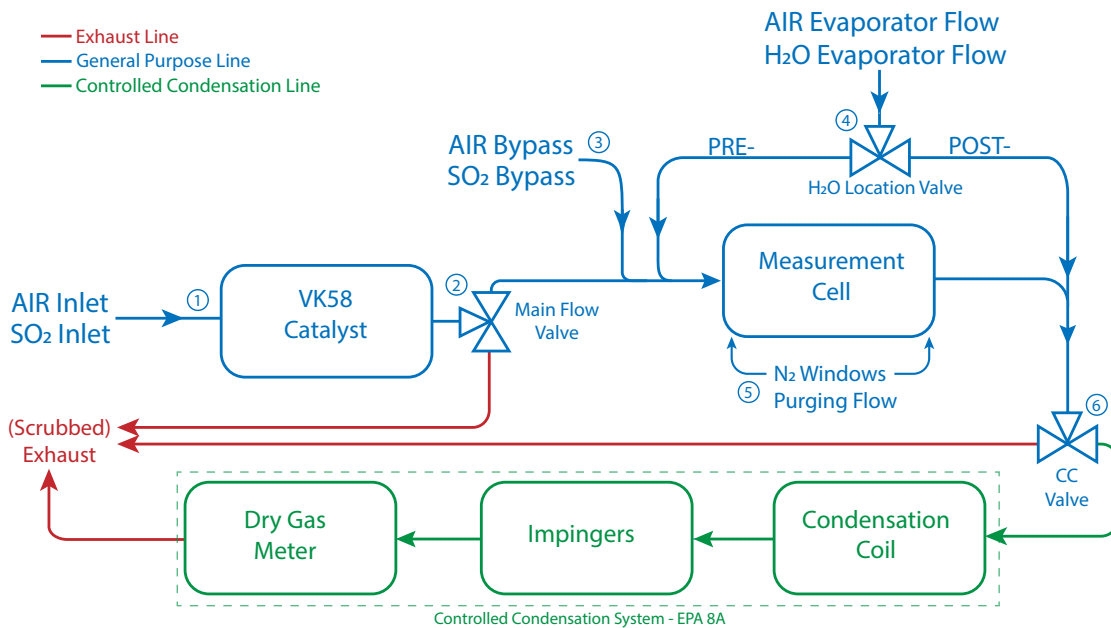


Figure 3.6: Simplified-logic schematic for the second design.

Figure 3.7 represents the locations where temperatures are monitored along the flow path, in a simplified-logic schematic. The different heating zones are shown in the same figure with different colors, and the parameters for each heating region are summarized in Table 3.4. The gas mixture from the flow controllers is warmed up in a heated line by an electrical heating cable (in red) and enters the catalyst bed reactor. Immediately before entering the catalyst, the temperature of the gas T1 is measured to verify that it is equal to the catalyst operating temperature. The catalyst chamber is enclosed in a quartz-tube furnace (in orange), and its feedback thermal control tracks the temperature of the gas inside the catalyst T2 and adjusts the power accordingly in order to set the appropriate catalyst operating temperature. Another electrically heated line (gray) raises the temperature of the gas flowing through the bypass line (T3) as it merges with the gas outlet from the catalyst. The temperature of this mixture is monitored before entering the measurement cell (T4). The measurement cell tracks the gas temperature at three different longitudinal locations (T5, T6, and T7 respectively) and acts on two different electrical heaters, in black and yellow, to help homogenize the temperature in the cell to the desired temperature values

for the spectroscopic measurement. Finally, the temperature of the gas is measured at the outlet of the measurement cell (T8). This line is controlled by a separate heater (green) to make sure that the temperature T8 does not drop below the dew point of sulfuric acid, which would allow undesired H_2SO_4 condensation before the EPA Method 8A measurement system setup. The white heated line is dedicated to water vapor, that can be injected before or after the measurement cell. This line is always heated to avoid water condensation and large temperature gradients in this flow when it mixes with the other gases carried in gray and blue heated lines. The thermocouple measurement locations are summarized in Table 3.3, and the different color-coded heating zones in Table 3.4.

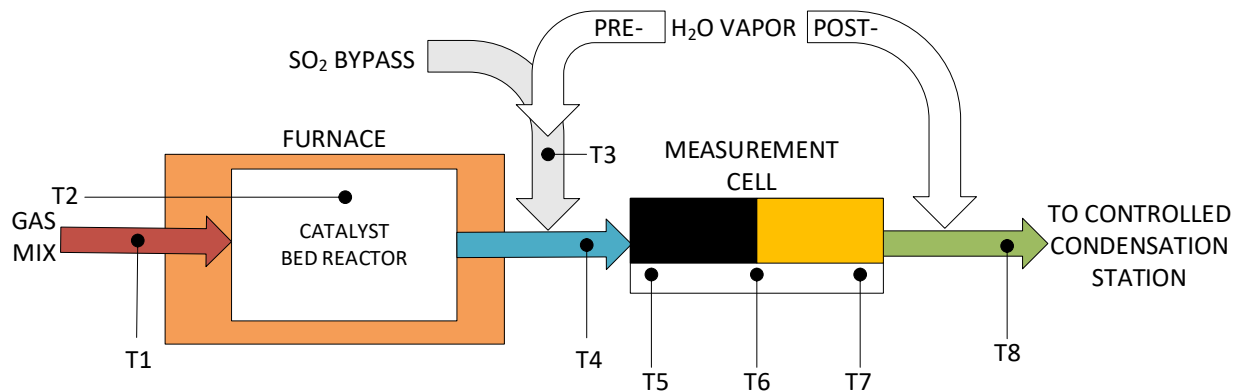


Figure 3.7: Temperature measurement locations for the second design, with color-coded heating zones.

Location	
T1	Temperature of the mixture before entering the CBR
T2	Temperature in the catalyst bed reactor
T3	Temperature of the bypass gas
T4	Temperature of the mixture after the CBR
T5	First temperature along the measurement cell
T6	Second temperature along the measurement cell
T7	Third temperature along the measurement cell
T8	Temperature at the outlet of the measurement cell

Table 3.3: Temperature measurement locations.









	Color	Power (W)	Length (ft)	Resistance (Ω)
Main line		520	10	28
Furnace		1100	-	-
Catalyst to Measurement chamber		208	4	71
Bypass Line		195	10	75
Measurement cell, 1st section		300	6	46
Measurement cell, 2nd section		300	6	46
Water lines		195	10	75
Exhaust		120	6	110

Table 3.4: Color-coded heating zones with heat cable characteristic parameters.

Some photos of the experimental setup follow. In Figure 3.8, the catalyst and measurement cell group is shown only for illustrating purposes after the first assembly without the presence of the water evaporation system. In the picture, the catalyst can be seen inside the quartz tube for a better understanding of the layout, but in experimental conditions the tube is enclosed by a stainless cell sealed with CF flanges, as explained previously. In Figure

3.8, the condensation coil of EPA Method 8A is set in place, but it is not shown connected to the water temperature control.

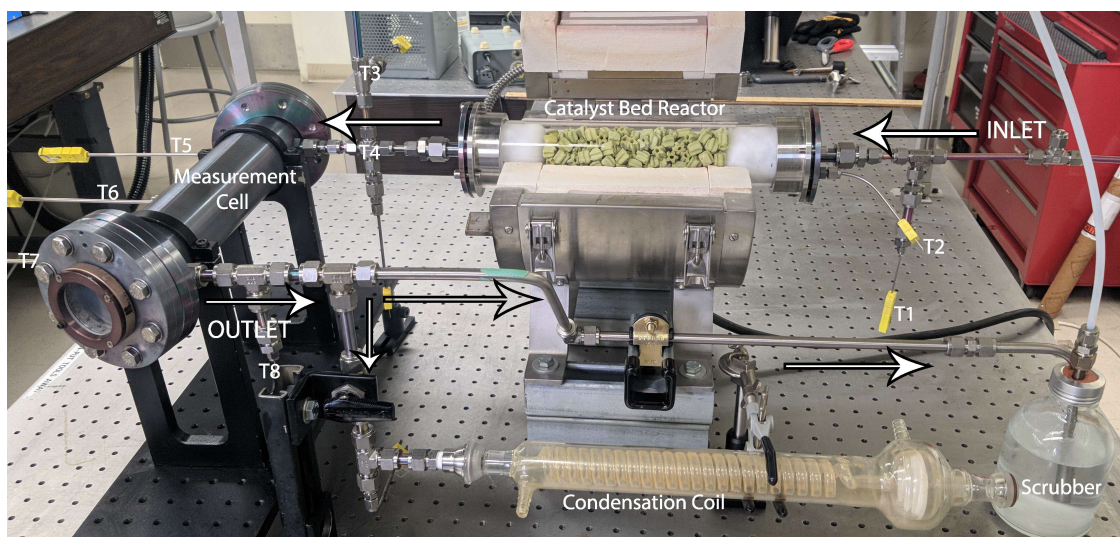


Figure 3.8: Overview of the bare system, with thermocouples installed and a temporary catalyst bed reactor, before the installation of water evaporator and main flow valve.

In Figure 3.9 the experimental system is seen ready to operate in dry conditions with the OKSI ECQCL7 laser. The appearance of the setup is significantly altered by the 1.5” to 2.5” mineral wool insulation layer around tubing and measurement cell. The photograph shows the system without the water evaporation system installed.



Figure 3.9: System ready to operate with OKSI ECQCL7, before the installation of water evaporator and main flow valve.

Figures 3.10 and Figure 3.11 use a visible red beam laser to highlight the multi-pass configuration for the laser measurements. A different number of passes is possible depending on the distance between the two mirrors. In Figure 3.10 a 44-pass (22 bounces per mirror) configuration is shown, while Figure 3.11 shows a 16-pass configuration.

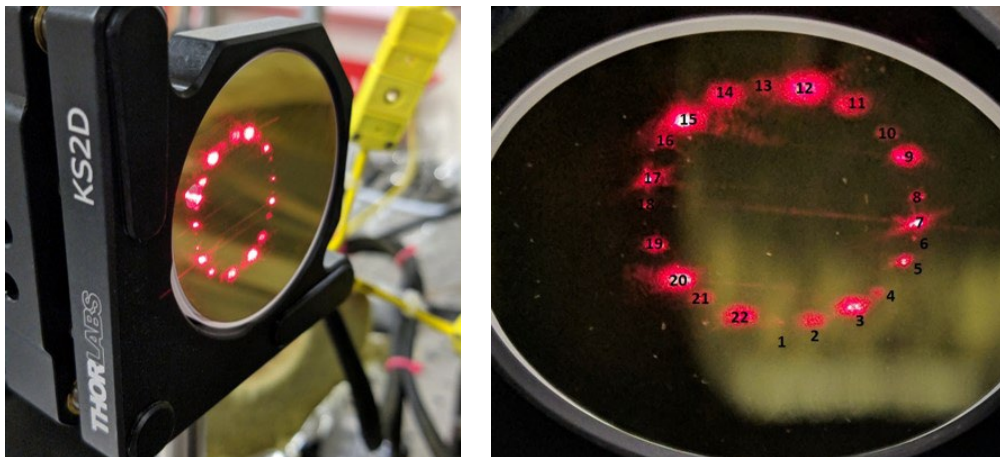


Figure 3.10: Gold plated mirrors of the Herriott cell in 44-pass configuration.



Figure 3.11: Mirrors of the Herriott cell in 16-pass configuration.

Figure 3.12 further clarifies the multi-pass configuration by using smoke and a visible red beam laser. The laser enters the left-hand side mirror of Figure 3.12 and bounces between mirrors to then exit from the same location where it entered, but with a different angle. The fan resulting from the laser bounces can be seen entering and exiting the cell in the right-hand side of Figure 3.12.

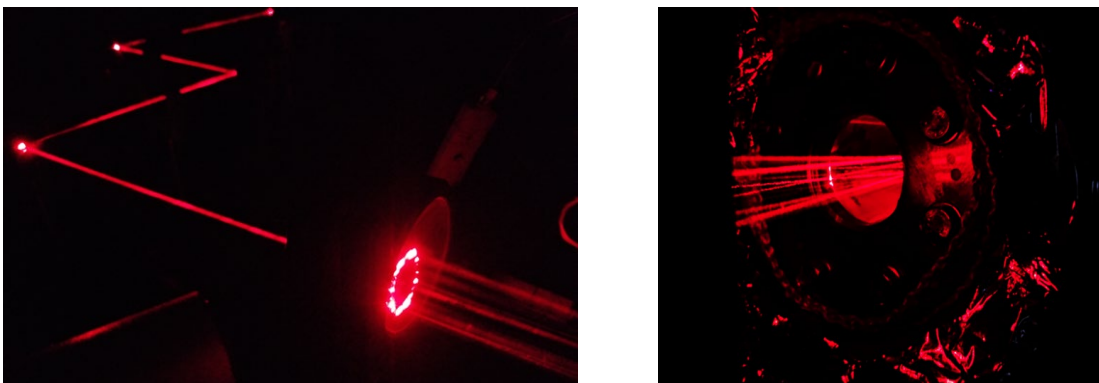


Figure 3.12: Visualization of the beam path with a visible red diode laser.

The installed water evaporator system can be seen in Figure 3.13. Liquid water from a nitrogen-pressurized tank is delivered to a liquid mass flow meter. After passing through a shut-off valve, the liquid water reaches the mixing valve on top of the CEM system, where it is mixed with air (from a gas mass flow controller) before entering the evaporator coil. The mixing valve is electrically connected to the liquid mass flow meter to provide

control capabilities on the water stream. The water and air flow rates are controlled through Labview. The liquid water and air mixture enters the CEM where it is evaporated in a heated coiled tube. The output water vapor at 200C can be directed after the measurement cell in the POST- configuration (towards the right-hand side of the figure) or before the measurement cell in the PRE- configuration (towards the left-hand side) by acting on the three-way H_2O location valve.

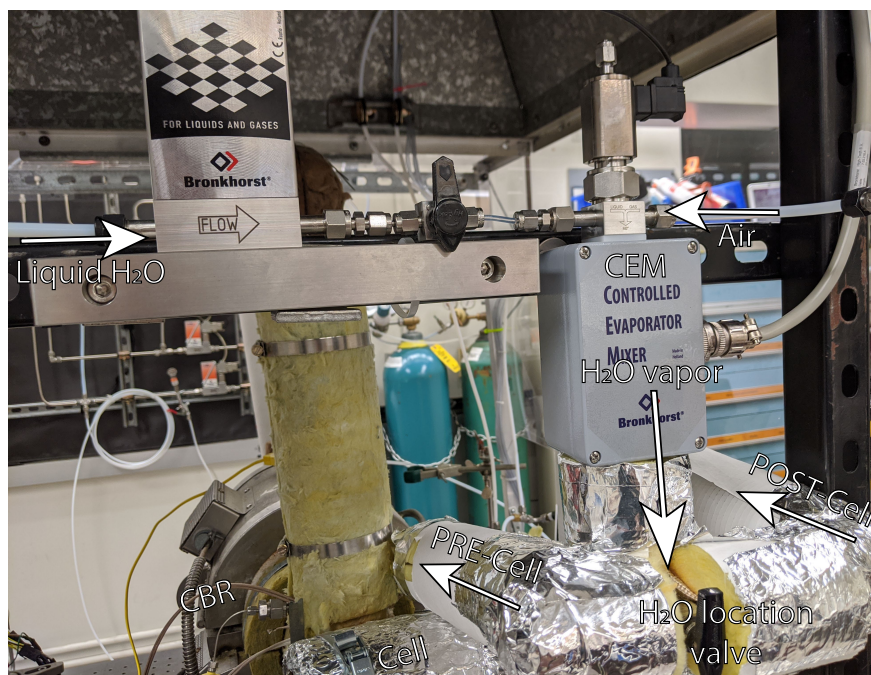


Figure 3.13: Closeup of the water evaporation system.

Figure 3.14 represents the complete setup exposed during maintenance. All components and lines are visible and labeled, according to Figure 3.6 and 3.7. The nitrogen purging lines, visible on the left and marked with the label '(5)', are not connected to the window holders, because they were not installed when the photo was taken.

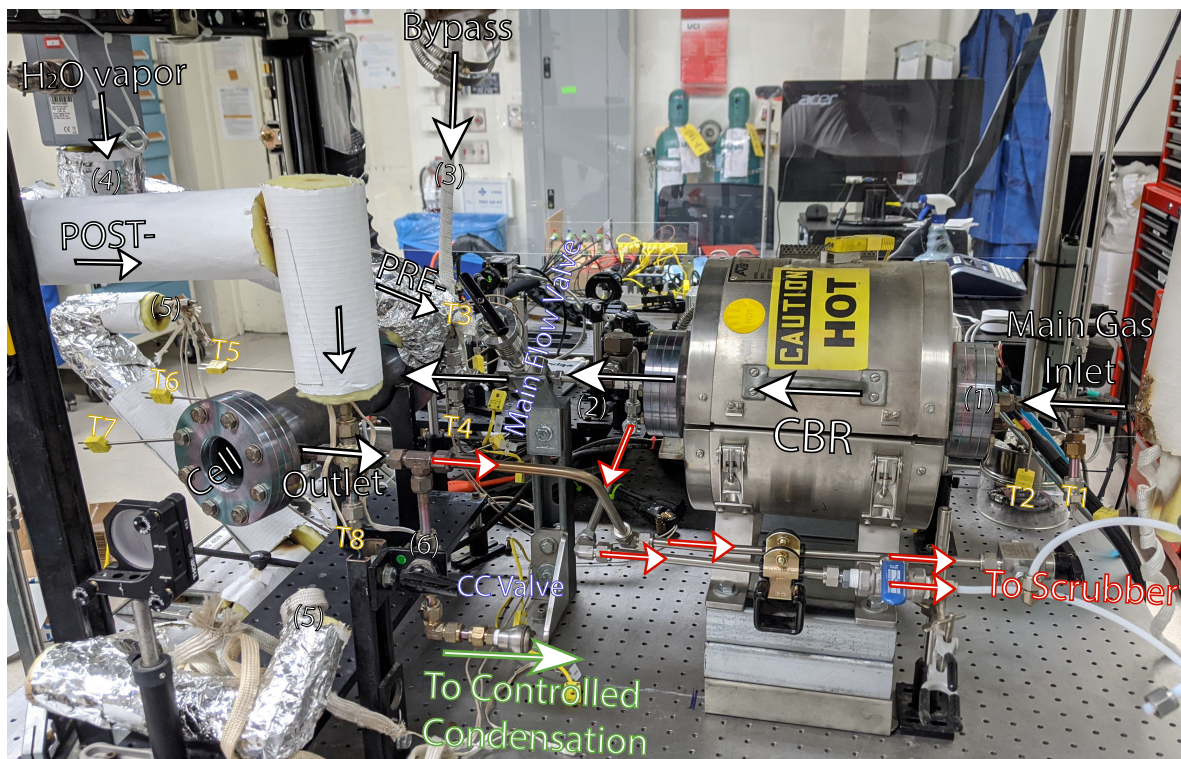


Figure 3.14: Full experimental setup undergoing maintenance.

Figure 3.15 shows a close-up of the upstream window (Window 1) with the different gas lines that compose the mixture entering the measurement cell. The purging nitrogen port (Inlet N_2 1) is visible, but not yet connected to the nitrogen line. A cloudy white $BaSO_4$ layer (from window damage described later in Section 5.3.5) is visible on the window.

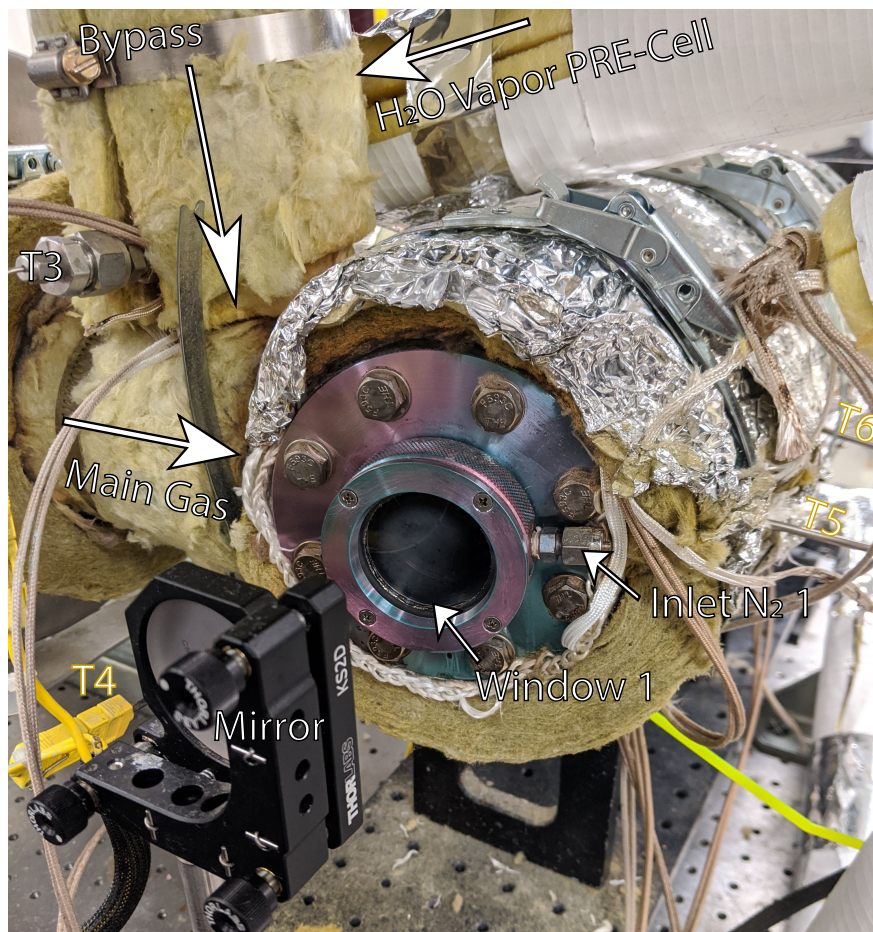


Figure 3.15: Closeup of the upstream window. The purging nitrogen line is not connected. A cloudy white BaSO₄ layer is visible on the window.

3.5 Root of sum of squares (RSS) uncertainty analysis for SO_x generation

This section is not strictly part of the experimental setup but it applies RSS uncertainty analysis to two different concentrations of SO₂ gas cylinders, 1650 and 300ppm, on the generation of a desired concentration of SO₂ in an overall volumetric flow of 5 slm. The higher concentration cylinder is needed to reach higher levels of SO₂ in the measurement cell but the desired concentration of SO₃ requires only a small fraction of SO₂ entering the catalyst. Using the higher concentration cylinder to provide low flow rates generates a

trade-off in flow precision.

The input variable SO_x is defined as the SO_2 concentration of the gas stream entering the catalyst. The definition is meant to avoid confusion between SO_2 concentration entering the catalyst and SO_2 concentration in the measurement cell, with the latter being affected by the catalyst conversion ratio and the possible introduction of additional SO_2 through the bypass line. In most experiment sets the concentration of SO_2 entering the oxidation catalyst is fixed to the value SO_x so that the output concentrations of SO_2 and SO_3 from the catalyst should sum up to the value of SO_x . The inlet gas flow entering the catalyst with SO_2 concentration equal to SO_x includes uncertainties that are related to the target value of SO_x , the SO_2 gas cylinder concentration, and the flow controllers uncertainty. Each of these variables is characterized by a degree of uncertainty, and the final result (the generated SO_x) is then characterized by a composite level of uncertainty.

In this section, a root of sum of squares (RSS) approach determines the typical levels of uncertainty on providing different SO_2 values at the inlet of the catalyst. The RSS is a statistical tolerance analysis method, and it relies on variables that are presumed to be normally distributed, and characterized by a mean value and a standard deviation or uncertainty. That is, every variable can be expressed as:

$$x_i = \bar{x}_i + u_i \quad i = 1 : m$$

where \bar{x}_i is the mean, and u_i is the related uncertainty. Assuming another quantity Q of interest (such as the generated SO_x) can be expressed as a function of the m variables x_i , as:

$$Q = f(x_i) \quad i = 1 : m$$

then the standard deviation of Q can be expressed as:

$$u_Q = \sqrt{\sum_{i=1}^N (Q_{/x_i} u_i)^2}$$

where $Q_{/x_i}$ is the partial derivative of Q with respect to x_i . The RSS approach is valid if the variables x_i are independent, and if the variable x_i is normally distributed. In this case, the variables are the SO₂ mixture flow controller reading x_1 , the air dilution flow controller reading x_2 , the SO₂ concentration in the SO₂ mixture gas cylinder x_3 . For the flow controllers, the uncertainty is:

$$u_i = 0.1\% \text{FS}_i + 0.5\% \text{RD}_i \quad i = 1, 2$$

where FS_i and RD_i are respectively the full scale reading in slm and the flow reading for flow controller i . For the gas cylinder, $u_3 = 0.6\%$ of the FTIR-measured average SO₂ concentration (the average value is provided by the gas cylinder vendor and it is specific to the gas cylinder). The function Q can be expressed as:

$$Q = \frac{x_3 x_1}{x_1 + x_2}$$

where the overall flow rate $x_1 + x_2$ is fixed at the nominal flow rate of 5 slm.

The results from the analysis are represented in Figure 3.16 for two different SO₂ gas cylinder mixtures, one with 300ppm SO₂ in nitrogen, and the other with 1650ppm SO₂ in nitrogen. The generation of low levels of SO_x is associated with higher uncertainty for the 1650ppm SO₂ cylinder, quantified around $\pm 7\%$ for SO_x=50ppm, and reducing to around $\pm 4\%$ for the SO_x=100ppm case. The 300ppm SO₂ gas cylinder produces lower uncertainty, albeit at the cost of reduced gas cylinder life and higher cost per experiment hour. In fact, each 150A cylinder contains roughly 144ft³ of gas, corresponding to about 4077 liters. With the commonly used flow rate of 5 slm and SO_x=100ppm the projected duration of a SO₂

cylinder is approximately 226 hours for 1650ppm and only 40 hours for 300ppm.

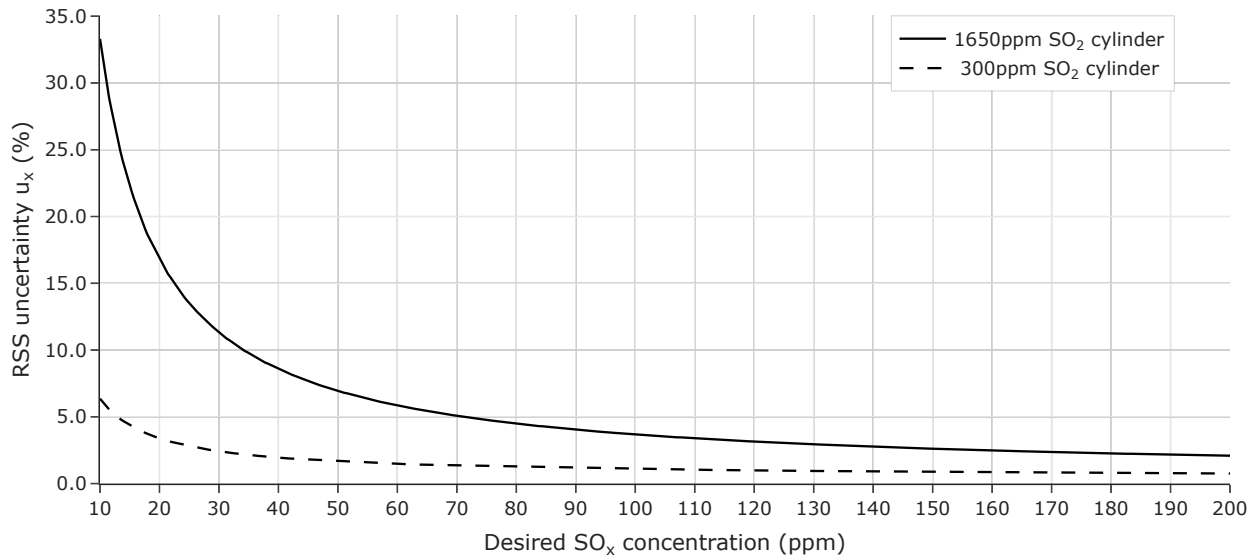


Figure 3.16: RSS uncertainty analysis on the generation of different SO_x levels with 5 slm overall flow rate.

With the experimental facility design and setup described, the remaining chapters present the numerical simulation model and the results of a wide range of experiments.

Chapter 4

Numerical methods

In this chapter a numerical model is developed with ANSYS[®] Chemkin[™]-Pro and ANSYS[®] Fluent[®] to simulate the conditions in the experimental gas cell. Chemkin-Pro is a proprietary software to solve chemical kinetics problems, while Fluent is a computational fluid dynamic (CFD) software used to predict fluid flow, heat and mass transfer, chemical reactions and other related phenomena [101]. The developed model will take into account the thermo-fluid dynamic aspects of the heated measurement cell, as well as the chemical composition and species diffusion in simulated-experiment conditions. First, a suitable chemistry model is developed with Chemkin (4.1), then, a thermo-fluid dynamic model of the experimental cell is developed in Fluent (4.2).

The goals for the numerical model are to assess the homogeneity of temperature in the heated cell and to quantify the effect of N₂ inert purging near the windows on temperature and species concentrations. An additional goal is to provide a tool that allows quantitative evaluation of the potential effects of non-uniformity on the absorption results.

4.1 Chemkin Model

The development of a chemical model requires first a clear definition of the experimental conditions and the species of interest, followed by the search in the literature for an appropriate chemical mechanism.

4.1.1 Define the experimental conditions and species interest

This study targeted measurements of SO_2 , SO_3 , and H_2SO_4 in realistic coal-fired power-plant flue-gas conditions. The temperature of this study targets the thermal conditions near the possible measurement locations (economizer outlet or across the SCR), as described earlier in Section 1.7, and ranges from 200C to 425C (470K to 700K). The chemical species derive from typical coal-fired power-plant flue-gas conditions with coals containing low to high levels of sulfur related to their source geographical origin [17].

The concentration of water vapor ranges from 3% to 12%. While the lower limit is below nominal power-plant conditions (where the expected concentrations range from 8 to 12%) it allows for comparison with previous spectroscopic measurements carried out at 3% water vapor concentration in the experimental tests. The maximum SO_2 concentrations will be limited to 2500ppm, while $\text{SO}_3/\text{H}_2\text{SO}_4$ expected concentrations do not exceed 100ppm. The simulated flow rate in the measurement cell is 5 slm and is determined by the requirement on space velocity imposed by the catalyst bed reactor (CBR) dimensions (see Table 3.1).

4.1.2 Gather an appropriate chemical mechanism

The chemical mechanism should be validated by literature and experiments, and focus on SO_2 , SO_3 , and H_2SO_4 . Ideally it would also be validated for the conditions of this study (4.1.1). A brief review of the literature studies on sulfur species in flue-gas conditions follows, with considerations that impact the choice of a mechanism for this work.

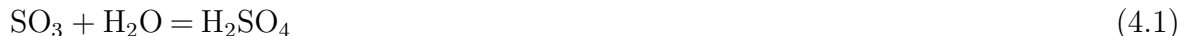
The initial mechanism that was considered was from Glarborg et al. [102]. Their work

studied SO_2 and SO_3 formation in post-combustion conditions in the presence of CO , and the formation of SO_3 . While it targeted oxy-fuel combustion conditions, it still contained a sulfur mechanism (H/S/O subset) that is suitable for this work, as it was validated experimentally. The study from Alzueta et al. [103] used the Glarborg et al. sulfur subset to study in experimental and theoretical conditions the interaction of SO_2 with the radical pool under combustion conditions. Hindiyarti et al. [104] refined the numerical model by investigating through ab initio calculations the reaction of SO_3 with H, O, and OH, also in the absence of combustibles, which represent the same condition of this study. Giménez-López et al. [105] studied experimentally and numerically the influence of the presence of SO_2 on CO oxidation in a CO_2 atmosphere characteristic of oxy-fuel combustion, comparing the results to traditional N_2 atmosphere, by using the chemical mechanism from Alzueta et al. and applying further corrections to the sulfur model based on the most recent sulfur studies. Fleig et al. [19] measured and modeled post-flame conditions effects of SO_2 , O_2 , NO, water, and CO_2 on SO_3 formation, with and without combustibles, using the validated model from Giménez-López et al. [105]. Choudhury et al. [18] applied the same model to an experimental and numerical study of SO_3 formation in oxy-fuel combustion.

These successive iterations and refinements of the original sulfur model from Glarborg et al. [102] have specifically targeted SO_2 and SO_3 formation in a variety of different high-temperature conditions, namely oxy-fuel or air-fired, with or without combustibles. The last iteration of that sulfur model (the H/S/O subset) was included in Gersen et al. [106], and was used in this work as it was validated by the literature numerically and experimentally. One important result from previous studies is that the thermal dissociation of SO_3 to SO_2 is not important for temperatures up to 1100K as the conversion of SO_2 to SO_3 is kinetically limited [107, 108]. Since the maximum temperature of this study is 700K (425C), SO_2 and SO_3 are not expected to react in the measurement cell. This would mean that the reactions in the measurement cell would involve SO_3 and H_2SO_4 only, while SO_2 remains chemically frozen.

The experimental studies in this work are carried out in the absence of some other typical flue gas species, such as carbon oxides and nitrogen oxides. The role of these species in the flue-gas has been reported in the literature, and they can alter the reaction paths of SO₂ and SO₃. Carbon species can act as collision partners with high third-body efficiency to promote reactions (for example, the high concentrations of CO₂ in oxy-fuel combustion impacts the SO₂ – SO₃ split [105]). SO₂ generally inhibits CO oxidation [102], while it can promote it under some conditions [103]. Direct reactions between NO_x and sulfur oxides are believed to be unimportant in flue-gas conditions [102], but this finding is still controversial [109]. NO_x appears unequivocally however to interact indirectly with sulfur oxides pathways through the radical pool [96, 102, 104, 110]. Hence, a possible effect of other species at experimental conditions can not be completely excluded. The primary objectives of the current work, definition of spectral libraries for SO₃, SO₂, and H₂SO₄, investigation of SO₃/H₂SO₄ chemical equilibrium, and verification of feasibility of continuous sulfur species measurements at flue-gas conditions, are not impacted by the possible chemical role of other species. In any case, additional species can be introduced after the different measurement techniques are validated for sulfur oxides and sulfuric acid. This experimental and numerical work did not include any additional carbon or nitrogen oxides. The avoidance of these species also permits the current work to exclude the H/C/O subset from the mechanism of Gersen et al. [106]. The modified mechanism used for this research ultimately consists of 308 reactions and 44 species.

As described previously, the general conventional mechanisms such as Glarborg et al. [102] or Gersen et al. [106] were used as the framework but they do not include H₂SO₄, as only the work from Choudhury et al. [18] includes an SO₃ hydration step. The global reaction



has been studied extensively in the literature (details were provided in Section 1.3) but not in flue-gas conditions. The hydration of SO₃ will hence need to be added separately to the

existing Gersen et al. high-temperature sulfur mechanism. The exact pathway to H_2SO_4 formation is still unclear, as at certain temperatures SO_3 is very reactive when water is present. Table 4.1 lists the current four different references providing a SO_3 hydration mechanism as a one-step simplified reaction.

Reaction	Rate	Source
1. $\text{SO}_3 + \text{H}_2\text{O} \longrightarrow \text{H}_2\text{SO}_4$	$9 \cdot 10^{-13}$	[24]
2.	$5.7 \cdot 10^{-15} \pm 16\%$	[31]
3.	$1.2 \cdot 10^{-15} \pm 20\%$	[30]
4. $\text{SO}_3 + 2 \text{H}_2\text{O} \longrightarrow \text{H}_2\text{SO}_4 + \text{H}_2\text{O}$	$3.9 \cdot 10^{-41} \exp(6830.6/T)[\text{H}_2\text{O}]^2 \pm 20\%$	[32]

Table 4.1: Possible hydration models for SO_3 and respective reaction rates.

When going through the choice of SO_3 hydration model, Castleman et al. [24] and Wang et al. [31] (Reactions 1 and 2 in Table 4.1) are not considered because they are affected by heterogeneous reactions on the walls, which is found to be very significant for Castleman et al. work [30]. Reiner et al. [30] and Jayne et al. [32] (Reactions 3 and 4 in Table 4.1) are most relevant for a detailed analysis and comparison.

The reaction mechanism from Jayne et al. successfully captures the experimental behavior of a second order water vapor concentration dependence. When the concentration $[\text{SO}_3] \ll [\text{H}_2\text{O}]$, the decay of SO_3 from the reaction can be represented by a pseudo-first order approximation [31], so also a formulation with a first order water vapor dependence (such as the one from Reiner et al.) could be appropriate under those circumstances. Since in this study $[\text{SO}_3] < 100\text{ppm}$ and $[\text{H}_2\text{O}] > 3\%$, the formulation from Reiner et al. can be appropriate as well, and the two models are expected to provide similar results. The reaction step from Reiner et al. was developed for a temperature of 298K, while the reaction step from Jayne et al. used a range of temperature from 283K to 370K, only marginally closer to the current experimental conditions. The reaction step from Reiner et al. was developed at pressures from 31 to 260 mbar (3kPa to 26kPa), while the one from Jayne et

al. was developed over the range from 100 to 760 Torr (13kPa to 101kPa), with the last condition reaching the atmospheric pressure of this study. The reaction step from Jayne et al. proceeds with a relatively high activation energy, while reaction step from Reiner et al. proceeds without activation energy. The latter seems more appropriate since SO_3 and H_2SO_4 in flue gas are assumed to be at equilibrium, indicating an extremely fast reaction. The results of the two SO_3 hydration models are going to be compared in relation to the residence time, temperature, and concentrations in the experimental measurement cell, and related to the chemical equilibrium between SO_3 and H_2SO_4 . The difference in H_2SO_4 estimations between the three models for the SO_3 hydration reaction (the chemical equilibrium assumption, a first-order mechanism in water concentration with no energy barrier, or a second-order mechanism in water vapor with a modest energy barrier) will bound the uncertainties on the $\text{H}_2\text{SO}_4/\text{SO}_3$ split in experimental conditions, with the ultimate goal of verifying experimentally if SO_3 and H_2SO_4 are in chemical equilibrium with each other.

4.2 Fluent model

Ansys Fluent is used to define and solve a reactive thermo-fluid-dynamic model of the experimental measurement cell in typical experimental conditions. In this section, a detailed explanation of the model setup and the solver settings are provided for clarity.

The first step is importing the 3D model of the measurement cell, and a mesh is created. The mesh will divide the fluid and solid domain in multiple regions (cells) with different geometries where the solutions are going to be computed. Models with finer meshes are generally more accurate at the expense of a higher computational cost, while coarser meshes lead to faster calculations with less accurate or even non-physical results. The mesh refinement depends on the level of accuracy required, and should always pass a mesh-independence test, i.e., using a finer mesh would lead to the same results (within an acceptable tolerance), without significantly altering the flow patterns and the distribution of the variables. A good

quality mesh is paramount for reliable simulation results.

4.2.1 Model and mesh

The measurement cell prototype was designed using Dassault Systèmes SolidWorks® software and then imported into Fluent for modeling. This section introduces the model creation, methods of importing the files, and mesh setting. Challenges encountered are also addressed.

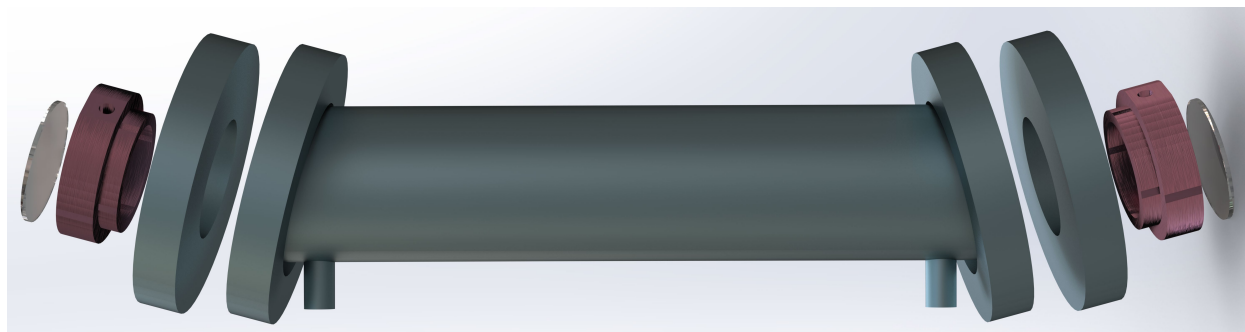


Figure 4.1: Rendering from ANSYS Solidworks measurement cell model.

The drawing of the measurement cell created in Solidworks follows the dimensions of the actual components in the measurement cell that this research is using, as shown in Figure 4.1. This means that no single component was simplified (except for the welding joints between parts). The cell is composed of a main body (center, formed by a stainless steel tube and two angled CF flanges welded at the extremities of the tube), two bored and tapped CF flanges mating with the cell main body and hosting two window holders (in red in Figure 4.1). The window holders fit two 2 in OD CaF_2 or BaF_2 windows. The cell main body and the two removable tapped CF flanges are merged into a single part for ease of modeling, and it will be referred to as the cell main body. As mentioned above, the model includes the cell main body, two window holders, and two windows.

The Solidworks models for the main body, holders, and windows are imported into ANSYS® SpaceClaim® to prepare the model for Fluent. In SpaceClaim the shared geometries between the parts are defined, the model is corrected for gaps, missing faces, extra edges, and inexact edges. The shared topologies are highlighted in green in Figure 4.2. Both

solid-fluid (common surfaces shared between walls of the measurement cell and fluid) and solid-solid (contact surfaces between flanges, windows, and window holders) connections are shown.

Importing a model with angled flanges from Solidworks led to imperfect edges where the flanges met the tube, creating gaps that could not be fixed or smoothed, resulting in unnecessary mesh refinement in those regions. Fortunately, it was also possible to edit parts directly in Spaceclaim, and in this case, the cell main body was imported with straight flanges that were later set at the correct angle. Following this approach the model did not present any issue with imperfect edges, resulting not only in a mesh with fewer nodes but also with higher mean and minimum orthogonal quality (a quality metric for meshes, the higher the better).

A last step in SpaceClaim is the definition and naming of the gas inlet and the gas outlet surfaces and the other surfaces where the boundary conditions will be applied. Fluent automatically recognizes surfaces named with the keywords *inlet* or *outlet* when importing. The definition of the origin is clear in Figure 4.3 : x is centered on the longitudinal axis of the measurement cell starting from the surface of Window 1 (upstream, closest to the Inlet Main Gas surface), and Inlet Main Gas and Outlet are located on the $x - z$ plane ($y = 0$).

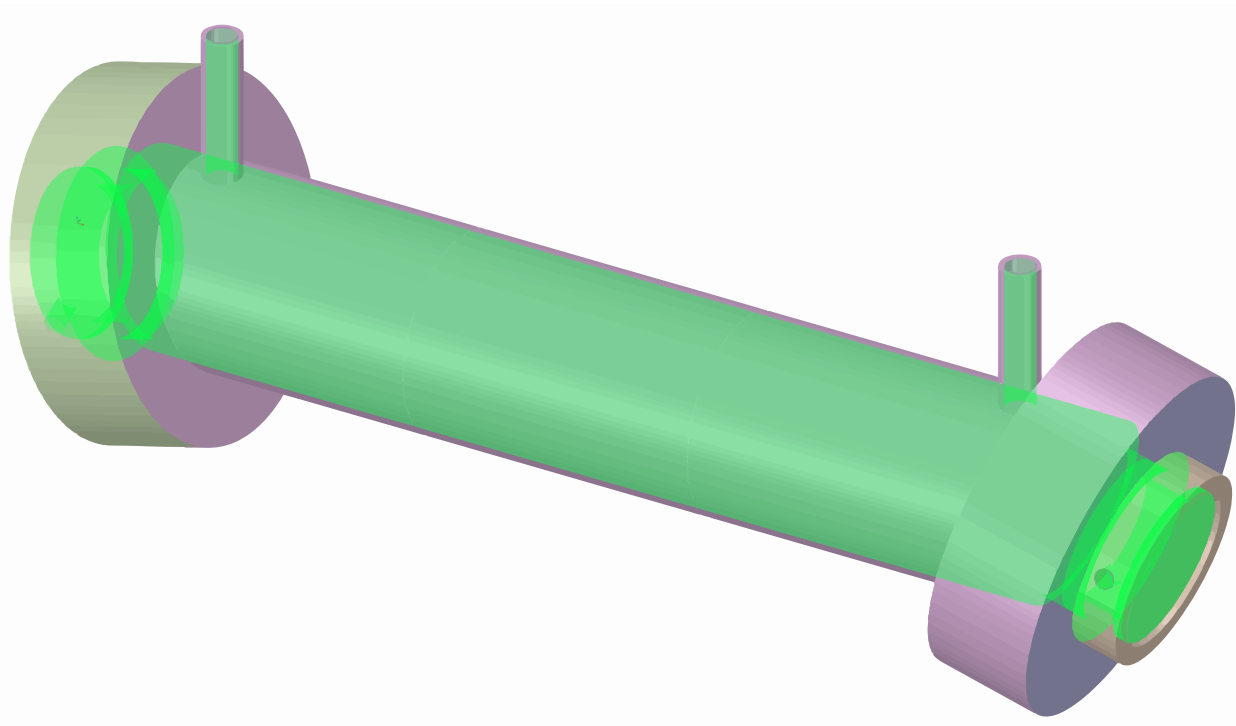


Figure 4.2: Trimetric view of the SpaceClaim measurement cell model. Shared topologies are highlighted in green.

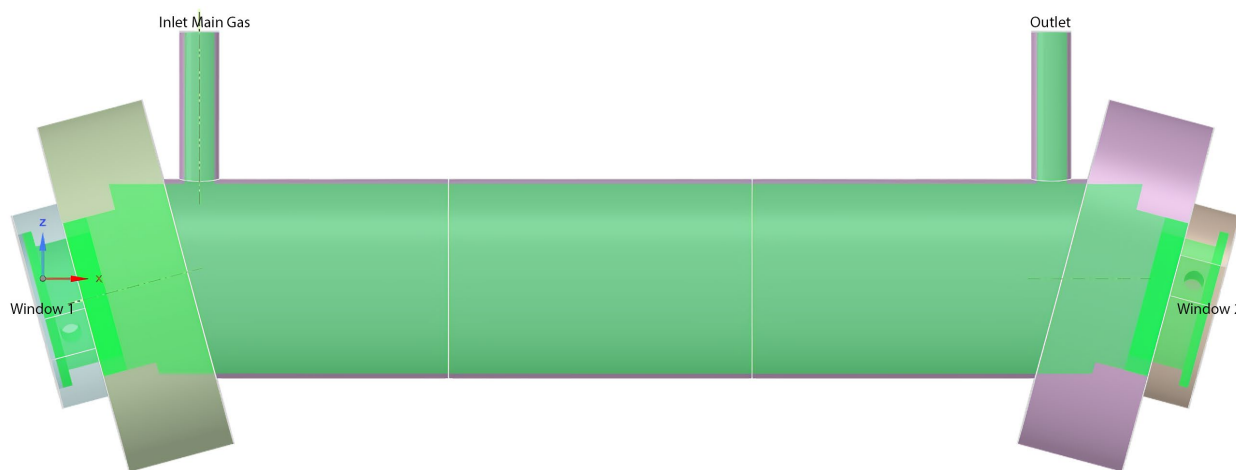


Figure 4.3: Side view of the SpaceClaim measurement cell model, with the definition of the origin.

The SpaceClaim model is then imported in ANSYS Fluent. The model is imported as a watertight geometry, with velocity inlets (the gas flow from the catalyst section, and two optional purging flows injected in front of the windows), and a pressure outlet (the gas exiting

the cell).

The mesh is generated using Fluent Mosaic Meshing Technology (poly-hexcore cells). According to ANSYS, the Poly-Hexcore feature achieves efficient meshing (significantly reducing cell count without affecting mesh quality) by filling the bulk region with octree hexes, a high-quality layered polyprism mesh in the boundary layer, and conformally connecting the two meshes with general polyhedral elements [101]. The resulting mesh is depicted in Figure 4.4 and Figure 4.5 and has 303186 cells, 1604132 faces, and 1088609 nodes. The mesh skewness for different regions is shown in Table 4.2. Low values are associated with good mesh quality: a value below 0.25 is considered excellent, between 0.25 and 0.5 is considered good, and values above 0.9 have to be avoided [101].

Cell Zone	Average	Maximum
Fluid	0.085	0.797
Holder 1	0.092	0.710
Holder 2	0.092	0.691
Main Body	0.094	0.799
Window 1	0.099	0.622
Window 2	0.099	0.554
Total	0.089	0.799

Table 4.2: Average and maximum skewness of the mesh in the different cell zones.

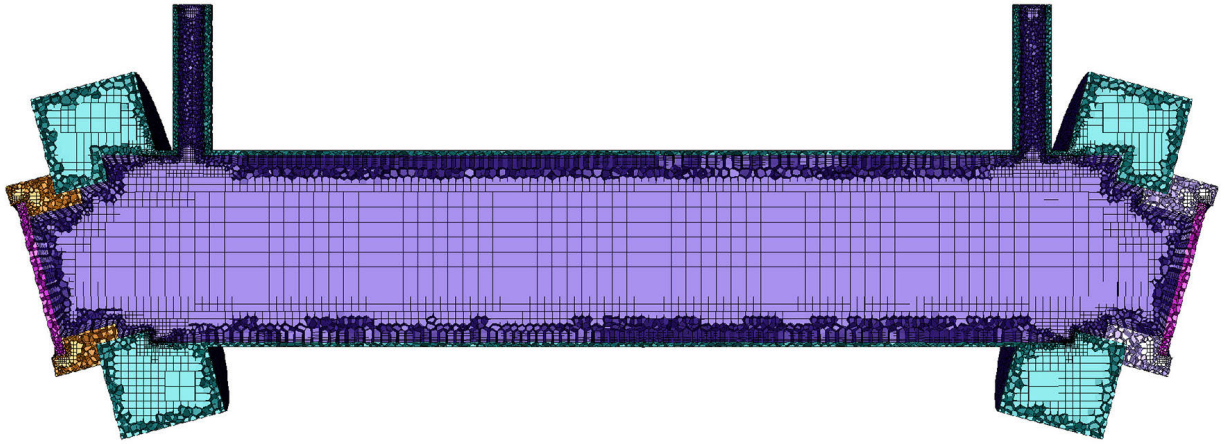


Figure 4.4: Mosaic mesh for the measurement cell. Fluid is represented in lilac color.

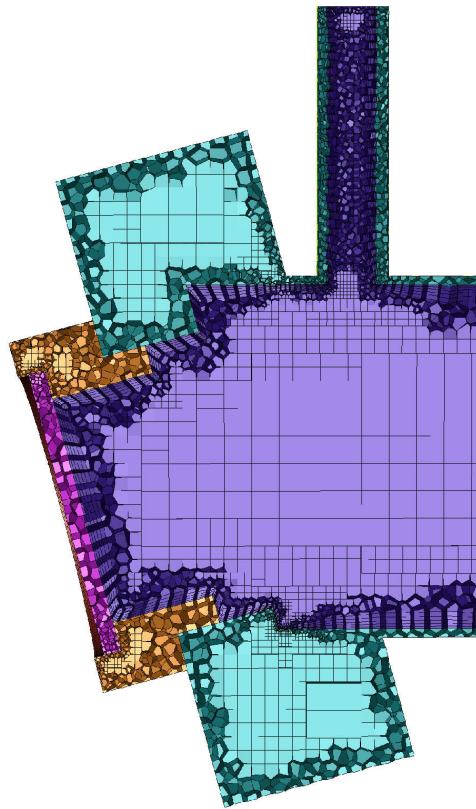


Figure 4.5: Detail of the mosaic mesh in close proximity to the gas inlet and the upstream window.

4.2.2 Boundary conditions

The surfaces of the model will require appropriate boundary conditions, depending on the type of boundary they represent. The boundary conditions are set on the surfaces seen in Figure 4.6, where different colors represents different boundary conditions/mesh zones which also reflects the experiment design. For example, the measurement cell thermal control uses one PID-controlled heating cable for region Heating 1 and one separate cable for region Heating 2. Regions Window 1, Holder 1 Face, Holder 1 Side, and Main Body Front Face 1 (and equivalent surfaces for Window 2) are exposed to room air at temperature T_{amb} and convective coefficient h_{amb} , as the need of optical access for laser measurements prevents insulation to be installed. Regions Main Body Side Faces and Port Walls are assumed adiabatic, since mineral wool insulation was installed. Region Heating 2 is considered adiabatic as well, as no heating cable is installed but it is covered in insulation material. The heat transfer coefficient and the thermal conductivity are listed in Table 4.3 along with the material for each section. In Figure 4.1, the stainless steel parts are represented in blue color, the aluminum parts are in red, and the two windows are in dark gray. The detailed boundary conditions are listed in Table 4.4, and Table 4.5.

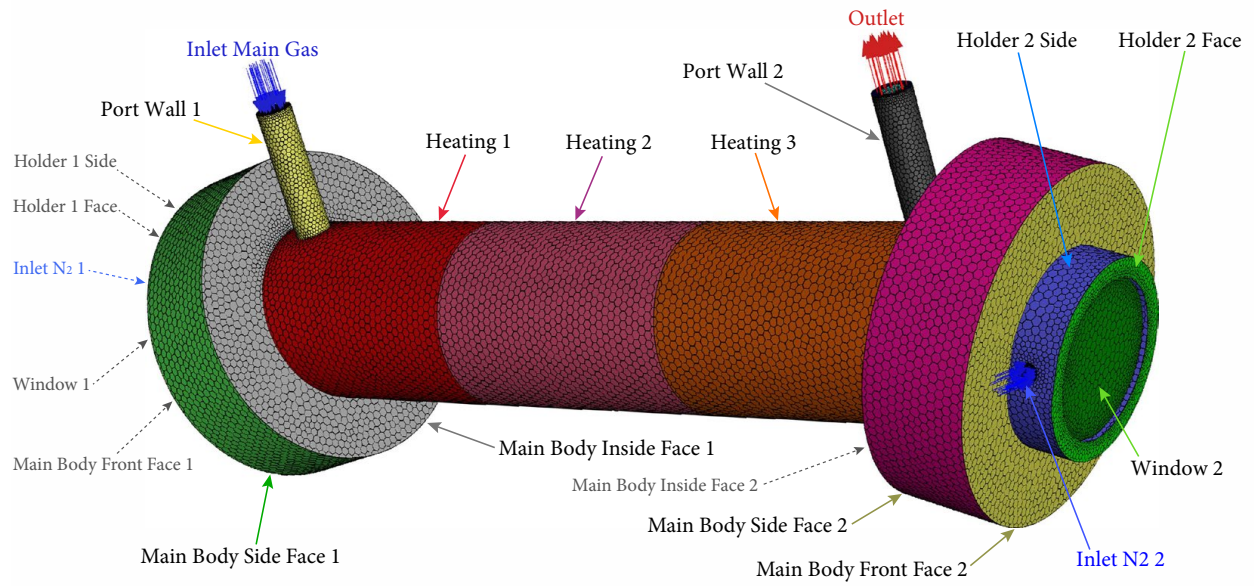


Figure 4.6: Representation of mesh zones, each one tied to a correspondent boundary conditions. Dashed arrows are related to surfaces not directly visible.

Factor	Description	Value
k_{st}	Stainless Steel conductivity	$16.3 \text{ W}/(mK)$
k_{al}	Aluminum conductivity	$202.4 \text{ W}/(mK)$
k_{BaF_2}	Barium Fluoride conductivity	$11.7 \text{ W}/(mK)$
h_{amb}	Convective heat transfer coefficient	$10 \text{ W}/(m^2K)$
T_{amb}	Ambient temperature around the cell	320 K

Table 4.3: Fluid and solid heat transfer-related parameters.

Surface	Condition	Value
Inlet Main Gas	Velocity Inlet	5 slm
	Temperature	700 K (425C)
	Composition (Mole Fraction)	0.711 N ₂ , 0.189 O ₂ , 0.1 H ₂ O, 3E-4 SO ₃
Inlet N ₂ 1	Velocity Inlet	0 to 1.25 slm
	Temperature	400 to 700 K (126C to 425C)
	Composition (Mole Fraction)	1.0 N ₂
Inlet N ₂ 2	Velocity Inlet	0 to 1.25 slm
	Temperature	400 to 700 K
	Composition (Mole Fraction)	1.0 N ₂
Outlet	Pressure Outlet	1 atm

Table 4.4: Boundary conditions for the fluid regions.

Surface	Condition	Value
Port Wall 1	Adiabatic Wall	0 W/m^2
Port Wall 2	Adiabatic Wall	0 W/m^2
Main Body Side Face 1	Adiabatic Wall	0 W/m^2
Main Body Inside Face 1	Adiabatic Wall	0 W/m^2
Main Body Side Face 2	Adiabatic Wall	0 W/m^2
Main Body Inside Face 2	Adiabatic Wall	0 W/m^2
Heating 2	Adiabatic Wall	0 W/m^2
Heating 1	Heat Flux	1200 W/m^2
Heating 3	Heat Flux	1200 W/m^2
Main Body Front Face 2	Convection	h_{amb}, T_{amb}
Main Body Front Face 1	Convection	h_{amb}, T_{amb}
Window 1	Convection	h_{amb}, T_{amb}
Window 2	Convection	h_{amb}, T_{amb}
Holder 1 Face	Convection	h_{amb}, T_{amb}
Holder 1 Side	Convection	h_{amb}, T_{amb}
Holder 2 Face	Convection	h_{amb}, T_{amb}
Holder 2 Side	Convection	h_{amb}, T_{amb}

Table 4.5: Boundary conditions for the solid regions.

4.2.3 Solver settings

The simulations are run with a *Pressure* solver (for incompressible flow) with the *SIMPLE* pressure-velocity coupling scheme, with *Energy equation* turned on, solving for a *Steady State* solution. Although a generally laminar flow is expected in the measurement cell, prior work has shown that laminar flow simulations underpredict transport and mixing driven by structural variations, and so a *k-epsilon* turbulence model is adopted for added flexibility at

the expense of a longer computation time. The settings are shown in Figure 4.7.

Viscous Model

Model

- Inviscid
- Laminar
- Spalart-Allmaras (1 eqn)
- k-epsilon (2 eqn)
- k-omega (2 eqn)
- Transition k-kl-omega (3 eqn)
- Transition SST (4 eqn)
- Reynolds Stress (7 eqn)
- Scale-Adaptive Simulation (SAS)
- Detached Eddy Simulation (DES)
- Large Eddy Simulation (LES)

Model Constants

Cmu: 0.0845

C1-Epsilon: 1.42

C2-Epsilon: 1.68

Wall Prandtl Number: 0.85

RNG Options

- Differential Viscosity Model
- Swirl Dominated Flow

Near-Wall Treatment

- Standard Wall Functions
- Scalable Wall Functions
- Non-Equilibrium Wall Functions
- Enhanced Wall Treatment
- Menter-Lechner
- User-Defined Wall Functions

Options

- Viscous Heating
- Curvature Correction
- Production Kato-Laundner
- Production Limiter

User-Defined Functions

Turbulent Viscosity: none

Prandtl Numbers

Wall Prandtl Number: none

k-epsilon Model

- Standard
- RNG
- Realizable

Figure 4.7: Settings for Fluent viscous model.

The settings for the species model are listed in Figure 4.8.

Species Model

Model

- Off
- Species Transport
- Non-Premixed Combustion
- Premixed Combustion
- Partially Premixed Combustion
- Composition PDF Transport

Reactions

- Volumetric
- Wall Surface
- Particle Surface
- Electrochemical

Chemistry Solver

Relax to Chemical Equilibrium

Integration Parameters...

Options

- Inlet Diffusion
- Diffusion Energy Source
- Full Multicomponent Diffusion
- Thermal Diffusion

Mixture Properties

Mixture Material: chemkin-import

Import CHEMKIN Mechanism...

Number of Volumetric Species: 7

Turbulence-Chemistry Interaction

- Finite-Rate/No TCI
- Finite-Rate/Eddy-Dissipation
- Eddy-Dissipation
- Eddy-Dissipation Concept

Coal Calculator...

Options

Flow Iterations per Chemistry Update: 1

Select Boundary Species

Select Reported Residuals

Figure 4.8: Settings for Fluent species model.

Notably, the *Volumetric reactions* option is initially deactivated to achieve a faster fluid-dynamic convergence of the model. Then, only after convergence is achieved, the volumetric reactions are introduced. A background on the process and steps that Fluent uses to determine numerical solutions is provided for clarity, as for example it gives insight into the

handling of diffusion processes and how they are relevant to this study. The explanations are extracted from the Fluent User’s Guide Manual 2020 R2 [101] and Fluent Theory Guide 2020 R2 [111]. When the *Volumetric reactions* option is activated, Fluent determines the mixing, transport, and reactions of chemical species by solving for every species a mass conservation equation (describing convection and diffusion) and a finite-rate reaction model. The mass conservation for species i takes the general form:

$$\frac{\partial}{\partial t}(\rho Y_i) + \nabla \cdot (\rho \vec{v} Y_i) = -\nabla \cdot \vec{J}_i + R_i + S_i \quad (4.2)$$

where R_i is the net rate of production of species i by chemical reaction and \vec{J}_i is the diffusion flux of species i . In laminar flows (such this study) Fluent uses by default a dilute flow approximation, where a Fickian description is accurate enough to model mass diffusion inside the mass conservation equations.

$$\vec{J}_i = -\rho D_{i,m} \nabla Y_i - D_{T,i} \frac{\nabla T}{T} \quad (4.3)$$

where $D_{i,m}$ is the mass diffusion coefficient for species i and $D_{T,i}$ is the thermal diffusion coefficient.

When kinetic-theory is specified for the thermal diffusion coefficient (as shown in Figure 4.9), Fluent computes the thermal diffusion coefficient using an empirically-based and composition-dependent expression ($D_{T,i} \propto T^{0.659}$). If kinetic-theory is specified for the mass diffusion coefficient, Fluent will use a modified Chapman-Enskog formula to compute the mass diffusion coefficient ($D_{i,m} \propto T^{1.5}$).

For multi-component systems where molecular transport processes are important, the diffusive mass flux is obtained instead through the Maxwell-Stefan equations (*Full Multicomponent Diffusion* description). Since the problem in analysis involves several species, and diffusion is expected to be important, the *Full Multicomponent Diffusion* option is enabled, as well as the *Inlet Diffusion* option (describing the diffusion flux of species at the

inlet), the *Diffusion Energy Source* option (includes the effect of enthalpy transport due to species diffusion in the energy equation), and the *Thermal Diffusion* option.

The *Turbulence-Chemistry Interaction* is set to *Finite-Rate/No TCI*. With no turbulence-chemistry interaction the reaction rates are not altered by turbulence mixing but proceed at a finite rate determined by the Arrhenius reaction rate. The Chemistry Solver is set to *Relax to Chemical Equilibrium*, with species reacting to chemical equilibrium instead of complete reaction. While this is an approximation of the SO_3 , H_2SO_4 , H_2O relationship, the validity of the hypothesis will be analyzed both experimentally (Chapter 6) and numerically (with a Chemkin model, Section 5.2.2), and this approach results in a lower computational cost, as the determination of the reaction rates is unnecessary. The model assumes no surface reactions (walls in the experimental cell are coated with Silconert) and no solid species present.

Properties of chemkin-import

Mixture Species	names	Edit...
Reaction	finite-rate	Edit...
Mechanism	reaction-mechs	Edit...
Density (kg/m ³)	incompressible-ideal-gas	Edit...
Cp (Specific Heat) (j/kg-k)	mixing-law	Edit...
Thermal Conductivity (w/m-k)	constant	Edit...
	0.0454	
Viscosity (kg/m-s)	constant	Edit...
	1.72e-05	
Mass Diffusivity (m ² /s)	kinetic-theory	Edit...
Thermal Diffusion Coefficient (kg/m-s)	kinetic-theory	Edit...

Figure 4.9: Settings for Fluent species model mixture properties

Convergence is determined according to the values of the residuals as shown in Figure 4.10. The residuals for H_2SO_4 and SO_3 are not used for convergence, but the mean value of H_2SO_4 and SO_3 in the cell is instead monitored. The convergence for those species is achieved

when over the previous 50 iterations the concentrations varied less than 0.1% (Figure 4.11).

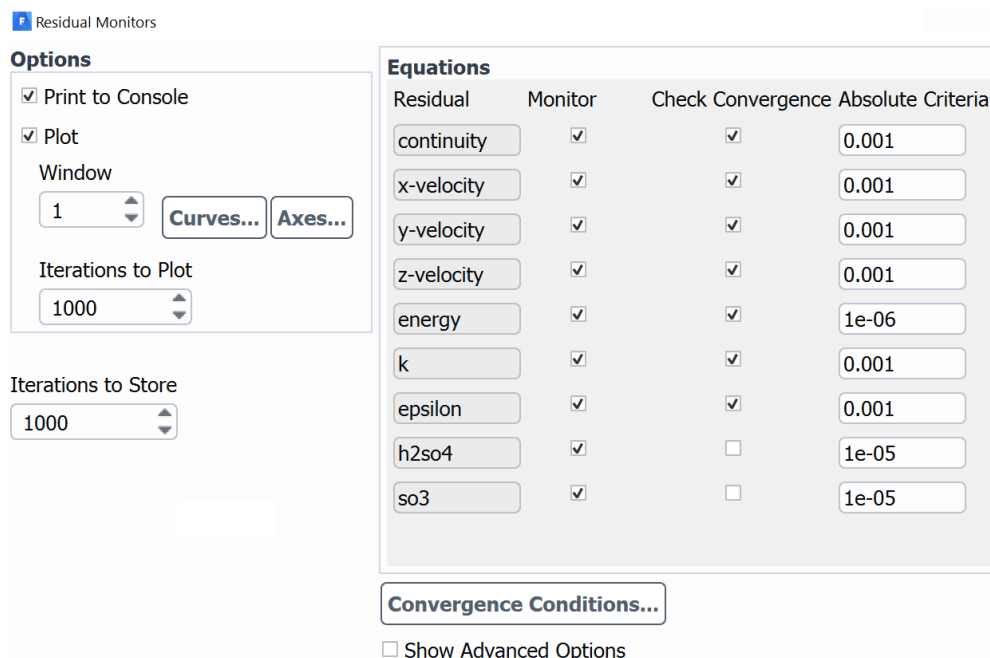


Figure 4.10: Settings for Fluent residual monitor.

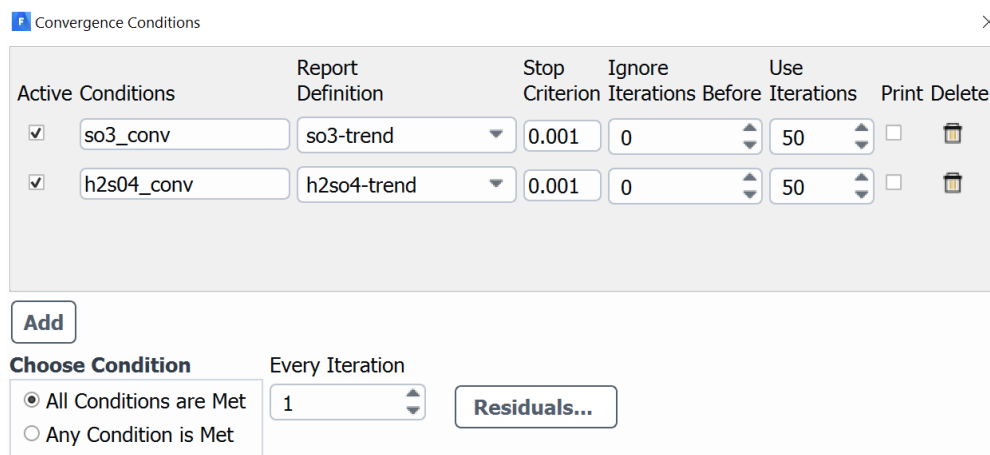


Figure 4.11: Settings for Fluent additional convergence conditions for SO₃ and H₂SO₄.

The Chemkin model described in Section 4.1 can provide insights into the expected behavior of SO₂, SO₃, and H₂SO₄ in experimental conditions, such as the possible chemical equilibrium of SO₃ and H₂SO₄, and the relationship between SO₂ and SO₃. While the selected sulfur mechanism (the S/H/O subset from Gersen et al.) has been experimentally

validated in the literature, the hydration reaction of SO_3 is still not completely accepted. Two different single step mechanisms (Jayne et al. and Reiner et al.) have been selected to be compared to the chemical equilibrium calculations to estimate the difference between the three models. The Fluent model provides a refined picture of the expected experimental conditions, including the temperature profiles in the measurement cell and chemical species spatial distribution. The latter is affected not only by temperature-dependent chemical reactions but also by advection and diffusion. The results from the models are analyzed and discussed in the next chapter.

Chapter 5

Numerical results

In this chapter, the numerical results from ANSYS[®] Chemkin[™]-Pro and ANSYS[®] Fluent[®] models described in Chapter 4 will be presented and analyzed. The simulated-experiment conditions relevant for this research cover 3-14% water vapor content over a temperature range 523K - 700K. Therefore, conditions outside this domain will not be addressed.

As a first step, Chemkin is used to study sulfur species at equilibrium conditions, followed by the analysis of the physical configuration of the experimental measurement cell to identify key aspects in the reaction paths, in order to develop an appropriate reduced chemical mechanism for implementation in Fluent. The equilibrium and kinetic study using Chemkin (Sections 5.1 and 5.2 respectively) include pure thermodynamic properties of species, and incorporates the *combined-mech1* (Gersen et al. plus Reiner et al.) and *combined-mech2* (Gersen et al. plus Jayne et al.) addressed in Chapter 4 for a detailed verification to be readily used in Fluent (Section 5.3).

Fluent simulations aim at evaluating the spatial temperature profile together with SO₃ and H₂SO₄ concentrations in the measurement cell. The model results describe the level of non-uniformity that is to be expected in the physical system. This is particularly important when referring to the core section of the gas cell, that is the window-to-window volume that

the Mid-IR laser is crossing. Moreover, the radial temperature profile near the measurement cell walls is useful to investigate the thickness of the thermal boundary layer as a guide for the temperature measurements location. They should experimentally be carried out outside the boundary layer and in the region where the flow is fully thermally developed.

During the actual experimental runs there was extensive window damage from the reaction of the window materials with sulfur species. The window damage magnifies especially at low temperature (250C), where all the $\text{SO}_3/\text{H}_2\text{SO}_4$ sulfur content is present in the form of H_2SO_4 . Sulfuric acid reacts directly with the BaF_2 (or CaF_2) from the windows to form BaSO_4 (or CaSO_4) according to the reaction:



The reaction results in a wavelength-specific degradation of windows performance (decrease transmissivity), and, if the adverse environmental conditions are prolonged in time, the windows show a white and cloudy layer and become completely opaque visually and optically. More details on the effect of the window damage on laser measurements and its implications appear in Section 5.3.5. The simulations will analyze the effect of a simple nitrogen purging solution in front of the windows to mitigate sulfuric acid attack in Section 5.3.

All the simulations make use of models, ranging from reactor models to turbulence models, and each of them is subject to a degree of uncertainty and might not accurately describe some experimental conditions. Models that are validated in the literature against experimental tests are more likely to be appropriate, however they are strictly valid only in very specific scenarios. In this chapter, the models that are more likely accurately describe the experimental conditions will be used, relying on the backing of the literature. However, it is still possible that the predictions from the models will not agree with the experimental readings, either because of experimental uncertainties and/or because of model uncertainties. One example is that the two models for the reaction step of sulfuric acid formation

used in this work by themselves present a $\pm 20\%$ uncertainty. The results from the modeling are very helpful to highlight major effects and expected behaviors, however, they should be trusted for their numerical accuracy only within reason.

5.1 Chemical equilibrium analysis using Chemkin

ANSYS Chemkin-Pro includes an Equilibrium Reactor (ER) model that can be used to study gas mixtures at chemical equilibrium. The gas composition at equilibrium depends only on the thermodynamic properties of the species in the chemistry set, as well as the starting composition and thermodynamic conditions specified. The equilibrium calculation relies on the minimization of Gibb's free energy (at constant temperature and pressure), and it ignores kinetic and transport limitations of chemical reactions. Therefore, with the Equilibrium Reactor model the results are not dependant on the chemical mechanism that is used except as regards the inclusion of the relevant species.

Figure 5.1 represents the results from the Chemkin Equilibrium Reactor model for sulfur species (H_2SO_4 , SO_3 , SO_2), with two different cases of initial water vapor concentrations, 3% and 12%, with 300ppmv SO_3 in air background. The results are normalized based on the total sulfur content at 300ppmv.

Water vapor substantially alters the equilibrium between H_2SO_4 - SO_3 at low temperatures. Moreover, the concentration of H_2SO_4 is significantly higher at all temperatures of power plant operation interest ($< 700\text{K}$) with high water vapor concentration. On the other hand, water vapor does not have a significant effect on the SO_3 - SO_2 equilibrium split at high temperatures, where SO_2 formation (from SO_3 thermal dissociation, previously seen in Section 4.1.2) starts for both water concentrations at about 700K (425C), which is at the upper end of this work's experimental operating temperature. This is because SO_3 shifts slightly ($\sim 50\text{K}$) to a relatively higher temperature region while SO_2 demonstrates almost no effects from the water content.

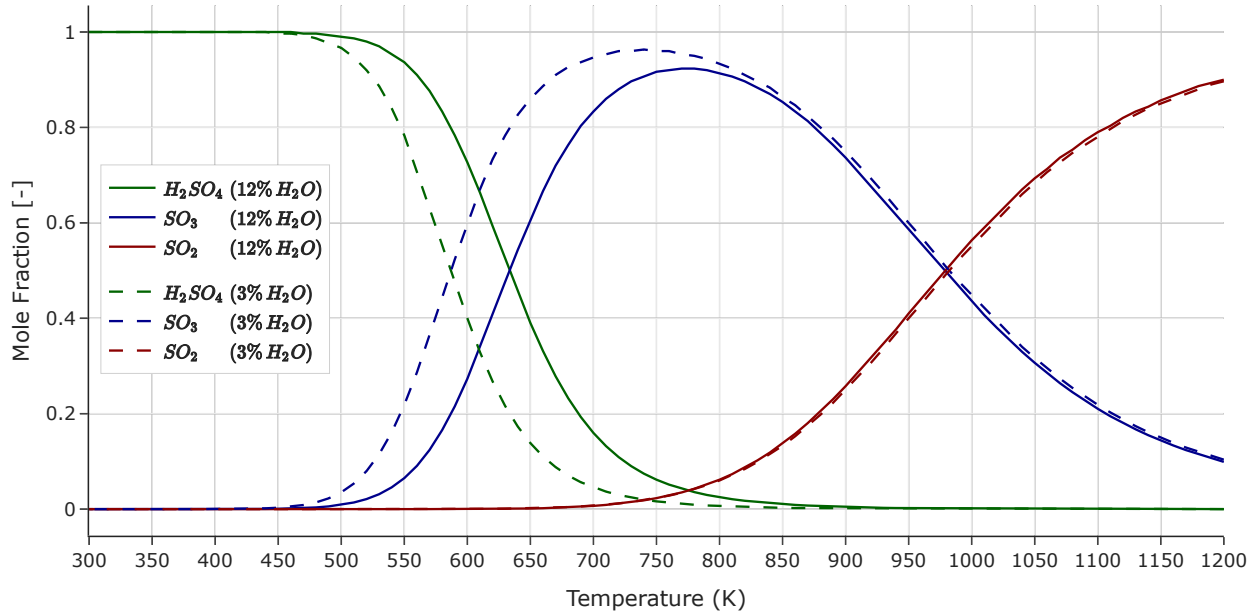


Figure 5.1: Normalized equilibrium curve for sulfur species as a function of gas temperature for two different water concentrations 12% (solid) and 3% (dash).

5.2 Identification of key aspects in the reaction paths for experiment conditions

In this section, the conditions in the experimental measurement cell are used as the conditions within the Chemkin simulation. The measurement cell has a volume of 1 liter and the inlet flow rate is 5 slm. The residence time can be, therefore, well characterized as it varies with the gas temperature. As a reference, the order of magnitude of the residence time of the gas in the measurement cell in experiment conditions is on the order of magnitude of 10 to the first power, which is ~ 10 seconds. It will be addressed as 10 seconds in the following content.

A Perfectly Stirred Reactor (PSR) is used (0-D Model) for which the gas mixture inside the reactor is assumed to be spatially uniform and the rates of conversion are controlled by chemical reactions rather than mixing processes. With this assumption, the reactor conditions can be well represented by spatially averaged properties. A suitable alternative

would be a Plug Flow Reactor (PFR, 1-D Model), where it is assumed that there is no mixing in the axial flow direction but perfect mixing in its perpendicular axis.

In this section a PSR is used to draw preliminary conclusions globally from the reaction paths, in absence of surface reactions locally. A more accurate detailed simulation using real aspects of local boundary conditions from the experimental system will be achieved later with the Fluent model, and the impact of multi-species diffusion as well as thermal and chemical non-uniformity will be evaluated.

5.2.1 SO₂ formation from SO₃ thermal dissociation

Figure 5.2 represents the comparison between the results of the Chemkin PSR model (solid line), based on the *combined-mech1* model and the Chemkin ER model (dashed line), starting from 300ppmv SO₃ and 10% water vapor in air, normalized based on the total sulfur content.

SO₂ does not start forming from the thermal dissociation of SO₃ until about 1050K. This is in line with literature research in flue gas conditions. Thermal dissociation is very slow below 1100K, and with temperature ranging from 1050K to 1425K the SO₃ conversion increases from being negligible to almost complete [107, 108]. The thermal dissociation of SO₃ is hence kinetically limited, and this also verifies the reliability of the combined mechanism. Considering that these temperatures are well above those in the experiment, this high-temperature decomposition is not active and can be neglected if equilibrium conditions dominate.

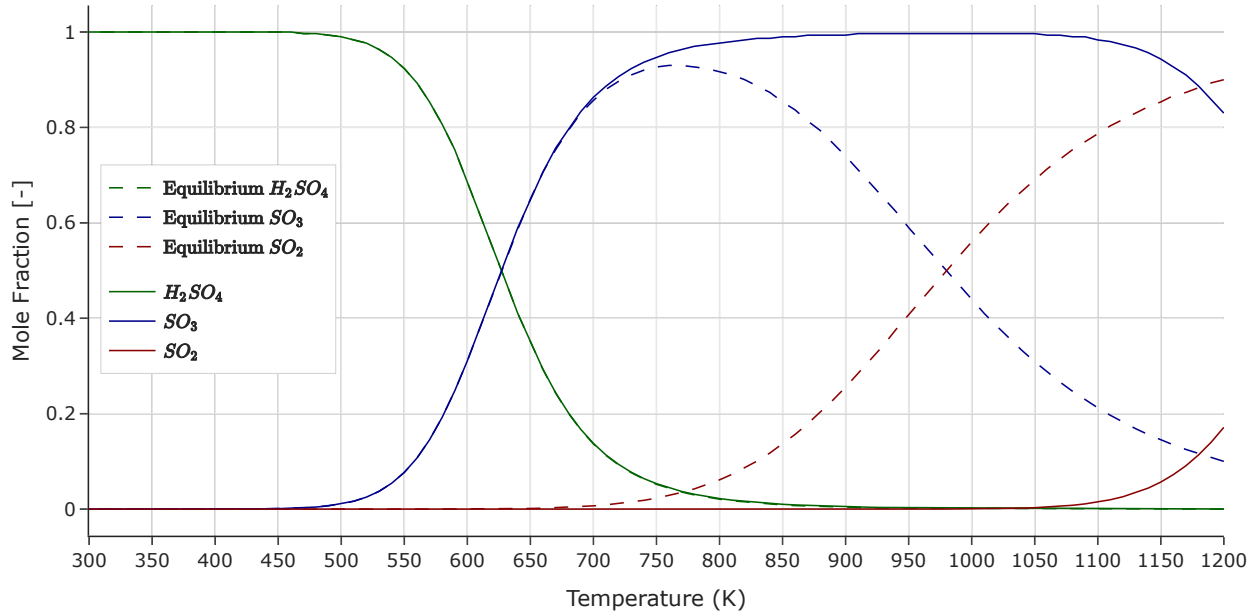


Figure 5.2: Normalized PSR simulated-experiment conditions results using the *combined-mech1* (solid) compared to ER equilibrium conditions (dash)

Figure 5.3 shows the impact of residence time on the SO_3 conversion to SO_2 for different gas temperatures, starting from 300ppm SO_3 and 10% H_2O normalized based on sulfur content using PSR *combined-mech1*. As described above, the gas flow in the experiment has around 10 seconds residence time when passing through the measurement cell. Figure 5.3 shows that SO_2 formation is negligible for 10 seconds at 800K and 1000K. Both temperatures are above 700K (425C), and therefore in experimental conditions the thermal dissociation of SO_3 to SO_2 is not a relevant process even when kinetics are taken into account. At 1200K and 10s, SO_2 reaches about 45% of its equilibrium value, and a full equilibrium is reached after about $5 \cdot 10^2$ seconds. Zhang et al. [108] has demonstrated that residence time is an important factor in the SO_3 thermal dissociation process, however, its effect decreases with increasing temperature. Therefore, the results of residence time of the PSR *combined-mech1* model at different gas temperatures also reflects the existing literature, and this further confirms the credibility of the model's indication that SO_3 thermal dissociation is not a significant contributor in the conditions of the current experiments.

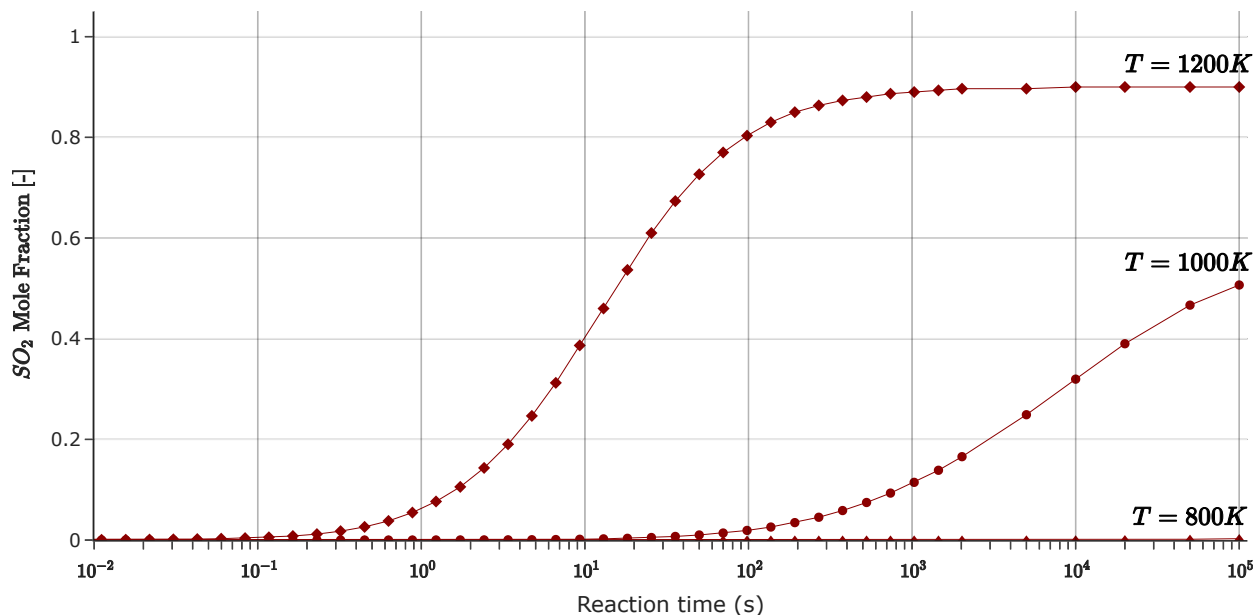


Figure 5.3: Formation of SO_2 from SO_3 thermal dissociation as a function of reaction time for different gas temperature.

5.2.2 Simulated H_2SO_4 and SO_3 are fundamentally at equilibrium

After verifying that the SO_2 formation is not influenced from SO_3 thermal dissociation, this section is focused on SO_3 and H_2SO_4 concentrations, and the equilibrium plot of *combined-mech1* and ER model as shown in Figure 5.2. Chapter 4 emphasized that there are only a few SO_3 hydration mechanisms available in the literature, and this section compares the *combined-mech1* and *combined-mech2* particularly for the purpose of understanding the sensitivity of this equilibrium to assumptions of the mechanism employed. Figure 5.4 represents these two different H_2SO_4 hydration reactions from Reiner et al. and Jayne et al. respectively, starting from 300ppmv SO_3 and 10% H_2O , normalized for sulfur content. In these conditions, the difference between the two reactions is very small across all the temperature range. Notice that the high temperature region is not represented in Figure 5.4

since the results from these two overlap in the temperature regime where SO_2 forms.

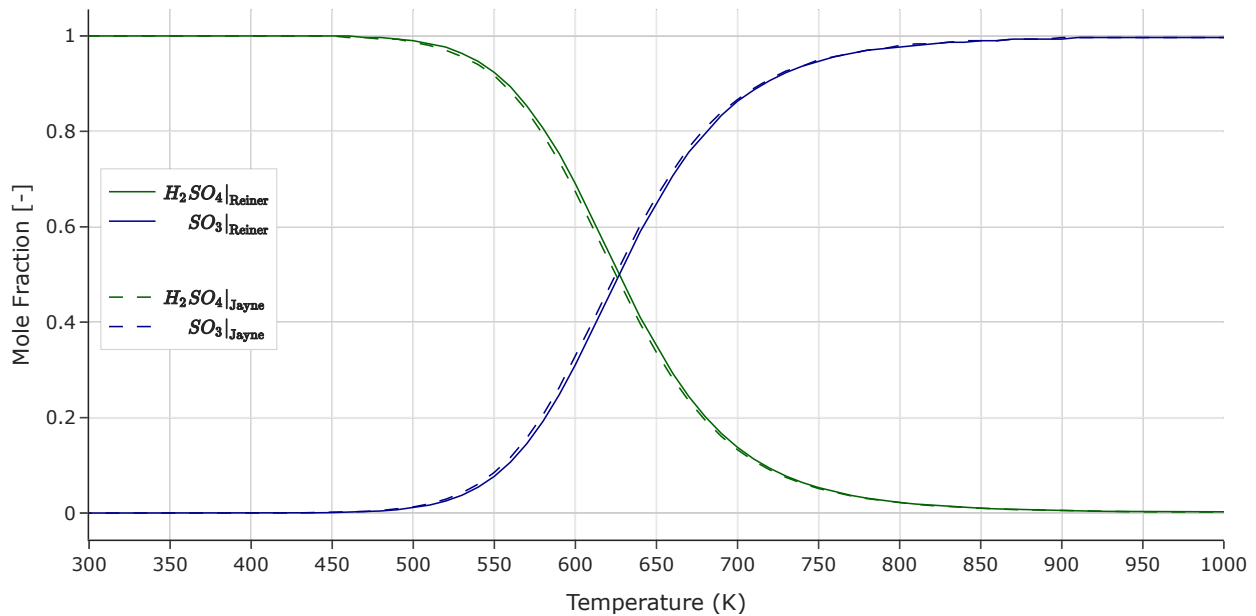


Figure 5.4: PSR simulated-experiment conditions for the *combined-mech1* model (solid) compared to the *combined-mech2* model (dash).

Figure 5.5 shows the difference of H_2SO_4 estimation between the two mechanisms, evaluated as:

$$E = 100 \cdot \frac{\text{H}_2\text{SO}_4|_{\text{Reiner}} - \text{H}_2\text{SO}_4|_{\text{Jayne}}}{\text{H}_2\text{SO}_4|_{\text{Reiner}}} \quad (5.2)$$

The difference in percentage based on *combined-mech1* is always less than 5% with water vapor ranging from 8-14% (flue-gas conditions relevant to this work), while the difference can reach around 15% at lower water vapor content (3% H_2O). The uncertainty on the reaction rate for each model is in the same range as the error between the two mechanisms. In simulated-experiment conditions, the two mechanisms yield similar results, and both of them offer the same performance in describing the experimental conditions in this work within their levels of uncertainty.

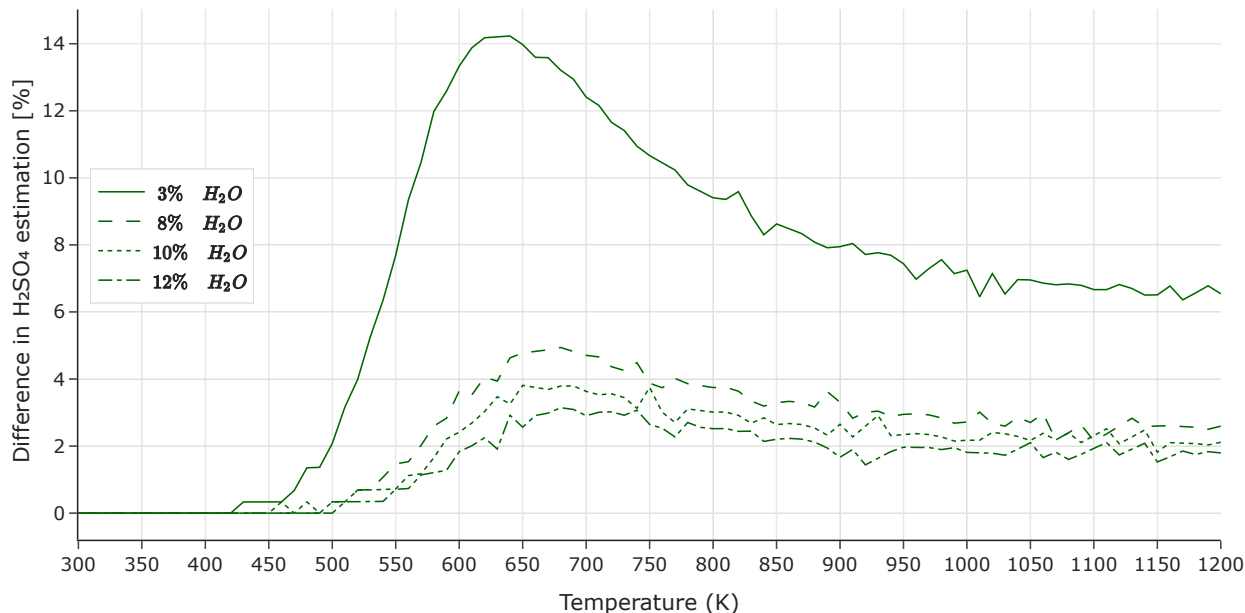


Figure 5.5: Difference in prediction of H_2SO_4 formation between *combined-mech1* and *combined-mech2* models as a function of temperature for different water vapor content.

A further confirmation of the reliability of the Chemkin results comes from the analysis of the reaction time for the formation of H_2SO_4 at different temperatures for the two mechanisms. The results using *mech2* represented in Figure 5.7 predict a slower reaction time, achieving $> 85\%$ of the equilibrium concentrations in 1 second and full equilibrium concentrations in 10 seconds. The results from *mech1* predict that equilibrium is reached in 0.1 seconds, as seen in Figure 5.6. The initial conditions for both simulations are 300ppm SO_3 and 10% H_2O in air, and H_2SO_4 concentrations are normalized for total sulfur content for both Figure 5.7 and Figure 5.6.

The difference in reaction time between the two is large. The reaction from Jayne et al. was derived in conditions more similar to this work with respect to Reiner et al., and it also captured a second-order behavior in water vapor that could better describe the experimental character of the reaction, according to the literature review of Section 4.1.2. The reaction from Jayne et al. could therefore provide better results for the flue gas case, but with the current residence time of 10 seconds the choice of the reaction does not have a significant impact on the expected H_2SO_4 concentrations. In fact, according to the numerical simulation

results SO_3 and H_2SO_4 can be considered to be in chemical equilibrium, while SO_2 can be considered as kinetically frozen. In Fluent simulations, the species will therefore be considered as equilibrium, reducing the numerical complexity of the model.

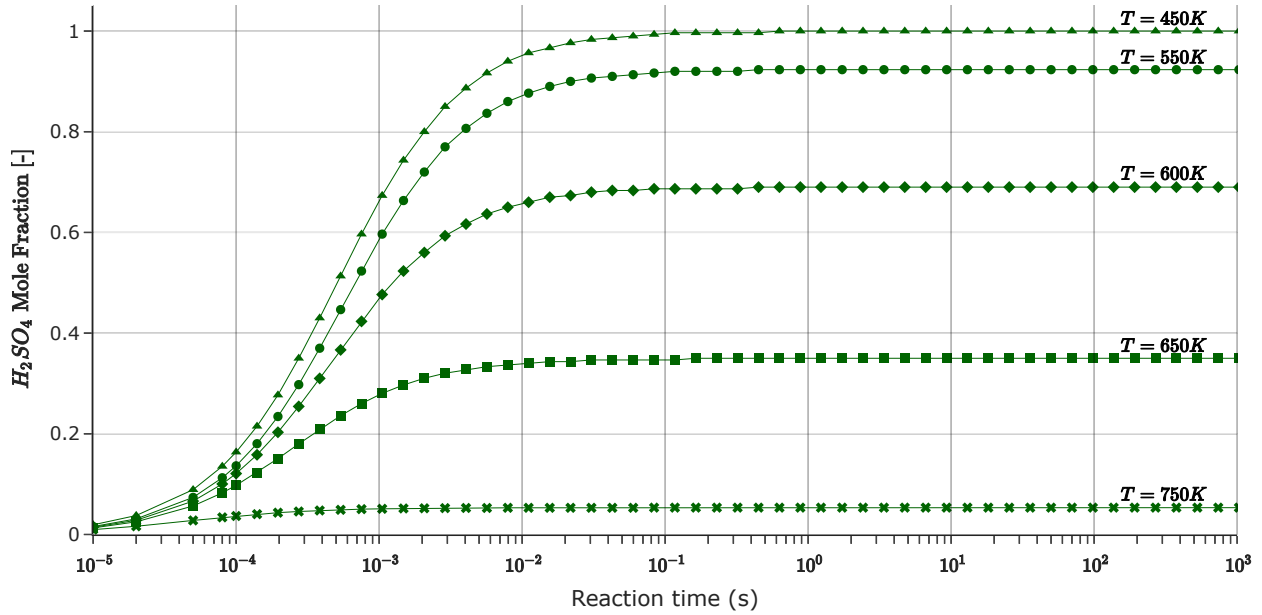


Figure 5.6: Formation of H_2SO_4 predicted from *combined-mech1* mechanism as a function of residence time for different gas temperatures.

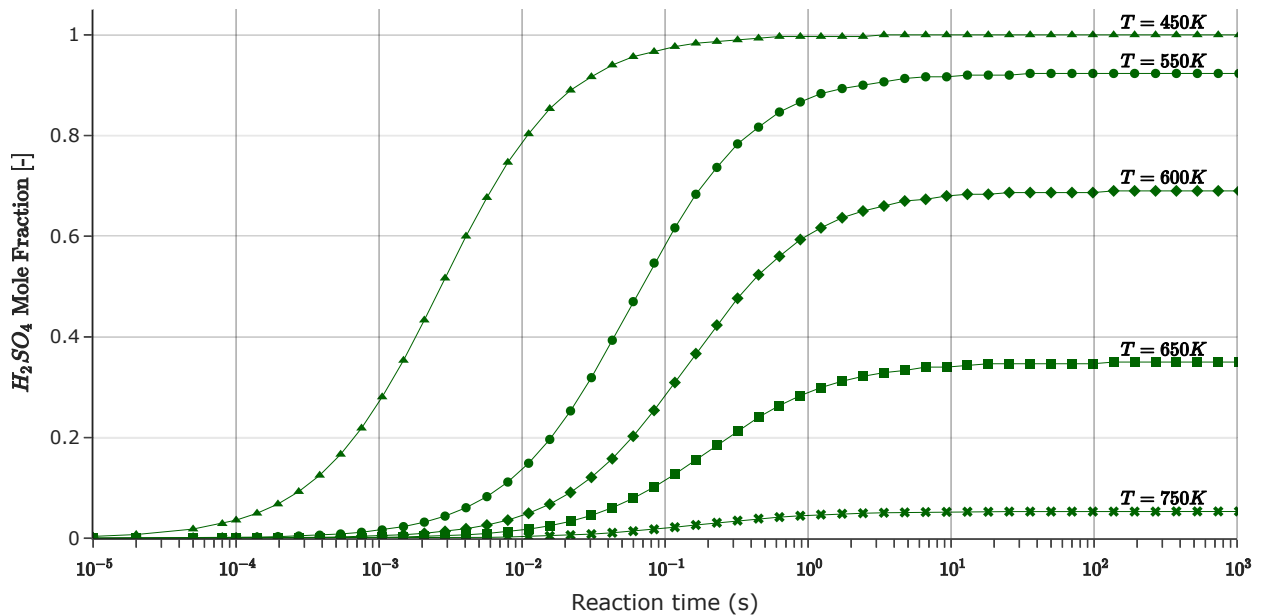


Figure 5.7: Formation of H_2SO_4 predicted from *combined-mech2* mechanism as a function of residence time for different gas temperature.

SO₂ in the measurement cell comes from the incomplete reaction of the SO₂ stream in the catalyst section, and it does not result from the interaction between SO₃, H₂SO₄, H₂O, and air in the measurement cell. The next sections will therefore report on SO₃ and H₂SO₄, since SO₂ is effectively in frozen concentration.

5.3 Fluent simulation results

The ANSYS Fluent simulation results are based on the model presented in Chapter 4, with the assumption of SO₃ and H₂SO₄ in chemical equilibrium. The assumption is supported from the H₂SO₄ formation models analysis in the previous section. The simulations aim to describe temperature profiles, as well as SO₃ and H₂SO₄ concentrations, in the measurement cell. Moreover, the effects of the injection of nitrogen purging flow in front of the windows is analyzed. The purging has the goal of decreasing the local concentration of H₂SO₄ in front of the windows.

The reacting flow is solved as a two-step process: first, the “cold-flow” (or unreacting flow) is resolved with volumetric reactions disabled. Next, the reactions are enabled, and a stable converged solution for the reacting flow is achieved.

Four different nitrogen purging flow temperatures, 400K, 500K, 600K and 700K, and eleven different nitrogen purging flow rates rates, 0.00, 0.09, 0.17, 0.25, 0.33, 0.41, 0.50, 0.60, 0.75, 1.00, and 1.25slm at each port are simulated, for a set of 44 simulated conditions. The four temperature cases at 0.00slm purging flow rate are equivalent. In fact, when no nitrogen flow is provided the inlet nitrogen temperature is unimportant.

It is helpful to define four corner cases, i.e., extreme cases that encompass the whole set of simulations. The rest of the cases will lead to results that are in-between the corner case results. This strategy allows general conclusions about the effect of purging on temperatures and concentration uniformity by analyzing a bounding subset of simulations only. The concept plot describing the corner cases is represented in Figure 5.8. Note that corner case

4 (bottom left) with purging nitrogen flow of 0.00slm and nitrogen temperature of 400K is effectively coincident with corner case 1, so three corner cases (1, 2, and 3) suffice for the current analysis. Corner case 1 is the *reference case*, with no nitrogen flow added to the main flow in the measurement cell (no purging).

In Figure 5.8, from left to right the nitrogen flow rate is increased from 0.00 slm to its maximum value of 1.25 slm for a single port, for a total of 2.50 slm of N₂ added from the two inlet ports. From top to bottom, the inlet temperature of the nitrogen flows is decreased from 700K to its minimum value of 400K.

The heat flux provided to the cell (*Heating 1* and *Heating 3* boundary conditions in Figure 4.6) is kept constant among all cases at 1250W/m² to analyze the individual effects of flow rates and temperatures of the N₂ purging streams on the H₂SO₄ concentration.

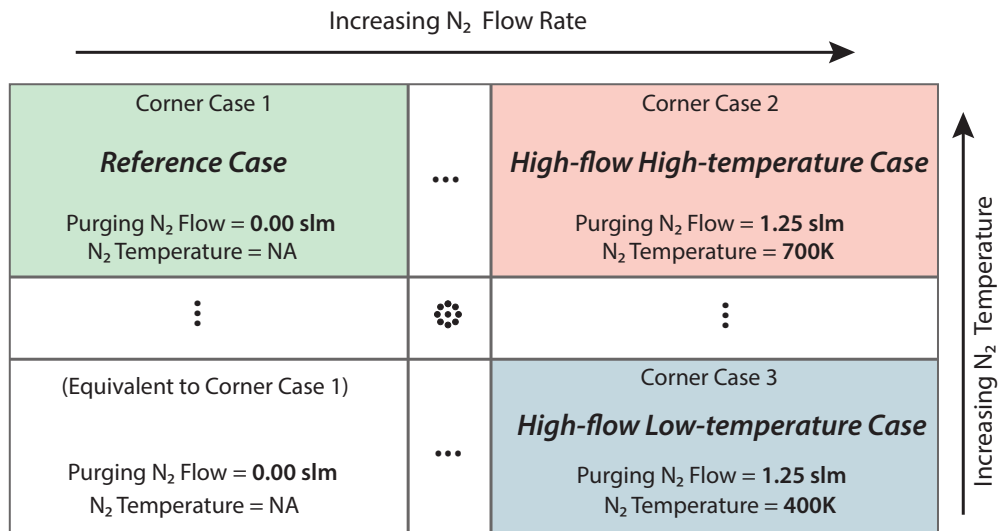


Figure 5.8: Fluent simulations corner cases.

The numerical analysis of temperature, and SO₃ and H₂SO₄ concentrations in the corner cases will extensively use contour maps as a graphical representation tool. The contour maps highlight the behavior of different purging conditions in a qualitative manner, they bring out the important three-dimensionality of the problem, and they draw attention to fluid structures and regions of particular importance. While offering these advantages, contour

maps lack quantitative information on average temperatures, concentration, and their axial variation. To address these concerns a quantitative analysis of the core region of the fluid is included in Section 5.3.4.

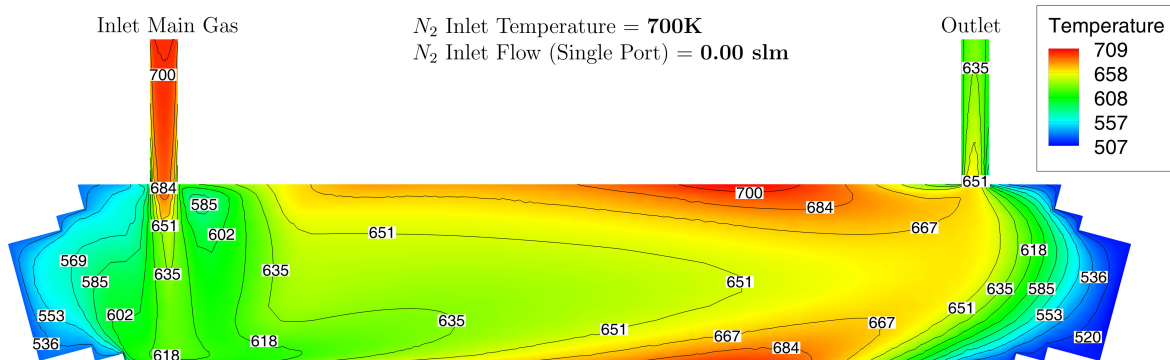
5.3.1 Reference case

The *reference case* does not include any nitrogen purging, and it is the most used during the experimental tests. The boundary conditions for the fluid are summarized in Table 5.1.

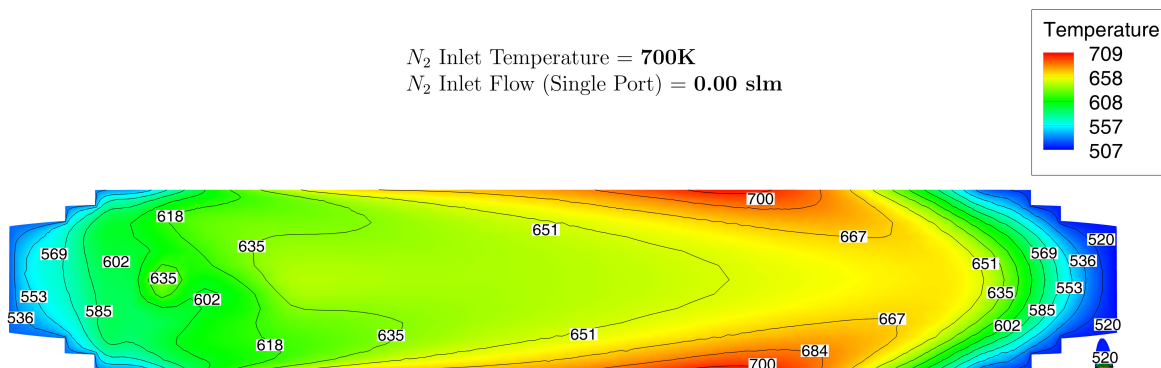
Surface	Condition	Value
Inlet Main Gas	Velocity Inlet	5 slm
	Temperature	700 K
	Composition (Mole Fraction)	0.711 N ₂ , 0.189 O ₂ , 0.1 H ₂ O, 3E-4 SO ₃
Inlet N ₂ 1	Velocity Inlet	0 slm
	Temperature	-
	Composition (Mole Fraction)	-
Inlet N ₂ 2	Velocity Inlet	0 slm
	Temperature	-
	Composition (Mole Fraction)	-
Outlet	Pressure Outlet	1 atm

Table 5.1: Boundary conditions for the fluid regions in the *reference case*.

The temperature and the composition of the purging flow in the *reference case* are irrelevant since there is no nitrogen flow injected in front of the windows.



(a) Temperature on zx plane ($y = 0$).

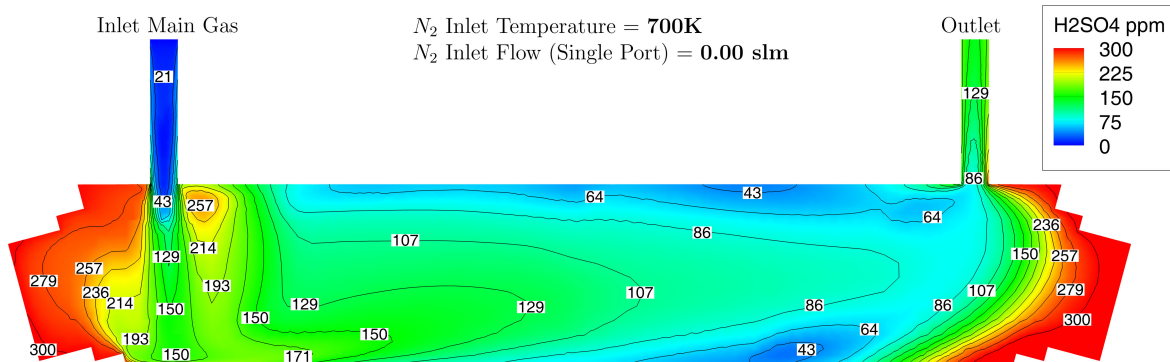


(b) Temperature on yx plane ($z = 0$).

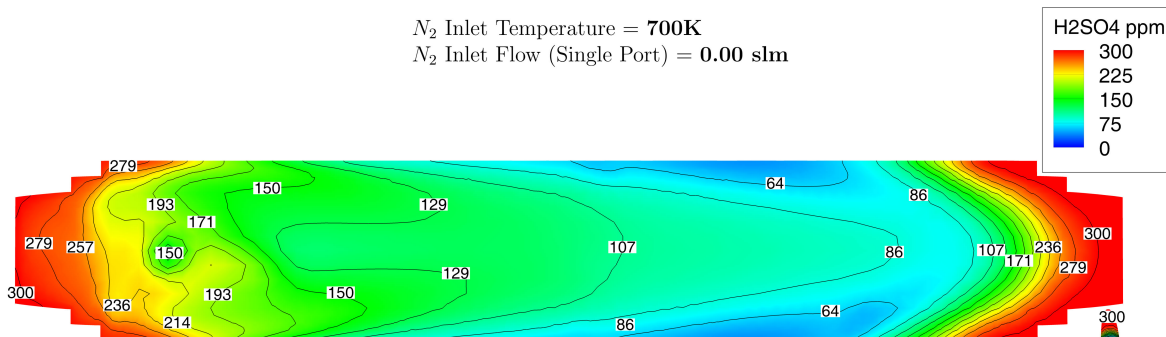
Figure 5.9: Temperature contour plots for the *reference case*. Temperature values are in Kelvin.

The temperature distribution in the cell is represented with contours plot in Figure 5.9 for the zx and yx section planes. The temperature along the x-axis in the core section is fairly uniform, with the notable exception of the area closest to the windows. The temperature drop at the extremities is due to convective heat transfer from the windows to the external ambient. Since the windows are thin (3mm) and they are fairly conductive ($k_{\text{BaF}_2} = 11.7 \frac{\text{W}}{\text{mK}}$), the temperature difference between the windows and the free stream inside the measurement cell is on the order of hundreds of degrees Kelvin. It is expected that the low temperature at the windows will drive the hydration reaction of SO_3 (Reaction 1.4a) towards the H_2SO_4 side. This effect is undesirable since H_2SO_4 reacts directly with the window material, that

is barium fluoride. Experimentally the phenomenon resulted in decreased transmissivity of the windows, as highlighted later in Section 5.3.5.



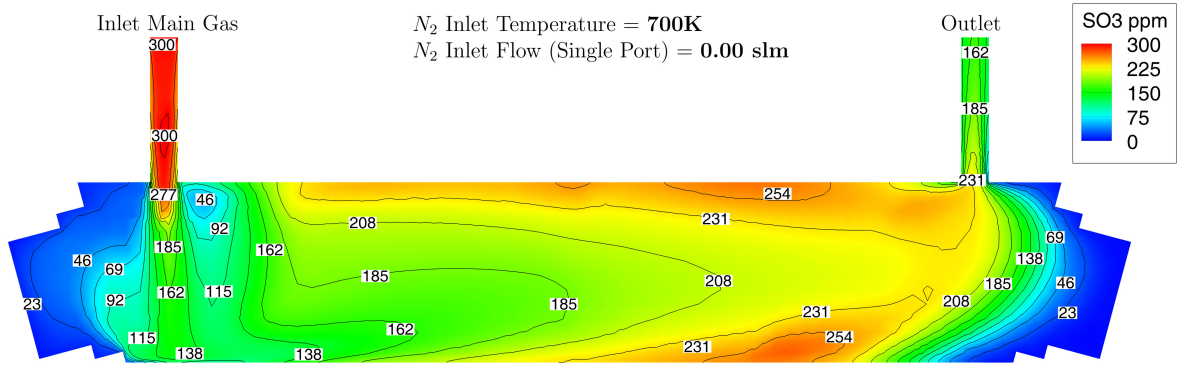
(a) H_2SO_4 concentration on zx plane ($y = 0$).



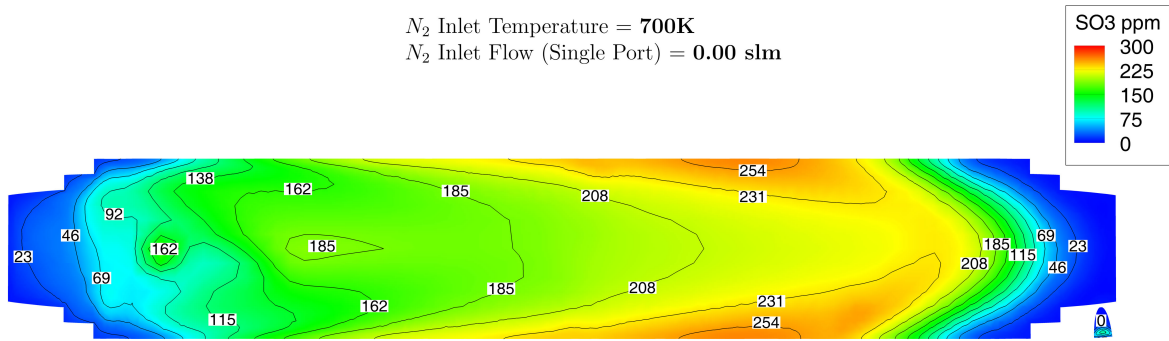
(b) H_2SO_4 concentration on yx plane ($z = 0$).

Figure 5.10: H_2SO_4 concentration contour plots for the *reference case*. Concentration values are in parts per million volume.

As expected, Figure 5.10 shows a very high concentration of H_2SO_4 close to the windows. The inlet concentration of sulfur species from *Inlet Main Gas* is 300ppmv, in the form of SO_3 . In the absence of purging, the concentration of SO_3 plus the concentration of H_2SO_4 will be on average equal to 300ppmv in every fluid mesh cell, as SO_2 does not contribute to these species in this temperature regime. Since the concentration of H_2SO_4 close to the windows is about 300ppmv, the concentration of SO_3 in those regions will be close to zero, as confirmed by the results represented in Figure 5.11.



(a) SO_3 on zx plane ($y = 0$).



(b) SO_3 on yx plane ($z = 0$).

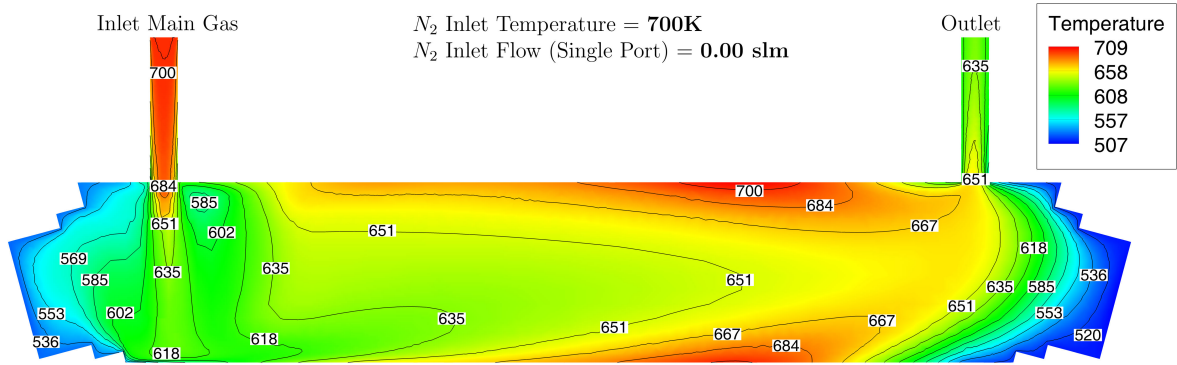
Figure 5.11: SO_3 concentration contour plots for the *reference case*. Concentration values are in parts per million volume.

The split between SO_3 and H_2SO_4 in the *reference case* is globally and locally dominated by the chemical equilibrium between the two species. In fact, the temperature contours and the SO_3 contours present the same trend (same colors in the contour maps), while the opposite holds for H_2SO_4 contours. The contribution of diffusion to the SO_3/H_2SO_4 split in the *reference case* appears to be unimportant. The main goal behind the idea of a purging flow of N_2 injected in front of both windows is to locally decrease the H_2SO_4 concentration as a means for extending the windows lifespan, and the purging flow effects are analyzed in the other corner cases.

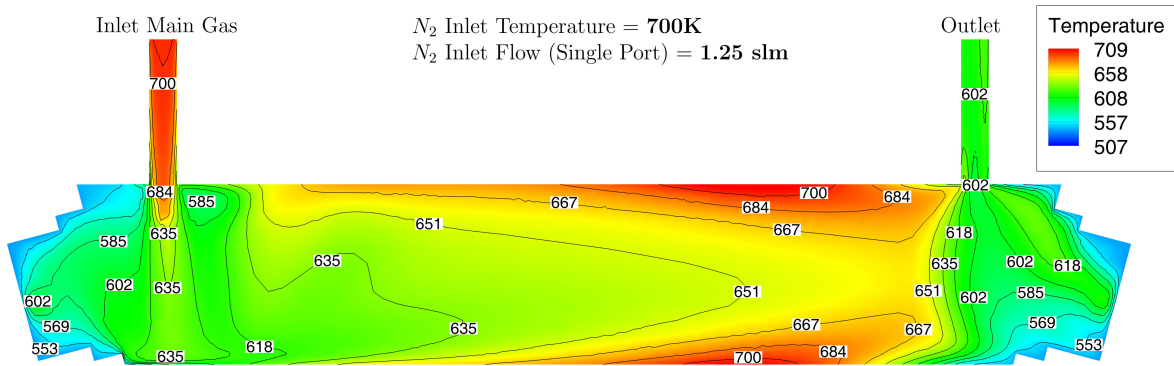
5.3.2 Corner case 1 and corner case 2 comparison

The goal of the comparison between corner case 1 (reference case) and corner case 2 (the high-temperature high-flow case) is to determine whether purging can have a positive impact in decreasing H_2SO_4 concentration in front of the windows. The corner case 2, with the highest flow (1.25 slm) coupled with the highest nitrogen temperature (700K), will be analyzed first since it has the best promise of minimizing H_2SO_4 concentrations by both increasing the local temperature to favor SO_3 and by increasing the presence of nitrogen in front of the windows as a buffer region.

The temperature of the high-flow high-temperature case is compared to the reference case in Figure 5.12 and Figure 5.13, on the zx and yx planes respectively. The minimum temperature near the windows is increased from 536K to 553K for the upstream window (left side in the figures), and from 520K to 553K near the downstream window (right side).

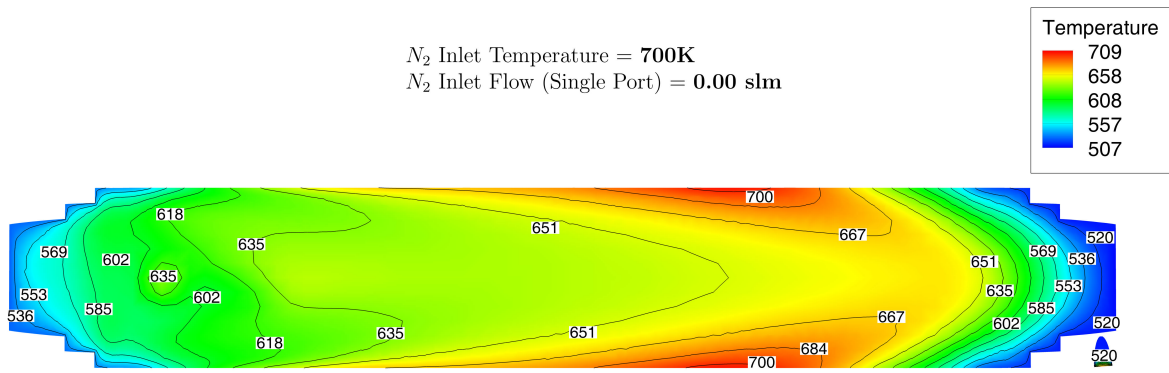


(a) Reference case (from 5.9a).

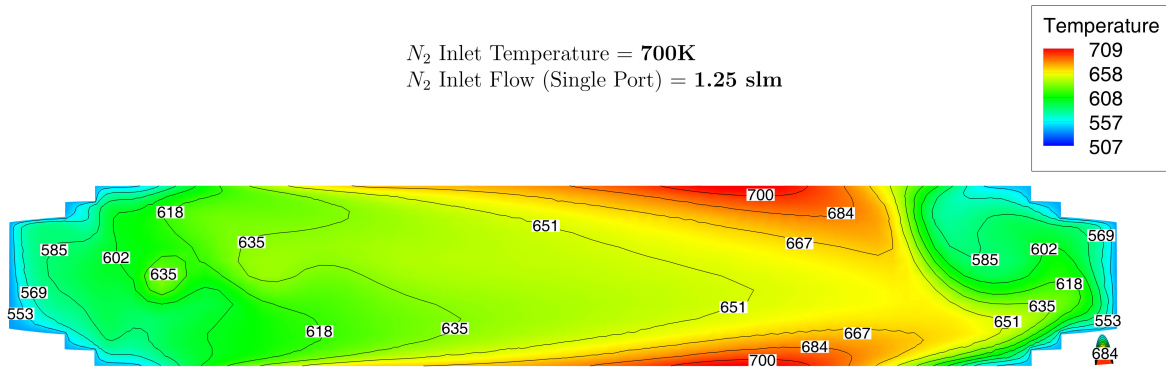


(b) 700K 1.25slm nitrogen flow case.

Figure 5.12: Temperature contour plots on zx plane ($y = 0$) for the reference case (top) compared to the high-temperature high-flow ($700K, 1.25slm$) nitrogen purging flow (bottom). Temperature values are in Kelvin.



(a) Reference case (from 5.9b).

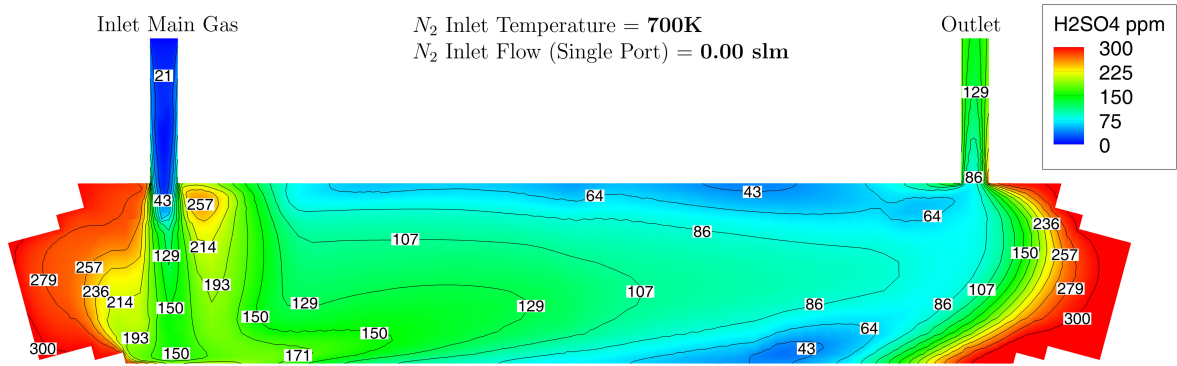


(b) 700K 1.25slm nitrogen flow case.

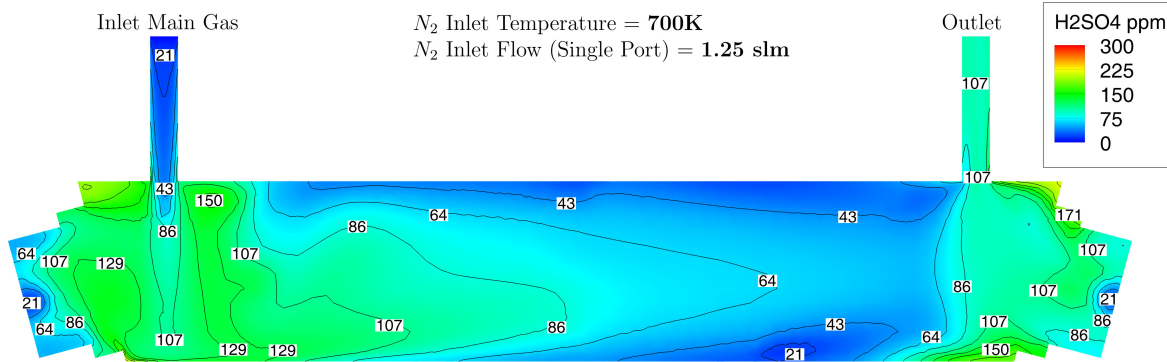
Figure 5.13: Temperature contour plots on yx plane ($z = 0$) for the reference case (top) compared to the high-temperature high-flow ($700K, 1.25slm$) nitrogen purging flow (bottom). Temperature values are in Kelvin.

The H_2SO_4 concentration in the high-flow high-temperature case is compared to the reference case in Figure 5.14 and Figure 5.15, on the zx and yx planes respectively. The maximum H_2SO_4 concentration in the proximity of the windows decreases from 300ppm to 64ppm for the upstream window (left side in the figures), and from 300ppm to 86ppm at the downstream window (right side). The drop in H_2SO_4 concentration amounts to 79% and 71% respectively. If the window damage is assumed to be linear in time, this high-flow high-temperature purging case would extend roughly fivefold the window lifespan for the upstream window, and more than three times the lifespan for the downstream window. In

the experimental setting the lifespan for the windows (intended as the time interval in which the windows performance degrades from as-new to poor) is empirically on the order of tens of minutes with no purging. A theoretical fivefold increase in windows lifespan would help but is still not sufficient if the measurement device is expected to operate continuously under powerplant conditions.

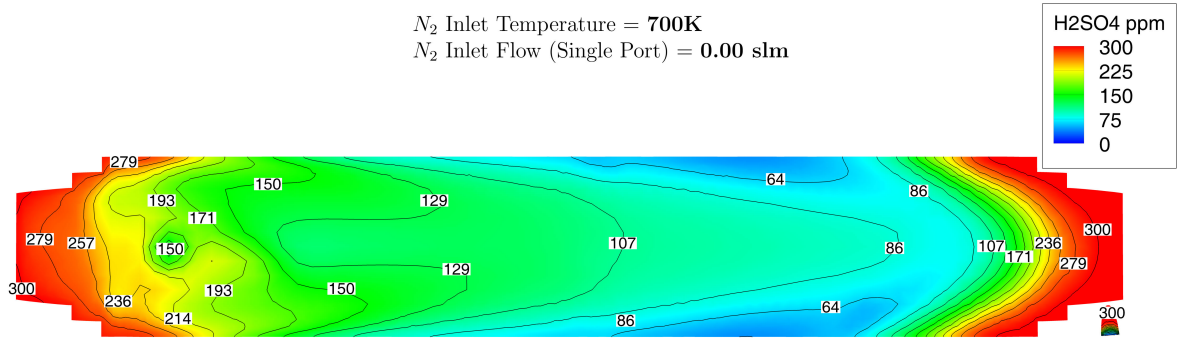


(a) Reference case (from 5.10a)

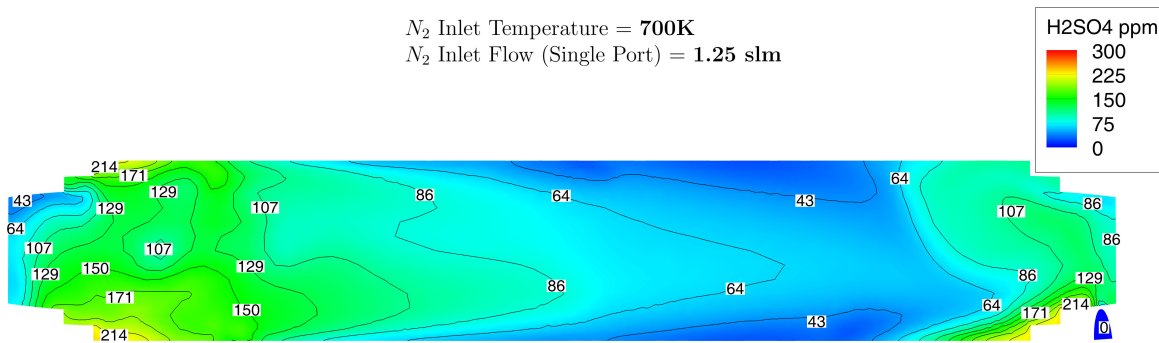


(b) 700K 1.25slm nitrogen flow

Figure 5.14: H₂SO₄ contour plots on zx plane ($y = 0$) for the reference case (top) compared to high-temperature high-flow (700K, 1.25slm) nitrogen purging case. Concentration values are in ppmv.



(a) Reference case (from 5.10b).



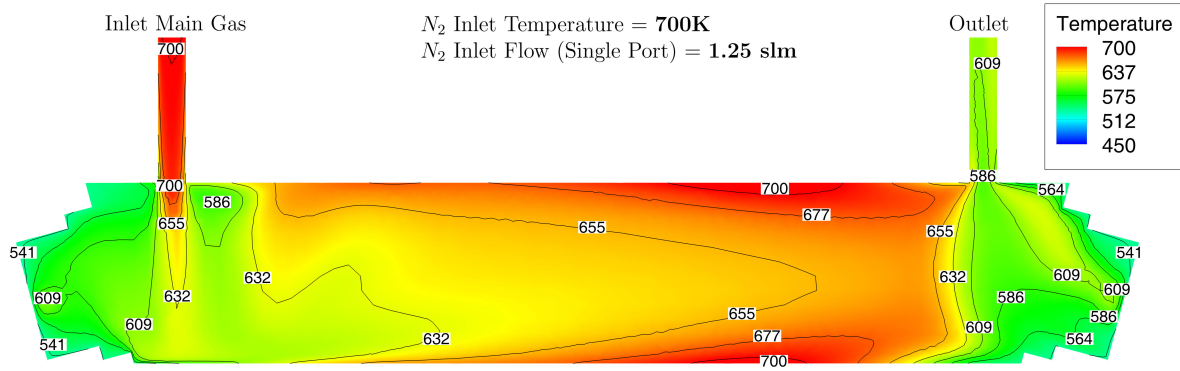
(b) 700K 1.25slm nitrogen flow.

Figure 5.15: H_2SO_4 contour plots on yx plane ($z = 0$) for the reference case (top) compared to high-temperature high-flow (700K, 1.25slm) nitrogen purging case. Concentration values are in ppmv.

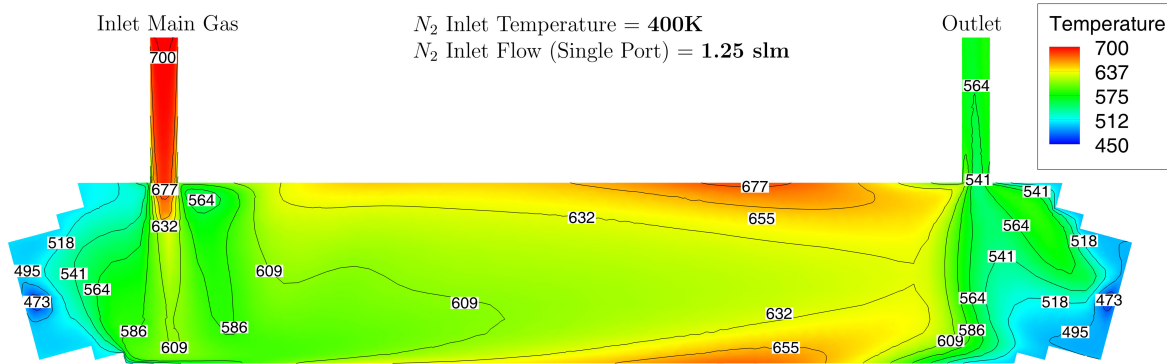
5.3.3 Corner case 2 and corner case 3 comparison

The third corner case is the low-temperature high-flow case. When compared to corner case 2 (the high-temperature high-flow case), corner case 3 will highlight whether the temperature in front of the windows impacts the local H_2SO_4 concentration. As seen in Figure 5.16 and Figure 5.17, the temperature difference at the windows between the two high-flow cases can be larger than 50K, resulting in even colder temperatures with respect to the reference case. Figure 5.16a represents the same conditions as Figure 5.12b, but re-scaled in order to match the same color scale of 5.16b. The same is valid for the yx -view temperature maps 5.17.

Although local window temperatures are lower, results in terms of local H_2SO_4 concentrations are very similar to the high-flow high-temperature case, as depicted in Figure 5.18 and Figure 5.19.

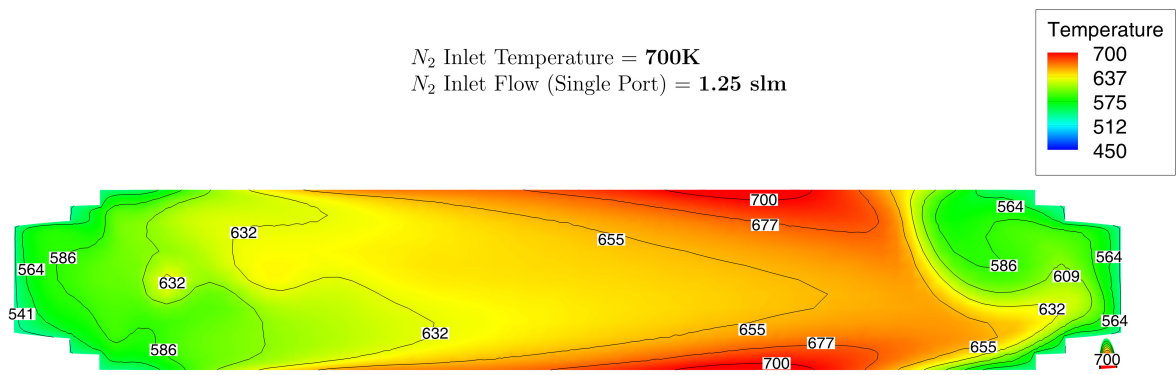


(a) 700K 1.25slm nitrogen flow (from 5.12b, re-scaled).

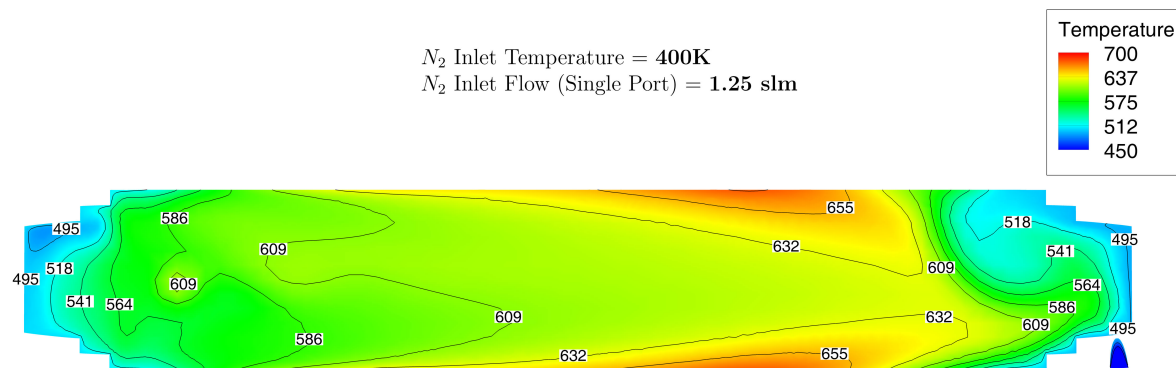


(b) 400K 1.25slm nitrogen flow.

Figure 5.16: Temperature contour plots on zx plane ($y = 0$) for the high-temperature high-flow (700K, 1.25slm) case compared to the low-temperature high-flow (400K, 1.25slm) nitrogen purging case. Temperature values are in Kelvin.

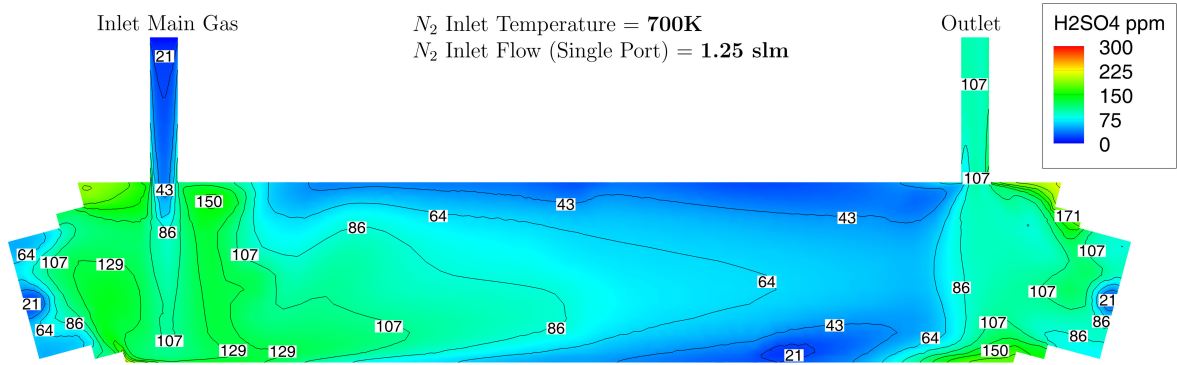


(a) 700K 1.25slm nitrogen flow (from 5.13b, re-scaled)

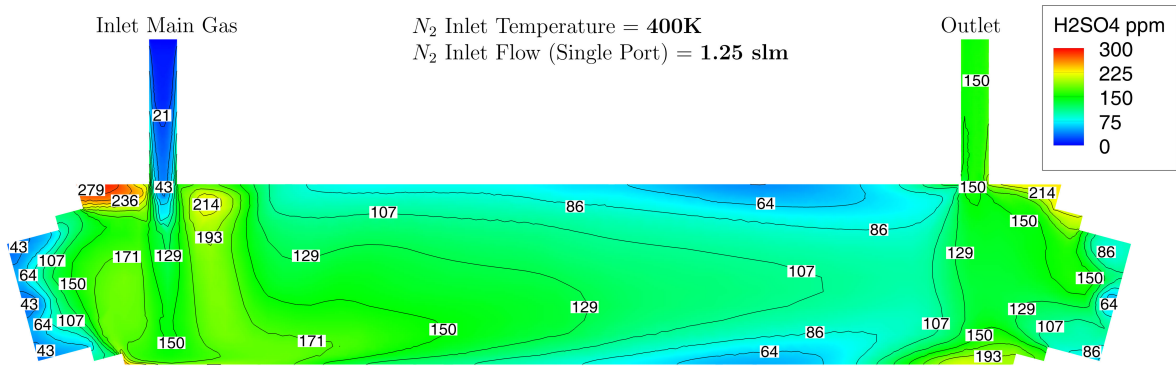


(b) 400K 1.25slm nitrogen flow

Figure 5.17: Temperature contour plots on yx plane ($z = 0$) for the high-temperature high-flow ($700K, 1.25slm$) case compared to low-temperature high-flow ($400K, 1.25slm$) nitrogen purging case. Temperature values are in Kelvin.

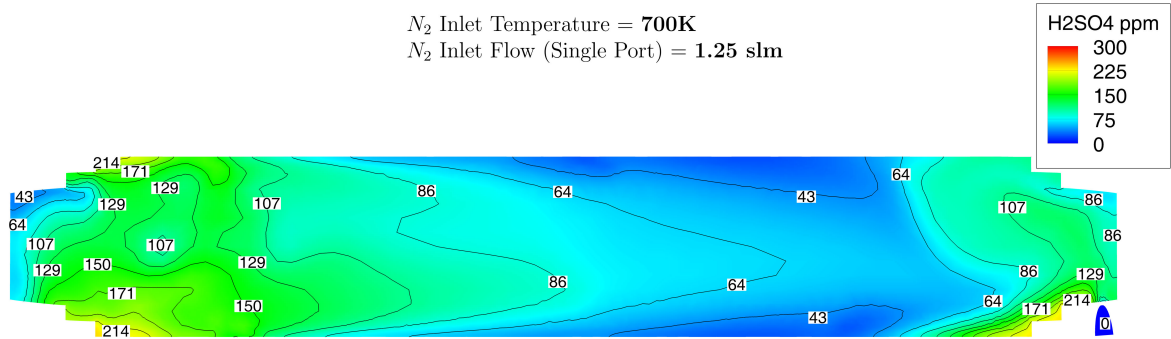


(a) 700K 1.25slm nitrogen flow (from 5.14b)

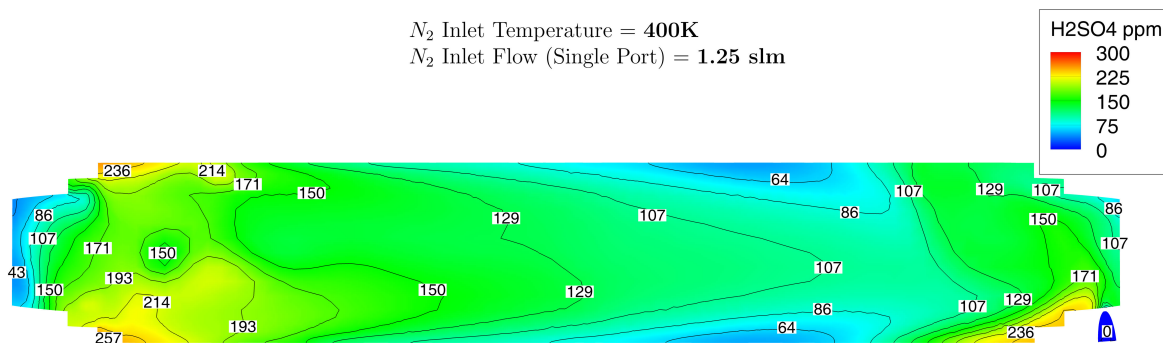


(b) 400K 1.25slm nitrogen flow

Figure 5.18: H_2SO_4 contour plots on zx plane ($y = 0$) for the high-temperature high-flow ($700K, 1.25slm$) case compared to low-temperature high-flow ($400K, 1.25slm$) nitrogen purging case. Concentration values are in ppmv.



(a) 700K 1.25slm nitrogen flow (from 5.15b)



(b) 400K 1.25slm nitrogen flow

Figure 5.19: H_2SO_4 contour plots on yx plane ($z = 0$) for the high-temperature high-flow ($700K, 1.25slm$) v. low-temperature high-flow ($400K, 1.25slm$) nitrogen purging flow. Concentration values are in ppmv.

5.3.4 Temperature and concentrations profiles along the core of the measurement cell

In the experimental laser measurements, a laser beam passes multiple times through the measurement chamber, in a Herriott cell configuration. The laser beam travels through the inner core volume of fluid in the measurement cell, and it is never close to the measurement cell cylindrical side walls. It is useful to evaluate the variables such as temperature, SO_3 and H_2SO_4 concentrations, along the longitudinal axis x , from window to window in the core

section to determine the uniformity and any possible effects of variability on the potential absorption measurement. Circular surfaces of radius 0.6in (15mm), representing the size of the spot pattern of the optical path, are defined along the x-axis as shown in Figure 5.20. The core planes in blue lie on the yz plane at different x coordinates. The planes in red start from each window and progressively transition into yz planes, merging smoothly with the blue core surfaces in order to better capture the gas behavior close to each window. Red planes and blue planes have the same radius, and each plane represents a local cross section for the simulation to compute the temperature and concentrations results. A full core analysis consists in averaging of the different variables on each blue and red plane.

ANSYS
2020 R2

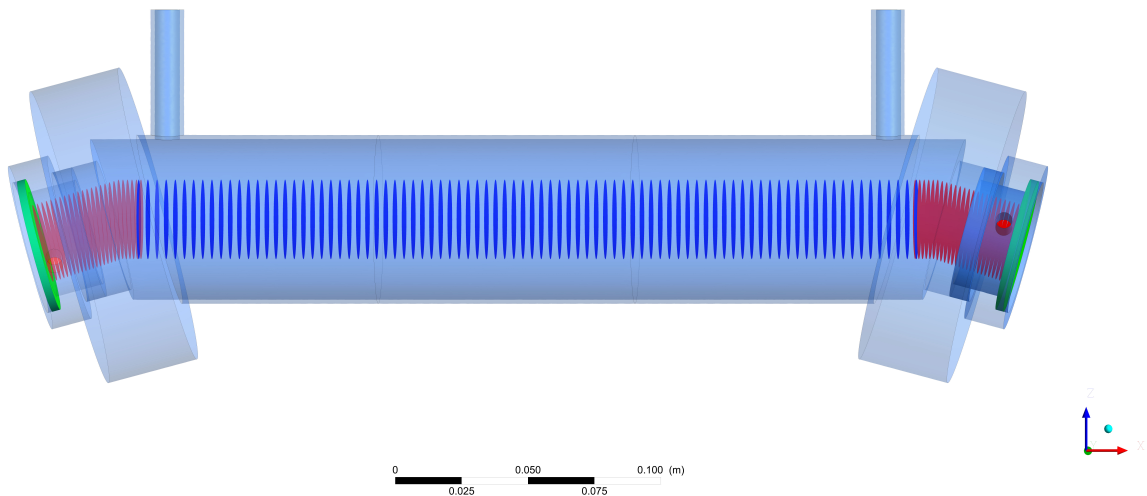


Figure 5.20: Definition of the core surfaces along the x-axis. The blue surfaces are parallel to the zy plane, while the red surfaces transition from parallel to each window to parallel to the zy plane.

The results in terms of temperature, SO_3 concentration, and H_2SO_4 concentration are represented in Figure 5.21. The figure includes data from two different N_2 purging flow temperatures, 700K (426C, left) and 400K (126C, right), for different purging nitrogen flow rates, from dark red (0.00 slm) to green (1.25 slm), as shown in the color bar on the right-hand side of the plot. The case with no nitrogen flow (dark red curve) is common to both

left and right plots.

The average temperatures along the x-axis are represented with a red dash-dot line for the cases with no nitrogen flow (0.00slm) and with a green dash-dot line for the case with the maximum nitrogen flow (1.25slm). The labels in the near proximity of the dash-dot lines show the mean value along the axis and its standard deviation expressed as a percentage of the mean value. The locations of gas inlets, outlet, and windows are highlighted with dark gray vertical lines on the x-axis, and labeled in the plots on the left side of the figure.

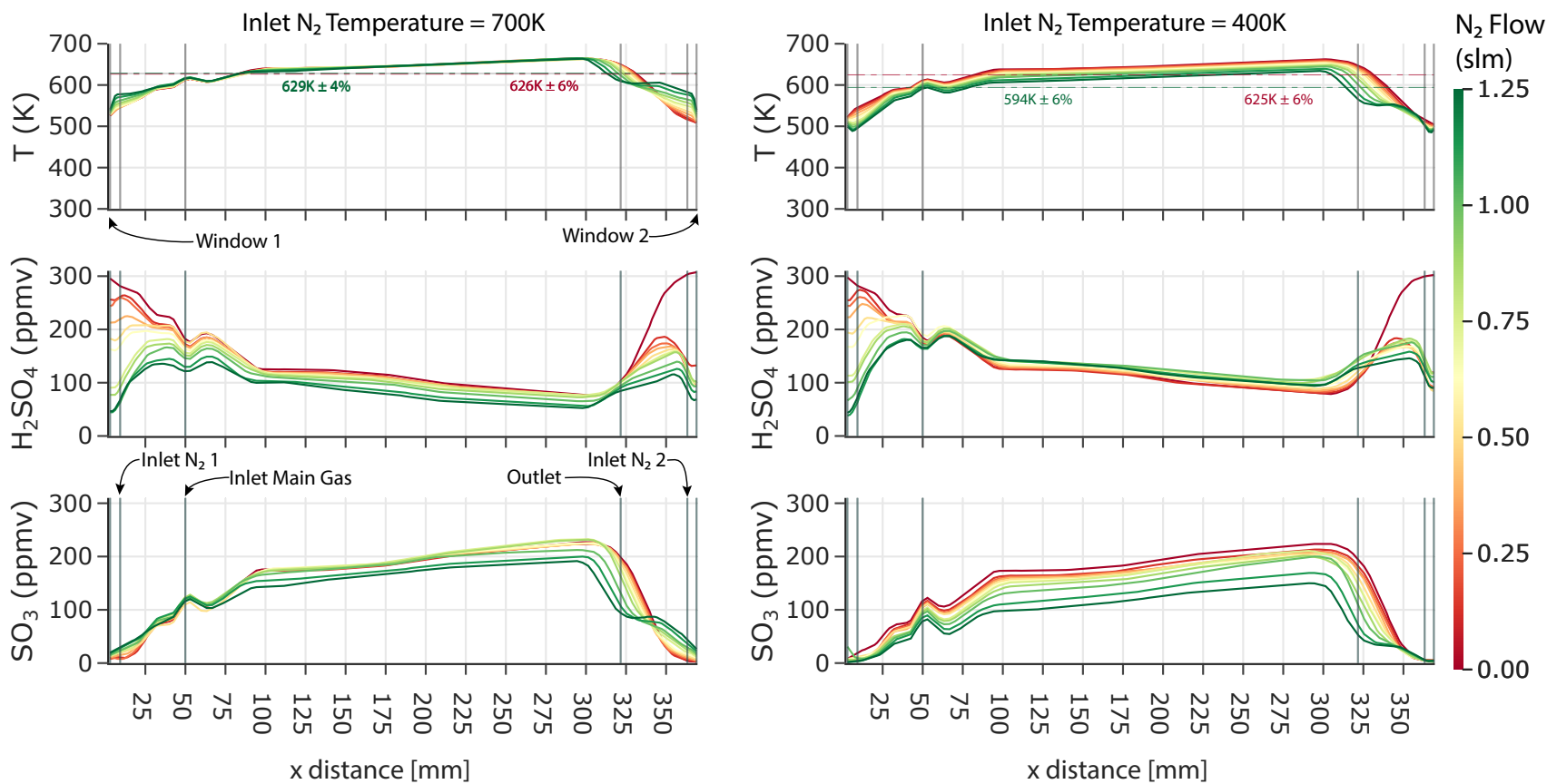


Figure 5.21: Temperature, H_2SO_4 and SO_3 concentrations, along the x-axis for different nitrogen purging flow rates and for two different nitrogen temperatures.

For the 700K case (left side of Figure 5.21), the temperature profile in the middle section of the cell (from Inlet Main Gas to Outlet) is not significantly altered by the addition of any of the simulated amount of nitrogen flow at 700K. The most significant effect occurs at Window 2, where the increase in nitrogen flow tends to flatten the temperature profile, probably due to increased mixing. The cell temperature profile has a standard deviation from the mean temperature of less than 6%.

For the case where the nitrogen temperature is 400K (right), the average cell temperature drops significantly, but its variation along the longitudinal axis is once again smaller than 6% in terms of standard deviation. The temperature along the core section of the measurement cell is hence fairly uniform, although the temperatures in proximity of the windows are significantly lower.

In terms of concentrations, H_2SO_4 and SO_3 are on average in chemical equilibrium for each different nitrogen flow case and for both nitrogen temperatures. In the case with no nitrogen addition (reference case), H_2SO_4 and SO_3 are in chemical equilibrium for all the cells in the domain, with very low SO_3 concentrations in front of the windows, where the low temperature favors H_2SO_4 . When a nitrogen flow is introduced, the concentration of H_2SO_4 decreases significantly in the region immediately adjacent to the windows. All the 44 purging nitrogen cases are analyzed separately for the local H_2SO_4 concentration in front of each windows, and the results are displayed in Section 5.3.5.

For the 700K case, the concentration of H_2SO_4 in the core section decreases as additional nitrogen flow is added. Since the mean temperature of the cell does not change significantly when nitrogen at 700K is added, the effect is not due to chemical reactions but to gas dilution. The same is valid for SO_3 .

When nitrogen is added at 400K, H_2SO_4 concentrations increase slightly as nitrogen is added. This is due to two counteracting effects, the dilution of the flow which tends to decrease the H_2SO_4 concentration, and the decrease in temperature which tends to favor the formation of H_2SO_4 from SO_3 . The two effects both participate in decreasing SO_3

concentrations.

Even with fairly uniform axial temperatures in the core section, SO_3 and H_2SO_4 concentrations present significant variations along the axis, since their chemical equilibrium is very sensitive in that temperature range. The significantly lower temperature near the windows also drives the hydration reaction of SO_3 to completion towards the H_2SO_4 side. Despite this variation, however, the integrated absorption (or concentration) along the optical path is almost identical to that obtained by assuming the average equivalent concentration for the entire path. That is, the absorption of the average concentration for the total path length is equal to the total absorption of the true concentration, including variations along the path.

5.3.5 Sulfuric acid concentrations adjacent to the windows

It is important to reduce the local concentration of H_2SO_4 at the windows to extend their lifespan. In this section, two separate fluid volumes are defined in order to capture the composition and temperature of the gas situated in front of each windows, in order to estimate the effectiveness of the different nitrogen purging solutions. Each volume is a cylinder with diameter equal to the wet diameter of the window, and thickness of approximately 3/64" (1mm). The exact volume conforms necessarily to the local mesh morphology, and therefore it is not represented by a perfect cylinder. The average volumetric H_2SO_4 concentrations and temperature in the gas enclosed in the two volumes is monitored. The graphical representation for the monitored volume for one of the window is shown in Figure 5.22.

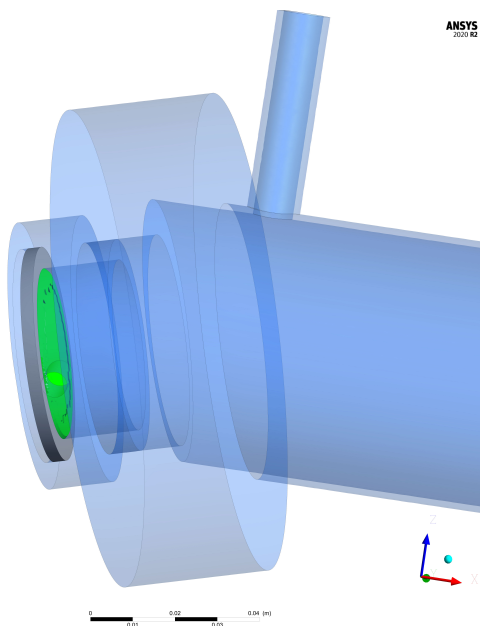


Figure 5.22: Gas volume monitored (green) adjacent to the window (gray).

The temperatures in proximity of Window 1 and Window 2 are represented in Figure 5.23 as a function of the nitrogen flow rate and for four different nitrogen temperatures. For the *reference case*, with purging nitrogen flow at 0.00 slm, Window 1 temperature (525K) is higher than Window 2 temperature (508K). As a result, a purging nitrogen flow entering at 600K and 700K will increase the local temperature, while flows at 400K and 500K will decrease it. For Window 1, the difference between the maximum temperature (registered in the corner case 2, the high-temperature high-flow case) and the minimum temperature (corner case 3, the low-temperature high-flow case) is +3% and -6% with respect to the reference case Window 1 temperature. For Window 2, the corner cases present +7% and -3% variation in temperature with respect to the reference case. Given the limited impact of purging on window temperatures, it is expected that the main factor in decreasing H_2SO_4 concentration with purging is not related to local temperature acting on the $\text{SO}_3\text{-H}_2\text{SO}_4$ equilibrium.

The H_2SO_4 concentration at Window 1 and Window 2 is represented in 5.24. Nitrogen temperature does not affect local H_2SO_4 concentrations, so the $\text{SO}_3\text{-H}_2\text{SO}_4$ equilibrium

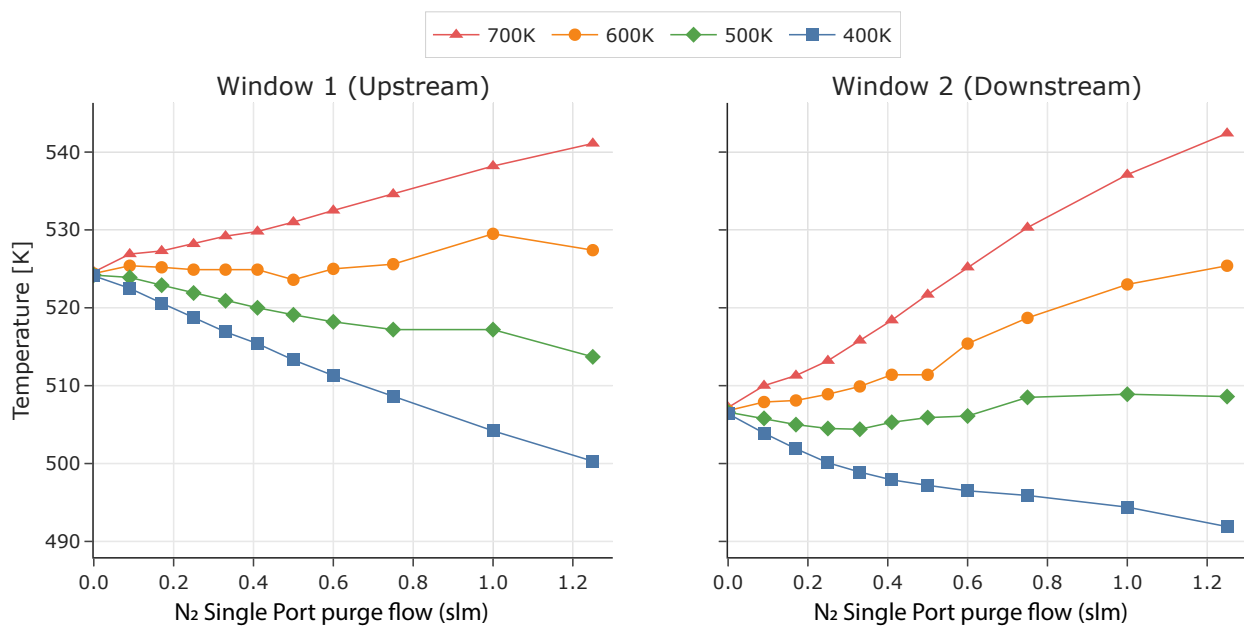


Figure 5.23: Window 1 and Window 2 temperatures as a function of purging nitrogen flow rate and for different nitrogen temperatures.

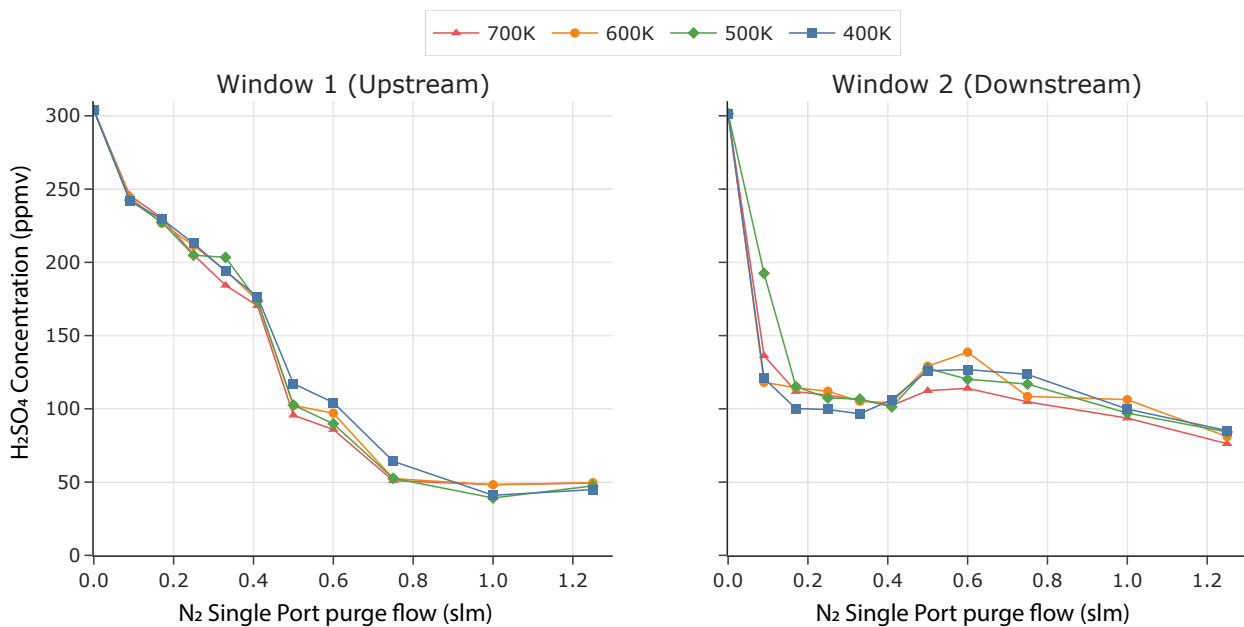


Figure 5.24: Window 1 and Window 2 H₂SO₄ concentrations as a function of purging nitrogen flow rate and for different nitrogen temperatures.

plays only a limited role in decreasing H_2SO_4 concentration. This is more clearly visible in Figure 5.25, where the numerical H_2SO_4 concentration resulting from the Fluent simulations is evaluated and compared to the chemical equilibrium H_2SO_4 concentration from Chemkin.

Notably, H_2SO_4 concentration for both Window 1 and Window 2 does not reach zero for the cases studied. For Window 1, H_2SO_4 concentration decreases almost linearly with increasing purging flow rate, to a plateau at around 0.9 slm. For Window 2, H_2SO_4 concentration decreases steeply with the addition of any small nitrogen flow, but it stabilizes at a minimum value that is about double the minimum value obtained for Window 1.

The drop in H_2SO_4 concentration is also not due solely to bulk dilution effects. For example, in the corner cases 2 and 3 (the high-flow cases), a nitrogen flow of 2.50 slm is added to the 5 slm main flow (50% increase), so at most a 33% drop in H_2SO_4 concentration is expected due to dilution, while the simulated H_2SO_4 local concentration drop amounts to 84% and 70% at Window 1 and Window 2 respectively.

The numerical H_2SO_4 concentration values likely are determined by a combination of the chemical reaction of SO_3 with H_2O , coupled with the local flow characteristics and velocities, and molecular and thermal diffusion. The gas flow in the measurement cell, especially close to the windows, is highly three-dimensional and presents a re-circulation area in front of Window 1 and a stagnation plane in front of Window 2. When purging flow is added, additional complications in the description of the flow field appear, as shown in Figure 5.26. The flow mixing overrides any diffusion contribution, so it is not possible to explain the numerical H_2SO_4 results with simple 1-D considerations.

Even if a simple explanation is not possible or would be formally incorrect, the model provides a complete numerical description and it achieves convergence. As the results between cases are coherent and consistent, the model could be sufficiently representative of the experimental conditions.

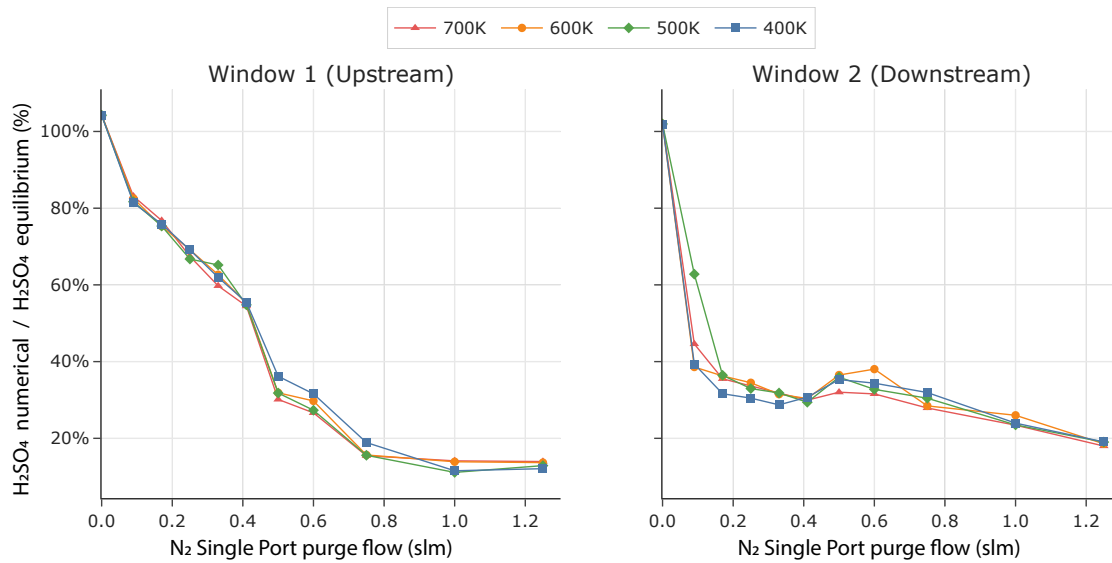


Figure 5.25: Ratio between H₂SO₄ concentration from numerical simulation results and H₂SO₄ concentration estimated from the diluted flow at chemical equilibrium.

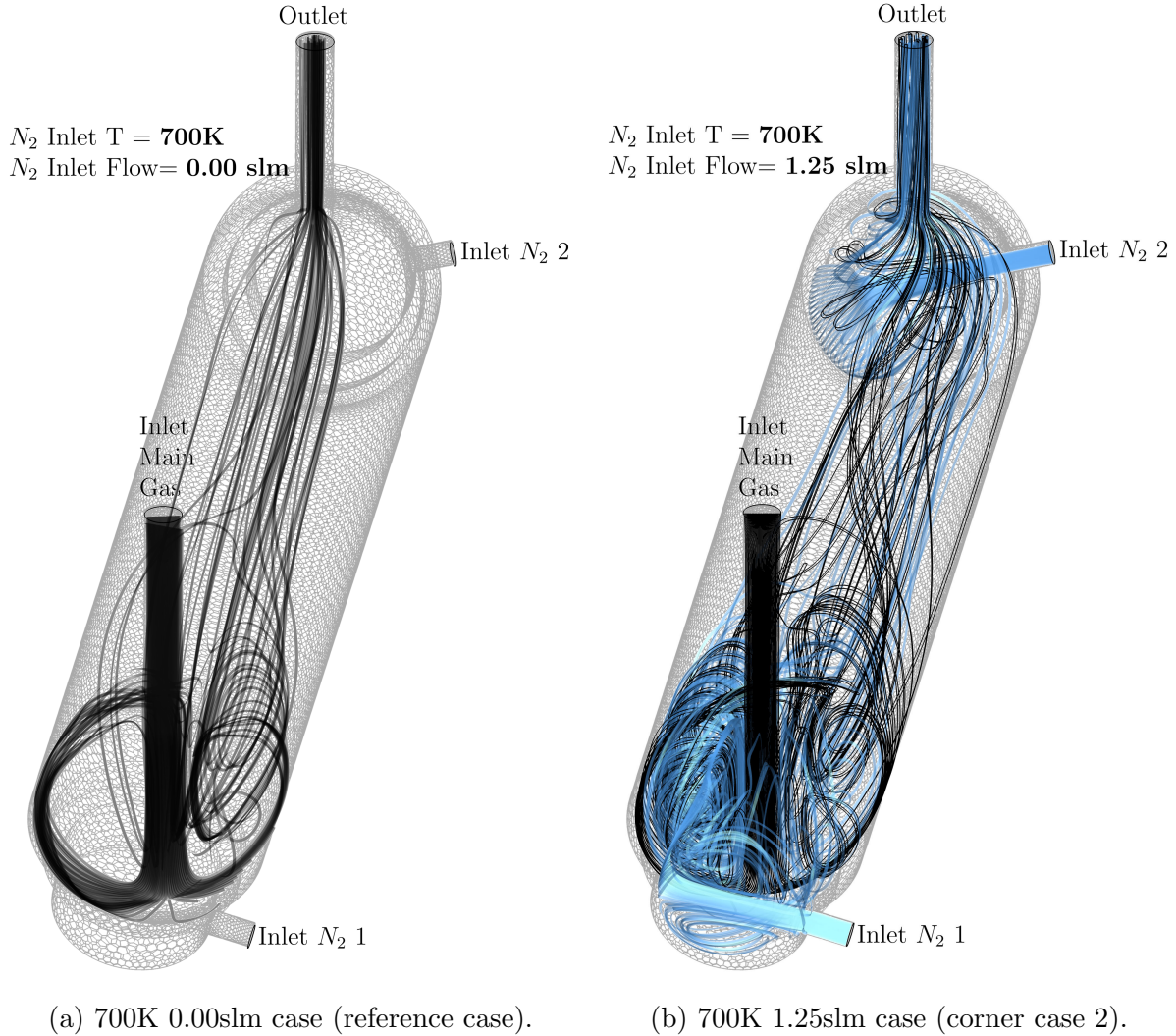


Figure 5.26: Stream traces for Corner Case 1 (Reference case, left) and Corner Case 2 (High-flow high-temperature case, right).

5.3.6 Thermal boundary layer and thermocouples location

Three thermocouples are installed in the measurement cell, at longitudinal coordinate x equal to 2.67" (68mm, thermocouple 1), 7.28" (185mm, thermocouple 2), 11.81" (300mm, thermocouple 3). To evaluate the thermal boundary layer thickness, the average temperature on 15 radially distributed 2mm thick surfaces is evaluated. The 15 surfaces for thermocouple 1 are represented in Figure 5.27, each with a different color for visualization purposes.

The thermal boundary layer thickness is important to establish how deep on the radial co-

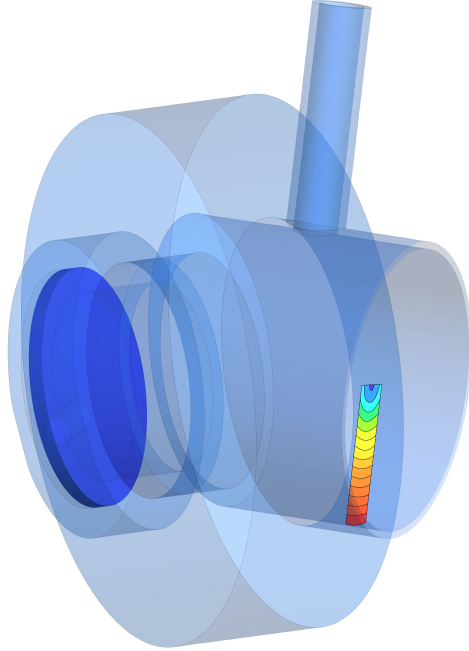


Figure 5.27: Cross section of the measurement cell highlighting the definition of 15 consecutive surfaces along the radial coordinate z at thermocouple 1 longitudinal location.

ordinate each thermocouple should be installed to effectively measure the core temperature. An additional goal is to determine if the core temperature at each of the three locations is representative of the mean axial core temperature. The results for purging N_2 temperature of 700K and purging N_2 flows varying from 0 to 1.25 slm are presented in Figure 5.28.

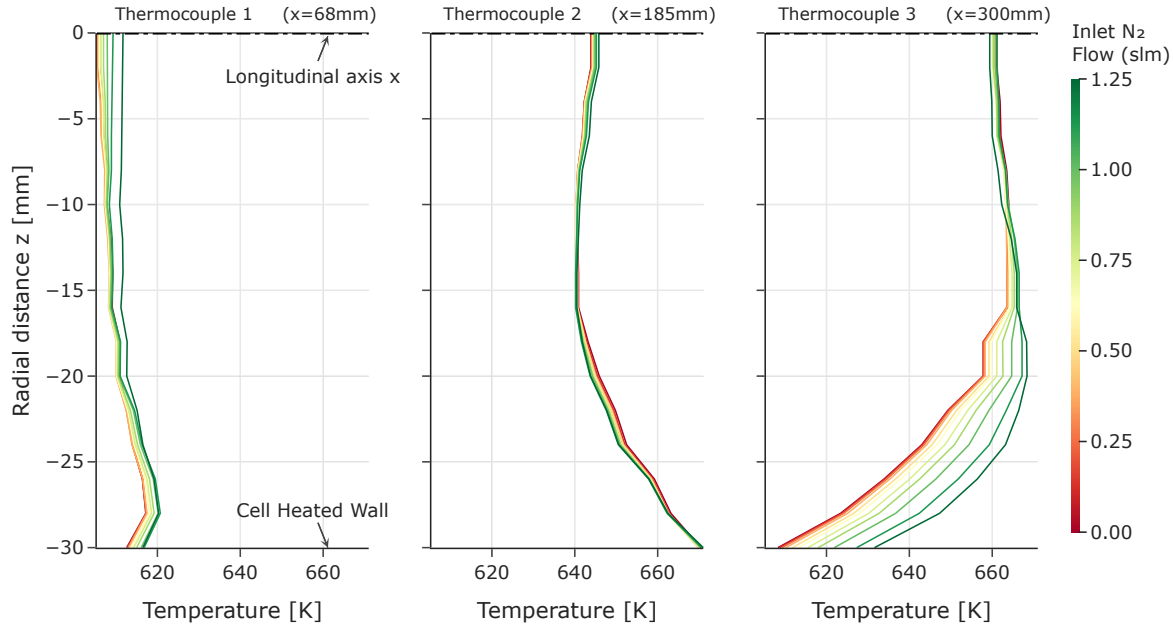


Figure 5.28: Temperature distribution along the measurement cell radial axis for three different thermocouple longitudinal locations.

From Figure 5.28, the thermal boundary layer thickness for all the three locations is around 0.4" (10mm). This is compatible with the 0.28" (7mm) result that was found by a LFA visiting scholar in the past using a similar modeling methodology [100]. For the case with no N_2 flow (red curve, reference case), the arithmetic mean temperature among the three core temperatures (606K, 644K, 661K) is 637K, which is 1.7% larger than the mean core temperature of 626K evaluated in Section 5.3.4, and it is well within the standard deviation of the mean core temperature.

For corner case 2 (high-flow high-temperature case), the three core temperatures are 612K, 646K, and 659K, and their arithmetic mean is 639K, which is 1.7% higher than the mean core temperature of 629K. For corner case 3 (high-flow low-temperature case) the three core temperatures are 581K, 617K, and 631K, with an arithmetic mean of 609K, a value 2.6% hotter than the mean core temperature of 594K.

The arithmetic mean among the readings of the three thermocouples is seen to be a reliable measure for the mean core temperature of the measurement cell. Since there is the expectations that the temperature in the measurement cell will be determined from the

thermocouple readings within $\pm 10\%$, the next section will simulate the effects of temperature changes and measurement uncertainties on spectroscopic measurements.

5.4 Simulated effect of axial temperature non-uniformity on spectroscopic measurements

The non-uniformity of temperature in the core section along the longitudinal axis of the cell can potentially impact the accuracy of the spectroscopic measurements, and in this section, the effect of this temperature variation will be analyzed. In addition, the influence of pressure changes in the measurement cell will be evaluated for typical pressure variations encountered experimentally in the measurement cell.

The above concerns are addressed uniquely for the SO_2 molecule since its cross-section is available on the HITRAN database allowing a comprehensive evaluation with general conclusions that would then hold for the other species. To simulate the high-temperature cross-section of the SO_2 molecule, the HITRAN on the Web (HotW) information system is used [112]. The system can simulate the spectrum of molecules in the HITRAN database at specified conditions, by evaluating several aspects such as partition functions, Boltzmann populations, and effects of stimulated emission for line strength, line positions shift due to pressure changes, and Doppler or Lorentz half-width for line width. The simulated spectra will be used to evaluate the effect of temperature and pressure changes inside the measurement cell on optical absorption measurements.

5.4.1 Effect of temperature changes on the absorbance spectrum

Beer-Lambert's Law can be expressed as:

$$I(\lambda) = I_0(\lambda) \exp(-\sigma(\lambda) \cdot N \cdot L) = I_0(\lambda) e^{-\tau(\lambda)} \quad (5.3)$$

This equation was previously referred to as 2.1 in Chapter 2, where $I_0(\lambda)$ is the initial intensity emitted by a light source, $I(\lambda)$ is the intensity collected at the detector after the radiation traveled through the media of thickness L . In the media, the concentration of the absorber is considered as uniform and represented as the number density N , number of molecules per unit volume, and $\sigma(\lambda, T)$ represents the absorption cross-section as a function of the wavelength and temperature and it is a characteristic property of the absorber species. For shortness of notation, the dependence on wavelength and temperature will be omitted hereafter.

If two homogeneous gas sections with equal volume, enclosing gases in different conditions, are consecutive along the beam path, then:

$$I = I_0 e^{-\tau_1} e^{-\tau_2} = I_0 e^{-(\tau_1+\tau_2)} \quad (5.4)$$

Where τ_1 and τ_2 are the optical depths of the two different volumes. Assuming a total cell length of $L = 100\text{cm}$, the length of each of the two sections is equal to $L/2$. Say n_1 is the number of moles of SO_2 in the first volume at ambient pressure and temperature T_1 . If the same gas composition is replicated in the second volume, but its temperature raised to T_2 at constant pressure (such is the case of the experimental measurement cell, where the outlet is always at ambient pressure), then the number of moles n_2 will be lower than n_1 . According to the ideal gas law:

$$n_2 = n_1 \frac{T_1}{T_2} \quad (5.5)$$

The two sections are hence characterized by a different number density (number of molecules per unit volume) $N_1 = n_1 N_A$ and $N_2 = n_2 N_A$ respectively, where N_A is Avogadro constant. The molecular cross-sections σ_1 and σ_2 are dependent on temperature and pressure, so they are going to differ for the two volumes. The optical depth for the two different volumes can

be expressed as:

$$\tau_1 = \sigma_1 N_1 L / 2 \quad (5.6)$$

$$\tau_2 = \sigma_2 N_2 L / 2 \quad (5.7)$$

Gathering for SO₂ the values of σ_1 at T_1 and σ_2 at T_2 from HotW simulations, it is possible to evaluate the total decadic absorbance for the gas in the two consecutive volumes as:

$$A_{1+2} = \frac{\tau_{1+2}}{\ln(10)} = \frac{\tau_1 + \tau_2}{\ln(10)} \quad (5.8)$$

The goal now is to determine if two volumes can be effectively described as a single section of length L at temperature $T_{avg} = \frac{T_1 + T_2}{2}$. As a reminder, the two volumes are characterized by temperature T_1 and T_2 respectively, with constant and homogeneous molar concentration of SO₂ equal for the two, and length $L/2$ each. It is not immediately clear if at experimental temperature and pressure the cross section can be approximated well with the arithmetic average of the cross-section at different conditions, since temperature and pressure can affect the strength, width, and position of the spectral lines. The cross section σ_A at T_{avg} is evaluated using HotW, as for σ_1 and σ_2 . The average optical depth τ_A leads to the calculated absorbance A_A , to be compared to A_{1+2} . Figure 5.29 represents the simulated absorbance for 300ppm SO₂ in the four different simulated conditions listed below:

1. A_1 , 1m cell at $T_2 = 593K$ (green)
2. A_2 , 1m cell at $T_1 = 693K$ (red)
3. A_{1+2} , 0.5m cell at $T_1 = 693K$ and 0.5m cell at $T_2 = 593K$ (orange)
4. A_A , 1m cell at $T_{avg} = 643K$ (blue)

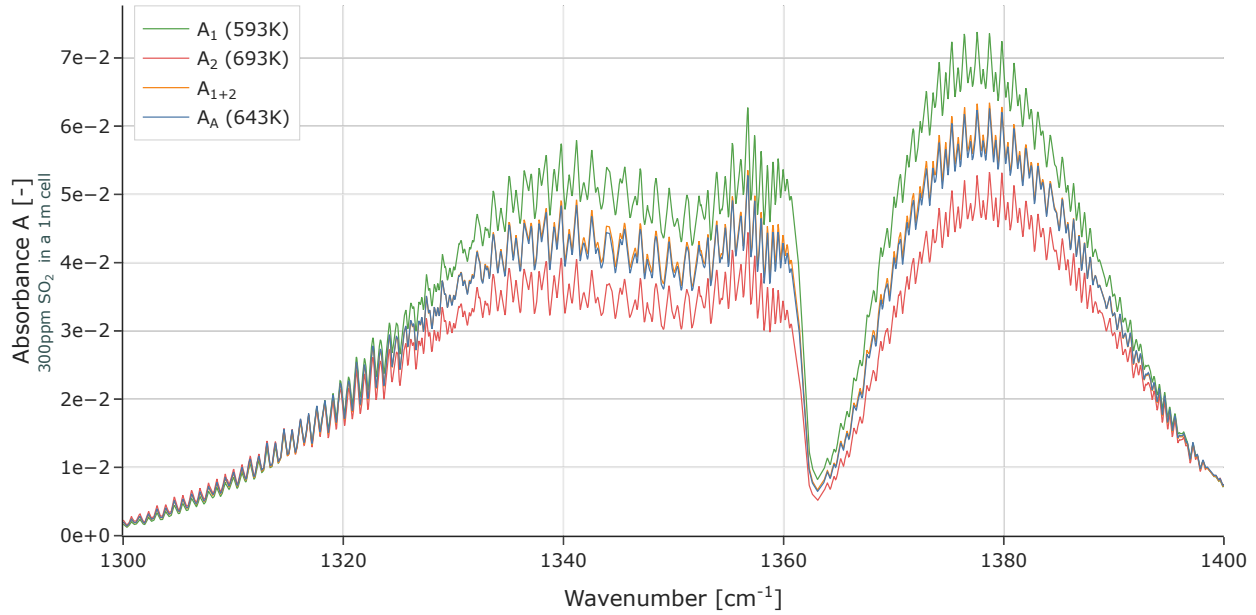


Figure 5.29: Simulated absorbance for 300ppm of SO_2 in two gas volumes at different temperatures.

The problem can be extended to more than two sections. Figure 5.30 represents the case for three sections at temperatures T_1 , T_2 , T_1 respectively, with:

- A_1 and A_3 , 1m cell at $T_1 = 593K$ (green)
- A_2 , 1m cell at $T_2 = 693K$ (red)
- A_{1+2+3} , $\frac{1}{3}$ m cell at $T_1 = 693K$, $\frac{1}{3}$ m cell at $T_2 = 593K$, and $\frac{1}{3}$ m cell at $T_1 = 693K$ (orange)
- A_A , 1m cell at $T_{avg} = 626K$ (blue)

From Figure 5.29 and Figure 5.30, the absorbance spectrum from SO_2 in the 1m measurement cell is equal to the absorbance spectrum calculated from the sum of the optical depths of each finite gas volume section.

The result is valid given a series of notable assumptions, such as accurate cross-sections from the HotW simulations, temperature in each gas volume section is uniform and known with accuracy, SO_2 concentration is uniform in every gas volume section, and changes in

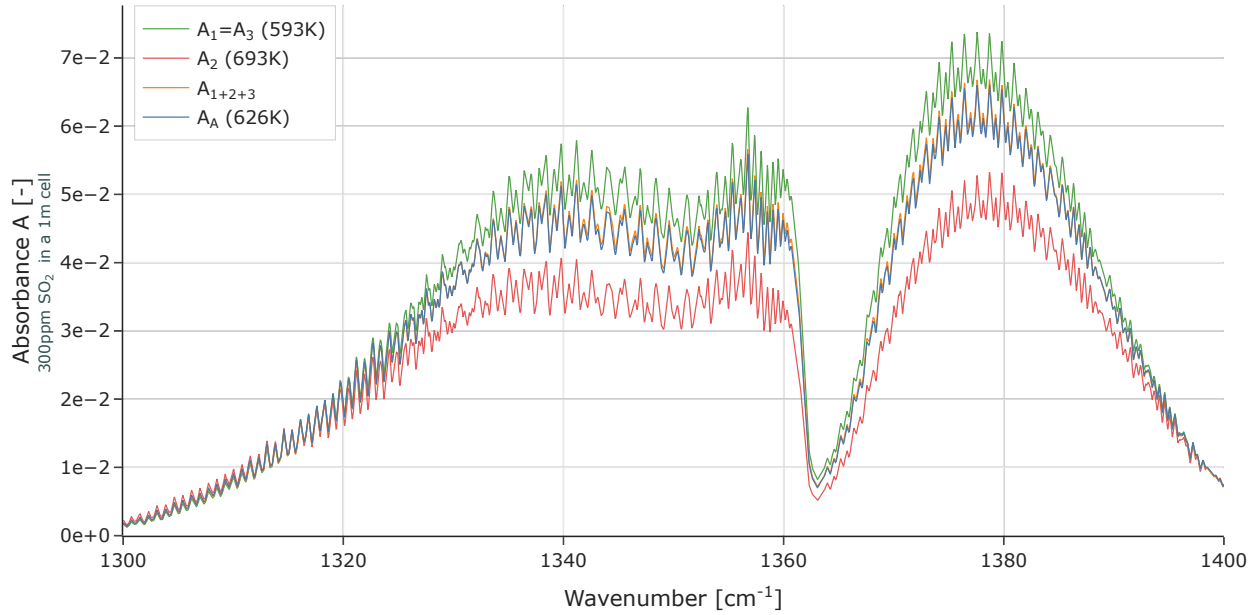


Figure 5.30: Simulated absorbance for 300ppm of SO_2 in three gas volumes at different temperatures.

the absorbance spectrum are due to the SO_2 molecule only. The next section will take into account the case where the temperature in one section is not known with accuracy.

5.4.2 Effect of temperature uncertainties on the measured absorbance spectrum

The previous section assumed the average temperature in the measurement cell is known with accuracy. If thermocouples are installed, this requisite is generally satisfied, however, thermocouple measurement uncertainties and factors such as proper thermocouples placement can affect the accuracy of the estimate. In this section, the real gas temperature in the measurement cell and estimated gas temperature from thermocouple readings are assumed to be different, with a difference between the two at $50K$. This allows an error propagation evaluation on the spectroscopic estimation of SO_2 concentration.

The average measurement cell temperature is $T_R = 693K$, while the estimated average temperature from the thermocouple measurement is $T_E = 643K$. The absorbance spectrum

is fitted with the cross-sections of the gas at T_E , introducing an error in the measurement since the real gas temperature is T_R . First, the SO_2 cross-sections σ_E at T_E are simulated using HotW. The error is introduced when assuming that the measured absorbance spectrum A_R (that is at $T_R = 693\text{K}$) is instead interpreted as a measured absorbance spectrum A_E at temperature T_E . The laser measurement provides an absorbance spectrum:

$$A_R = A_E \quad (5.9)$$

Hence:

$$\frac{\tau_R}{\ln(10)} = \frac{\tau_E}{\ln(10)} \rightarrow \tau_R = \tau_E \quad (5.10)$$

$$\rightarrow \sigma_R N_R L = \sigma_E N_E L \quad (5.11)$$

The only unknown is now $N_E = \frac{\sigma_R N_R}{\sigma_E}$. Going from the number of molecules of SO_2 to the number of moles:

$$n_{\text{SO}_2, T_E} = \frac{N_E}{N_a} \quad (5.12)$$

It is now possible to compare $\frac{n_{\text{SO}_2, T_E}}{n_R}$ with $\frac{n_{\text{SO}_2, T_R}}{n_R}$ to estimate the measurement error introduced from an erroneous temperature measurement. Since σ is dependent on the wavelength, only the central part of the SO_2 spectrum from 1324cm^{-1} to 1388cm^{-1} is considered, where its spectral features are the most pronounced.

Starting from $T_R = 693\text{K}$ in a 1m cell with SO_2 concentration of 300ppm, a temperature uncertainty of 50K (with $T_E = 643\text{K}$) would lead to an estimation of 273.3ppm SO_2 in the cell, for a 8.9% estimation error. The discrepancy between real and measured temper-

ature of 50K (7.2%) is approximately the maximum discrepancy value that is expected in experimental conditions.

Factors that can introduce a temperature estimation uncertainty include: thermocouples margin of error, incorrect thermocouple positioning into the gas flow, or spatial non-uniformity of the temperature. In turn, the SO_2 estimation error upper bound should theoretically be limited to less than 9% (absorbance results are represented in Figure 5.31).

This analysis is valid when the temperature estimation difference is not too large. The analysis is subject to the same constraints of accurate HotW simulations at different temperatures, constant and uniform SO_2 concentrations, and changes in the absorbance spectrum uniquely due to SO_2 and exclusion of any other broadband background change.

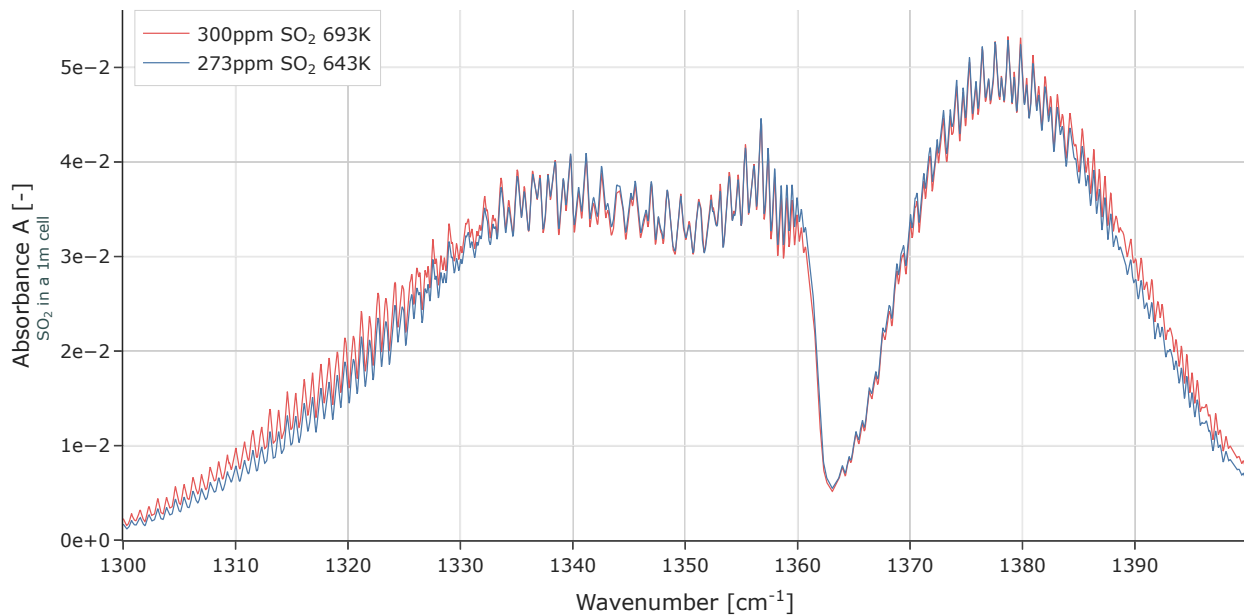


Figure 5.31: Simulated absorbance A_R and A_E resulting from a 50K temperature measurement error.

5.4.3 Effect of simultaneous temperature and concentration change

The analysis will be extended to the case where the SO_2 concentrations are not the same in the modeled sections. This represents well the experimental conditions for SO_3 (or H_2SO_4),

whose concentration change locally because of chemical reactions that are directly related to temperature. Assuming gas temperatures and SO₂ concentrations in three different sections are:

$$T_1 = 605K \quad c_1 = 107ppm$$

$$T_2 = 665K \quad c_2 = 230ppm$$

$$T_3 = 650K \quad c_3 = 196ppm$$

Where c_i is the SO₂ concentration for section i . The number density (evaluated from the number of SO₂ moles in each section) is:

$$N_1 = 1.29 \cdot 10^{15} \frac{\text{molecules}}{\text{cm}^3}$$

$$N_2 = 2.53 \cdot 10^{15} \frac{\text{molecules}}{\text{cm}^3}$$

$$N_3 = 2.20 \cdot 10^{15} \frac{\text{molecules}}{\text{cm}^3}$$

The optical depth for each section can be calculated as:

$$\tau_i = \sigma(T_i) N_i \frac{L}{3} \tag{5.13}$$

with $i = 1, 2, 3$ and $L = 100\text{cm}$. The overall simulated absorbance can be evaluated as:

$$A_{1+2+3} = \frac{\tau_{1+2+3}}{\ln(10)} = \frac{\tau_1 + \tau_2 + \tau_3}{\ln(10)} \tag{5.14}$$

Comparing the absorbance A_{1+2+3} with the absorbance A_E resulting from averaging of the variables on the three sections:

$$T_{avg} = \frac{T_1 + T_2 + T_3}{3} = \frac{605 + 665 + 650}{3} = 640K \tag{5.15}$$

$$c_{avg} = \frac{c_1 + c_2 + c_3}{3} = \frac{107 + 230 + 195.5}{3} = 177.5\text{ppm} \quad (5.16)$$

The molar density is different for each of the three gas sections depending on temperature only (since the three sections are communicating and isobaric) according to the ideal gas law, as seen in Equation 5.5. Starting from the global gas molar density of any section (not just the SO₂ fraction), it is possible to determine the molar density for the cell. Evaluating the molar density in the cell starting from that of section 3:

$$n_E = n_{Section3} \cdot \frac{T_3}{T_E} \quad (5.17)$$

and the average SO₂ molar density:

$$n_{E,SO_2} = n_E \cdot c_{avg} \quad (5.18)$$

The average number of SO₂ molecules per unit volume in the cell is:

$$N_E = n_{E,SO_2} \cdot N_A \quad (5.19)$$

Average optical depth and absorbance are, respectively:

$$\tau_E = \sigma_E N_E L \quad (5.20)$$

$$A_E = \frac{\tau_E}{\ln(10)} \quad (5.21)$$

where σ_E is simulated at T_{avg} using HotW. The comparison between A_{1+2+3} and A_E is shown in Figure 5.32.

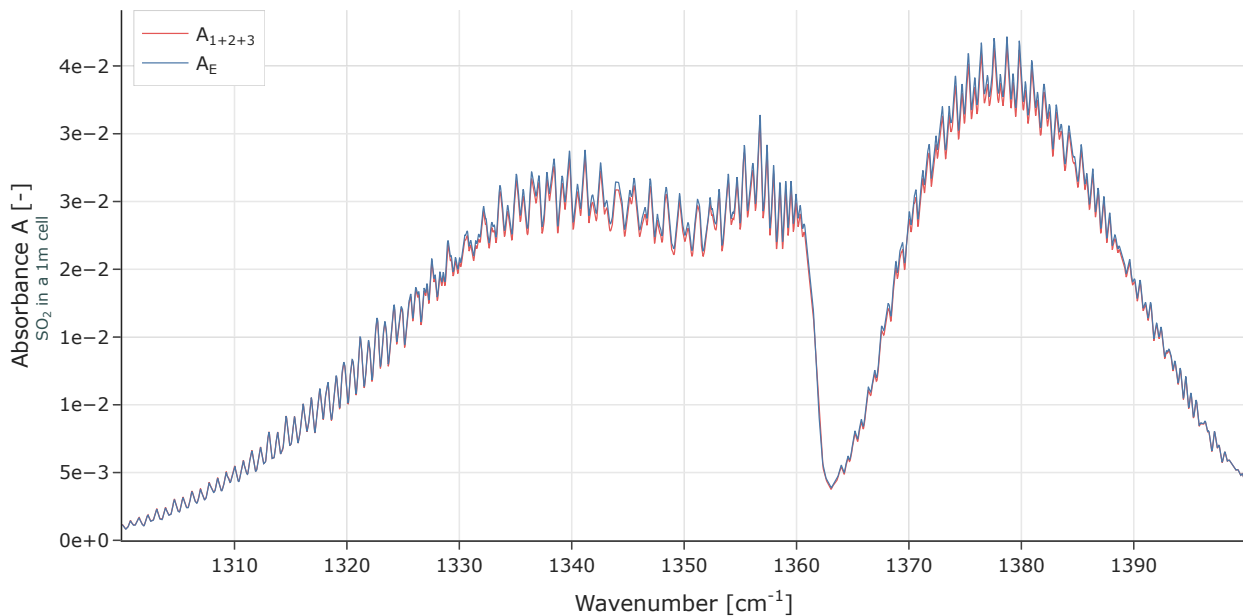


Figure 5.32: Simulated absorbance A_{1+2+3} and A_E for gas sections with different temperature and concentration.

In conclusion, the absorbance of n gas sections each with temperature T_i , SO_2 concentration c_i , and length L/n is equal to the absorbance of a single gas section with averaged variables T_{avg} and c_{avg} , and length L . This result is valid in a close vicinity of the considered values of T_{avg} and c_{avg} and could not extend to much larger temperature, pressure, or concentration differences that could significantly alter intensity, width, position of the molecule cross-sections, or that could invalidate Beer-Lambert Law.

5.4.4 Effect of pressure variations

In experimental conditions, the pressure in the measurement cell increases when the controlled condensation system is activated. In fact, the controlled condensation apparatus adds a significant pressure drop due to flow restrictions in coil and impingers nozzles, hydrostatic pressure to overcome in the impingers, bends in the flow path, silica gel beads, and dry gas

meter. The pressure in the measurement cell at ambient temperature has been measured as a function of the main inlet flow rate with a high-accuracy low-pressure gauge (0-3psi) and the result is shown in Figure 5.33. The typical pressure increase in the measurement cell in regular flow conditions of 5 slm is 0.0238atm (0.35psi), while at 10 slm it is 0.0728atm (1.07psi).

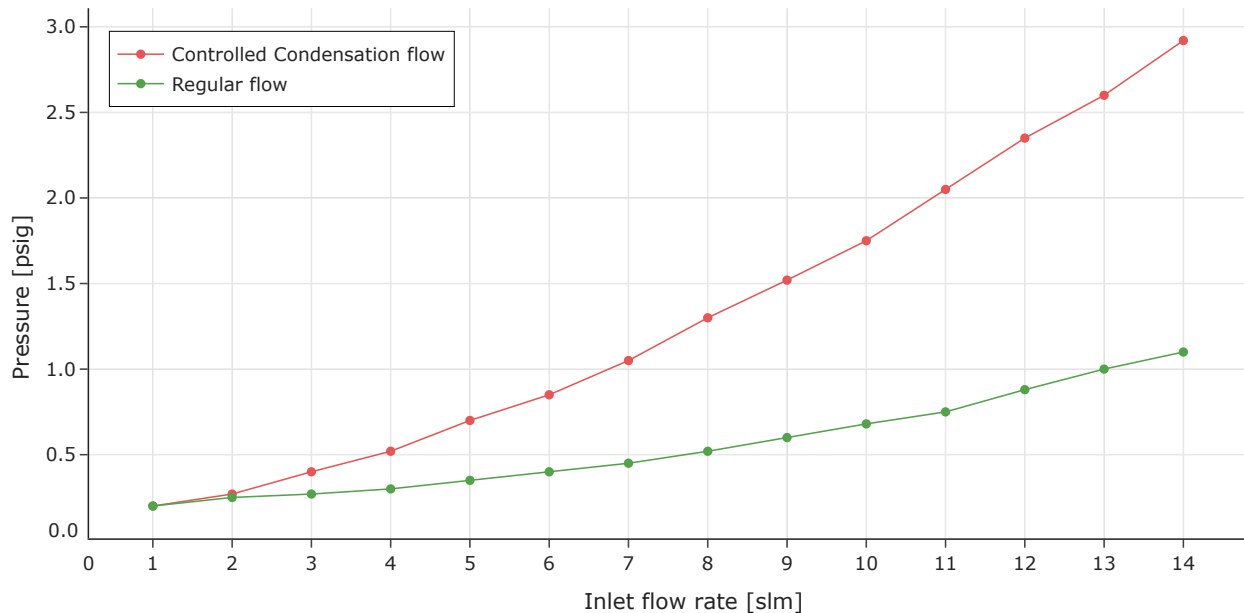


Figure 5.33: Experimental pressure change in the measurement cell as function of main inlet flow rate at ambient temperature.

As shown in Figure 5.34 the absorbance at 640K for three different pressure increases corresponding to flows of 5 slm, 8 slm, and 10 slm respectively, does not present a significant difference with respect to the ambient pressure case and does not change the estimated SO₂ concentrations.

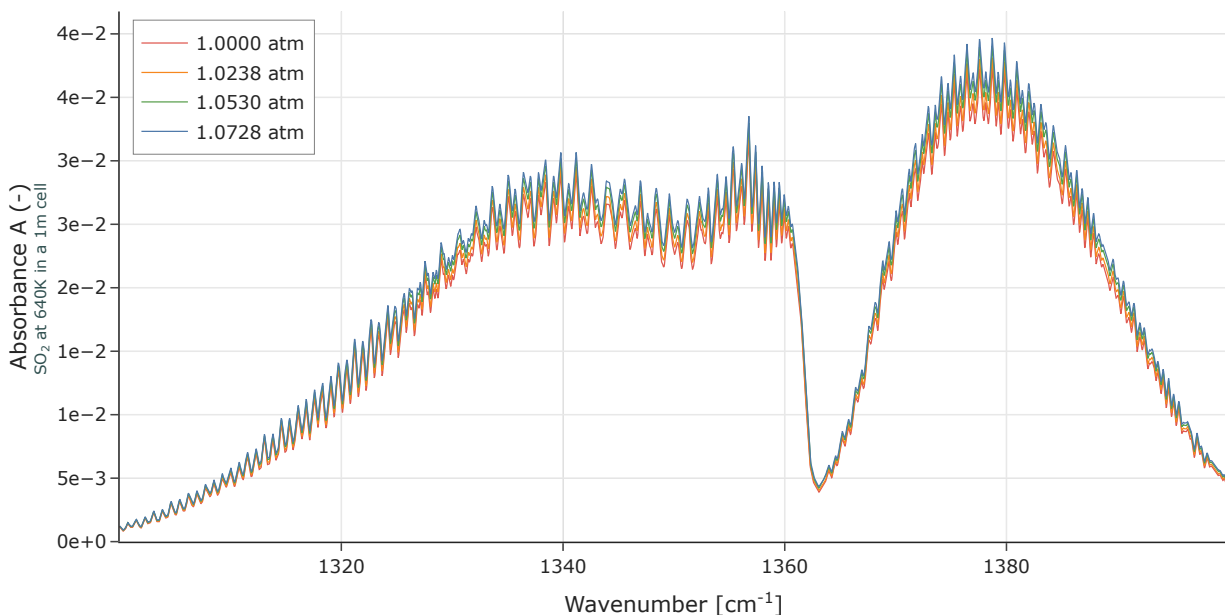


Figure 5.34: Simulated absorbance for different measurement cell pressure values.

When the temperature in the cell is increased to experimental conditions, the pressure inside the measurement cell can differ from this analysis, but the extent of the change is unlikely to cause a major difference on the absorbance spectrum.

5.5 Conclusions

This chapter provided a numerical analysis of the gas behavior in the measurement cell. The last section, relying on *Hitran on the Web* simulations, should be considered valid only when the variations of temperature, concentrations, and pressure are sufficiently close to the mean values. Moreover, in experimental conditions several complications arise, for example related to window damage or changes in the background gas absorbance spectrum.

The Fluent simulations rely on turbulence models and on the assumption of chemical equilibrium between SO_3 and H_2SO_4 . These assumptions are appropriate, however, in experimental conditions factors such as heterogeneous reactions and wall surface reactions can offset the experimental results from the numerical solution. Even if the simulations required several assumptions and simplifications, the results obtained are consistent and physically

reasonable, and they provide significant insights regarding the experimental conditions.

According to the simulations, temperatures, as well as SO_3 and H_2SO_4 concentrations, exhibit large three-dimensional variation in the measurement cell, but temperature values in the core section along the measurement cell axis are fairly uniform ($\pm 6\%$ standard deviation). On the contrary, H_2SO_4 and SO_3 concentrations in the core section present significant variations along the cell axis, but their average composition corresponds to the chemical equilibrium values evaluated in correspondence of the average cell temperature.

The addition of purging N_2 flows decreases the local H_2SO_4 concentration in front of the windows up to a factor of 5 for the nitrogen flow rates considered (up to 50% of the inlet main flow rate). The reduction is important, but in the timescales of interest it is likely not to accomplish the desired improvement. In fact, the desired lifespan of the windows is days/weeks, while empirical observation show window degradation occurring in tens of minutes.

The addition of nitrogen at different temperatures can change the mean temperature inside the measurement cell, altering the concentration of SO_3 and H_2SO_4 by both shifting their chemical equilibrium and by increasing dilution.

The thermal boundary layer in the measurement cell is approximately 0.4" (10mm) thick at the longitudinal coordinates where the thermocouples are installed, and the arithmetic mean of the thermocouple readings is an appropriate measure of the average core section gas temperature.

In a first approximation, spectroscopic measurements should be able to rely on the averaged measured temperature to calculate with sufficient accuracy the species concentration values ($\pm 9\%$) even if temperature in the cell is not uniform along the beam path and even if the temperature reading was associated with uncertainties ($\pm 50K$). The spectroscopic measurement do not appear to be affected by the pressure changes typical of this experimental setup.

After bounding the expected temperature and concentration uncertainties with the use

of numerical models and simulation, the next step will be the collection and analysis of experimental data for ECQCL 7 and ECQCL 8 Mid-IR lasers.

Chapter 6

Experimental results

The experiments are the heart of this dissertation. They represent the only absorption measurements for flue-gas conditions of the reactive species SO_3 and H_2SO_4 under sufficient control to provide clarity on the potential for continuous measurements. As has been alluded to in Chapter 2, there are two main sets of measurements - one in the UV using DOAS, the other in the mid-IR using ECQCL lasers. There are challenges in both cases, particularly the DOAS measurements, but together they provide the state-of-the-art for the species measurement.

With such a comprehensive set of experimental results, the chapter is divided between the DOAS measurements (6.1) and the more extensive ECQCL measurements (6.2). The results are provided in a uniform tabulated presentation to allow a clear comparison between conditions. Because part of the contribution of this dissertation is the absorption data itself, as well as the conclusions drawn from the behavior of SO_3 and H_2SO_4 under flue gas conditions, the chapter is necessarily bulky. Ultimately the results also provide quantitative information that can be used to evaluate the potential for continuous monitoring of the reactive sulfur species as was described as a key goal and motivation for the work.

6.1 Differential Optical Absorption Spectroscopy

The first experimental design described in Section 3.3 was used to evaluate the performance of the DOAS system. In these experiments, no H_2O was added to the gas stream, since the goal was to observe the spectrum of SO_2 and SO_3 only. Eventually, the evaluation of equilibrium between SO_3 and H_2SO_4 could then occur by difference from the collected samples in the controlled condensation coil of EPA Method 8A. That is, if the total sulfur were known and the SO_2 and SO_3 concentrations were measured separately then the total acid condensation would be SO_3 and H_2SO_4 from the test cell.

6.1.1 Sulfur dioxide (dry tests)

The first tests were focused on the measurement of SO_2 , which has a known spectrum in the UV, even at high temperature.

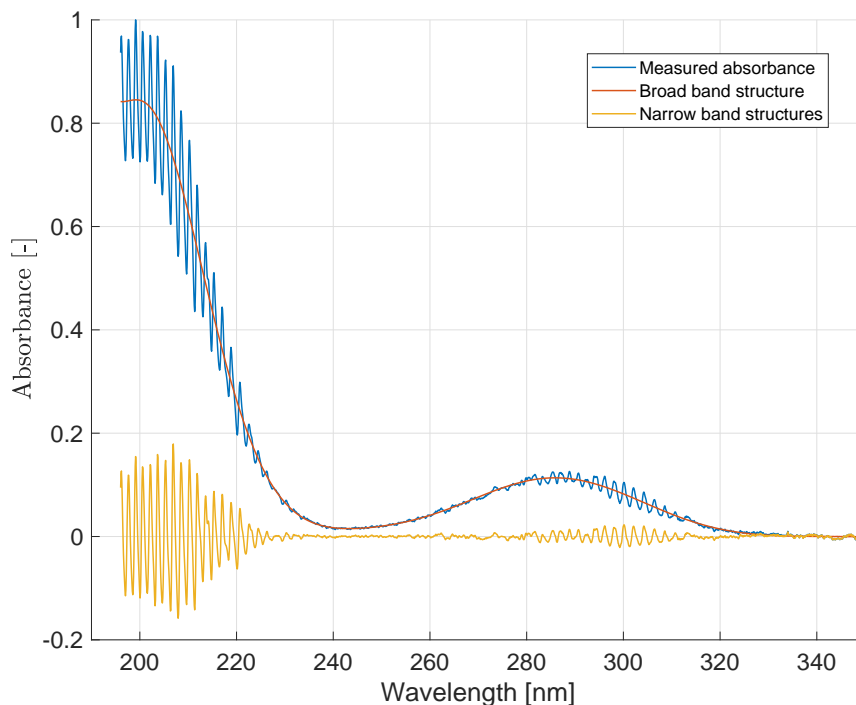


Figure 6.1: UV spectrum of 54ppmv SO_2 at 400 °C and 1atm pressure with 1m path length

As seen from Figure 6.1, the DOAS instrument is able to successfully detect the narrowband features of SO_2 even at high temperature, and it was able to measure down to 1ppmv.

6.1.2 Sulfur trioxide (dry tests)

In initial tests, SO_3 could not be distinctly detected by the DOAS. The presence of low concentrations of SO_2 in the measurement cell, however, suggested that the catalyst was operating correctly and the SO_2 was converting to SO_3 as desired. In Figure 6.2, the efficiency of the oxidation catalyst was evaluated in a first approximation based on the residual SO_2 presence in the measurement cell.

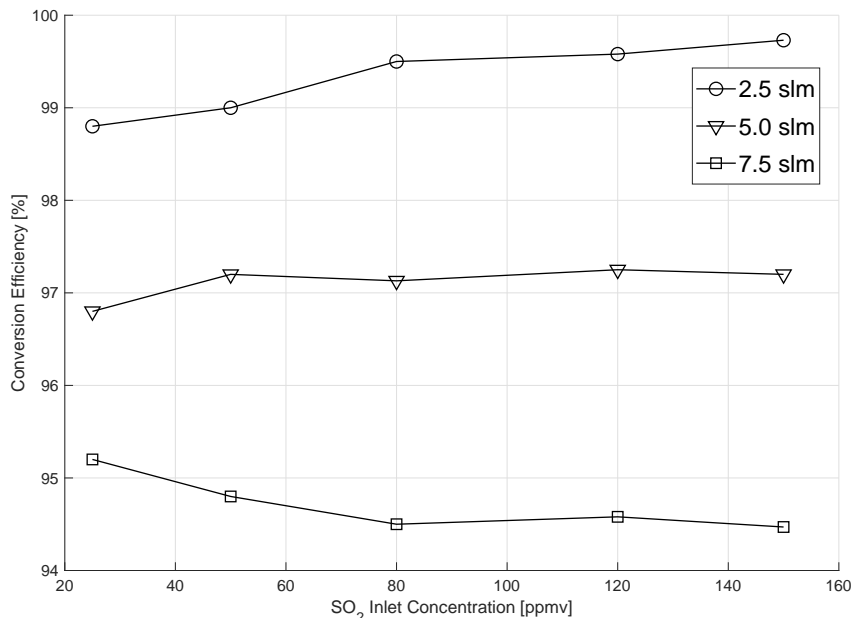


Figure 6.2: Estimated conversion efficiency of the catalyst reactor for different flow rates and initial SO_2 concentrations based on SO_2 disappearance rather than by direct measure of SO_3 .

However, the absorbance spectrum was not consistent with the very high levels expected from the SO_2 conversion data. The lack of SO_3 signature spectrum suggested the possibility that sulfur trioxide was not reaching the measurement cell in a high enough concentration to be distinguished clearly. The lack of SO_3 in the cell could be attributed to sulfur losses

along the pipeline, or to no SO_3 production from the catalyst. As was determined in later studies the culprit is likely the very long time needed for conditioning the catalyst. This first experimental facility used a large quantity of catalyst to ensure high SO_2 to SO_3 conversion but this also led to an excessively long conditioning phase. It now appears that the catalyst never reached a condition where the generated SO_3 was released to the system at detectable levels.

To temporarily test the potential of a DOAS technique in measuring SO_3 while recognizing the possibility that SO_3 was not being delivered as expected by the catalyst conversion system, liquid sulfur trioxide was injected into the measurement cell through an injection port. The liquid was captured and evaporated by the hot gas flow. The carrier flow for the injection was nitrogen or preferably air, as the presence of additional oxygen keeps SO_3 from decomposing into SO_2 . After the injection of pure SO_3 in the carrier gas, the absorption spectrum was compared to that of a known concentration of SO_2 . Due to the difficulty of handling liquid sulfur trioxide, the concentration of SO_3 (and SO_2) in the measurement cell was unknown, but the concentration of SO_3 was estimated to be in the order of a percent, that is a concentration much larger than typical in flue gas and far higher than the target sensitivity demanded of the desired continuous monitoring system. Post-processing the absorbance spectrum, and subtracting the SO_2 contribution, led to a result comparable to Kurata et al. (Figure 2.6), as illustrated in Figure 6.3. Since the concentration of SO_2 was not known, the subtraction was performed by scaling the peak at 280nm so that both spectra would have the same absorbance at that location. This scaling is appropriate because there is no spectral feature of SO_3 at this wavelength so the SO_2 value properly scales the spectrum. After the scaling was performed, the spectrum of SO_2 was subtracted from the measured spectrum, leaving the SO_3 spectrum as result.

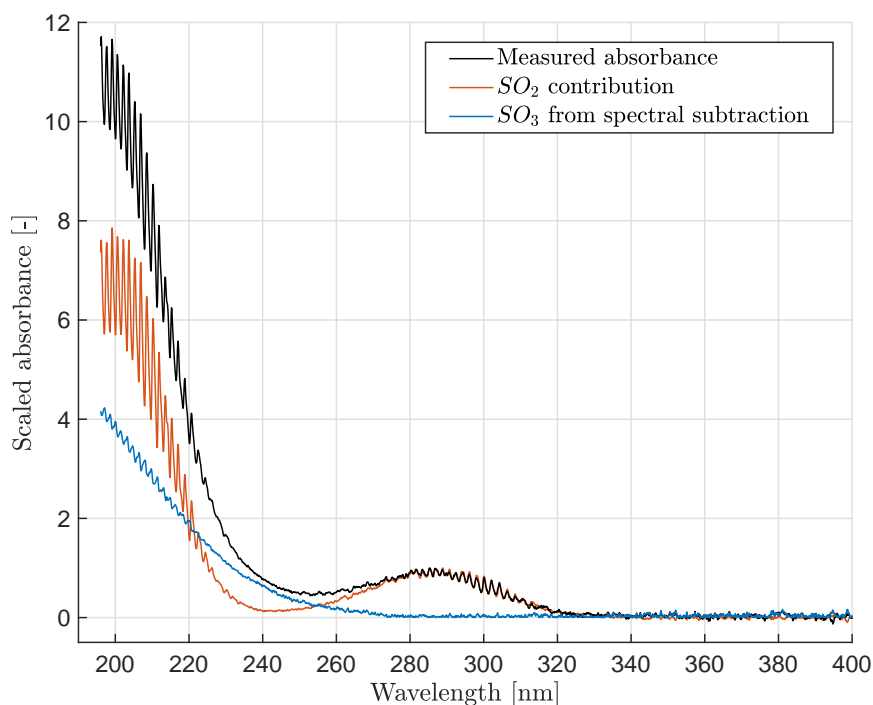


Figure 6.3: Subtraction of the SO_2 spectrum from the spectrum of SO_3 collected by direct injection of SO_3

The result confirmed the characteristic broadband absorbance of SO_3 in the UV. Weak narrow band features are visible. Even if the features were to be attributed to SO_3 , and not to artifacts related to the spectral subtraction, it would not be possible to detect them in realistic flue-gas concentrations. Narrow band components are essential for DOAS measurement and they were not clearly detected even in conditions of extremely high SO_3 concentration. Research groups have been able to estimate the concentration by just analyzing the broad band component [73]. Unfortunately, however, different molecules in flue gas could scatter the light differently creating an overlapping broad band absorbance which would severely compromise the reliability of the measurement. Moreover, at wavelengths between 180nm and 210nm, the absorbance of the Schumann-Runge bands of molecular oxygen further complicates the region for the measurement of species that absorb weakly, such as SO_3 .

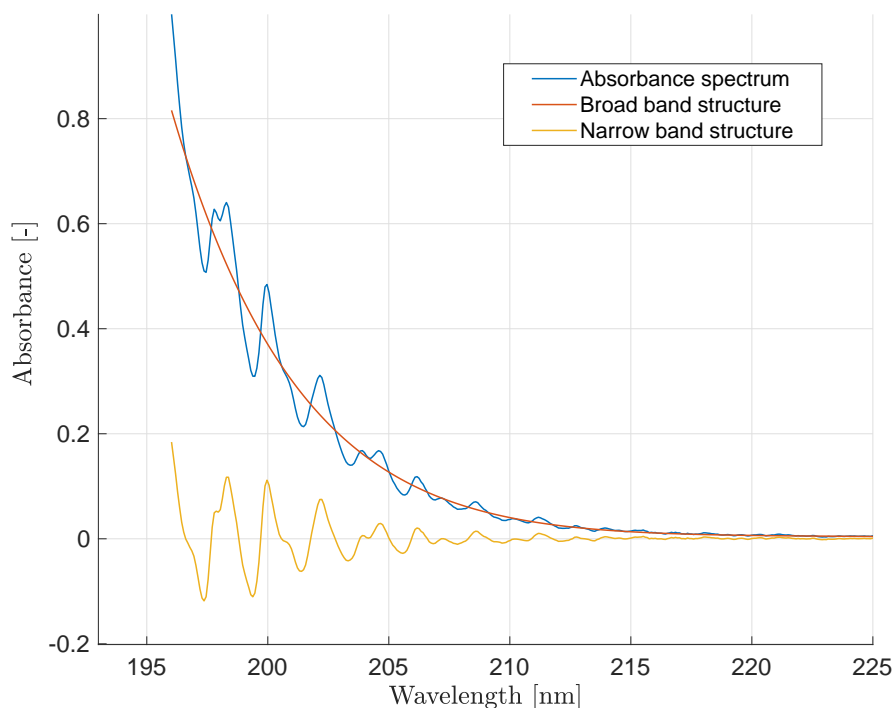


Figure 6.4: Experimental Schumann-Runge bands resulting from flowing air with a nitrogen background

Based on the forgoing results, while the DOAS technique proved suitable for SO_2 measurements in flue-gas conditions, it did not appear to be suitable for SO_3 measurement, as its signature spectrum can easily be affected by the Schumann-Runge bands and other molecules broadband scattering, even when the concentration of SO_3 was well above those typical of coal-fired power plant flue gas. Moreover, sulfuric acid is not an absorber species at these wavelengths. Fortunately, as was mentioned earlier (Chapter 2) the advances of quantum cascade laser technology have provided light sources that can now reliably reach the mid-infrared spectral region where SO_2 , SO_3 , and H_2SO_4 have the potential to be detected and measured.

6.2 External Cavity Quantum Cascade Laser (ECQCL)

The experimental setup for the ECQCL tests is described in Section 3.4. The objectives of the experimental test plan are to gather SO_2 , SO_3 , H_2SO_4 , H_2O spectral libraries at relevant temperatures (250C, 300C, and 350C), and to then analyze the feasibility and performance of the measurement system in simulated realistic flue gas conditions, $\sim 8\%$ water vapor, up to 50ppm SO_3 and/or H_2SO_4 , up to 2500ppm SO_2 . As shown in Chapter 2, for ECQCL 7 the measurements are expected to be heavily influenced by the high absorbance of H_2O and SO_2 . Since SO_3 is present at much lower concentrations, and because it is so highly reactive, an appropriate spectral library for SO_3 is of paramount importance.

The measurement campaign is carried out in two different steps to collect spectral libraries at idealized conditions and then to test the system at realistic conditions. That is, in step 1 both dry and wet conditions are tested, water vapor concentration of about 3% and 8%, with low SO_2 concentrations (comparable to SO_3 concentrations, from 0 up to 100ppm), and reference condition levels of SO_3 , up to 100ppm, to define accurate spectral libraries. In step 2, wet conditions of water vapor concentration at $\sim 8\%$ are analyzed, with high SO_2 concentrations up to 2500ppm, and reference conditions for SO_3 to evaluate the performance of the measurement system in the realistic flue gas target environment. Both the water vapor and SO_2 concentration will start from low levels and gradually increase to the maximum. The reason for separating the experimental effort into Steps 1 and 2 is simply that the initial investigation for the first phase/round provides the foundation for looking further into more extreme hydration and concentration levels at the second phase/round.

6.2.1 Experiment test structure

For Step 1 experiments, each single test in the campaign is identified by its principal variables T , SO_x , and $\beta\%$. Auxiliary variables x and $\dot{V}_{Air,Evap}$ are necessary to fully define each measurement condition. The variables correspond to:

T - Cell temperature (C or K): when water is present, the cell temperature will determine the SO_3 to H_2SO_4 ratio. It should match the useful power-plant temperature ranges 250C to 350C, or 523K to 623K.

SO_x concentration (in ppm): the input variable SO_x is defined as the SO_2 concentration of the gas stream entering the catalyst. The total volumetric flow rate entering the catalyst (inlet main gas) is 5 slm. The definition is meant to avoid confusion between SO_2 concentration entering the catalyst and SO_2 concentration in the measurement cell. The main inlet flow goes through the oxidation catalyst, and part of the SO_2 is oxidized to SO_3 . If water is added, part of the SO_3 will hydrate to H_2SO_4 . If no additional SO_2 is added through the bypass line, then the variable SO_x represents the overall amount of sulfur present in the measurement cell (useful for sulfur balance calculations). If any flow other than the main inlet flow is added (such as bypass flow, water flow, or purging flow), then the additional dilution has to be accounted for.

$\beta\%$ water vapor percentage: $\beta\%$ is the percentage of water vapor referred to the overall flow (main inlet flow, bypass flow, evaporator flow). \dot{V}_{H_2O} is its equivalent water vapor flow rate. When $\dot{V}_{H_2O} > 0$, also the carrier gas flow rate $\dot{V}_{Air,Evap}$ must be > 0 necessarily.

$$\beta\% = \frac{\dot{V}_{H_2O}}{\dot{V}_{H_2O} + \dot{V}_{Main\ Inlet} + \dot{V}_{Bypass} + \dot{V}_{Air,Evap}} \quad (6.1)$$

x ppm of SO_2 in bypass air: it describes a condition where a flow of x ppm of SO_2 is present in the cell. For example, it is useful to provide a known amount of SO_2 in air in the measurement cell for library spectrum purposes.

$\dot{V}_{Air,Evap}$ *slm of evaporator air*: carrier gas flow rate for water vapor production. It is usually set to 1 slm when activated. The evaporator air flow $\dot{V}_{Air,Evap}$ can be activated also when water vapor is not added to the flow ($\dot{V}_{H_2O} = 0$), but it must always be $\dot{V}_{Air,Evap} > 0$ if $\dot{V}_{H_2O} > 0$.

Every test in the campaign consists in a predefined sequence of test conditions, each with different targets (optical, spectroscopic, or both). The possible test conditions are summarized in Table 6.1. In order to make referencing the different kinds of tests more consistent, a keyword is associated with the test type and these keywords are also described in the table. Table 6.2 analyzes the same test conditions, this time addressing the specific experimental settings, such as flow rates and valve configurations, and highlighting the target species for each condition.

Keyword	Description
Air	This condition is useful to capture the background signal in the measurement cell at temperature T without any of the target species (SO_2 , SO_3 , H_2O)
Bypass x ppm	It allows to capture the spectrum of pure SO_2 at temperature T . It can be used for path length estimation as well, since SO_2 spectrum is well characterized and a precise SO_2 concentration can be provided directly. The flow in the Bypass line allows to skip the catalyst only (not the measurement cell), as seen in Figure 3.6
Regular	A flow of SO_x ppm of SO_2 in air enters the catalyst. The output flow consists of both SO_2 and SO_3 in air. In this condition water vapor is absent
Regular (Controlled Condensation)	In this condition, a mixture of water vapor and air is added to the flow past the measurement cell (POST-cell configuration). The flow on the back-end of the cell is hence wet, and it can be analyzed with controlled condensation. Since the amount of H_2O and air injected POST-cell is known, from the controlled condensation measurements it is possible to estimate the concentration of $\text{SO}_3/\text{H}_2\text{SO}_4$ and SO_2 in the measurement cell. Since in <i>Regular</i> condition the flow in the cell is dry, if water was not added POST-cell the controlled condensation system would not operate correctly

Keyword	Description
Equalized	Same as <i>Regular</i> , with additional air dilution through a PRE-cell air flow. This condition is useful because it "equalizes" the total cell flow rate with the one in the conditions <i>Equalized decay</i> , <i>Water only</i> , and <i>Water Add</i> so that they will be mutually comparable
Equalized Decay	In this condition, the inlet main flow consists of 5 slm of air only. In <i>Regular</i> conditions the outlet SO ₂ is the portion that has not been converted by the catalyst (unconverted SO ₂). If the SO ₂ flow is shut down, the catalyst keeps desorbing SO ₃ , with SO ₂ no longer present in the cell. This test conditions take advantage of the catalyst operating mechanism (SO ₃ desorption) to allow the measurement of a pure SO ₃ spectrum
Water only	Air (through the Bypass line) and a water vapor-air mixture (through the PRE-cell line) is present in the cell. This allows the capture a reference water spectral library
Water only + Bypass x ppm	It allows for the capture of a combined spectrum of SO ₂ and H ₂ O vapor

Keyword	Description
Water Add	Equivalent to the <i>Equalized</i> condition, with a portion of the PRE-cell air (\dot{V}_{H_2O}) substituted by water vapor instead of air. A part of the SO_3 present in the cell will convert to H_2SO_4 . From the spectroscopic point of view, this section has the double goal of measuring the drop in SO_3 with respect to the <i>Equalized</i> condition once water vapor is added, and measuring the H_2SO_4 concentration
Nitrogen purging	This condition is an add-on applicable to all previous conditions, when needed. 1.4 slm of nitrogen are added to the flow present in the cell, 0.7 slm at the downstream window and 0.7 slm at the upstream window. This flow will decrease the local concentration of H_2SO_4 in front of the windows but will also dilute the flow in the measurement cell
Step 2, Regular	For Step 2, <i>Regular</i> flow consists of a flow of SO_x ppm of SO_2 in air that enters the catalyst (5 slm) with the addition of 5 slm air through the Bypass line, with a total flow in the cell of 10 slm.

Keyword	Description
Step 2, Regular with x ppm SO ₂	<p>The flow rate in the cell is maintained at 10 slm, like for <i>Step 2, Regular</i>. The Bypass line injects additional SO₂ with respect to the <i>Step 2, Regular</i> case, for an overall estimated concentration of SO₂ in the cell of x ppm. The SO₂ concentration is only estimated because the unconverted fraction of SO₂ exiting the catalyst is not known with certainty (albeit it can be estimated from <i>Step 2, Regular</i>). If a lower SO₃ concentration in the cell is desired, there are two possible solutions: one is to decrease SO_x in the inlet main flow, although it would require long catalyst conditioning times. Alternatively, the flow rate in the Bypass line can be increased to values larger than 5 slm. With the latter strategy it is possible to study the absorbance spectrum for reduced levels of SO₃.</p>
Step 2, Regular with x ppm SO ₂ (Controlled Condensation)	<p>5 slm main inlet flow of air with SO_x ppm SO₂ + 5 slm of SO₂ and air mixture through bypass line Resulting mixture totals about x ppm SO₂ in the measurement cell POST-cell: 1.2 slm of air + 0.8 slm water vapor (added for controlled condensation measurement only)</p>

Keyword	Description
Step 2, Water Add	The overall flow rate in the cell is fixed at 10 slm, as for <i>Step 2, Regular with x ppm SO₂</i> . The Bypass line, however, carries only 3 slm of SO ₂ mixture. The remaining 2 slm consists of PRE-cell injection of a water vapor mixture. The resulting gas composition in the cell will be of approximately x ppm SO ₂ and 8% H ₂ O vapor. If a different H ₂ O percentage is desired, the split between $\dot{V}_{Air, Evap}$ and \dot{V}_{H_2O} will be changed, while keeping $\dot{V}_{Air, Evap} + \dot{V}_{H_2O} = 2\text{slm}$
Step 2, Water Only + Bypass x ppm SO ₂	The overall flow rate in the cell is fixed at 10 slm. PRE-cell injection of a 2 slm water vapor mixture will result in 8% H ₂ O vapor in the measurement cell. The remaining 8 slm consists of a SO ₂ /air mixture, so that the concentration of SO ₂ in the measurement cell is x ppm

Table 6.1: Explanation of different test conditions

Keyword	Conditions in measurement cell	Target Species
Air	Air only	Background
Bypass x ppm	x ppm of SO ₂ in air through bypass line	SO ₂
Regular	Catalyst output only (Main inlet is 5 slm of air with SO_x ppm of SO ₂)	SO ₂ , SO ₃
Regular (Controlled Condensation)	Regular + POST-cell: $\dot{V}_{Air, Evap}$ slm of air + \dot{V}_{H_2O} slm = $\beta\%$ H ₂ O vapor (added for controlled condensation measurement only)	H ₂ SO ₄ , SO ₂ with EPA 8A
Equalized	Regular + PRE-cell: $\dot{V}_{Air, Evap}$ slm + the equivalent of \dot{V}_{H_2O} slm of <i>air only</i> (no water vapor)	SO ₂ , SO ₃
Equalized Decay	Main inlet flow of 5 slm air only + PRE-cell: $\dot{V}_{Air, Evap}$ + \dot{V}_{H_2O} slm of air only (no water vapor, like for Equalized)	SO ₃

Keyword	Conditions in measurement cell	Target Species
Water only	Bypass line with 5 slm air only + PRE-cell: $\dot{V}_{Air, Evap}$ slm of air + \dot{V}_{H_2O} slm = $\beta\%$ H ₂ O vapor	H ₂ O
Water Add	Regular + PRE-cell: $\dot{V}_{Air, Evap}$ slm of air + \dot{V}_{H_2O} slm = $\beta\%$ H ₂ O vapor	H ₂ SO ₄ , SO ₂ , SO ₃
Water only + Bypass x ppm	5 slm of SO ₂ and air mixture through bypass line + PRE-cell: $\dot{V}_{Air, Evap}$ slm of air + \dot{V}_{H_2O} slm = $\beta\%$ H ₂ O vapor Resulting mix totals x ppm SO ₂ in the measurement cell	H ₂ O, SO ₂
Step 2, Regular	5 slm main inlet flow of air with SO_x ppm SO ₂ + 5 slm air through bypass line	SO ₂ , SO ₃
Step 2, Regular with x ppm SO ₂	5 slm main inlet flow of air with SO_x ppm SO ₂ + 5 slm of SO ₂ and air mixture through bypass line Resulting mixture totals about x ppm SO ₂ in the measurement cell	SO ₂ , SO ₃

Keyword	Conditions in measurement cell	Target Species
Step 2, Regular with x ppm SO ₂ (Controlled Condensation)	5 slm main inlet flow of air with SO_x ppm SO ₂ + 5 slm of SO ₂ and air mixture through bypass line Resulting mixture totals about x ppm SO ₂ in the measurement cell POST-cell: 1.2 slm of air + 0.8 slm water vapor	H ₂ SO ₄ , SO ₂ with EPA 8A
Step 2, Water Add	5 slm main inlet flow of air with SO_x ppm SO ₂ + PRE-cell: 1.2 slm of air + 0.8 slm = 8% H ₂ O vapor + 3 slm of SO ₂ and air mixture through bypass line Resulting mixture totals about x ppm SO ₂ in the measurement cell	H ₂ SO ₄ , SO ₂ , SO ₃
Step 2, Water Only	8 slm bypass flow of air + PRE-cell: 1.2 slm of air + 0.8 slm = 8% H ₂ O vapor	H ₂ SO ₄ , SO ₂ , SO ₃
Step 2, Water Only + Bypass x ppm SO ₂	8 slm bypass flow of SO ₂ and air mixture + PRE-cell: 1.2 slm of air + 0.8 slm = 8% H ₂ O vapor Resulting mixture totals x ppm SO ₂ in the measurement cell	H ₂ SO ₄ , SO ₂ , SO ₃

Table 6.2: Test conditions as a function of the test variables

6.2.2 Experiment matrix

For Step 1, 24 different tests ($4 SO_x \times 3 T \times 2 \beta\%$) are required to cover the desired combinations of SO_2 main inlet concentration (variable SO_x), temperature (variable T), and water vapor concentration (variable $\beta\%$), as summarized in Table 6.3. Since each case is defined by SO_x , $\beta\%$, and T variables, the cases can be compared to each other. For example, cases with the same SO_x and $\beta\%$ can be compared at different cell temperature T .

Step 2 is focused on assessing the performance in realistic flue-gas conditions, so the experiments are defined by the target variable SO_2 , SO_3 , H_2O , and H_2SO_4 levels in the measurement cell, rather than the inlet variable SO_x . The inlet variable SO_x for Step 2 doesn't provide helpful information, since the inlet main flow will be purposely diluted with air or an SO_2 /air mixture to alter the levels of SO_3 and SO_2 in the measurement cell without altering the catalyst steady state. The total number of Step 2 conditions evaluated was 5 and 8, for ECQCL 7 and ECQCL 8 respectively.

Variable	Values
SO_2 Main Inlet (SO_x , ppm)	300 - 150 - 100 - 50
Temperature (T , C)	350 - 300 - 250
Water vapor (β , %)	0 - 3 - 8

Table 6.3: Step 1 experiments

Variable	Values
SO_2 Target (SO_2 , ppm)	50 - 530 - 2550
Temperature (T , C)	350 - 300 - 250
Water vapor (β , %)	1.6 - 8
SO_3 Target (SO_3 , ppm)	50 - 40 - 30 - 20 - 10

Table 6.4: Step 2 experiments

The experiment log, detailing parameters and note for each test, is provided for reference in Appendix A. In the next sections, two individual datasets, one for ECQCL 7 and one for ECQCL 8, are described chronologically to distinctly investigate each test condition.

6.2.3 Raw data set overview for an ECQCL 7 experiment

In this section, the structure of a single ECQCL 7 experiment will be analyzed in temporal order and the raw data from the detector will be evaluated and explained. The typical data set being used for clarifying the different elements of a single test run is the Step 1 ECQCL 7 07/14/2020 experiment, with $T = 350C$, $SO_x = 150$ ppm, $\beta = 3\%$. The timeline of the experiment is represented in Figure 6.5, with test conditions labeled at the top of the figure. The timeline plot shows the results of the data fit processed with appropriate libraries. The libraries and their use in the fitting procedure will be discussed in Section 6.2.6.

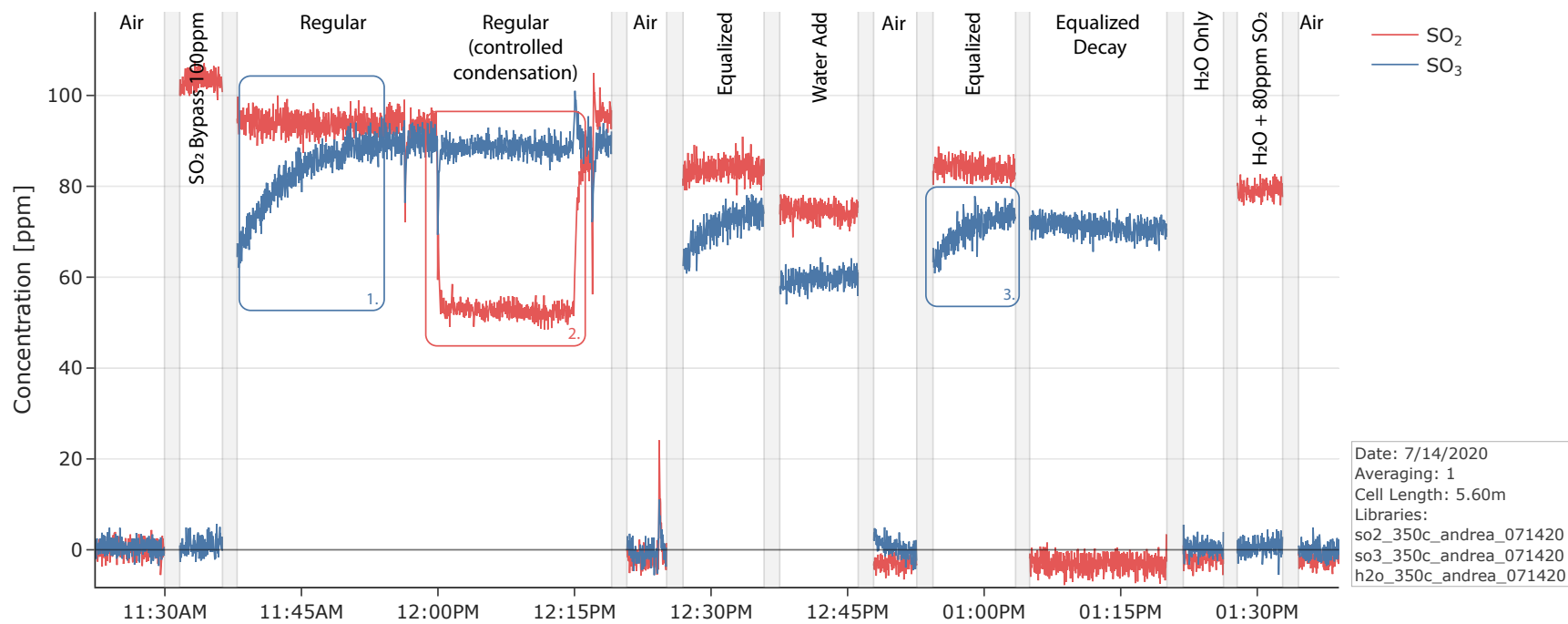


Figure 6.5: SO₂ and SO₃ concentrations in the Step 1 ECQCL 7 07/14/2020 $T = 350C$ experiment timeline.

A few peculiarities related to the measurement rig are highlighted in Figure 6.5:

1. *Catalyst transition time*

In *Air* and *100ppm SO₂ Bypass* test conditions, no SO₃ is in the measurement cell, and hence the gas flow through the catalyst is interrupted for approximately 10 minutes for this test. When gas starts to flow through the catalyst again (in *Regular* conditions), the SO₃ concentration ramps up to its steady-state value. The ramp-up can take from 5 to 15 minutes. To avoid this issue, a high-temperature valve (Main Flow Valve, in the schematics of Figure 3.6) was later installed. The valve assures that the catalyst is always continuously operating during an experiment, with its outlet flow simply being redirected to the scrubber, if SO₃ is not desired in the measurement cell. The catalyst transition time is a short-term transient, and it is a different phenomenon from the catalyst conditioning. The latter is characterized by a much slower transient in the order of tens of hours even for the relatively small amount of catalyst used in this laboratory facility.

2. *SO₂ drop during controlled condensation*

The value of SO₂ concentration drops considerably when the controlled condensation system is activated. The value of SO₂ measured by controlled condensation agrees well with the ECQCL7 measurement in *Regular* test conditions, so the estimated drop in SO₂ appears to be an artifact of changes in the background conditions affecting the spectral fitting outcome. During the controlled condensation, the measurement cell pressure increase is in the order of 1 psi, measured experimentally at room temperature. Even if the pressure was to increase five fold at high temperature, under the theoretical spectral analysis presented in Section 5.4.4, pressure alone would not be enough to explain the estimated concentration difference. From Table 6.5, under these conditions the absorbance spectrum shows water-like features, as the water vapor appears to be reduced with respect to the reference condition. The overall absorbance is reduced as well. The origins of this effect are still unclear. In order to maintain consistent

results, measured values are reported under the verified conditions with the controlled condensation flow path off.

3. *Catalyst transition time in Equalized conditions*

The effect of the short-term catalyst transition time manifests also in *Equalized* conditions.

The concept of a background spectrum will be often recurring in this chapter. The background is defined as the detector signal I_0 when a flow consisting only of air is present in the cell. This background can be saved as a reference spectrum. The absorbance spectrum, defined as $A = -\log_{10}(I/I_0)$, evaluated in the background condition is hence zero at all wavelengths since the raw detector signal (I) corresponds to the reference spectrum (I_0). If an absorber species is later added to the measurement cell, the detector signal I will change, and the absorbance A will now match the spectrum of the absorber species. It is also possible to capture a background signal in a condition that is different from only air. In that case, the absorbance spectrum will only reflect the presence of new absorber species that were not present in the measurement cell when the background frame was captured (or present at different concentrations).

In Figure 6.5, all concentration readings derive from a single time-averaged background spectrum definition, captured at the start of the test in *Air* conditions. This single background definition would be most common in real-time measuring, as the measurement cannot be interrupted often just in order to capture a new background signal definition. Unfortunately, this is also the most inconvenient condition, as background changes that alter the absorbance baseline can happen frequently, for example as a result of window damage or temperature changes, and can significantly impact the accuracy of the measurement. Nevertheless, the single background approach is used for the data evaluation in this dissertation study.

The raw data from the detector (voltage signal V), the decadic absorbance (non-dimensional), along with a description of the test conditions are collected in Table 6.5. The background

spectrum I_0 is represented with a red-shaded area, to highlight the difference between I_0 (red area) and the raw detector signal I in the specified test condition (white area with black border). This table is a comprehensive record of the collected and analyzed ECQCL signals for the different test conditions. While overwhelming, this tabular format permits the graphical comparison of the raw and processed signals among any of the cases tested so that the most dramatic differences can be highlighted easily. The raw detector signal axis range is fixed among all rows. The absorbance signal is constant among the rows with no water addition. The conditions where water is present are represented with a different absorbance scale, but consistent among the water cases, since water absorbs strongly in this wavelength regime, and it tends to hide all other spectral features.

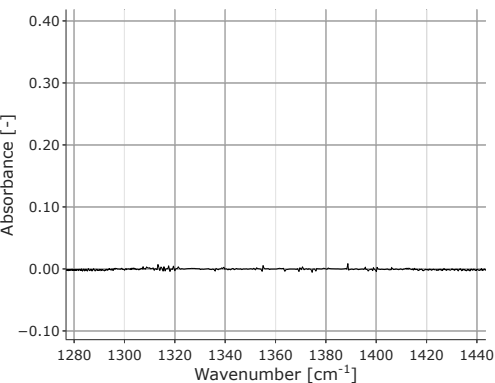
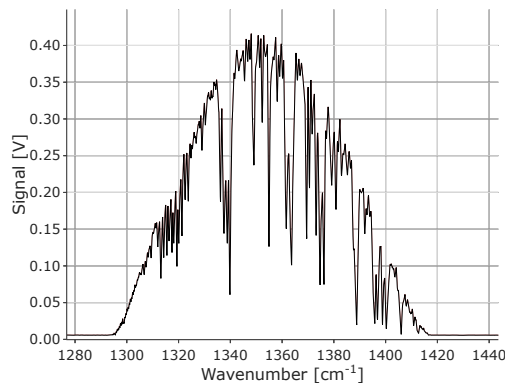
Description

Raw detector signal [V]

Absorbance spectrum [-]

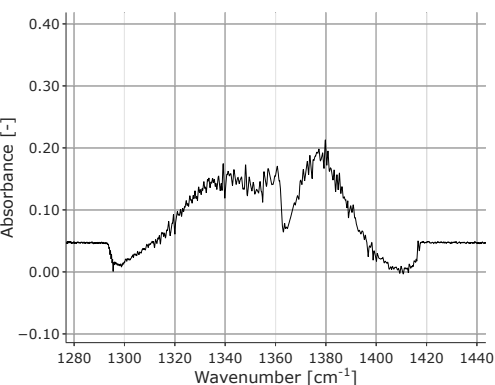
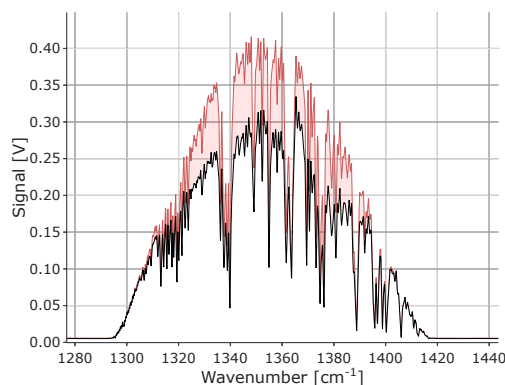
Air 11:27:51 AM

The raw detector signal in this test constitutes the background signal. The absorbance spectrum (right-most) is a line at zero absorbance (since this frame is taken as the background signal).



Bypass 100ppm SO₂ 11:33:39 AM

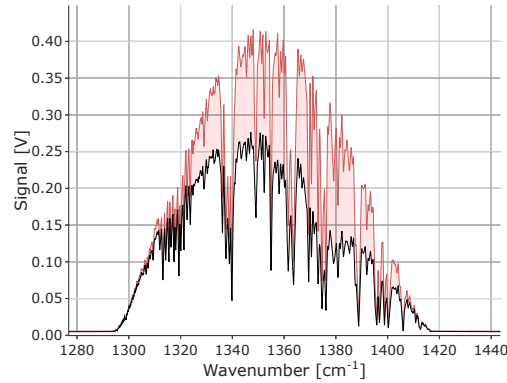
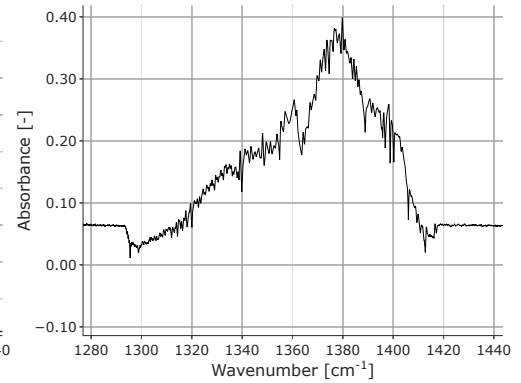
The raw detector signal changes since an absorbing species (SO₂) is present. The absorbance, with respect to the background, is reported under the absorbance column, and represents the absorbance spectrum of SO₂.



Description
Regular

11:41:53 AM

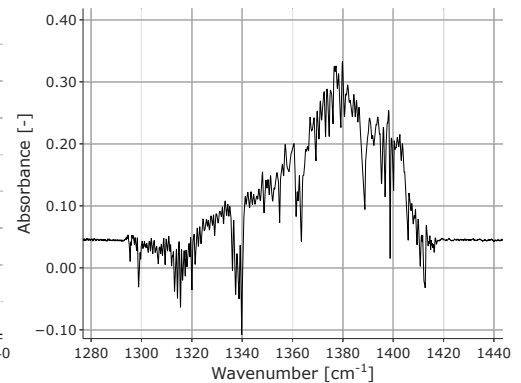
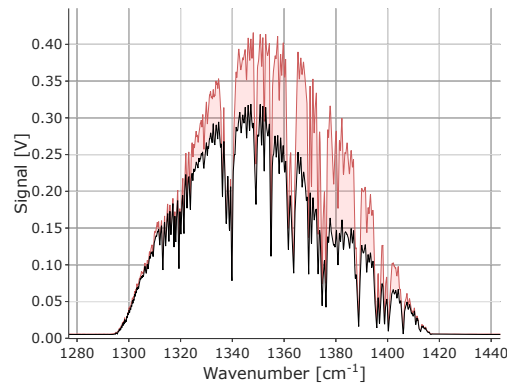
The absorbance spectrum is given by the overlapping SO_3 and SO_2 absorbance. The sum of SO_2 and SO_3 concentrations is approximately equal to the SO_x input parameter for this experiment set at 150 ppm.

Raw detector signal [V]

Absorbance spectrum [-]
*Regular (Controlled Condensation)*

12:05:59

PM

No changes in the inlet gas composition with respect to *Regular* conditions. The pressure inside the measurement cell increases (estimated at less than 2 psi or 0.15 atm increase). The spectrum shows water-like sharp features, similar to a reduction in H_2O concentration.

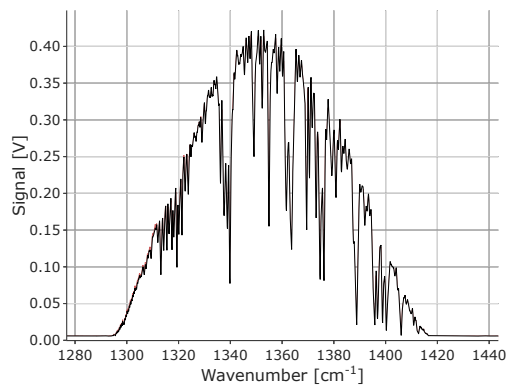
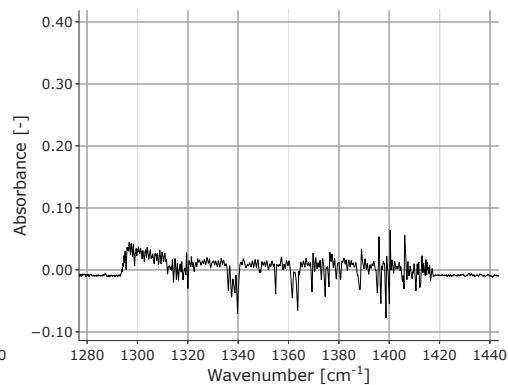


Description

Air

12:23:43 PM

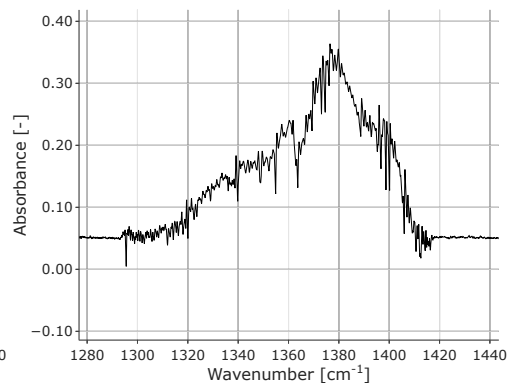
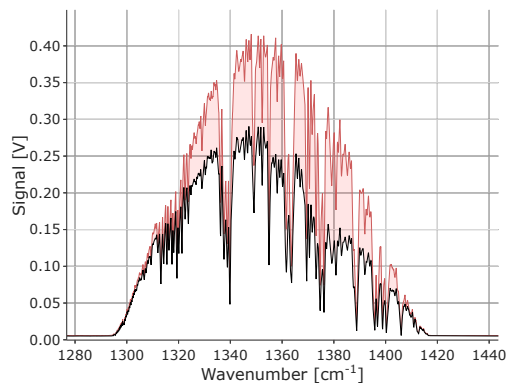
With air in the cell, the absorbance spectrum should be zero along all wavelengths or a background change occurred. It can be related to a temperature change, to window damage, or to a small water vapor concentration change. In this case, it is attributed to a water vapor change.

Raw detector signal [V]**Absorbance spectrum [-]**

Equalized

12:30:50 PM

The absorbance spectrum is given by the overlapping SO₃ and SO₂ absorbance. The SO₂ and SO₃ concentrations are lower than in the *Regular* case because of the added dilution.

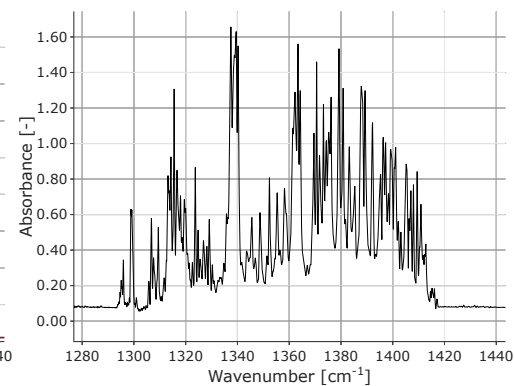
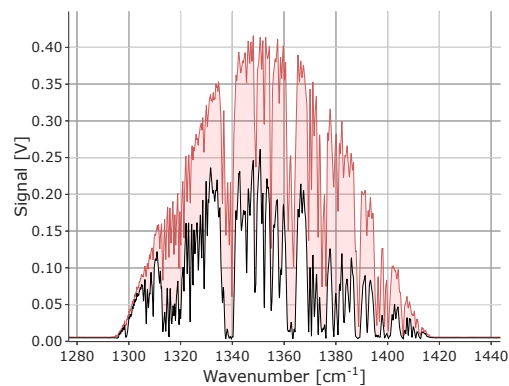


Description**Raw detector signal [V]****Absorbance spectrum [-]**

Water Add (3%)

12:40:42 PM

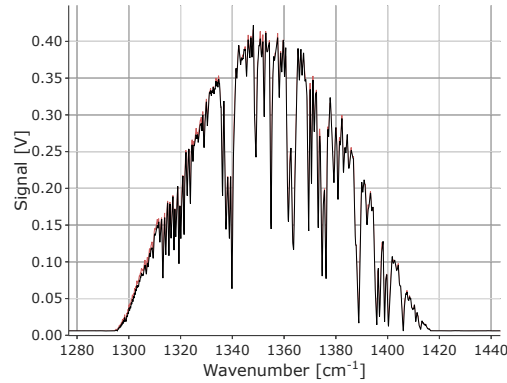
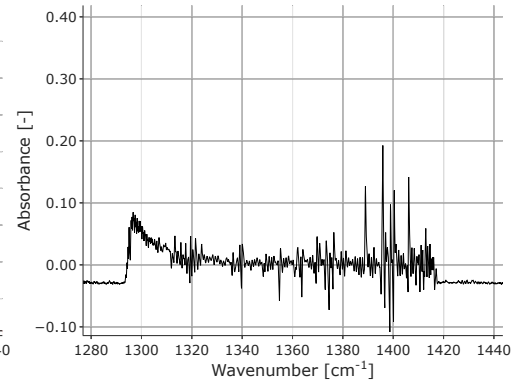
The absorbance spectrum is given by the overlapping SO_3 , SO_2 , and H_2O absorbance. The SO_3 concentration decreases slightly (according to the $\text{SO}_3\text{-H}_2\text{SO}_4$ equilibrium notion, as a small fraction of SO_3 is expected to hydrate into H_2SO_4 at 350C). At 1340, 1360, and 1400 cm^{-1} the water vapor almost saturates the absorbance (with raw detector signal dropping to almost zero). Those regions, when saturated, should be excluded from the data-fitting procedure, as this affects the accuracy or even the feasibility of a measurement since once all the light is absorbed it is not possible to extract any information on the concentration of the absorber. Please note the different absorbance axis scale for this test case with H_2O vapor presence.



Description
Air

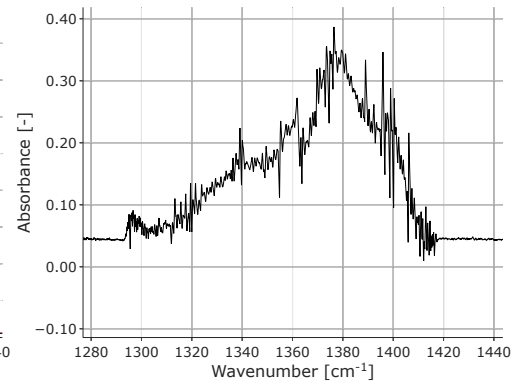
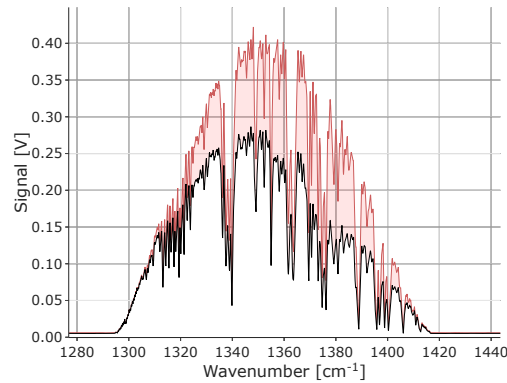
12:49:49 PM

The absorbance spectrum should be zero along all wavelengths. The discrepancy is likely due to trace water vapor presence, as the absorbance spectrum shows very sharp features. It is unclear if a transient temperature change could also have contributed to the change in detector signal.

Raw detector signal [V]**Absorbance spectrum [-]***Equalized*

12:56:49 PM

The absorbance spectrum is given by the overlapping SO₃ and SO₂ absorbance. The SO₂ and SO₃ concentrations are lower than in the *Regular* case because of the added dilution.



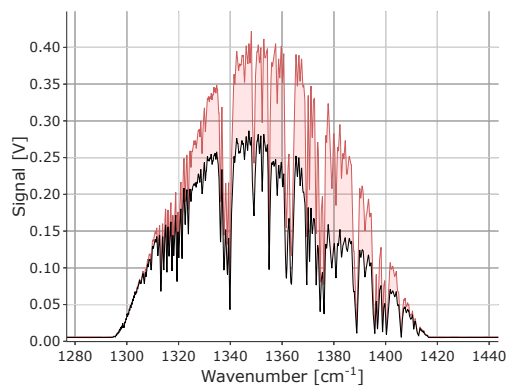
Description

Equalized (with 12:49 PM air background)

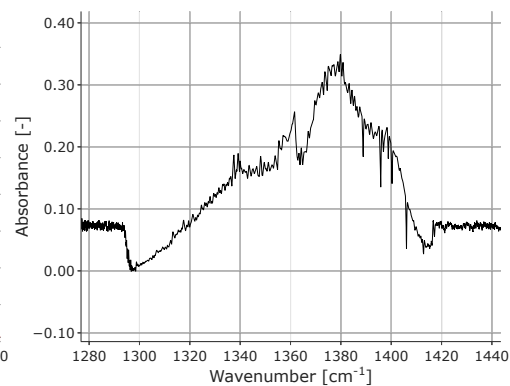
12:56:49 PM

A new background is captured at the last *Air* condition. The raw detector signal doesn't change when compared to the last *Equalized* condition. The absorbance spectrum does, since it is extracted using a new background reference frame.

Raw detector signal [V]



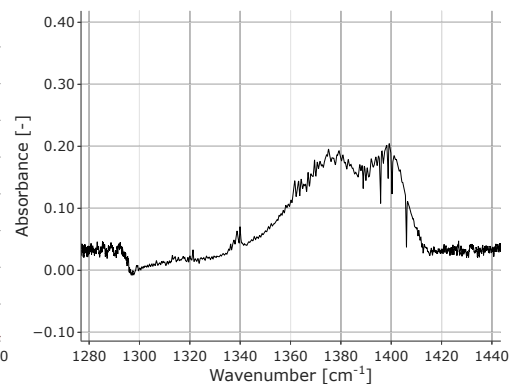
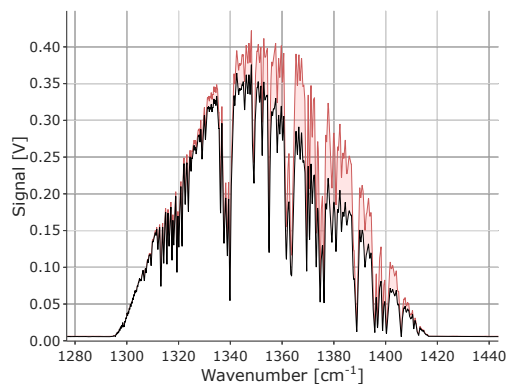
Absorbance spectrum [-]



Equalized Decay

01:09:18 PM

The absorbance spectrum is the one of SO₃ only. It is evaluated using the last updated air background.



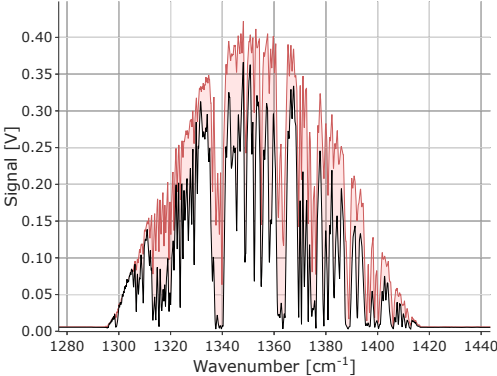
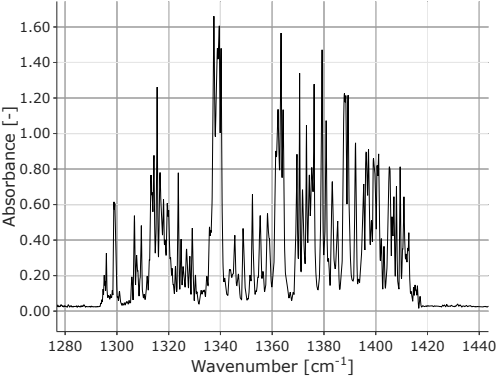
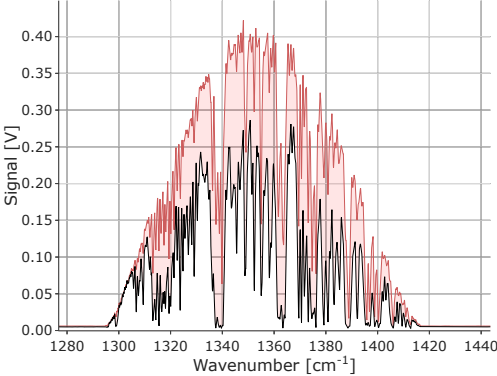
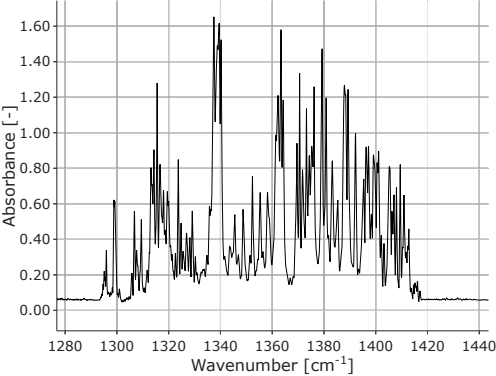
Description	Raw detector signal [V]	Absorbance spectrum [-]
<p data-bbox="212 272 453 305"><i>Water Only (3%)</i></p> <p data-bbox="678 272 852 305">01:23:45 PM</p> <p data-bbox="212 402 852 623">The absorbance spectrum is given by uniquely H₂O vapor absorbance. Please note the different absorbance axis scale for this case with H₂O vapor presence.</p>		
<p data-bbox="212 699 852 732"><i>Water Only (3%) + Bypass 80ppm SO₂</i></p> <p data-bbox="678 764 852 797">01:28:27 PM</p> <p data-bbox="212 894 852 1050">The absorbance spectrum is given by the combined absorbance of H₂O vapor and 80ppm SO₂.</p>		

Table 6.5: Description, raw detector signal, and absorbance for each test condition, for Step 1 ECQCL 7 07/14/2020 $T = 350C$ experiment, represented in temporal order.

6.2.4 Raw data set overview for an ECQCL 8 experiment

The analyzed data set is the Step 1 ECQCL 8 07/14/2020 experiment, with $T = 350C$, $SO_x = 150$ ppm, $\beta = 3\%$. The timeline of the experiment is represented in Figure 6.6, with test conditions labeled at the top of the figure. The timeline plot shows the final concentration data, processed with the fitting algorithm and the appropriate libraries. The libraries will be described later in Section 6.2.6.

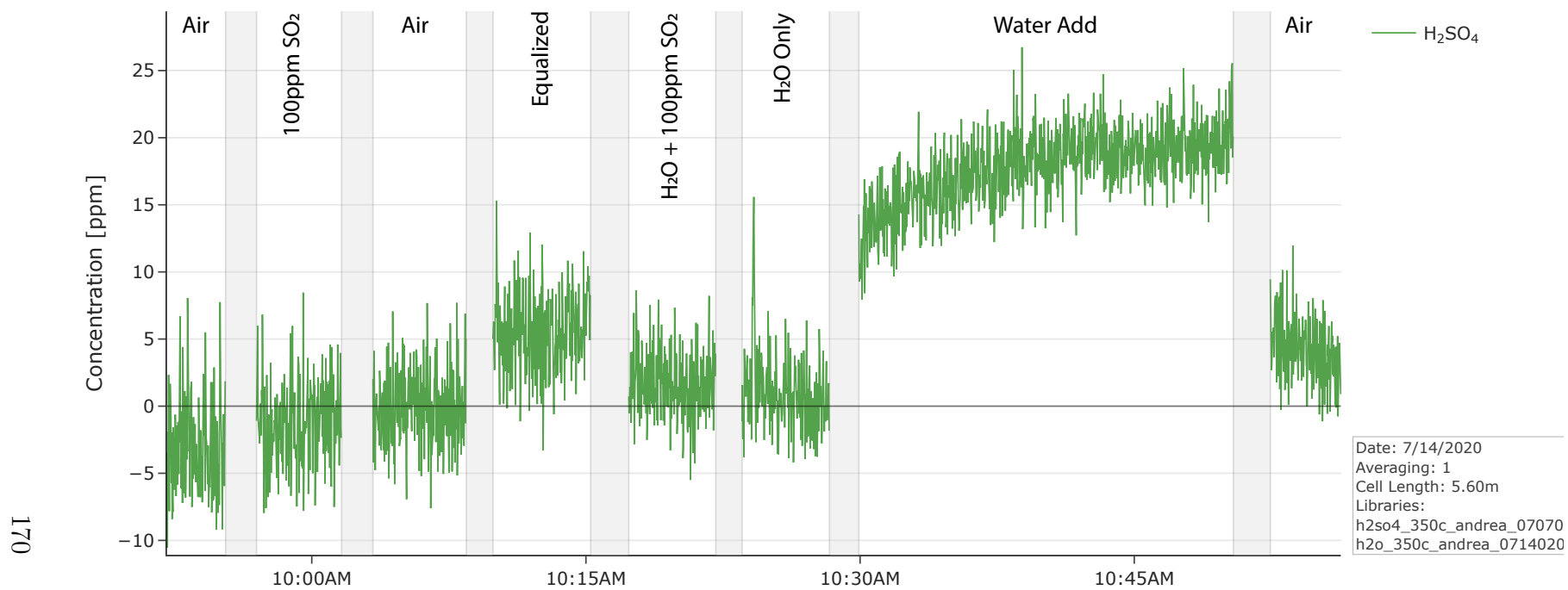


Figure 6.6: H₂SO₄ concentration in the Step 1 ECQCL 8 07/14/2020 $T = 350C$ experiment timeline.

The raw data from the detector (voltage signal V), the absorbance (non-dimensional), along with a description of the test conditions are collected in Table 6.6. The raw detector signal axis range is constant among all the rows. The reference background spectrum I_0 is represented with a red-shaded area in the detector signal column. The absorbance signal range is constant among the rows where water is not added, while all the conditions with water vapor employ a different absorbance scale, since water at high concentration is a dominant absorber species. The scale is consistent among all the water cases.

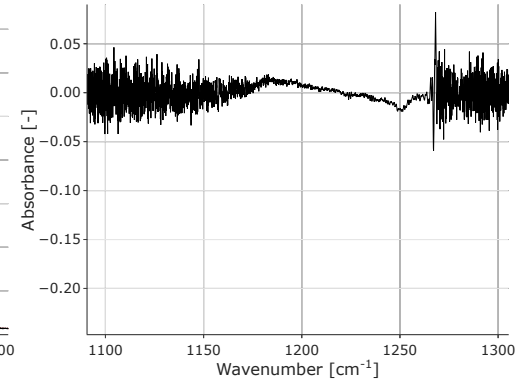
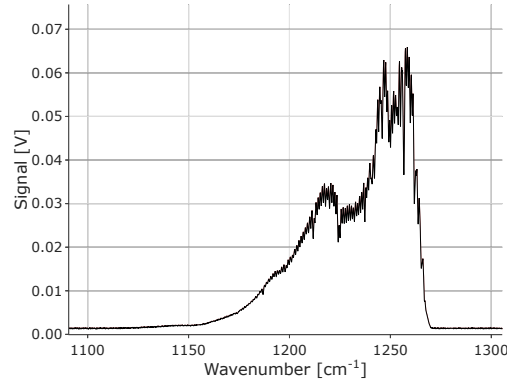
Description

Raw detector signal [V]

Absorbance spectrum [-]

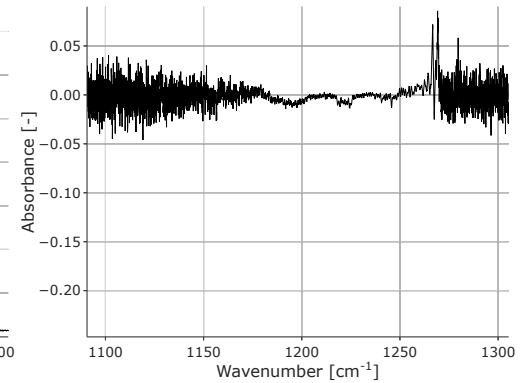
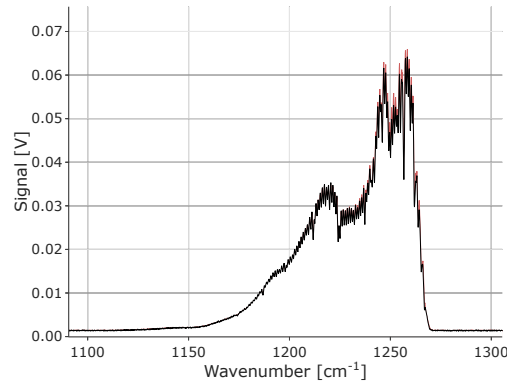
Air 10:03:33 AM

The raw detector signal in this test condition is used as background spectrum to determine the absorbance in the next conditions.



Bypass 100ppm SO₂ 09:59:38 AM

The absorbing species SO₂ is present. However, the spectrum of SO₂ is not clearly noticeable from the absorbance figure. SO₂ has low absorbance in this wavelength region.



Description

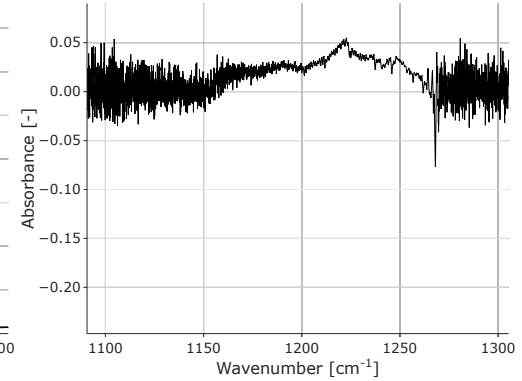
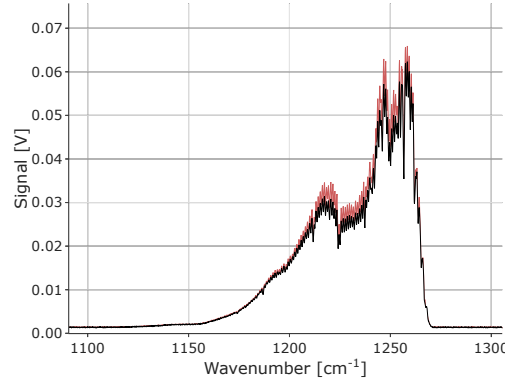
Raw detector signal [V]

Absorbance spectrum [-]

Equalized

10:11:17 AM

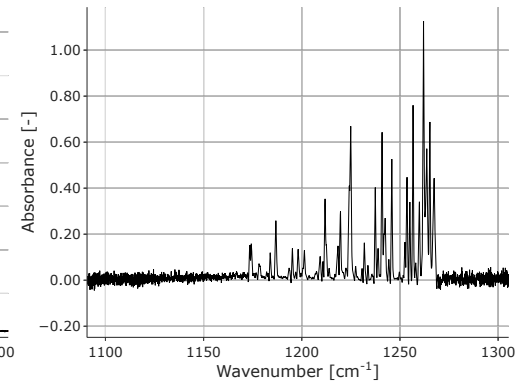
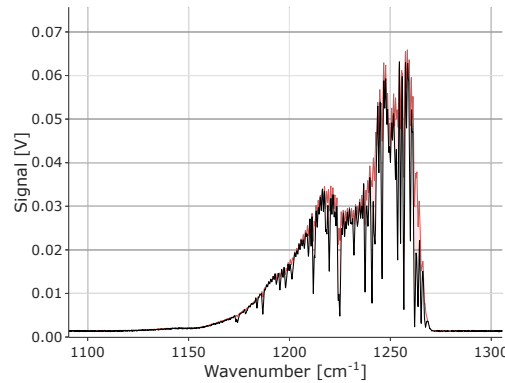
The absorbance spectrum in absence of water should consist in a small fraction of SO₂ only, since SO₃ does not absorb in this regime. The sharp spectral features of H₂O are absent, however, the H₂SO₄ spectrum appears and peaks at around 1220 cm⁻¹.



Water Only (3%) + Bypass 80ppm SO₂

10:17:34 AM

The absorbance spectrum is given by the combined spectrum of H₂O vapor and 80ppm SO₂. Please note the different absorbance axis scale for this case with H₂O vapor presence.

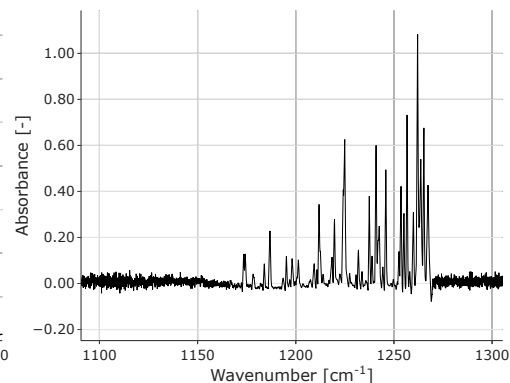
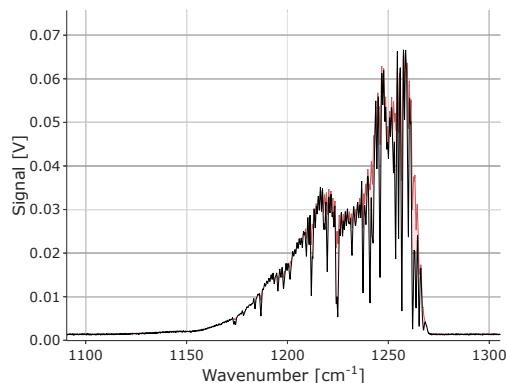


Description
Raw detector signal [V]
Absorbance spectrum [-]

Water Only (3%)

10:26:00 AM

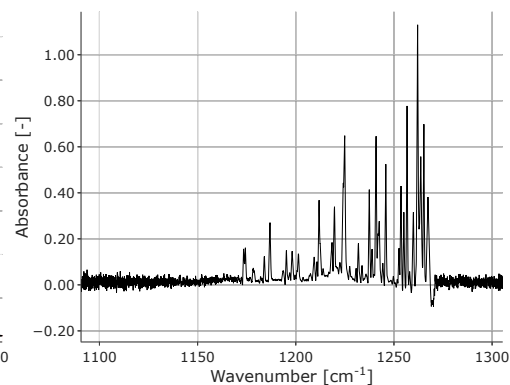
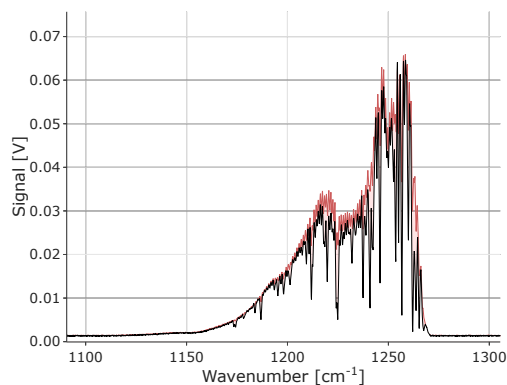
The absorbance spectrum is given by uniquely H₂O vapor absorbance, and it presents very sharp peaks.



Water Add (3%)

10:33:55 AM

The absorbance spectrum is given by the overlapping H₂SO₄, SO₂, and H₂O contributions. SO₃ does not absorb in this regime. According to the SO₃-H₂SO₄ equilibrium, only a small fraction of SO₃ hydrates into H₂SO₄ at 350C. The absorbance of water dominates the spectrum.



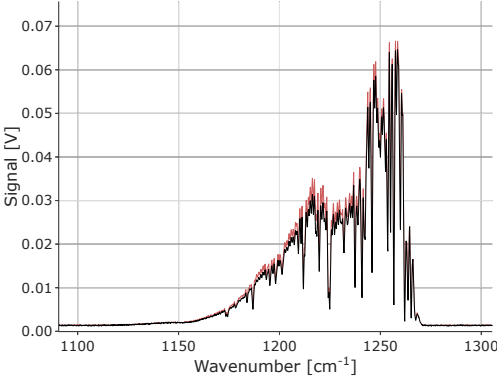
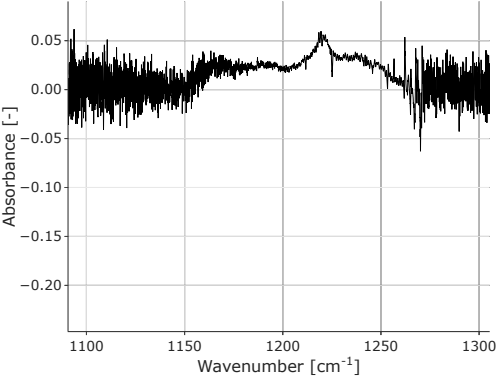
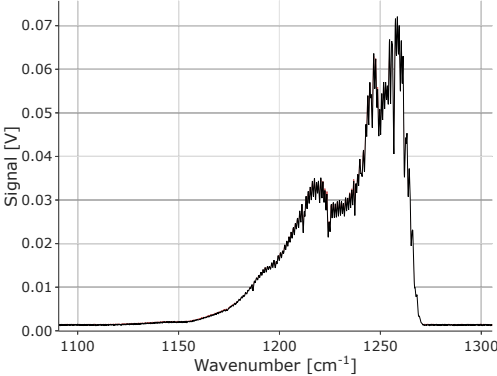
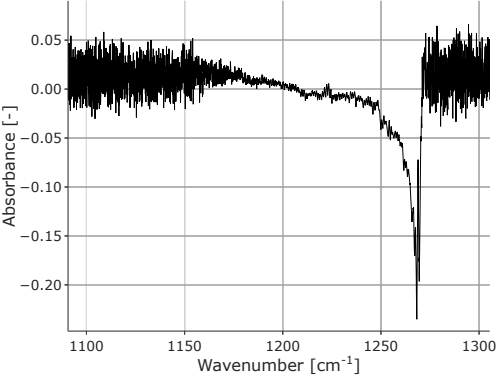
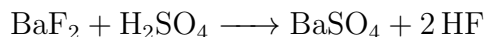
Description	Raw detector signal [V]	Absorbance spectrum [-]
<p data-bbox="212 272 852 305"><i>Water Add (3%)</i> 10:33:55 AM</p> <p data-bbox="212 402 852 813">This condition is identical to <i>Water Add (3%)</i> at 10:33:55 AM but the absorbance is evaluated using <i>Water Only (3%)</i> at 10:26:00 AM as background. This allows to highlight the H_2SO_4 spectrum only. Note that SO_2 also contributes, but the contribution at this concentration is minor or negligible.</p>		
<p data-bbox="212 889 852 922"><i>Air</i> 10:54:50 AM</p> <p data-bbox="212 1019 852 1302">The absorbance spectrum should be zero along all wavelengths. The absorbance region at wavenumber 1250cm^{-1} displays a dip. This behavior is attributed to a drift in the generated laser signal (see Section 6.2.6).</p>		

Table 6.6: Description, raw detector signal, and absorbance for each test condition, for Step 1 ECQCL 8 07/14/2020 $T = 350\text{C}$ experiment, represented in temporal order.

6.2.5 The role of H₂SO₄ damage on optical windows

Sulfuric acid decreases window transmittance by reacting with barium fluoride, as well as calcium fluoride, and forming a white opaque layer on the window surface. The hypothesized mechanism for the reaction, for BaF₂, is:



Experimentally, the layer does not create many issues at around 7 μm (where ECQCL 7 operates), but it is problematic at 8 μm (where ECQCL 8 operates). Operations at high temperature (350C) and low water vapor minimize the H₂SO₄ concentration in the cell, and theoretically and empirically lead to slower performance degradation. For the experimental setup of this work, H₂SO₄ and SO₂ measurements at 8 μm 300C and 250C are possible only in time frames on the order of minutes before the window performance degrades significantly.

The damage occurs rapidly at the onset of H₂SO₄ formation, while the degradation slows down as the windows are damaged. Used windows can extend the measurement time, albeit it is not ideal to operate in those conditions since the sensitivity and the range of measurement will decrease. The change in transmissivity is not uniform but has a wavelength-dependent behavior. The background signal, i.e., the raw signal at the detector when only air is flowing at the target temperature, is effectively changing as the windows damage significantly challenging the fitting algorithm.

The extent of window damage is shown in Table 6.7, with the data set from Step 2 ECQCL 8 08/11/2020 at 300C. The absorbance spectra and raw detector signals in Table 6.7 are all collected in the same *Step 2, Water Add* test condition, with a concentration of 8% H₂O vapor, and expected concentrations of around 530ppm of SO₂, and 40ppm of H₂SO₄. The difference in detected signal compared to the first time frame captured at 11:27:23AM is highlighted with a red-shaded area.

The absorbance spectrum is calculated with respect to the background condition of *Water*

Only (8%), to extract the features of H_2SO_4 and SO_2 and to better show the extent of window damage.

Time	Raw detector signal [V]	Absorbance Spectrum [-]
11:27:23 AM		
11:29:07 AM		
11:30:51 AM		
11:32:35 AM		

Table 6.7: Time, raw detector signal, and absorbance in *Step 2, Water Add* test conditions with respect to *Water Only (8%)* background condition for Step 2 ECQCL 8 08/11/2020 $T = 300C$ test.

In the first two rows, 11:27 AM and 11:29 AM, SO_2 is clearly visible, showing a double peak centered around 1130 and 1170 cm^{-1} respectively, and sulfuric acid is visible as well with a peak centered at 1220 cm^{-1} . As time goes on, raw detector signal frames show a decrease in amplitude even if the test conditions has not changed, especially in the region from 1100 to 1250 cm^{-1} , manifesting the effect of window damage. The raw detector signal change impacts the absorbance spectrum, which increases significantly. The effect is the disappearance of the H_2SO_4 features, and an apparent increase of SO_2 concentration. This effect is entirely due to window damage.

If two different *Air* conditions are compared, one occurring before H_2SO_4 onset, and the other one occurring after H_2SO_4 has been present in the measurement cell, it is possible to determine the spectral features of the window damage. The resulting spectrum is represented in Figure 6.7.

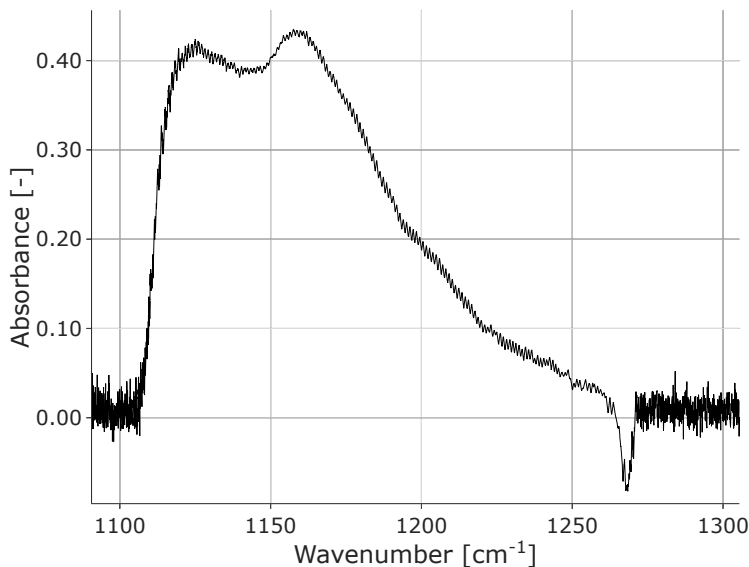


Figure 6.7: Spectral absorbance of BaSO_4 evaluated by comparison of two *Air* conditions, before and after H_2SO_4 damage respectively.

This spectrum can be compared with the spectrum of BaSO_4 from the literature [113–115]. The result is represented in Figure 6.8. The BaSO_4 spectrum from the different sources are not scaled, the spectra for all the literature sources are captured at room temperature, and the UCI ECQCL8 spectrum is extracted at 300C. Therefore the different sources should

not be compared in terms of magnitude. However, Figure 6.8 confirms the formation of a BaSO₄ film on the BaF₂ windows, showing two peaks that are typical of the symmetric stretching vibration of SO₄²⁻ group [113]. As visible from the figure, the film effect in the ECQCL7 region is less important and mostly uniform across that region. Hence, there is a uniform decrease in transmissivity of the window after the formation of BaSO₄.

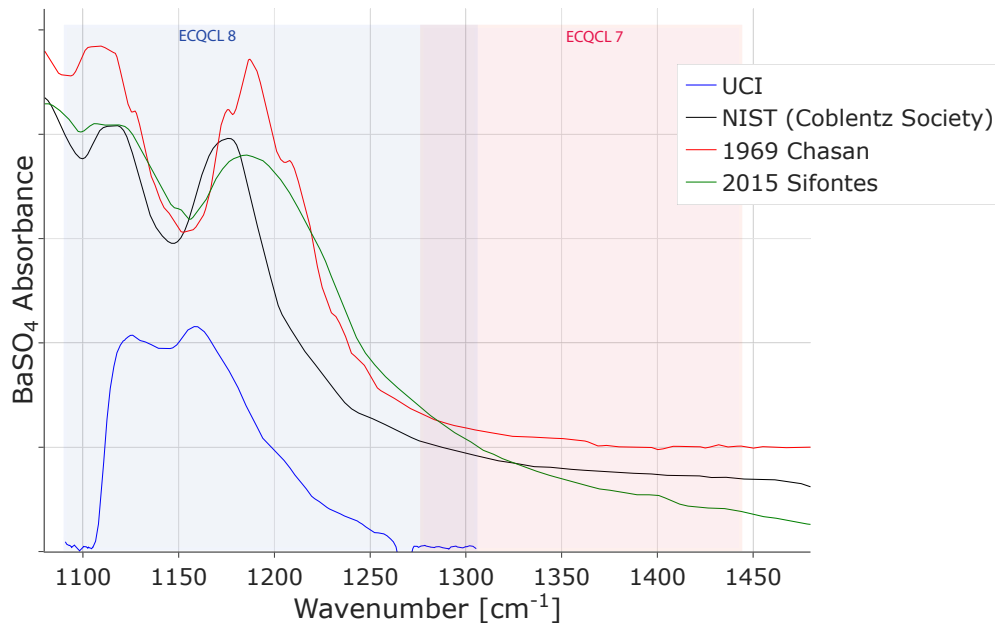
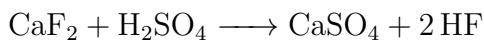


Figure 6.8: Absorbance spectrum of BaSO₄ from different sources in comparison to the UCI ECQCL 8 measured signal through the damaged windows.

It is expected that CaF₂ windows would exhibit the same problems, as they react with acid according to the reaction:



The absorbance of CaSO₄ is represented in Figure 6.9, from [115]. Calcium sulfate exhibits the same behavior as barium sulfate. Since CaF₂ has lower transmissivity in the 8 μm region compared to BaF₂, ECQCL 8 is used uniquely with BaF₂ windows, and the problem of CaSO₄ formation does not apply to ECQCL 8. For ECQCL7, the window degradation process is fairly uniform across all wavelengths, and it will result in a broadband signal

decrease.

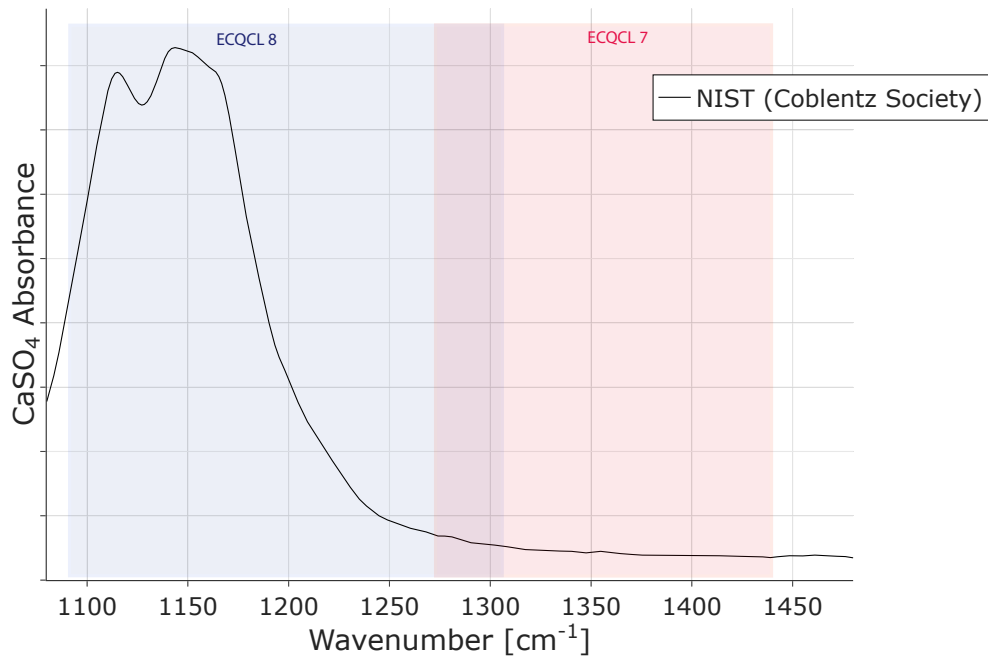


Figure 6.9: Absorbance spectrum of CaSO₄ from NIST [115]

6.2.6 Spectral libraries

The spectral libraries are acquired for three different temperatures at 250C, 300C, and 350C. The ideal scenario for a spectral library is the presence of a known amount of one absorber species only in a clean air background. The procedure to define a spectral library consists of three steps:

1. *Definition of a background spectrum*

A flow consisting only of air is present in the cell, at temperature T . The raw detector signal I_0 in this condition is saved as a reference spectrum.

2. *Capture of the absorbance spectrum*

A known amount of one absorber species is added to the cell. The raw detector signal I in this condition is captured. The absorbance spectrum $A = -\log_{10}(I/I_0)$ now results from the absorbing species only. For a more reliable result, the absorbance

spectrum is averaged along multiple temporal readings (with constant concentration of the absorber species).

3. *Definition of a spectral library*

According to Beer-Lambert's Law, with the Pacific Northwest National Library (PNNL) spectral database notation:

$$A = -\log_{10}(I/I_0)$$

and also:

$$A = \epsilon c L$$

where L is the path length in meters, c is the absorbant concentration in ppm (volume-based), and ϵ is absorption coefficient in $(ppm \cdot m)^{-1}$. With known path length and absorber concentration, it is possible to evaluate the absorption coefficient ϵ for the absorber species, as a function of wavenumber and at the temperature T . The spectral library at T consists of the values of ϵ for every wavenumber. The absorption coefficient will hence be equivalent to the decadic absorbance (defined as $A = -\log_{10}(I/I_0)$) of one ppmv of absorber species in a 1m cell.

ECQCL7, Sulfur dioxide, SO₂

Sulfur dioxide can be injected in the cell directly through the Bypass line (see point 3 in Figure 3.6), with a SO₂/N₂ mixture from a cylinder tank diluted with air. The uncertainty on this flow is related to the operation of two flow controllers (one for the air flow, one for the SO₂ mixture) and the concentration of SO₂ in the gas cylinder, as explained in Section 3.5.

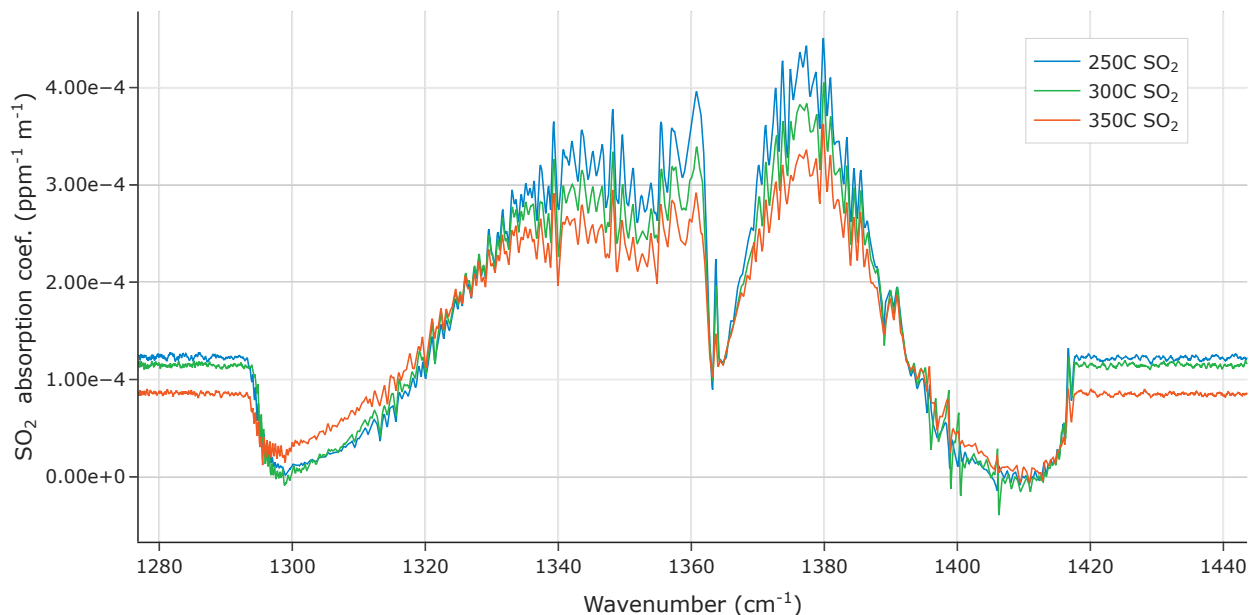


Figure 6.10: Library spectrum for SO_2 at different temperatures.

ECQCL7, Sulfur trioxide, SO_3

Sulfur trioxide is generated through catalysis of sulfur dioxide, so in principle it is not possible to generate a flow where the only absorber is SO_3 unless the catalyst conversion rate reaches 100%. However, due to the catalyst mechanism that involves triox desorption, it is possible to generate a SO_3 -only flow (in air) by flowing air through a conditioned catalyst without any SO_2 feed (*Equalized Decay* test condition). Since no SO_2 is provided, the outlet gas will not present any SO_2 . At the same time, SO_3 is desorbed and flows to the measurement cell. While this process implies a depletion of the catalyst (with SO_3 progressively diminishing), it has not been observed experimentally under these experimental conditions, with SO_3 concentration staying constant for long periods of time (>20 minutes). The duration of this effect is likely to depend on the amount of catalyst installed and the gas flow rate used.

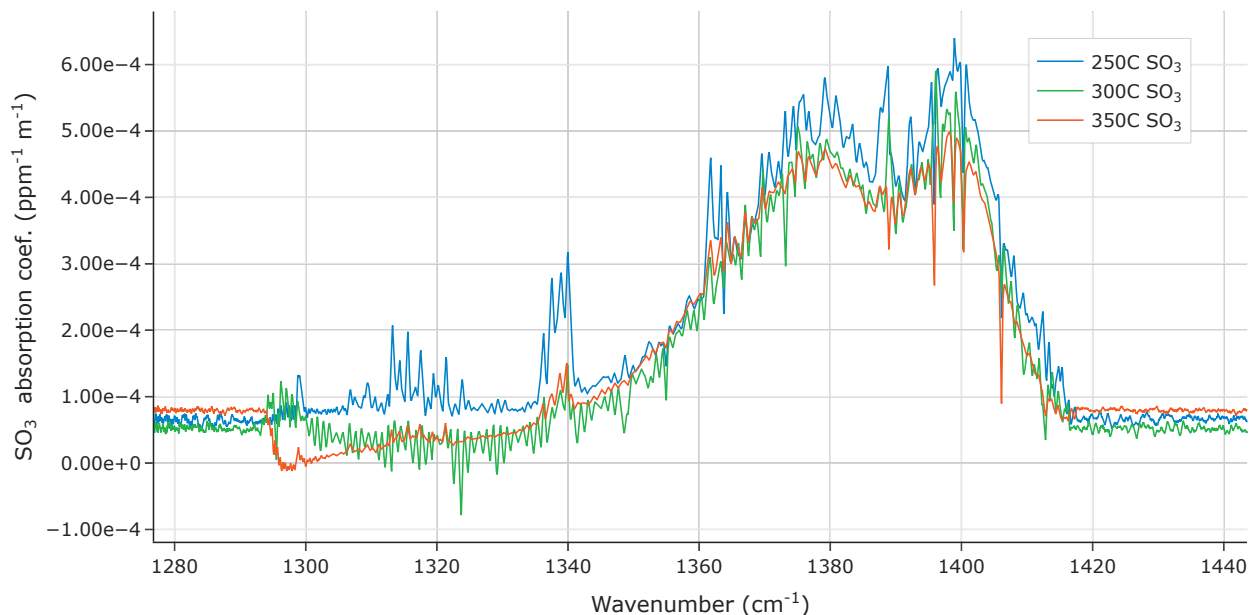


Figure 6.11: Library spectrum for SO_2 at different temperatures for ECQCL 7.

Some water-related features can be observed on the SO_3 spectrum, most notably in the 250C case (see regions at 1340 and 1320 cm^{-1}), even if the feed flow provided by the gas cylinder was dry. This highlights that water is always present (maybe only at trace levels) and it is detrimental to an accurate measurement. While this is not optimal, it can be compensated for by using an appropriate water library together with the SO_3 library when fitting the experimental data.

ECQCL7, Water vapor, H_2O

The water vapor library is generated by activating the *Water Only* test condition.

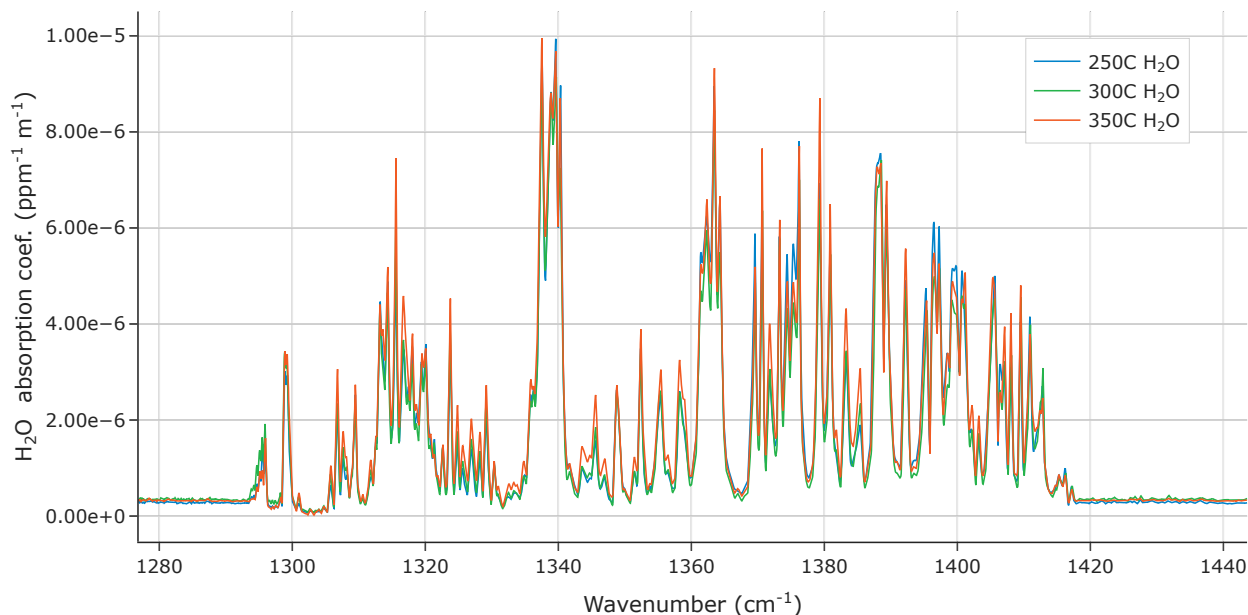
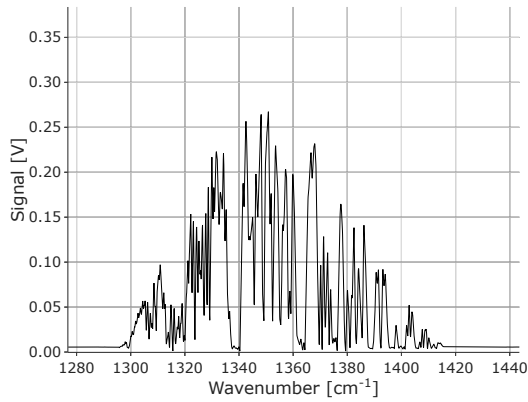


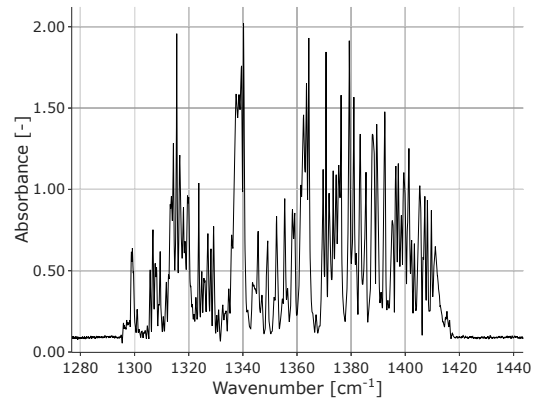
Figure 6.12: Library spectrum for H_2O at different temperatures for ECQCL 7.

Water vapor is a weaker absorber than SO_2 and SO_3 , however it is usually present in much higher concentration so it can dominate the overall absorbance spectrum. When large amounts of water vapor are present, such as a concentration of 8%, water absorbance can be so strong that for some wavelengths the laser signal barely reaches the detector (an effect referred to as saturation). The saturation is noticeable from Figure 6.13, at 1340, 1360, and 1400 cm^{-1} . As mentioned earlier, operating under these conditions implies that the absorbance spectrum in those wavelengths is not be reliable or sensitive enough, and those regions should be excluded from the spectral fit. Moreover, libraries captured under these conditions are unreliable because spectral line width and amplitude are affected by the saturation. These problems get worse with window degradation. The water libraries presented in figure 6.12 are captured at 3% water vapor concentrations, where spectral structures are still well defined and saturation is not prevalent.

For the reasons above, the concentration of water estimated by these libraries is often not accurate, as factors that are not accounted for in a Beer-Lambert's description come into play. However, the measurement of SO_2 and SO_3 in the presence of water vapor is still

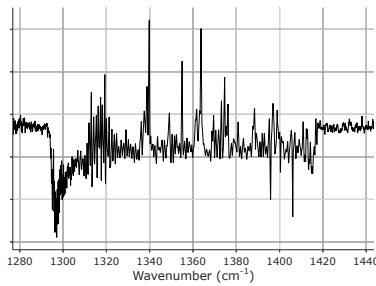


(a) Raw detector signal.

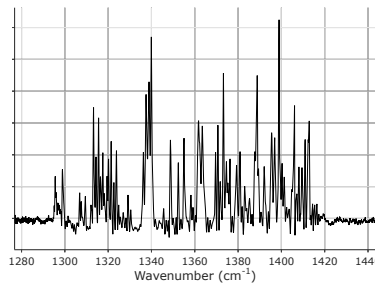


(b) Water vapor absorbance spectrum.

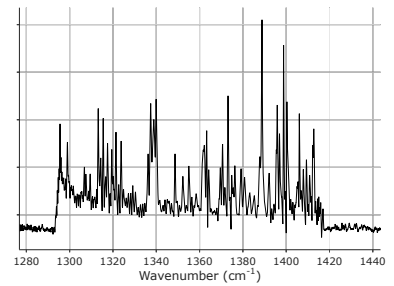
Figure 6.13: Saturated detector and correspondent water absorbance spectrum.



(a) 250C.



(b) 300C.



(c) 350C.

Figure 6.14: Water libraries for small concentrations/oscillations, at different temperatures for ECQCL 7.

possible when the water library is used in conjunction with those of SO_2 and SO_3 .

To further improve the quality of the absorbance fit, three additional water libraries are used to account for small water vapor oscillations. These libraries are captured with both the reference signal I_0 and the library signal I captured in *Air* test conditions, where a weak water presence was the only difference between the two. The captured low-water concentrations libraries are not quantitative, and they are used to simply increase the accuracy of the fit for SO_2 and SO_3 by removing unaccounted for water oscillations.

ECQCL8, Water vapor, H_2O

Also for ECQCL8, the water vapor absorbance is weaker than the one of H_2SO_4 and SO_2 . The library spectrum for H_2O is captured in *Water Only* test conditions. Since water is a

weaker absorber in this region, a library for smaller water concentration is not needed, as they do not significantly affect the absorbance spectrum.

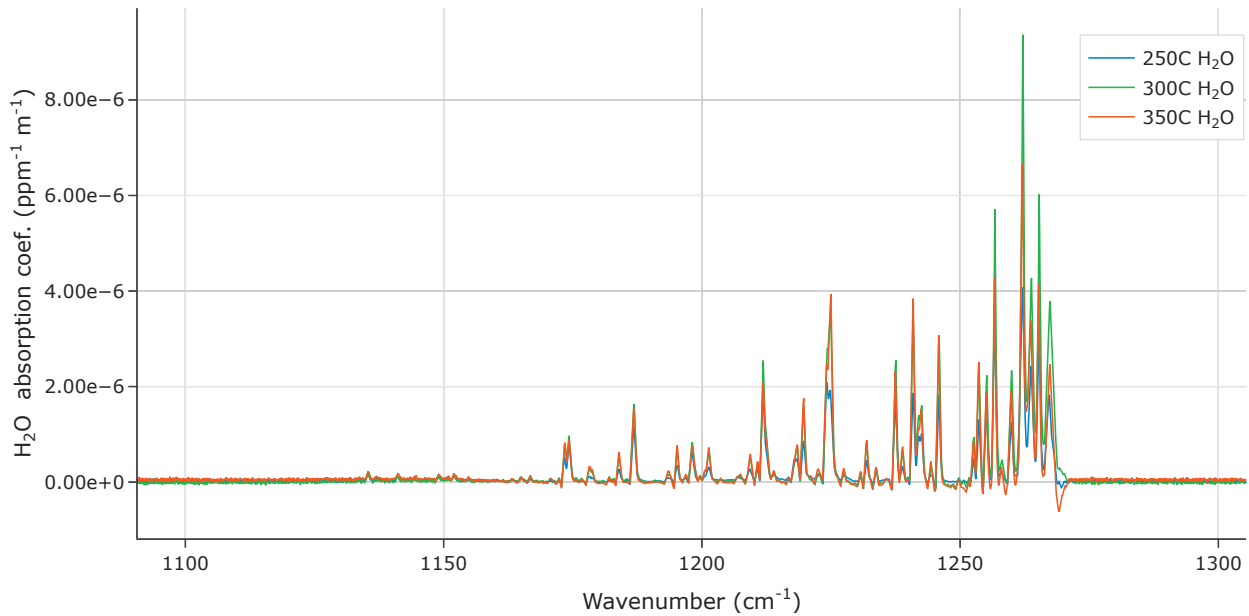


Figure 6.15: Library spectrum for H₂O at different temperatures for ECQCL 8.

ECQCL8, Sulfur dioxide, SO₂

The library spectrum for SO₂ is captured in *Bypass Only* conditions, like for ECQCL 7. The absorbance for SO₂ is about one order of magnitude larger than the one of H₂O. However, in target conditions the concentration of H₂O can be as much as 30 times larger than the one of SO₂ at 8% water vapor and 2500 ppm respectively. In general, spectral fitting of SO₂ did not perform well at low SO₂ concentrations. It is unclear whether the issues are related to the weak absorbance of SO₂, to over-fitting of the measurement noise, to the influence of water features, or to a combination of these.

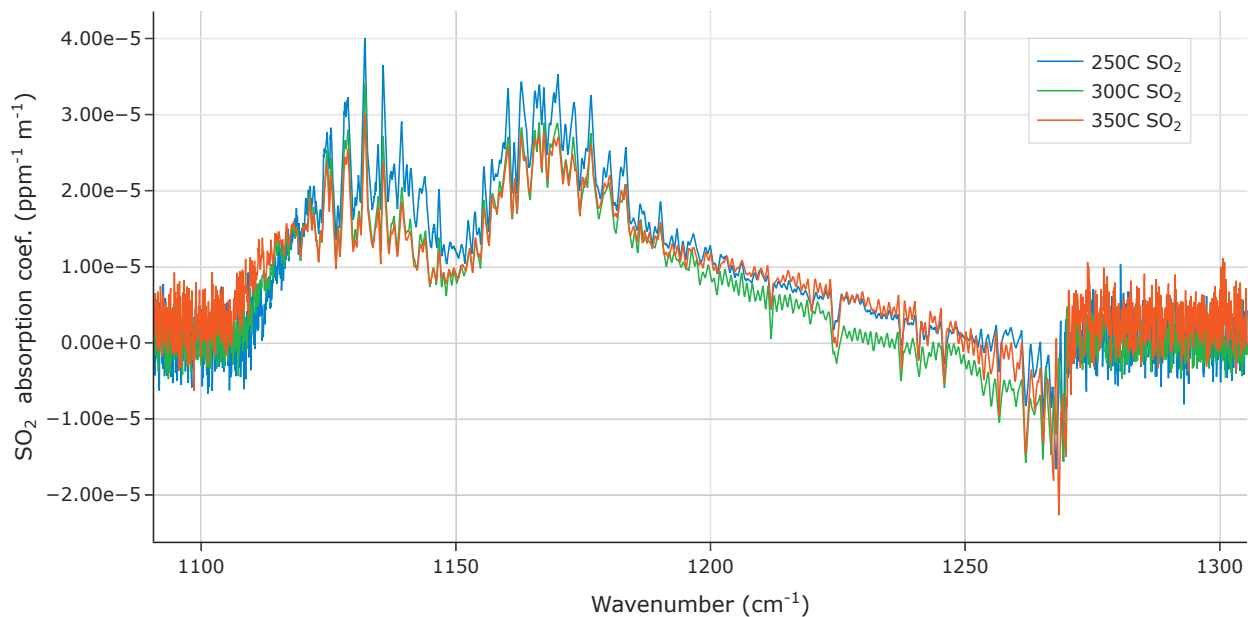


Figure 6.16: Library spectrum for SO_2 at different temperatures for ECQCL 8.

ECQCL8, Barium sulfate, BaSO_4

As briefly described earlier, barium sulfate forms when the windows material, BaF_2 , reacts with sulfuric acid to form a BaSO_4 solid phase. Barium sulfate appears as a white, cloudy, and opaque layer on the window surface exposed to the simulated flue-gas flow. The reaction can manifest on the timescale of minutes under the experimental conditions, and BaSO_4 is highly absorbent in the ECQCL 8 wavelength regime. When the BaSO_4 libraries are used in the fit, they effectively reduce the impact of windows damage and offer a more reliable H_2SO_4 concentration measurement. However, as the BaSO_4 layer progressively builds up on the window surface, the light reaching the detector significantly decreases, the signal-to-noise ratio decreases, and the measurement sensitivity is reduced. The workaround of BaSO_4 fitting is valid only for timescales in the order of tens of minutes. Furthermore, due to the reduced sensitivity as the window degrades, the laser can fail to resolve the two “peaks” features of SO_2 and BaSO_4 and the absorbance spectrum appear distorted forming a single “peak” in the 1150cm^{-1} region. When operating under these conditions the measurement is not reliable, since the accuracy of the fit is poor.

The library spectra for BaSO_4 at different temperatures is shown in Figure 6.17. It is possible in principle to scale the spectral libraries to quantify the extent of window damage in terms of thickness of the BaSO_4 layer but the main goal for these libraries is only to filter out the BaSO_4 contribution to a given absorbance spectrum. The three libraries have been normalized in Figure 6.17. As previously stated, the libraries are not quantitative, and they can not be compared to each other in terms of magnitude, but only in terms of shape.

The libraries are captured by acquiring the detector signal I_0 in *Air* test condition. After sulfuric acid has been present in the cell (in a *Water Add* test condition), the test condition *Air* is repeated, and the detector signal I is captured. The only difference between the two *Air* test conditions is hence the presence of a BaSO_4 absorbing layer on the windows surface.

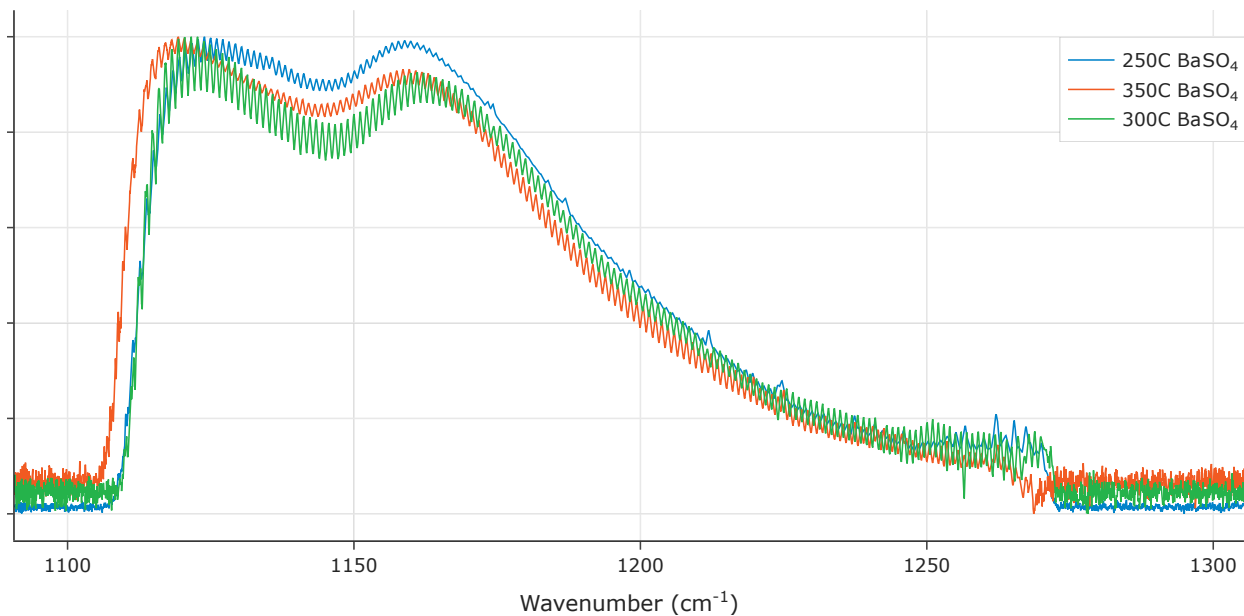


Figure 6.17: Library spectrum for BaSO_4 at different temperatures for ECQCL 8

ECQCL8, Sulfuric acid, H_2SO_4

The definition of sulfuric acid libraries at different temperatures is complicated by several factors:

1. sulfuric acid concentration at high temperatures is significantly reduced due to the chemical equilibrium shifting toward SO_3

2. the presence of H_2SO_4 in the cell necessarily implies the formation of a BaSO_4 layer on the windows (window damage), so the absorbance spectrum will progressively degrade in time. This is especially true for the 250C case, where the H_2SO_4 concentrations are the highest (due to the chemical equilibrium shift)
3. sulfuric acid is present only when water vapor is present, and water vapor absorbs strongly due to its high concentration levels
4. the concentration of sulfuric acid in the cell is not known with certainty at high temperature, where H_2SO_4 and SO_3 coexist
5. catalyst transient ramp-up times mean the H_2SO_4 concentration will increase in time to reach its asymptotic value, but it takes up to five minutes to reach the steady state

The H_2SO_4 libraries are captured by acquiring the background signal (detector signal I_0) in *Water Only* test conditions. *Water Add* conditions are activated immediately following *Water Only* conditions, and the detector signal I is captured. In this way, the water contribution is effectively excluded (even if small oscillations in the water vapor concentration can still affect the recorded libraries). The detector signal I does not consist of a single temporal measurement but it is averaged over multiple temporal readings. The averaging time is a compromise between obtaining a higher quality spectrum by increasing the sampling time to exclude transient phenomena and decreasing sampling time so that the contribution of BaSO_4 formation will be limited. It was empirically found that windows that have already experienced partial reaction to form BaSO_4 , hence with only fair transmission performance, will degrade at a relatively slower pace with respect to brand new windows. Using this advantage, it is possible to delay the acquisition of the detector signal I for some minutes so that H_2SO_4 concentration levels are at steady-state and uniform among all the captured time frames.

The 250C case is the most demanding in terms of window damage, but it offers the significant advantage of a fairly well known H_2SO_4 concentration. In fact, at 250C and 3% water

vapor, the equilibrium steers towards the almost complete formation of H_2SO_4 . Note that from equilibrium, only 8.9% of $\text{SO}_3 + \text{H}_2\text{SO}_4$ will be in the form of SO_3 . Controlled condensation measurement are taken as a reference, providing the $\text{H}_2\text{SO}_4 + \text{SO}_3$ concentration in the measurement cell. The exact H_2SO_4 concentration, needed for the definition of the library, is then calculated with the assumption of chemical equilibrium with SO_3 . Since for the 250C case only a small part of the $\text{H}_2\text{SO}_4 + \text{SO}_3$ will be in the SO_3 form, the assumption will lead to the smallest estimation error for the real H_2SO_4 concentration in the cell with respect to the cases at higher temperatures. The 250C case also offers the strongest H_2SO_4 signal (both due to concentration and absorption coefficients), hence it will be the cleanest H_2SO_4 spectrum in the library, since its strong absorbance can mask the effect of other absorbers.

The procedure to capture the experimental H_2SO_4 spectrum is repeated for the remaining temperatures. The libraries at 300C and 350C present significantly more noise, as they are characterized by lower H_2SO_4 concentrations, smaller absorption coefficients, and are hence more susceptible to water fluctuations, which is visible at around 1170 cm^{-1} of Figure 6.18 as an example, and measurement noise. The measurement at 300C presents the most important water disturbances among the three library cases, and the absorption coefficients do not align as expected with the other two cases, with the absorption coefficients being the lowest for the 300C case. This is not expected and could not be fully explained.

It is important to notice that all the libraries definitions had to rely on the discussed notion of chemical equilibrium, since the SO_3 concentration could not be established during the *Water Add* test conditions as the two ECQCL lasers could not be operated simultaneously. That is, the concentration of SO_3 is presumed to be that in equilibrium with the measured H_2SO_4 at the test temperature. The combination of these two then provides the total convertible $\text{SO}_3/\text{H}_2\text{SO}_4$ in the experiment, that can be evaluated with the measurement from EPA Method 8A.

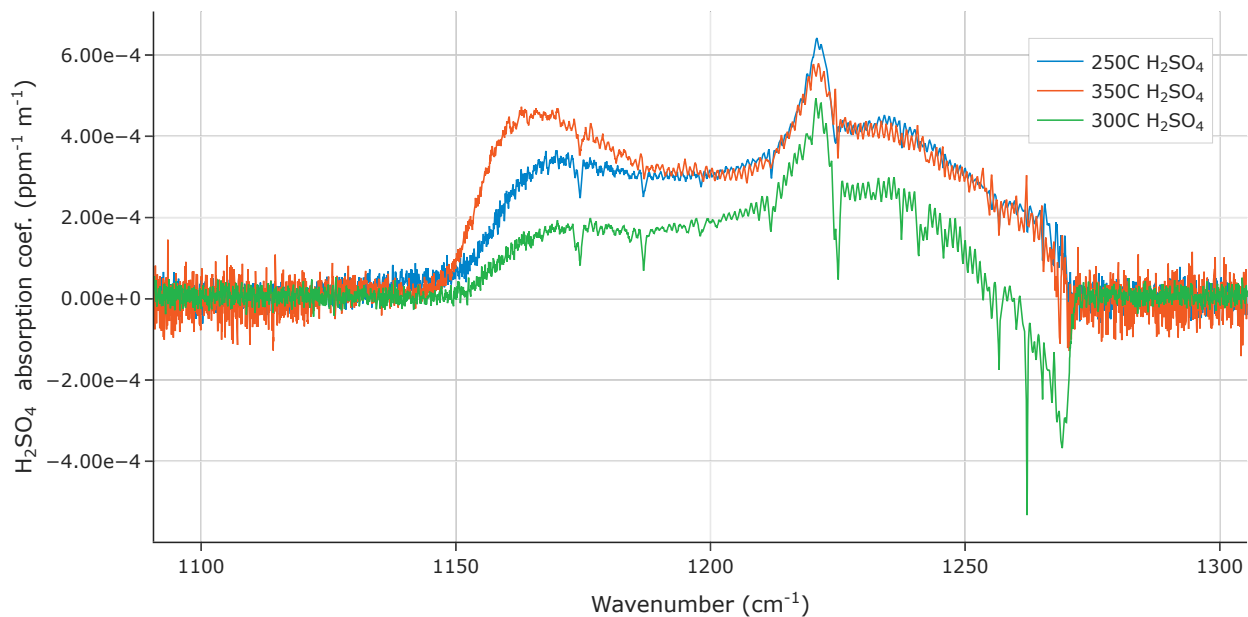


Figure 6.18: Library spectrum for H_2SO_4 at different temperatures for ECQCL 8.

ECQCL8, Laser drift

The ECQCL 8 exhibited a laser signal drift in time, independent from the gas present in the cell. The same detector is used for ECQCL7 and ECQCL8, so the effect is attributed to an instability of the laser itself. Two different libraries are used for 250C and 350C; the 250C library is used also in the 300C cases. The origin of the signal drift is unclear and requires further work.

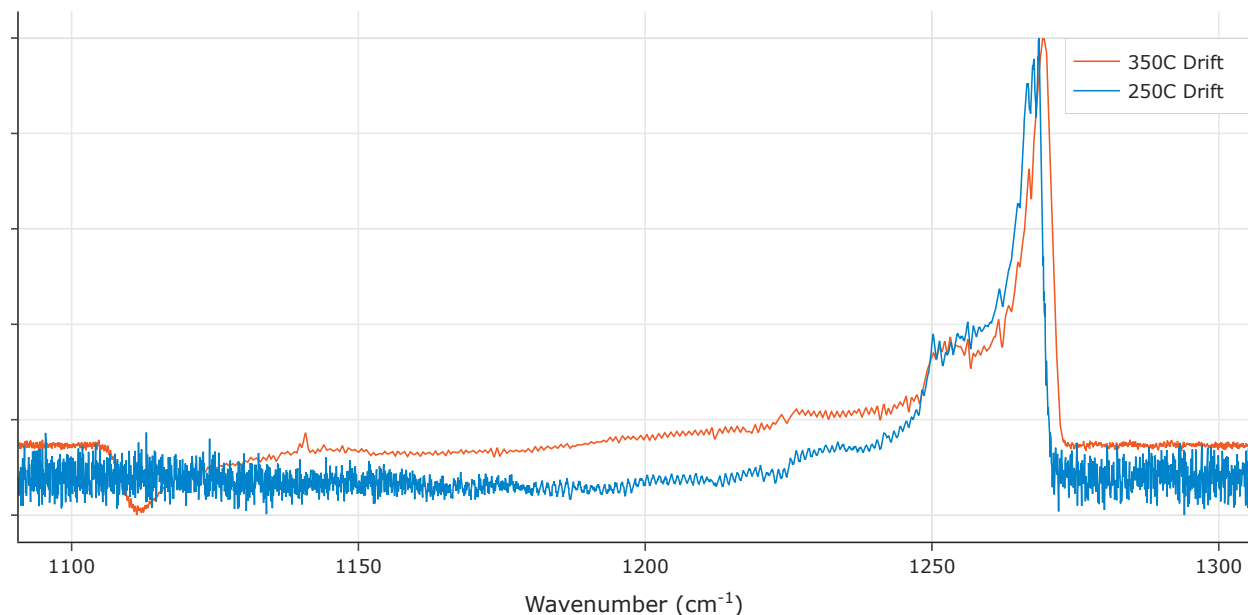


Figure 6.19: Library spectrum to correct for laser drift at different temperatures for ECQCL 8

The two libraries have been normalized to be represented in Figure 6.19. The libraries are not quantitative, and they are used only to compensate for the presence of the drift in the absorbance data.

6.2.7 Ion chromatography measurement uncertainty

In order to have any confidence in the absolute optical absorption measurement of these sulfur species, it is important to compare the laser-based measurement results with an industry standard method currently employed for monitoring the same species as the target for the ECQCL system. The EPA Method 8A is currently the industry standard for the measurement of SO_2 and $\text{SO}_3/\text{H}_2\text{SO}_4$ in flue-gas. The aqueous samples from the condensation coil and impingers are analyzed for sulfur content, through titration or ion chromatography techniques, and the concentration of SO_2 and $\text{SO}_3/\text{H}_2\text{SO}_4$ in flue-gas is estimated.

In this work, the aqueous samples collected with EPA Method 8A are analyzed for their sulfate ion content with ion chromatography at the UCI Mass Spectrometry Facility, with

a Metrohm 940 Professional IC Vario (Metrosep A Supp 5 - 150/4.0 column and carbonate eluent). Before the measurements, six sulfate solutions as standards with different concentrations, 30, 60, 120, 240, and 480 mg/L, are prepared and analyzed to define a calibration curve for sulfate ion concentrations. The initial source of liquid H_2SO_4 is a Fisher Scientific 0.01N H_2SO_4 . The 0.01N source contains 0.005 mol/L of H_2SO_4 in water, and the molecular weight for sulfate ion 96.06g/mol, resulting in a concentration of 480 mg/L. To verify the consistency of the measurements, five samples, 0, 60, 120, 240, and 480 mg/L, are prepared independently from the standards. Each sample is stirred and split in identical HDPE vials, one vial to be analyzed at the UCI facility and one vial provided to an external testing company. The testing samples are themselves subject to a concentration uncertainty due to the sample preparation.

The nominal, UCI, and external sulfate concentration estimation are collected in Table 6.8. UCI results appear to overestimate the expected sulfate concentration, but the discrepancy is within 10% of the expected value. On the other hand, the results from the external testing company are in general closer to the expected values, with the notable exception of the sample UCI5, but the estimation error is in the opposite direction with respect to the UCI testing.

Sample Name	Nominal (mg/L)	UCI (mg/L)	UCI error (%)	External (mg/L)	External error (%)
UCI1	120	131	9	110	8
UCI2	0	0	-	0	-
UCI3	480	494	3	473	1
UCI4	240	256	7	237	1
UCI5	60	63	5	139	132

Table 6.8: Ion chromatography measurement uncertainty

This test aims at highlighting that the ion chromatography measurement step (which is

the last step of the EPA Method 8A technique) is itself subject to an considerable margin of uncertainty. A confidence interval can not be established with this limited amount of data, but this partial analysis shows that the ion chromatography results could be expected to be reliable within a margin of $\pm 10\%$.

6.2.8 Step 1 experiment results analysis

Experiments in Step 1 follow a predefined set of instructions, so several experiments can be effectively compared. The experiment sets based on the test day and temperature conditions used for this analysis are summarized in Table 6.9. Some experiments have been excluded from the list presented in Table 6.3. For example, tests with reduced path length, or any path length different from 5.60m, have been excluded to compare only the results collected under the same laser operating conditions. Additionally, experiments that failed the controlled condensation leak test were excluded, with the dry gas meter of EPA Method 8A used for leak-checking. The gas flow rate from the flow controllers - adjusted from standard flow rate to room temperature flow rate - was required to match the reading from the dry gas meter within 5% to pass the test. This verification is valid to detect both leaks in the Method 8A setup and leaks occurring in the measurement cell. Some tests also presented unacceptable levels of etaloning noise occurring when the laser was improperly aligned. These experiments have been excluded as well, as the etaloning degraded the quality of the measurements. Experiments presenting major instabilities in the measurement cell temperatures or with erroneous flow conditions have been removed from the list.

Most experimental problems arise from window maintenance. Since the multi-pass cell mirrors are located very close to the windows, the laser alignment was often lost in the process of removing windows for maintenance. Re-alignment often resulted in lowered signal intensity, variation of the path length, and increase of etaloning noise. While a few of the remaining experiments sets still present some instabilities, mostly attributed to less than stable temperatures, they have been included in the analysis, for a more complete and

realistic picture. In general, longer experiment sets reach a better temperature stability, probably because of the significant thermal inertia of the rig.

For a single measurement set, only one background measurement is used. A background measurement consists in the capture of a detector signal I_0 in a determined condition (in this case, *Air* test condition). Every other captured detector signal I along the timeline is going to be compared to I_0 to determine the absorbance spectrum. The performance of the laser can be improved by using more than one background measurement along the experiment timeline (for instance, recapturing a background signal I_0 for every *Air* condition present in the set) as background changes - due to windows damage, temperature changes, or water traces - are the most important obstacle to a successful measurement. The use of more than one background reference is possible during the post-processing of the data, however, for in-situ measurements it is difficult to interrupt a test in order to acquire a new background measurement. The experiment sets are hence oriented toward a more realistic strategy, where all the absorbance frames are extracted from a single background measurement.

In plots with laser direct readings, the error bars represent the standard deviation of the data collected along the duration of the related test condition (unless specified differently), as the knowledge of the standard deviation can be used to define the limits of detection. In plots with derived data (for example, the ratio of two measurements) no error bars will be present. In plots where several averages of samples from different data sets in the same test conditions are in turn averaged, the error bars will represent the 95% confidence interval for the measure. When the sample size is small, the student-t distribution is used to determine the confidence interval.

$T = 250\text{C}$	$T = 300\text{C}$	$T = 350\text{C}$
05/25/2020	05/25/2020	05/26/2020
05/27/2020	05/27/2020	05/28/2020
05/29/2020	06/09/2020	06/13/2020
06/16/2020	06/18/2020	07/02/2020
06/30/2020	07/07/2020	07/06/2020
07/07/2020	07/09/2020	07/07/2020
07/13/2020	07/14/2020	07/14/2020

Table 6.9: Experiment sets used in Step 1 ECQCL 7 analysis.

The results from the spectral fit of each of the experiment sets of Table 6.9 with the spectral libraries of Section 6.2.6 are analyzed and compared. The spectral fitting consists in a linear regression algorithm proprietary of Opto-Knowledge Systems, Inc. (OKSI). Although the details of the algorithm are proprietary, the method follows the general best practices where an initial guess of species concentration is used to build a theoretical spectrum based on the spectral libraries of each species. This composite is compared with the experimental spectrum after a the background has been subtracted and the differences between measured and computed spectra are assessed. The concentrations are then adjusted and the process repeated until the difference is minimized.

SO₂ performance with ECQCL 7

The performance of ECQCL 7 for SO₂ measurement is estimated using test conditions where the SO₂ concentration is known, such as *Bypass 100ppm* and *Water only + Bypass 81ppm*. The SO₂ reading from the laser is hence compared to 100ppm and 81ppm respectively. The *Water only + Bypass 81ppm* condition is a benchmark for the performance of both H₂O and SO₂ libraries, as the SO₂ concentrations resulting from the fit should ideally not be affected by the presence of water.

Figure 6.20 represents the SO₂ reading resulting from the fit of the absorbance spectrum on different test days, grouped by measurement cell temperature. The dash lines represent the mean of all the SO₂ readings at that measurement cell temperature. The expected value for SO₂ is 100ppm (solid black line). Each plot is labeled with the 95% confidence interval for the data. Figure 6.21 represents the error of the SO₂ reading with respect to the nominal SO₂ concentration (100ppm in this case).

As seen in Figure 6.20 and Figure 6.21, the mean of the readings differs 5% (for 350C) to 10% (250C case) from the expected value of 100ppm, with 95% confidence intervals of $\pm 6\%$ for the 350C case and $\pm 11\%$ for the 250C case (the case with wider uncertainty). The measurements at 350C (the case with the best performance for this test) are both more precise and more accurate than the measurements at 250C (the case with the lowest performance). These calculations assumed a real reference value of 100ppm SO₂, though this value is subject to experimental uncertainties as well, with a RSS uncertainty of about $\pm 4\%$ when using a 1650ppm SO₂ cylinder, as seen in Section 3.5.

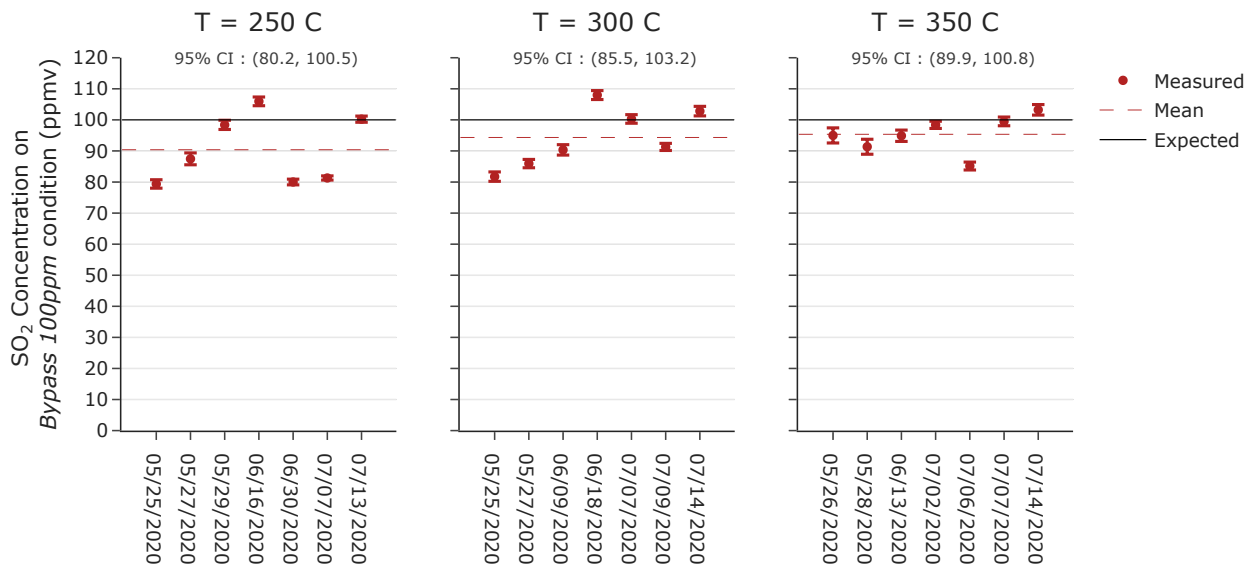


Figure 6.20: SO₂ measurements in *Bypass 100ppm* test conditions.

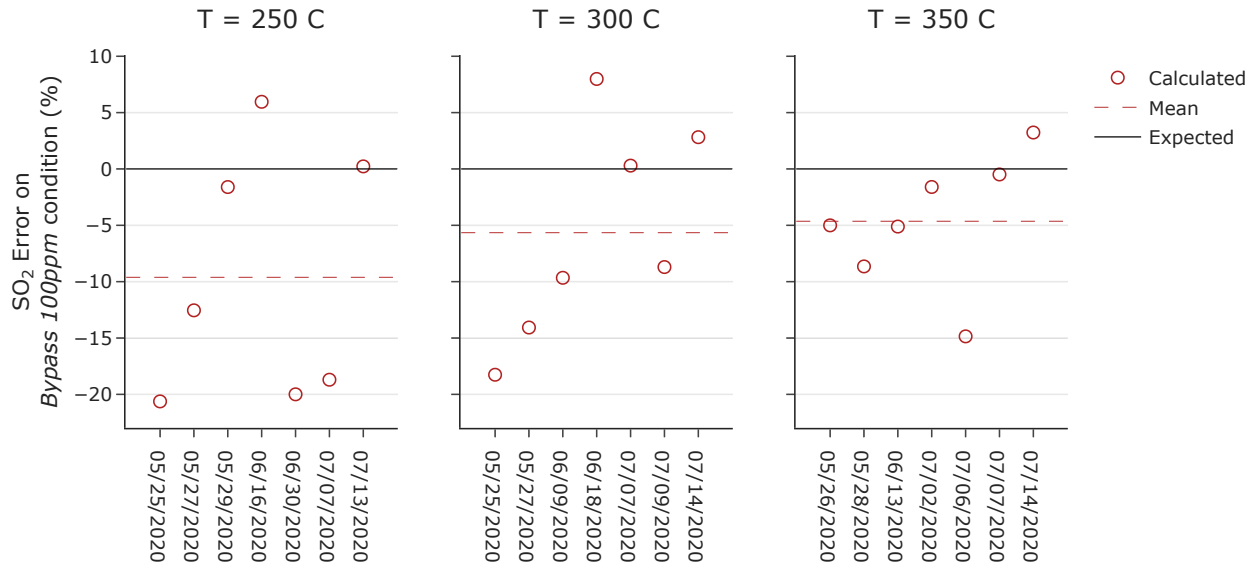


Figure 6.21: SO₂ estimation error in *Bypass 100ppm* test conditions with respect to the nominal expected SO₂ concentration.

In the presence of 3% water, as seen in Figure 6.22 and Figure 6.23, the situation marginally improves for the 250C case (mean value is 6% off the expected value), but it is still characterized by a 95% confidence interval of $\pm 11\%$ from the mean, for both the 250C case and the 350C case. Ideally, SO₂ reading should not be affected by the presence of water. In this analysis, the effect of H₂O on SO₂ measurement is within the uncertainty level of the dry SO₂ measurement.

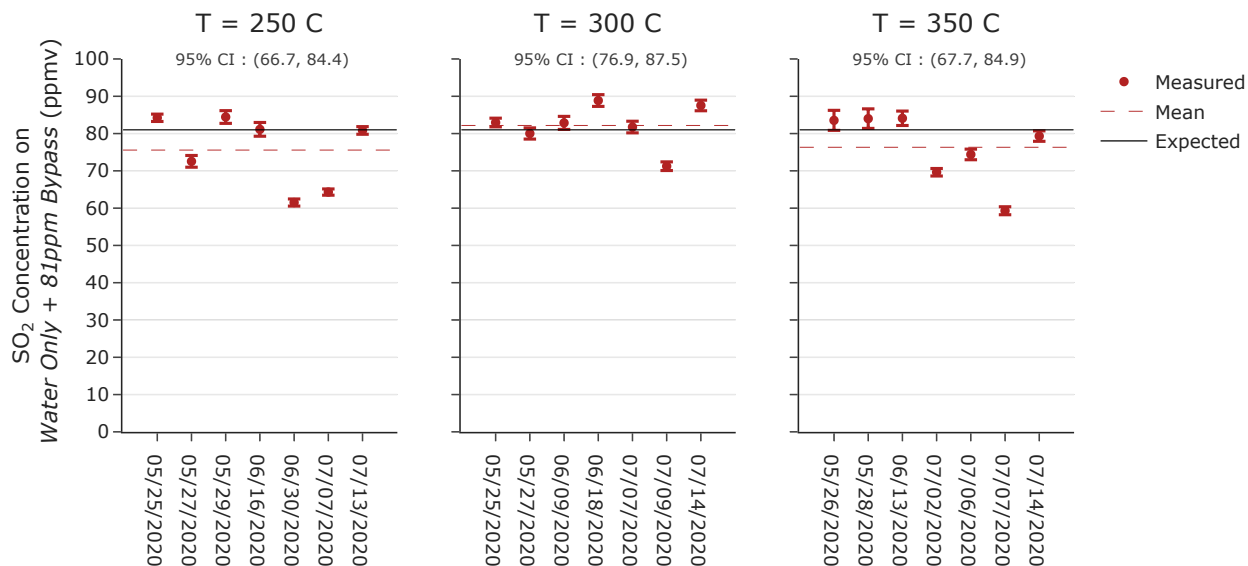


Figure 6.22: SO₂ measurements in *Water only + Bypass 81ppm* test conditions.

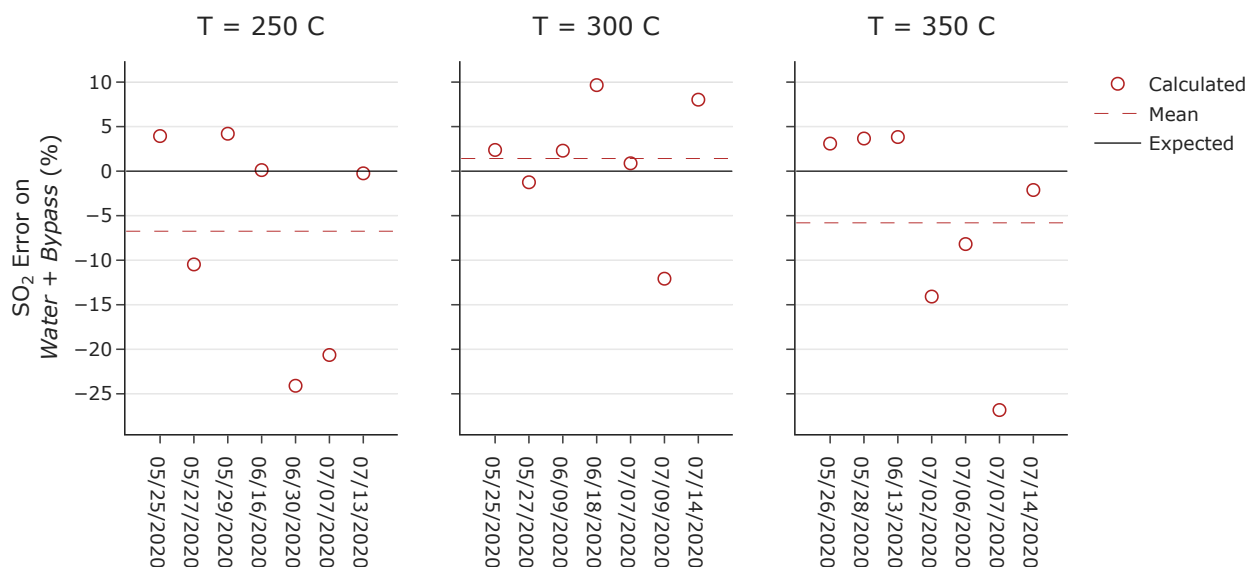


Figure 6.23: SO₂ estimation error in *Water only + Bypass 81ppm* test conditions with respect to the nominal expected SO₂ concentration.

SO₂ measurements reported in Figure 6.24 are related to *Regular* test conditions, where SO₃ and SO₂ coexist. The measurements are sorted chronologically, and grouped based on the amount of SO₂ entering the catalyst (variable SO_x). The mean SO₂ concentration

measured in the cell should be the best estimator of the catalyst efficiency, assuming that all the SO_2 that entered the catalyst and is not present in the cell is in the form of SO_3 . In this case, there is no expected value from the measurements, except the requirement that all measurements of SO_2 should be lower than the correspondent SO_x concentration. As for the previous case, the generation of 50ppm, 100ppm, and 150ppm SO_2 are associated with an uncertainty error that is estimated in 7%, 4%, and 3% respectively, as seen in Figure 3.16. The mean measured SO_2 concentrations in the cell are $34.8 \pm 14\%$, $58.5 \pm 8\%$, $89.8 \pm 8\%$. The derived estimated conversion efficiencies would hence estimated to be around 32%, 42%, and 40%, for 50ppm, 100ppm, and 150ppm of inlet SO_2 (variable SO_x) respectively.

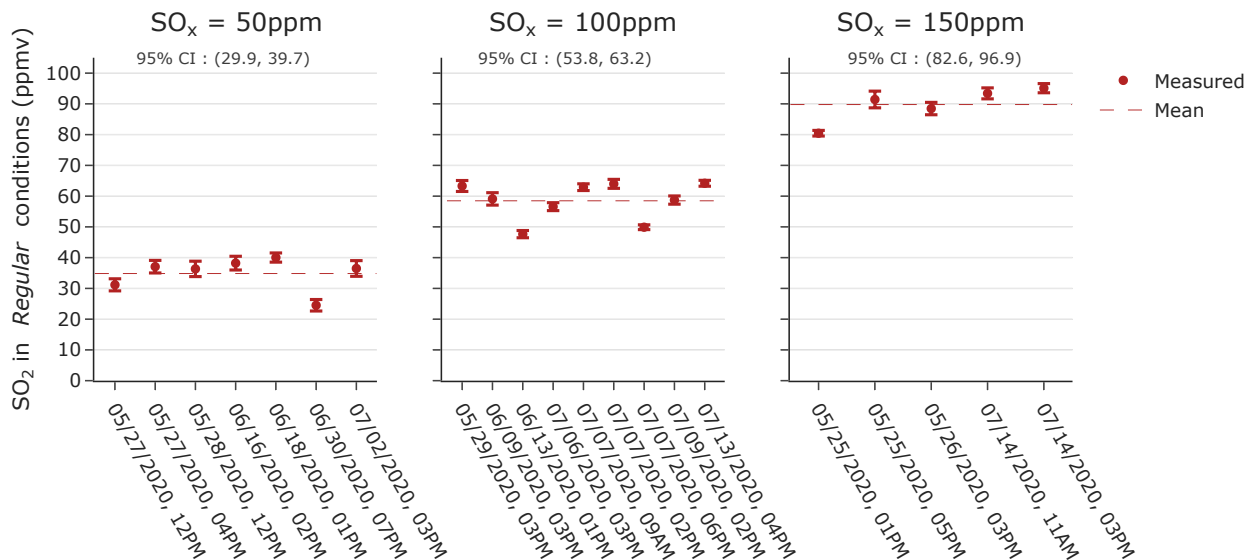


Figure 6.24: SO_2 measurements in *Regular* test conditions.

A further measurement of SO_2 libraries and fitting performance is given by the comparison between the *Regular* and the *Equalized* test conditions, and it is represented in Figure 6.25. *Equalized* conditions present a known dilution of the flow in *Regular* conditions, so the ratio between the two concentration readings should be constant. Specifically, the concentration of SO_2 in *Equalized* should be 81% the concentration in *Regular* conditions. Since the values plotted in Figure 6.25 are not immediate readings, but rather the ratio of two

different readings, the error bars are not reported. Each date includes two different readings, as *Equalized* conditions are present twice in each data set. The ratio between the two test conditions readings is on average 6%, 5%, and 1% off for 250C, 300C, and 350C, respectively. The correspondent 95% confidence intervals are $\pm 6\%$, $\pm 4\%$, and $\pm 7\%$ of the mean.

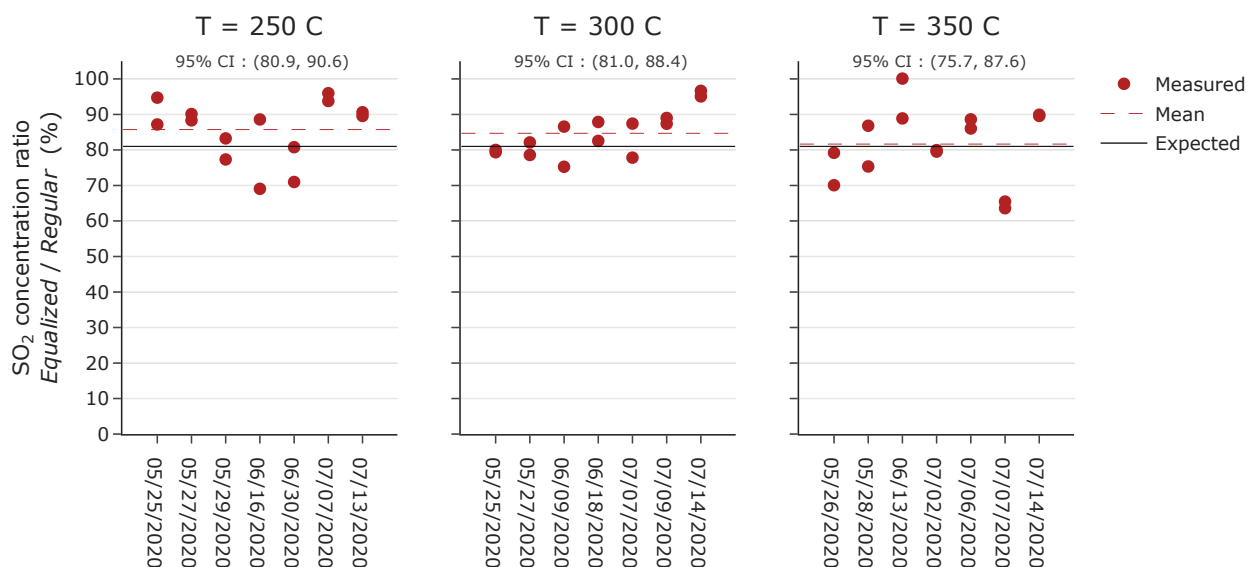


Figure 6.25: SO₂ ratio between *Equalized* and *Regular* test conditions readings.

Figure 6.26 represents for each test date measurements for two different techniques, EC-QCL 7 laser (circles) and EPA Method 8A (squares), with the aqueous samples from EPA 8A processed with ion chromatography. The SO₂ ECQCL 7 readings are taken from the *Regular* conditions, with the controlled condensation system not activated. The reason behind it is that the laser measurements during controlled condensation presented a SO₂ concentration drop, as previously explained in Section 6.2.3. The readings are an average over a 40 samples subset of *Regular* conditions, correspondent to about 52 seconds, either at the start of the *Regular* conditions or right before the activation of the EPA 8A setup.

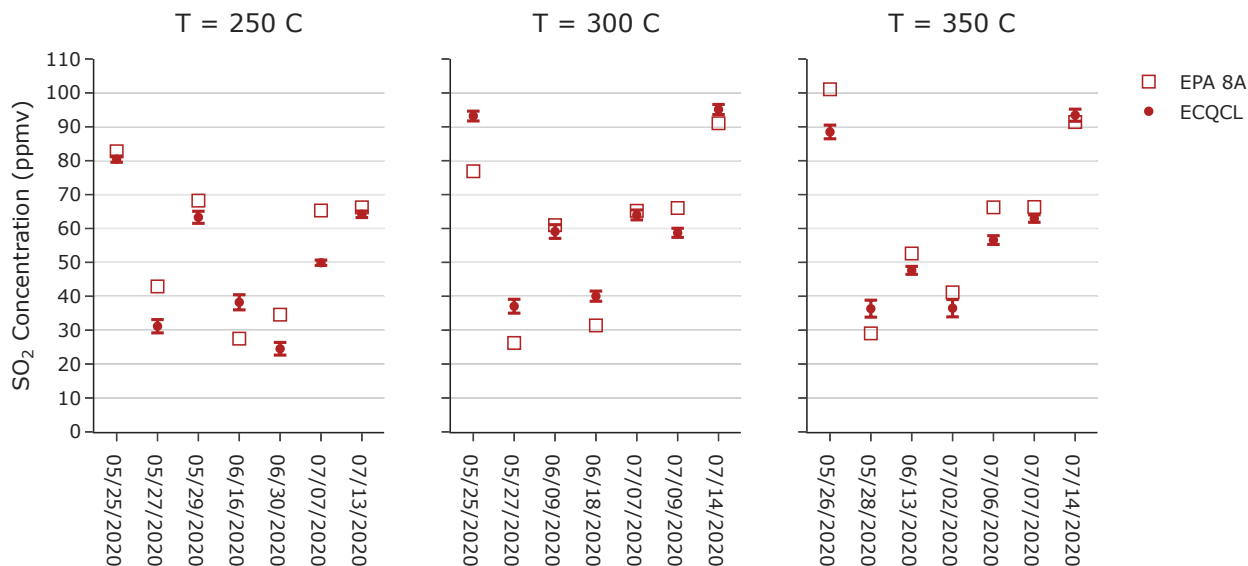


Figure 6.26: SO₂ ECQCL7 measurements and EPA Method 8A measurements for *Regular* test conditions.

Figure 6.27 represents the same information, where the discrepancy between the ECQCL7 and EPA 8A method is estimated with respect to the EPA 8A results. While Figure 6.27 presents large errors, the maximum absolute difference among all data sets at all temperature is around 15ppm. In realistic conditions, where SO₂ concentrations are in the order of thousands of ppm, an absolute error of 15ppm is acceptable. The performance of the SO₂ laser and EPA 8A method will be further analyzed in Section 6.2.10 for the Step 2 experiments in realistic conditions.

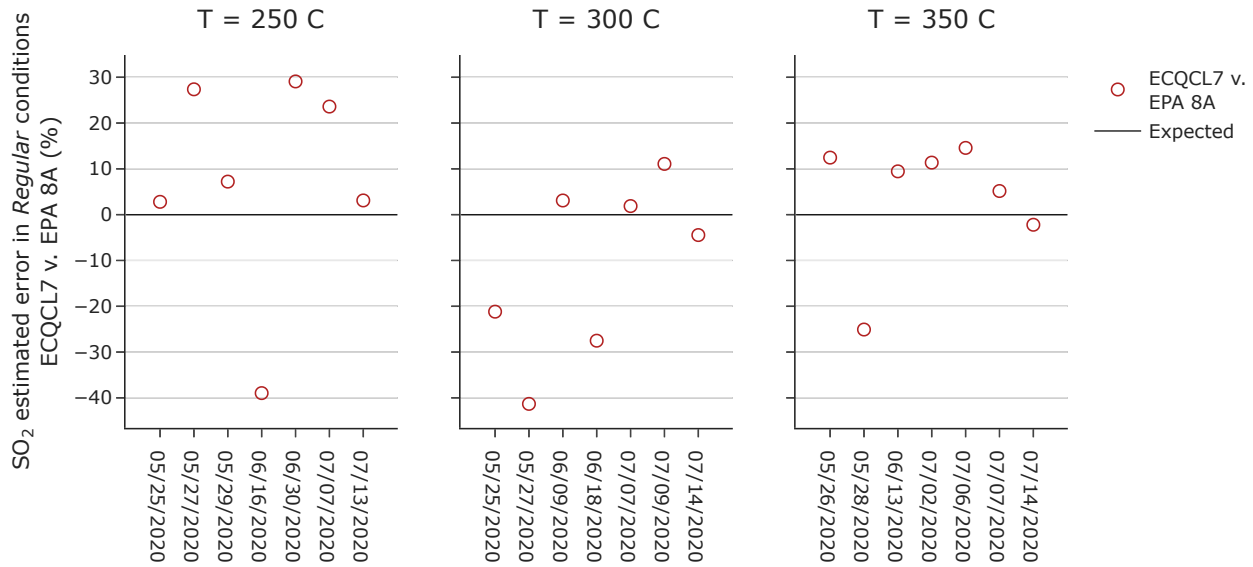


Figure 6.27: Error between SO₂ ECQCL7 measurements and EPA Method 8A measurements for *Regular* test conditions.

SO₃ performance with ECQCL 7

Evaluating the performances of the ECQCL 7 for SO₃ measurements has the additional complication of the lack of reference values with which to compare, as SO₃ is generated through the oxidation reaction of SO₂ and is not provided by a direct calibrated source, unlike the case of SO₂. The performance will hence be evaluated by grouping tests characterized by the same flow and/or temperature conditions, using EPA Method 8A as benchmark.

Figure 6.28 represent the measured SO₃ concentrations in *Regular* test conditions, grouped by concentration of sulfur dioxide entering the catalyst (variable SO_x), ordered chronologically. Since SO₃ concentrations in *Regular* conditions are subjected to the catalyst short-term transient, the represented SO₃ value (and standard deviation) for every test case consists of the average on a 40 samples subset, correspondent to about 52 seconds, either when the controlled condensation system is active or at the end of the *Regular* test conditions. The difference between the two is mostly negligible, as SO₃ concentrations converge to a stable value after the initial catalyst short-term transient.

The SO_3 concentrations in Figure 6.28 do not display a clear behavior, unlike the equivalent SO_2 case represented in Figure 6.24. In the last test cases for each inlet SO_x value the concentration values of SO_3 stabilize at constant levels.

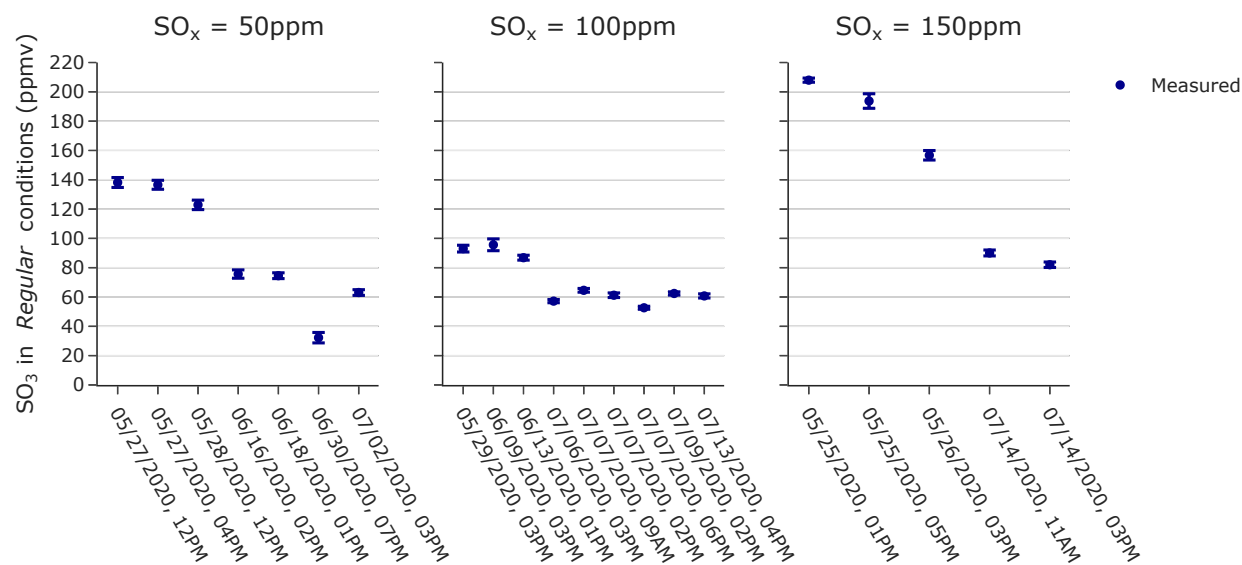


Figure 6.28: SO_3 measurements in *Regular* test conditions.

Figure 6.29 represents concentrations of both SO_2 and SO_3 for each test day, sorted chronologically. The black solid line represents the inlet SO_x . As previously seen in Figure 6.24, SO_2 readings respond immediately to a sudden change in the inlet variable SO_x . On the other hand, SO_3 concentration response is much slower and associated with the conditioning time for the catalyst. In fact, SO_3 concentrations show a substantial “memory” of the previous operating conditions. For instance, before 05/25/2020, the inlet SO_x was set to 400ppm to allow to prime the catalyst faster. Unfortunately, that initial load had lasting repercussions on the SO_3 output from the catalyst. The concentrations were not just larger than expected, but also larger than the overall inlet sulfur content even after hours of testing. Sulfur trioxide concentrations leveled in the July 2020 experiments.

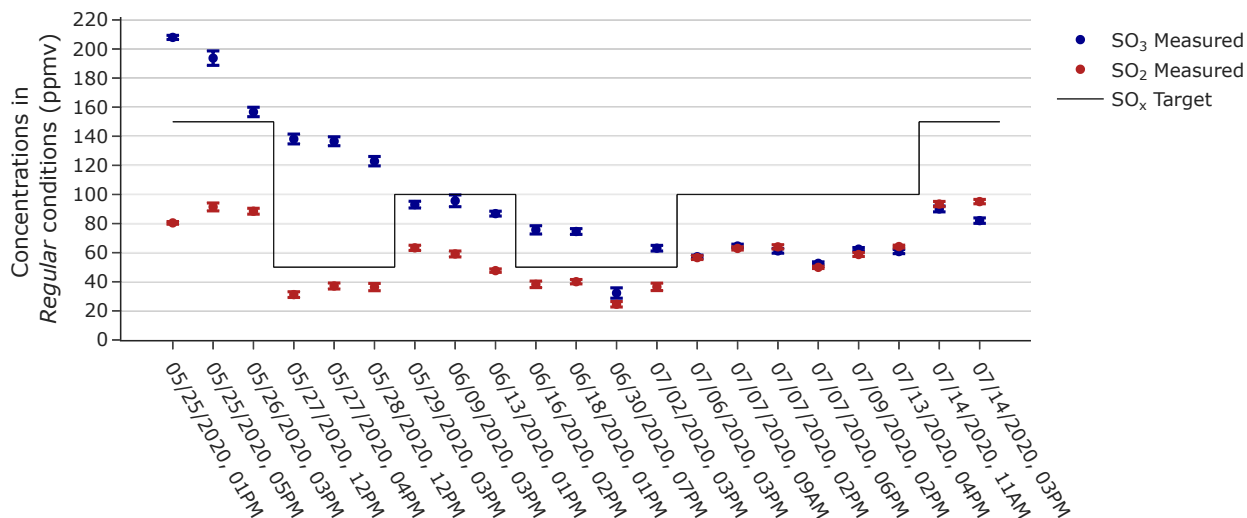


Figure 6.29: Complete timeline for SO₃ and SO₂ measurements in *Regular* test conditions for ECQCL 7 Step 1 tests.

Figure 6.30 represent the error between the inlet variable SO_x and the sum of the laser-measured SO₂ + SO₃ concentration. If the total sulfur content was preserved from the inlet of the catalyst to the measurement cell, the error would be zero. As previously mentioned, this is not valid in most of the condition tested, since the SO₃ output greatly exceeded the expectations. The error decreased with time, especially when the inlet SO_x concentration was increased from one test to the next. The conditioning time of the catalyst appears to be a very important factor in evaluating the sulfur balance. Hence, it is difficult and possibly fallacious to rely on the concept of sulfur balance to estimate the SO₃ concentration in the measurement cell when operating with a vanadia catalyst, since the status of the catalyst conditioning state is not known at any given time.

Figure 6.29 and Figure 6.30 highlight the long temporal transients associated with SO₃ generation from the oxidation of SO₂ promoted by a vanadia catalyst, with conditioning times possibly in the order of tens of hours. The conditioning time is experimentally observed as depending on gas flow rates, SO₂ concentration, and amount of catalyst used. It is possibly convenient to start operating the catalyst at the desired flow conditions long before measuring

the SO_3 yield. Also, in this experiment it is best to progress the tests in the direction of increasing SO_x input rather than decreasing, since the conditioning is faster when increasing the inlet sulfur dioxide concentrations. Ideally, the catalyst should be operated continuously and always under the same inlet flow conditions to promote a steady SO_3 yield. The addition of the high-temperature *Main Flow Valve* (number 2 in Figure 3.6) is a step in this direction, since it allows uninterrupted catalyst operations.

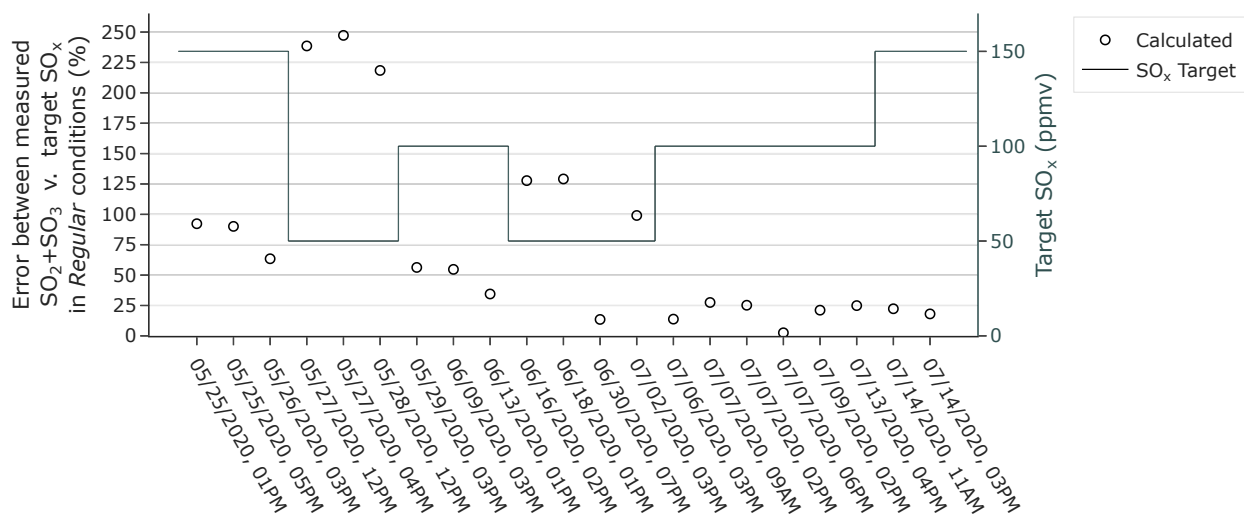


Figure 6.30: Error between the measured concentration of $\text{SO}_2 + \text{SO}_3$ with respect to the inlet variable SO_x , in *Regular* test conditions for ECQCL 7 Step 1 tests.

Figure 6.31 shows for each test date two separate measurements, one from the ECQCL 7 laser (circles) and one from the EPA Method 8A (squares), with the aqueous samples from EPA 8A being processed with ion chromatography. For each cell temperature T , one case of close match between the ECQCL 7 and the EPA 8A measurements is expected, since the very definition of the SO_3 library relies on a calibration point that is provided by a single EPA 8A measurements. In all the latest test cases for each temperature the ECQCL 7 and the EPA 8A results match within less than 5% difference, as seen in Figure 6.32. The earliest tests proved more noisy and less stable, with the catalyst not at steady-state. On the other hand, these factors should not significantly impact the accuracy of SO_3 measurements for both

measurement techniques. Further tests would be required to shed light on the discrepancy, possibly analyzing cases with high SO_3 concentrations (>100 ppm) to verify if the EPA 8A measurement method is successful in determining high concentrations of SO_3 . However, those conditions would never be encountered under power-plant conditions.

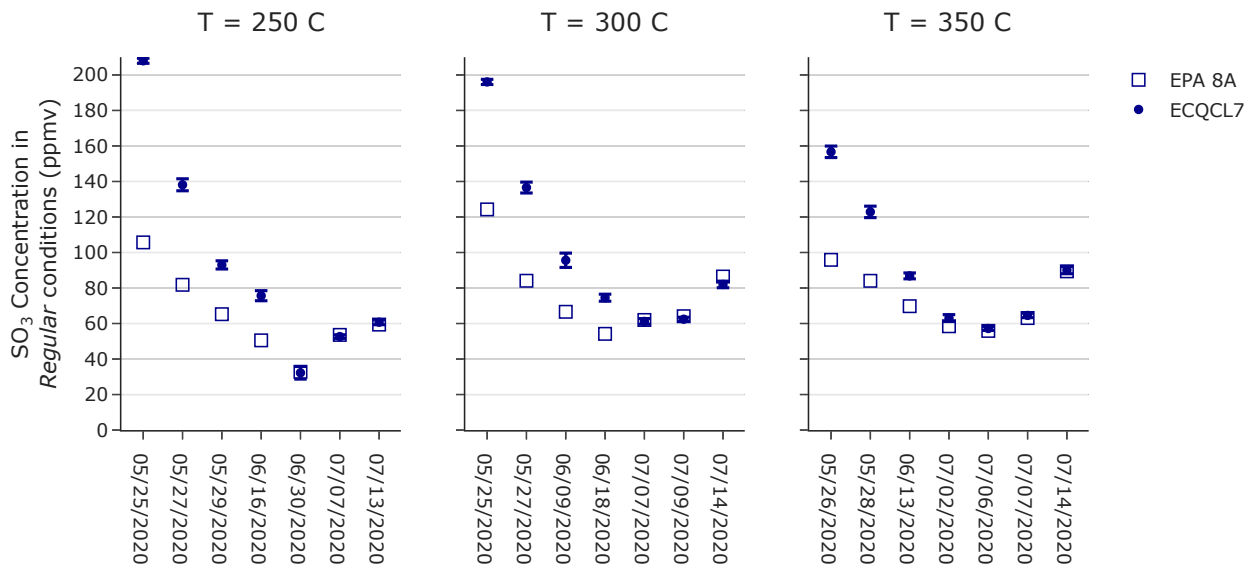


Figure 6.31: SO_3 ECQCL7 measurements and EPA Method 8A measurements for *Regular* test conditions.

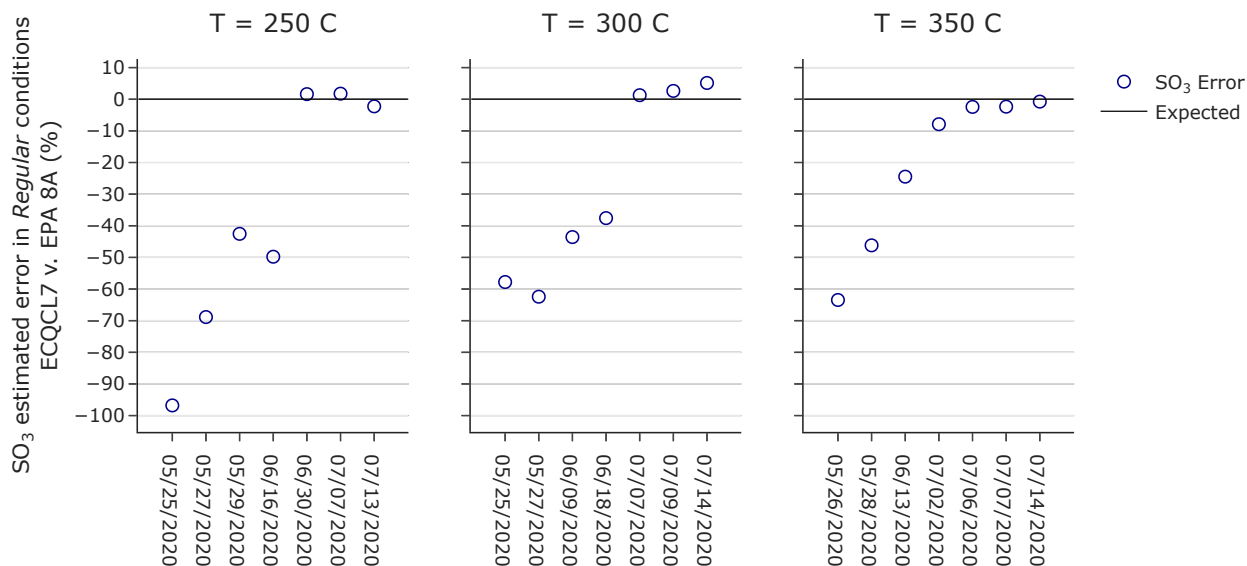


Figure 6.32: Error between SO₃ ECQCL7 measurements and EPA Method 8A measurements for *Regular* test conditions.

A further assessment of SO₃ libraries and fitting performance is given by the comparison between the *Regular* and the *Equalized Decay* test conditions, as for the SO₂ case, and represented in Figure 6.33. The *Equalized* test conditions are not used for SO₃ since in most cases they were affected by the short-term catalyst transient. The concentration in *Equalized Decay* test conditions is expected to be 81% the value of concentration in *Regular* conditions, as for the *Equalized* case. Error bars are not present in Figure 6.33 since they are not direct readings, but are calculated from two separate measurements. The reading between the two test conditions is on average 6%, 1%, and 4% off for 250C, 300C, and 350C, respectively. The 95% confidence intervals are $\pm 4\%$, $\pm 4\%$, and $\pm 3\%$.

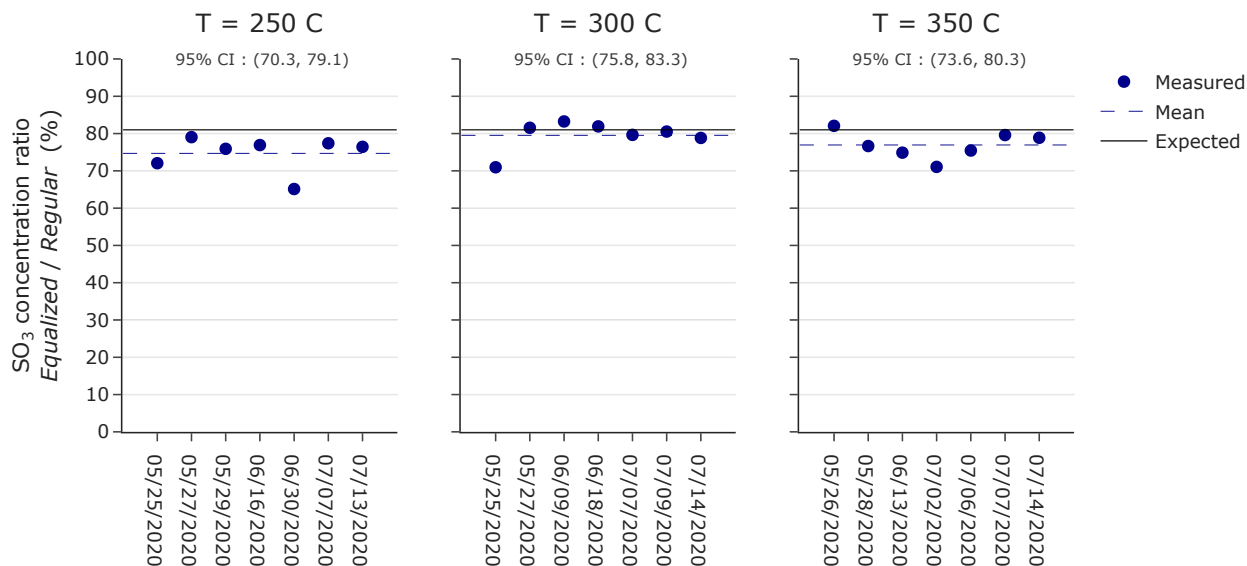


Figure 6.33: SO₃ ratio between *Equalized Decay* and *Regular* test conditions readings.

In *Equalized* test conditions, a steady concentration of SO₂ and SO₃ should be present in the measurement cell, diluted in air. In *Water Add* test conditions, a part of the diluent air is replaced with water vapor, maintaining the overall flow rate constant at the same level as *Equalized* conditions. Sulfur dioxide concentration will stay constant, while SO₃ concentration will drop due to the reaction of SO₃ with H₂O to form H₂SO₄. It is possible to evaluate the fraction of SO₃ that has not reacted with water by calculating the ratio between the concentration of SO₃ in *Water Add* and *Equalized* conditions. For instance, a ratio of 0.75 means that of the initial SO₃ concentration (measured in *Equalized*), only 25% is in the form of H₂SO₄ in *Water Add* conditions, while 75% is still in the form of SO₃. Since in *Equalized* conditions the SO₃ concentration is not stable (due to the catalyst short-term transient), the SO₃ concentration in *Equalized Decay* is used instead. The two conditions (*Equalized* and *Equalized Decay*) present the same steady-state levels of SO₃, so no error is introduced. Notably, one outlier case at 250C (06/30/2020) has been dropped from the analysis, since the data set presented a strong variation in background close to the *Water Add* condition. Consequently, a zero-concentration baseline for SO₃ could not

be well established, and the SO_3 ratio between the two condition did not provide a reliable measurement.

Figure 6.34 represents the SO_3 and H_2SO_4 normalized theoretical chemical equilibrium curves at 3% water vapor as a function of cell temperature, together with the calculated SO_3 fraction present in the measurement cell in *Water Add* conditions and evaluated with ECQCL 7 laser. For each test temperature T , Figure 6.34 represents with a circle the mean of the ratio between SO_3 readings in *Water Add* and *Equalized Decay* conditions between all test cases, and each error bar represents the 95% confidence interval evaluated with a student-t distribution, since only about six data sets per temperature were used.

In Figure 6.34, the experimental points lie above the SO_3 curve, indicating a higher than expected SO_3 concentration. However, the points would fall almost exactly on the theoretical SO_3 curve if the thermocouple temperature measurements were underestimating the cell temperature by only 30C, amounting to a temperature estimation error of 8.5% to 12% (for the 350C and the 250C case respectively).

Ultimately, the hypothesis of chemical equilibrium is verified in the experimental conditions of this work, even if not perfectly matching the theoretical expectations. The difference between theoretical expectations and experimental results could be explained by a less than 12% temperature measurement difference, so the assumption of chemical equilibrium is verified with a level of uncertainty of no worse than 12%. It cannot be established if the small discrepancy is due to other factors, as it lies within the uncertainty levels of the experimental setup. Ideally, the discrepancy could be further analyzed by coupling ECQCL 7 and ECQCL 8 lasers for a simultaneous SO_3 and H_2SO_4 measurement. However, the H_2SO_4 measurement libraries are themselves subject to the assumption of chemical equilibrium, as explained in Section 6.18.

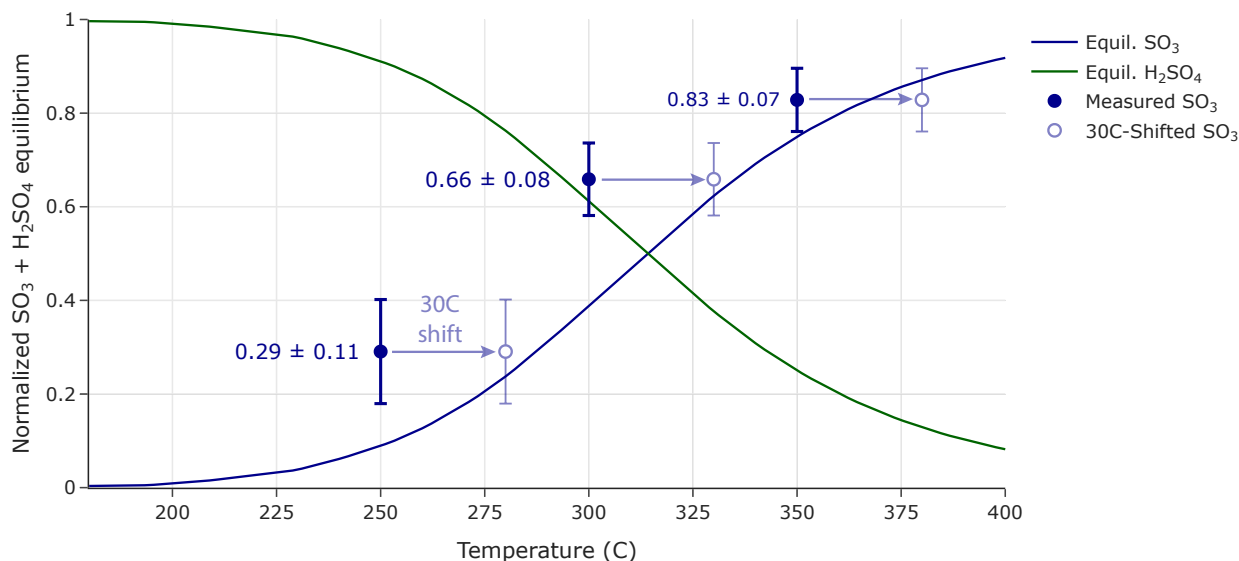


Figure 6.34: SO₃ and H₂SO₄ normalized theoretical equilibrium at 3% water vapor as a function of temperature, with ECQCL7-measured SO₃ fraction.

H₂SO₄ performance with ECQCL 8

As explained in Section 6.18, the procedure to define H₂SO₄ libraries is convoluted and prone to introduce measurement errors. The measurement of H₂SO₄ with ECQCL 8 is similarly intricate, and follows the steps below:

1. EPA Method 8A measurement

First, the controlled condensation system is activated in *Regular* test conditions, with additional water vapor injected after the measurement cell, to gather the overall SO₃+H₂SO₄ cell content. The ECQCL 7 laser is operating during this time to measure SO₂ and SO₃ simultaneously, to compare the two to the EPA Method 8A results (Figure 6.31 and Figure 6.26). Since in *Regular* conditions the water vapor present is virtually absent, all SO₃+H₂SO₄ is in the form of SO₃ in the measurement cell.

2. Activation of ECQCL 8 laser

To measure H₂SO₄ concentrations, the ECQCL 8 has to be operating. The procedure

involves some changes in the physical arrangement of the setup, namely a flipper mirror and a different data acquisition system, while using the same detector. As such, ECQCL 7 and ECQCL 8 could not be operated simultaneously, and the transition takes up to 1 hour, since the acquisition of a new background signal for ECQCL 8 is also needed to start the measurement.

3. *Dilution effect*

To measure H_2SO_4 , water needs to be present in the measurement cell. When water vapor is injected before the cell (*Water Add* conditions, where the ECQCL 8 needs to operate to visualize sulfuric acid), the gas flow rate in the measurement cell is different with respect to *Regular* conditions (where EPA Method 8A was operated). This difference in flow is well characterized, and it is accounted for by scaling the EPA 8A measurement results.

4. *Assumption of equilibrium*

Since EPA 8A method provides the total $\text{SO}_3+\text{H}_2\text{SO}_4$ content in the measurement cell, the assumption of equilibrium is used to separate the two distinct SO_3 and H_2SO_4 contributions, based on temperature and water vapor content.

This approach presents several issues. First, it introduces a time-lag, since the ECQCL 8 reading and EPA Method 8A measurement do not occur simultaneously. The issue with the time-lag does not create uncertainties if the catalyst behavior is stable on that time-scale of ~ 1 hour. The flow dilution, due to the different flow rate in *Regular* and *Water Add* conditions, is also not problematic, as it is known and well characterized by the flow controllers. The chemical equilibrium assumption, however, introduces the most uncertainties.

Analyzing the H_2SO_4 libraries, at 300C the magnitude of the H_2SO_4 absorbance spectrum (per ppm·m) should be larger than the one at 350C and smaller than the one at 250C, but using experimental data and equilibrium assumption this result is not verified. This is a factor that decreases the confidence in the scale of the libraries and the accuracy of the

measurements. A possible step to improve the libraries would be the simultaneous operation of ECQCL 7 and ECQCL 8, since with a direct SO_3 measurement the definition of a library would not need to rely on the assumption of chemical equilibrium.

The results for Step 1 tests are summarized in Figure 6.35 and Figure 6.36.

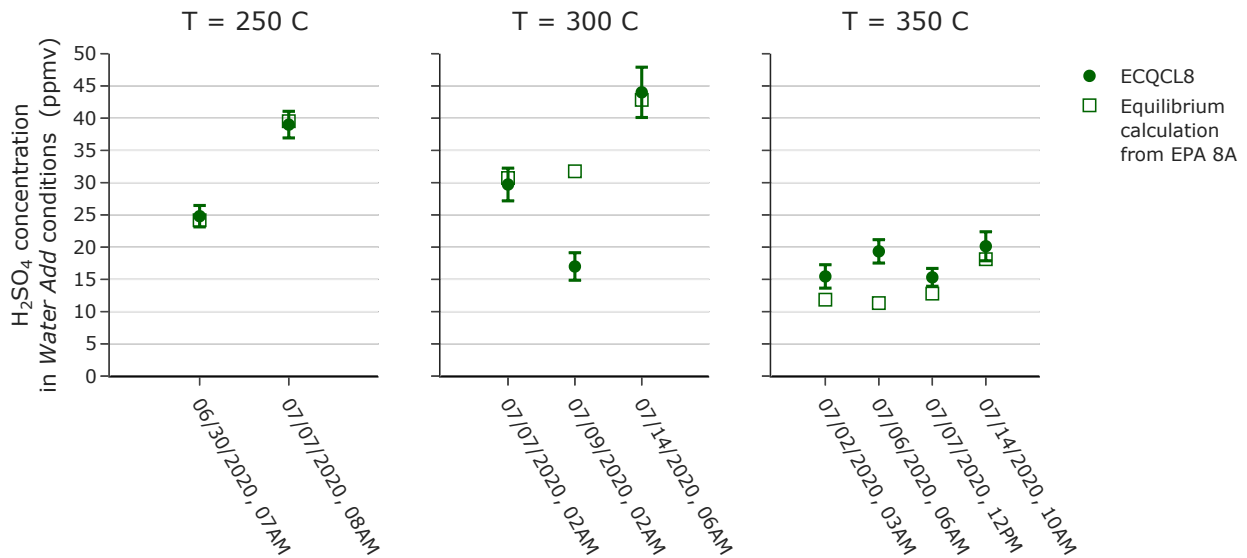


Figure 6.35: Measured H_2SO_4 concentrations (ECQCL8, circles) and H_2SO_4 concentrations estimated from the EPA Method 8A measurements under the assumption of chemical equilibrium.

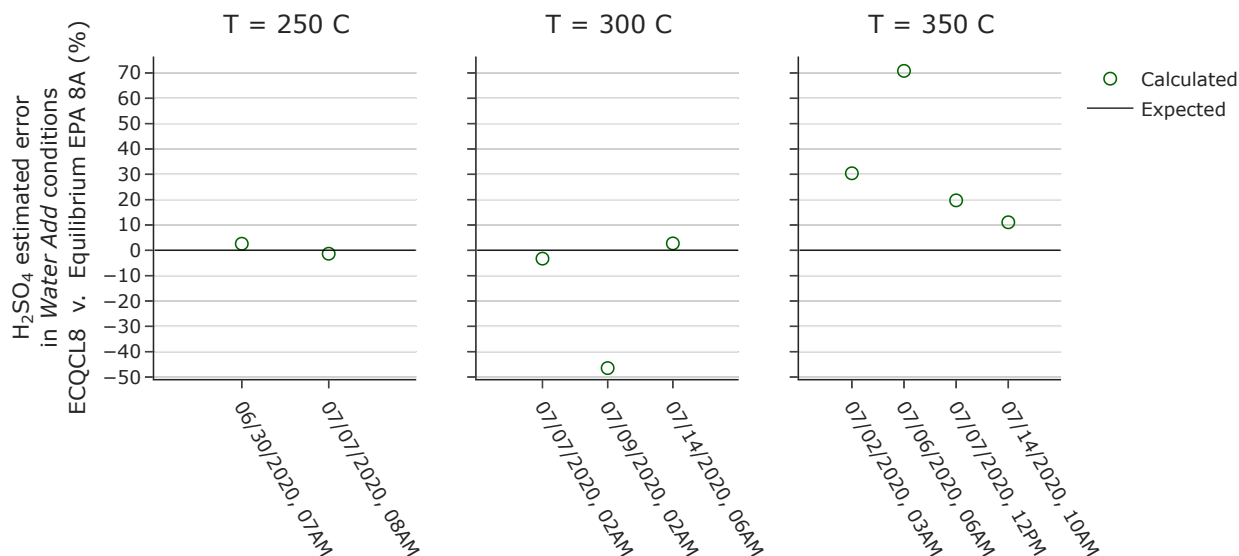


Figure 6.36: Estimated H₂SO₄ measurement error of ECQCL 8 with respect to the H₂SO₄ concentrations estimated from the EPA Method 8A measurements under the assumption of chemical equilibrium.

The experimental points in Figure 6.35 closely capture the estimated equilibrium concentrations. In terms of measurement error, as shown in Figure 6.36, the results at 350C are comparatively larger. However, the H₂SO₄ concentrations at 350C are reduced with respect to 300C and 250C, so a small absolute concentration difference can turn into a large percentage error. Since the H₂SO₄ libraries are defined based on one EPA Method 8A measurement for each temperature, it is expected for one ECQCL 8 - EPA 8A measurement pair per temperature to match. The standard deviation of the H₂SO₄ ECQCL 8 laser measurements often lies at $\pm 10\%$ of the mean value, indicating a noisier measurement.

While these numerical results look encouraging, the measurements suffer greatly from background changes. A zero-concentration baseline could not be maintained for long periods of time because of the continuous degradation of the windows. The formation of BaSO₄ decreases the sensitivity and accuracy of the measurement by lowering the signal-to-noise ratio.

6.2.9 Summary of Step 1 results

In the simplified conditions of Step 1, the ECQCL 7 SO₂ and SO₃ readings were precise (< 4% standard deviation) and accurate ($\pm 10\%$ for SO₂, evaluated on calibrated concentrations). The accuracy could be further improved by using a different calibration source. The negative effect of the presence of 3% water vapor on spectroscopic measurements was limited and it did not preclude successful measurements of SO₂ and SO₃. At 3% water vapor concentration, the comparison of SO₃ levels with and without water confirmed the chemical equilibrium between SO₃ and H₂SO₄ at different temperatures within the experimental uncertainty. To date, this is the first investigation of the chemical equilibrium in flue-gas conditions by direct measurements.

The ECQCL 8 performance in measuring low levels of SO₂ was unsatisfactory, as at 100ppm concentration the SO₂ contribution was not visible in the absorbance spectrum and not reliably extracted by the spectral fitting algorithm. Due to the weak absorbance of SO₂, it is likely that the limit of detection in this configuration is probably larger than 100ppm and measurements at low concentrations are precluded. H₂SO₄ was consistently detected, albeit with limited precision (10% standard deviation). The measured H₂SO₄ was generally accurate with respect to the controlled condensation results, using the assumption of chemical equilibrium. Some practical issues include the important window degradation occurring only minutes after H₂SO₄ was present in the measurement cell and a laser signal drift in time. While the laser drift issue can be solved by spectral fitting, the window degradation is a significant issue that can prevent the possibility of continuous measurements.

The next section will analyze the performance of the two lasers under realistic flue-gas conditions, increasing the concentrations of SO₂ and H₂O vapor to test the capabilities of the two systems. The tests in Step 2 were focused on covering a wide combination of conditions, and are therefore less structured. The limited number of test days available also precluded the possibility of replicating the same conditions for every temperature. The investigation

of the results of Step 2 tests will be more oriented to the feasibility of the measurement and the spectroscopic limitations encountered, as not enough structured tests were available for a statistical analysis like the one above for Step 1.

6.2.10 Step 2 experiment results

In this section, the structures of a single ECQCL 7 experiment and a single ECQCL 8 experiment are analyzed to investigate the feasibility of the two different spectroscopic measurements in realistic coal-fired power-plant flue-gas conditions. In Step 2 experiments, the system is operating at nominal expected power plants conditions, with 8% water, around 2500ppm of SO₂, and 40 to 60ppm of SO₃/H₂SO₄.

ECQCL 7 in realistic conditions

The data set for this section is the Step 2 ECQCL 7 08/13/2020 experiment, with $T = 350C$ and 8% water vapor. High concentrations of SO₂ (larger than 1600ppm of SO₂) cannot be generated using a 1650ppm SO₂ gas cylinder, and an additional gas cylinder, containing 1.0% SO₂ in nitrogen, is used to feed SO₂ to the measurement cell to reach the 2550ppm SO₂ level. The use of a 1.0% SO₂ cylinder introduces a larger uncertainty on the generation of high concentration of SO₂.

As seen in Figure 6.37, no SO₃ concentration short-term catalyst transient is present (unlike Figure 6.5) since the high-temperature valve was added to the system, allowing for continuous catalyst operations. A perturbation of SO₂ concentration when the EPA Method 8A setup is activated is still present, and the effect could not be attributed to a precise cause. The raw data from the detector (voltage signal V), the absorbance (non-dimensional), along with a description of the test conditions are collected in Table 6.10. The reference background spectrum I_0 is highlighted with a red-shaded area.

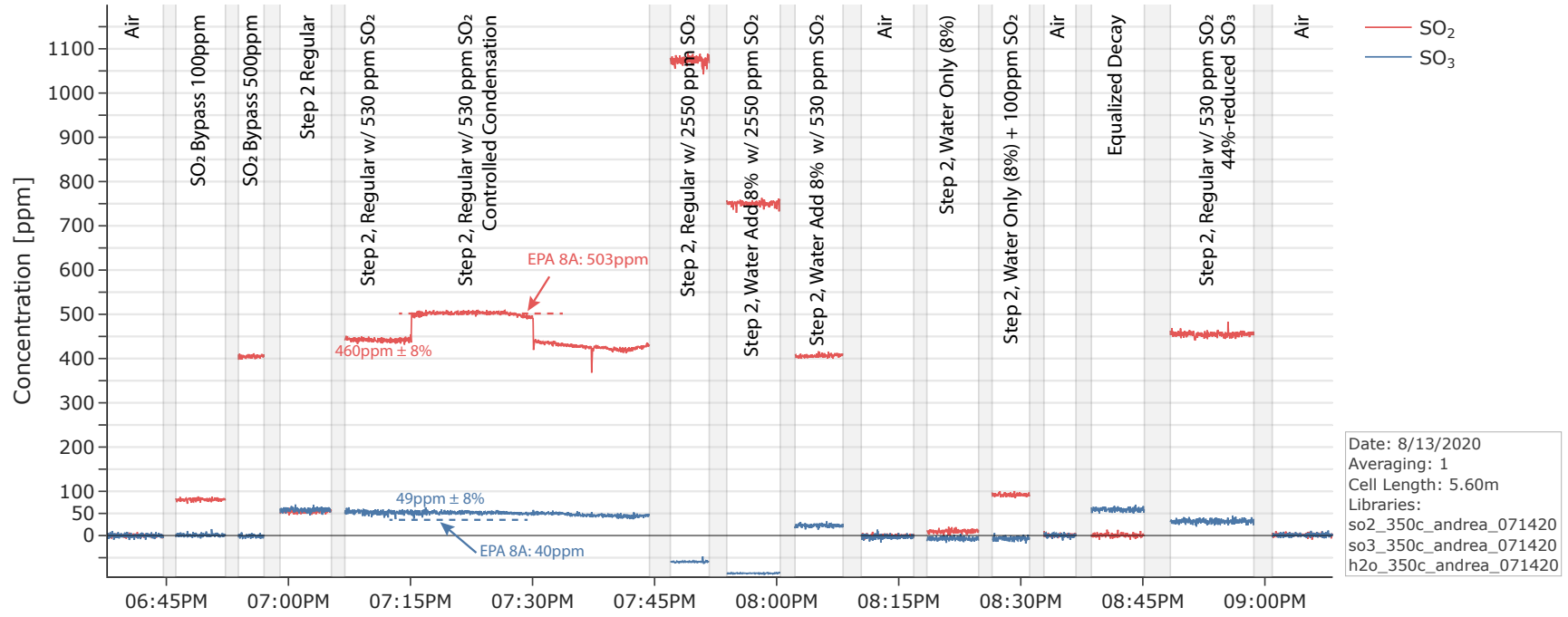


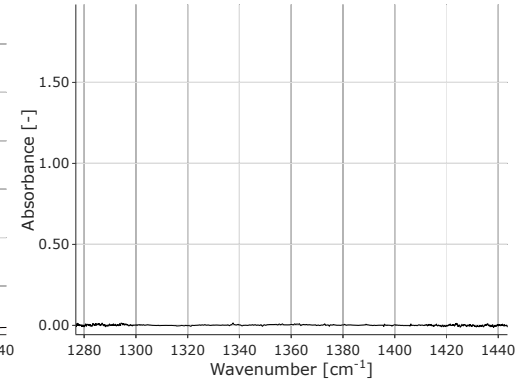
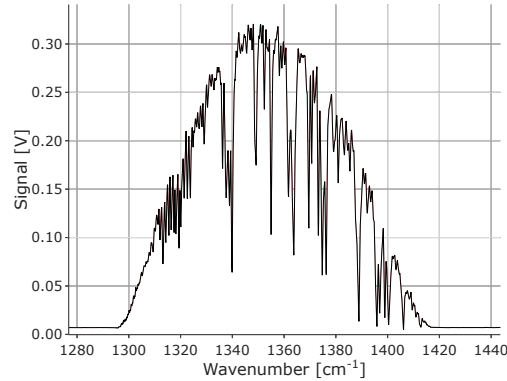
Figure 6.37: SO₂ and SO₃ concentrations in the Step 2 ECQCL 7 08/13/2020 $T = 350C$ experiment timeline.

Description
Raw detector signal [V]
Absorbance spectrum [-]

Air

06:45:02 PM

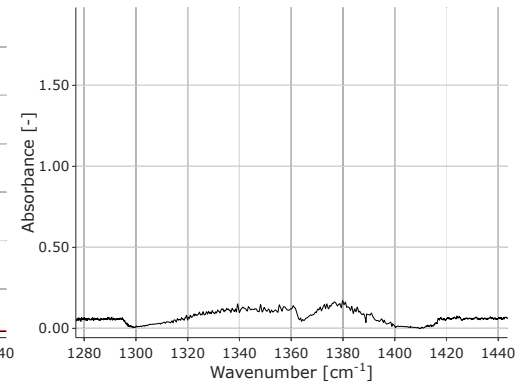
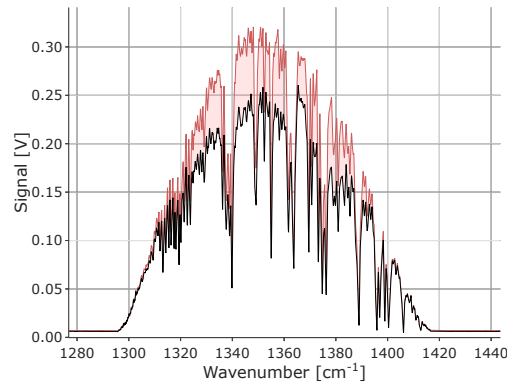
The raw detector signal in this test conditions constitutes the background signal. The absorbance spectrum (right) is a line at zero absorbance (since this frame is taken as the background signal).



100ppm SO₂ Bypass

06:47:51 PM

A low concentration of SO₂ is present in the cell. The spectral structures are not fully visible since the y-axis scale is fixed among all cases and it is determined by test conditions presenting very large absorbance (such as high SO₂ concentrations).



Description

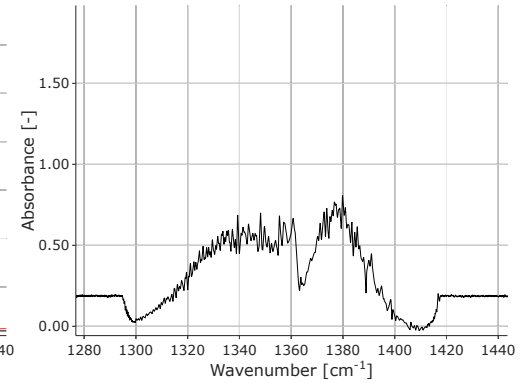
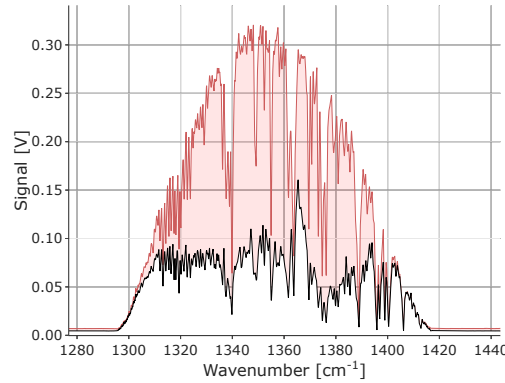
Raw detector signal [V]

Absorbance spectrum [-]

500ppm SO₂ Bypass

06:56:57 PM

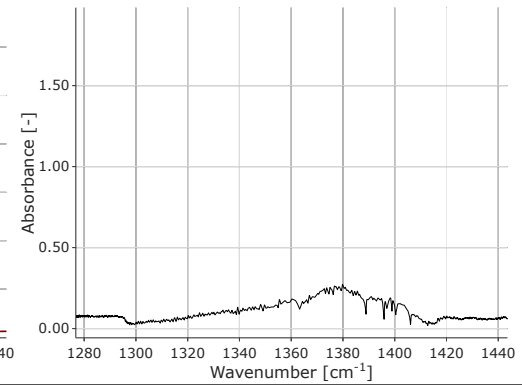
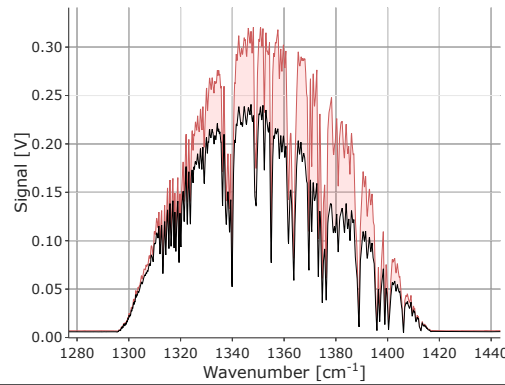
500ppm of SO₂ are present in the cell. Notably, the SO₂ concentration reading from the data fitting process does not match the expected value.



Step 2, Regular

07:03:40 PM

In this conditions, SO₂ and SO₃ are present in the measurement cell at low concentration levels (<100ppm).

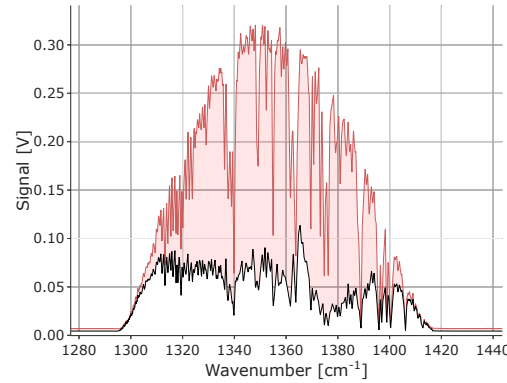


Description

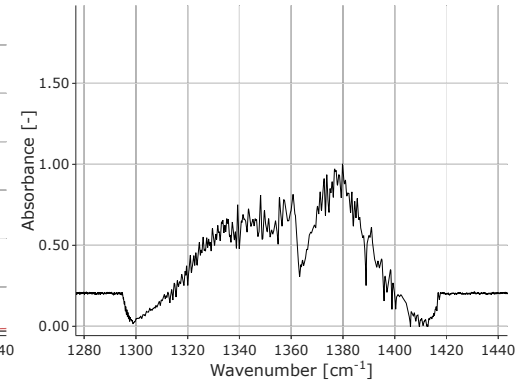
Step 2, Regular with 530ppm SO₂ 07:07:21 PM

With respect to the previous case, additional SO₂ is injected in the cell to increase the concentration of SO₂ to around 530ppm (a level of uncertainty is due to the unconverted SO₂ from the catalyst output). The SO₃ contribution to the spectrum is not directly visible, but its concentration is extracted by the fitting algorithm.

Raw detector signal [V]

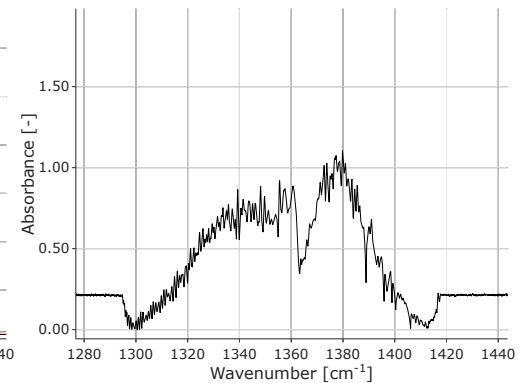
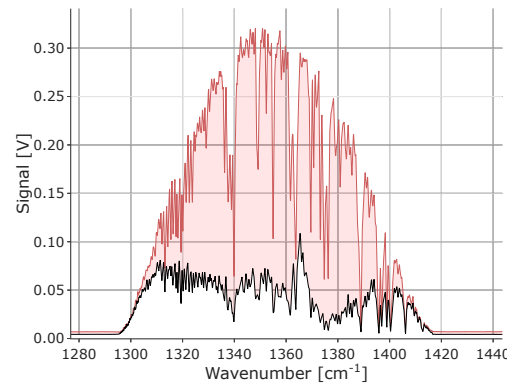


Absorbance spectrum [-]



Step 2, Regular with 530ppm SO₂ (controlled condensation) 07:18:11 PM

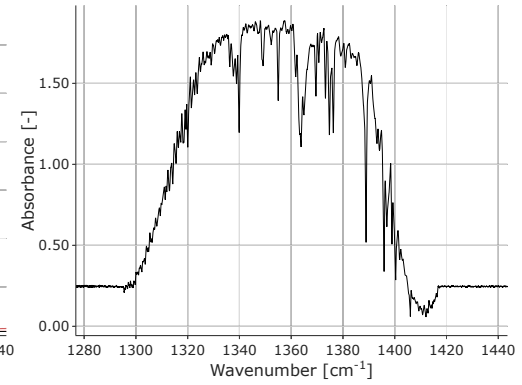
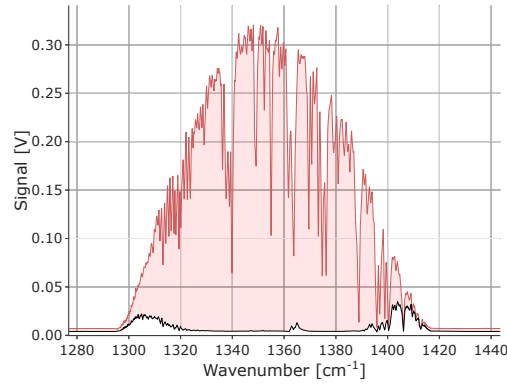
When the EPA Method 8A system is activated, the mathematical fit estimates an increase in SO₂ concentrations. The origins of this influence are unclear.



Description**Raw detector signal [V]****Absorbance spectrum [-]**

Step 2, Regular with 2550ppm SO₂ 07:48:19 PM

SO₂ is further increased to around 2550ppm. Under these conditions, the absorbance is saturated at almost all wavelengths. No measurement is possible. The result of the fit in this test condition has to be discarded, since virtually no light from the laser reaches the detector.

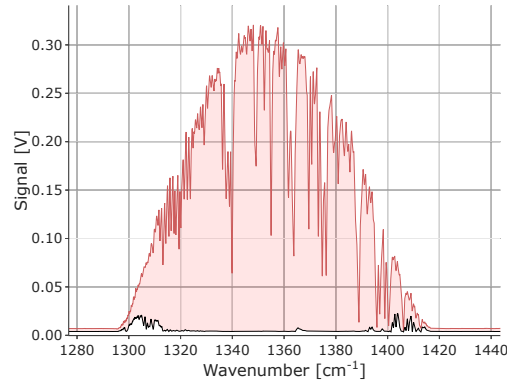
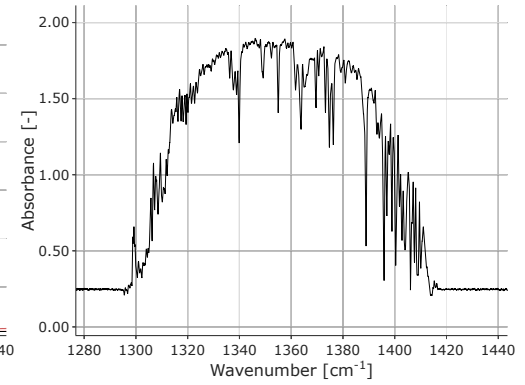


Description

Step 2, Water Add 8% with 2550ppm SO₂

07:53:57 PM

Part of the inert gas flow from the previous step is substituted with water, for a water vapor concentration of 8% with the same total flow rate. The presence of 8% water vapor and 2550ppm SO₂ is incompatible with the current laser configuration. The result of the fit in this regime has to be discarded, since virtually no light from the laser reaches the detector.

Raw detector signal [V]**Absorbance spectrum [-]**

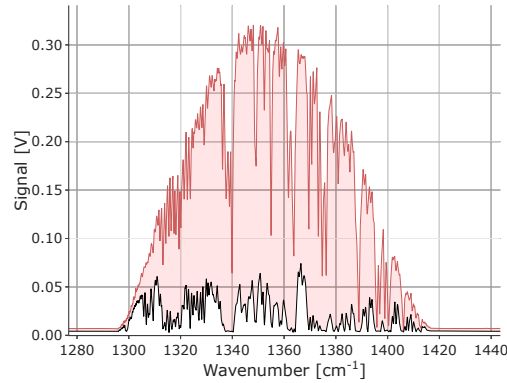
Description

Step 2, Water Add 8% with 530ppm SO₂

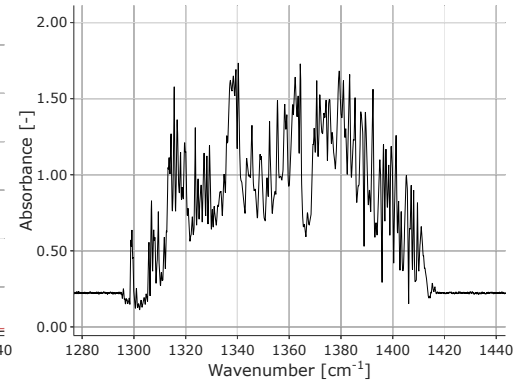
08:03:16 PM

SO₂ concentration is reduced to 530ppm, with less than 100ppm SO₃ and 8% H₂O vapor. Under this condition, it appears that a measurement is possible. However, the signal at the detector is greatly reduced, and some areas related to water features are saturated (as explained in Section 6.12).

Raw detector signal [V]



Absorbance spectrum [-]

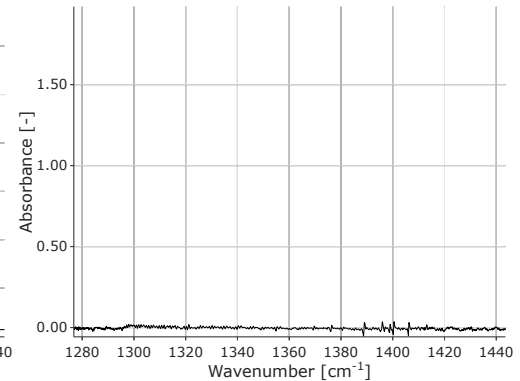
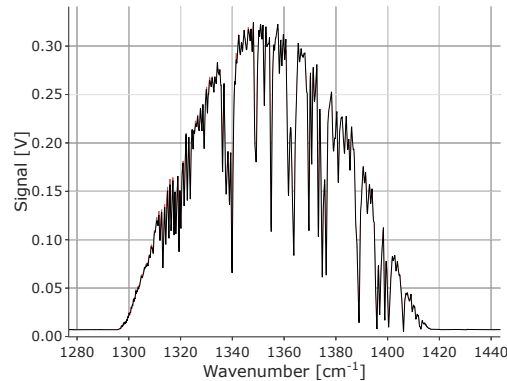


223

Air

08:13:46 PM

Air. No significant background changes occurred.



Description

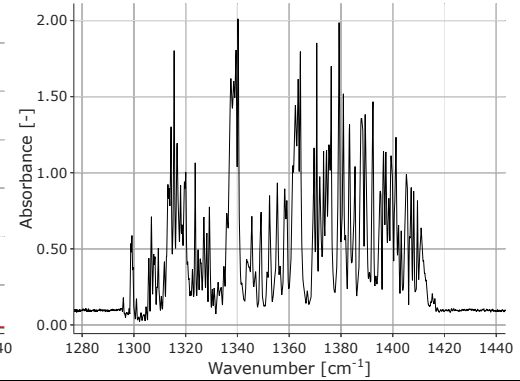
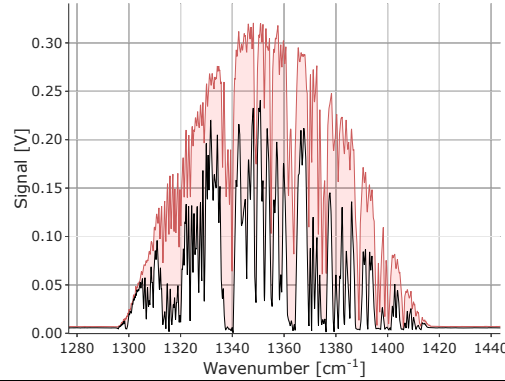
Raw detector signal [V]

Absorbance spectrum [-]

Step 2, Water Only 8%

08:21:08 PM

Water presents very sharp features that saturate the detector in some regions (as explained in Section 6.12).

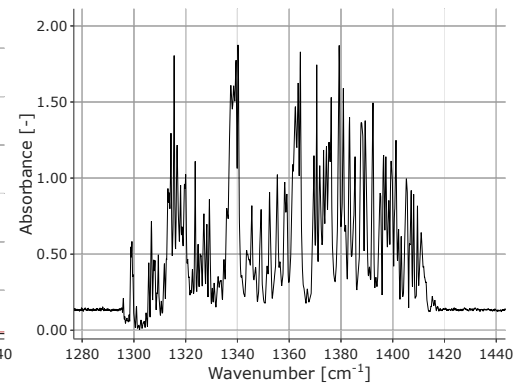
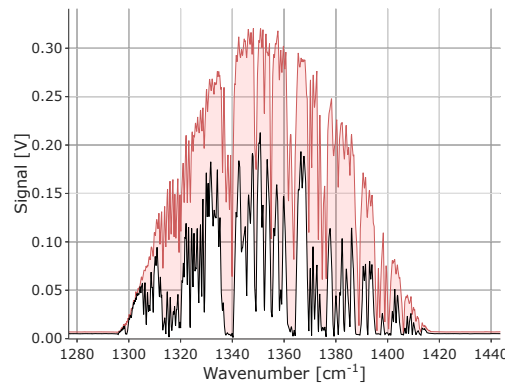


Step 2, Water 8% with 100ppm SO₂

08:28:56

PM

8% water vapor and 100ppm SO₂ are present in the cell. SO₂ concentrations can be extracted successfully from the absorbance spectrum, but it is not directly visible in the absorbance spectrum.



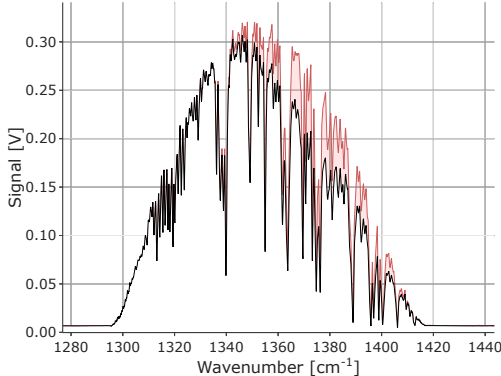
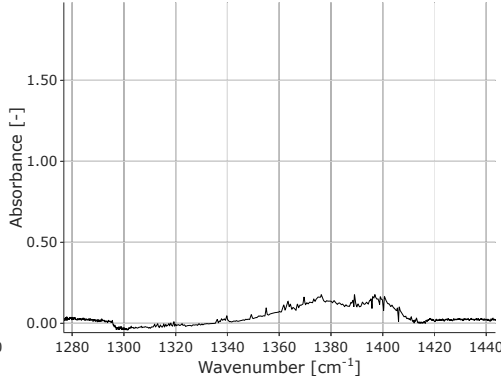
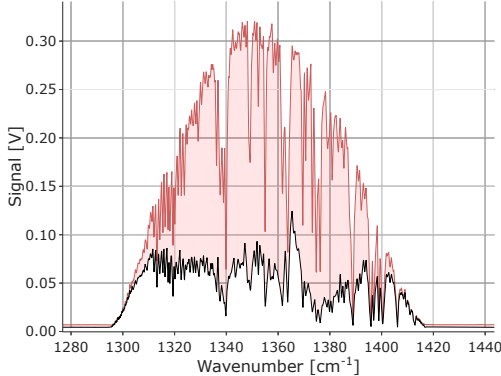
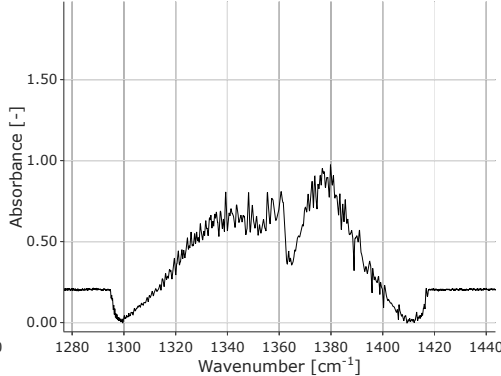
Description	Raw detector signal [V]	Absorbance spectrum [-]
<p data-bbox="212 272 436 305"><i>Equalized Decay</i></p> <p data-bbox="674 272 852 305">08:41:11 PM</p> <p data-bbox="212 402 852 621">No SO₂ is entering the catalyst, so only air and SO₃ are present in the cell. No issues in this condition, previously analyzed also in Step 1.</p>		
<p data-bbox="212 699 852 792"><i>Step 2, Regular with 530ppm SO₂ and reduced SO₃</i></p> <p data-bbox="674 760 852 792">08:57:32 PM</p> <p data-bbox="212 889 852 1174">Additional air and SO₂ are added to reduce by 44% the concentration of SO₃. At these conditions, SO₃ concentrations can still be extracted from the fit of the absorbance spectrum.</p>		

Table 6.10: Description, raw detector signal, and absorbance for each test condition, for Step 2 ECQCL 7 08/13/2020 $T = 350C$ experiment, represented in temporal order.

Some conclusions can be drawn from the data presented in Table 6.10, strictly related to the current multi-pass laser configuration. Moderate concentrations of SO_2 (around 500ppm) do not saturate the absorbance and can be successfully characterized. However, the data fit using the low concentrations library (Section 6.10) do not behave as expected. A different data fit technique is required for high values of absorbance, possibly involving the capture of several SO_2 libraries for different concentration levels. It is possible that in the current multi-pass configuration under moderate to high concentration of SO_2 , Beer-Lambert's linear relation between absorbance and concentration is not accurate. At high levels of H_2O vapor, measurements are still possible. However, due to the saturation of the absorbance at some wavenumbers (as shown in Section 6.12), the spectrum is not reliable in some locations, that should be properly excluded from the spectral fit.

At very high levels of SO_2 (around 2500ppm) the measurement is not possible, as no laser light reaches the detector. Measurements with any combination of very high SO_2 concentration and high water vapor concentration are problematic as well.

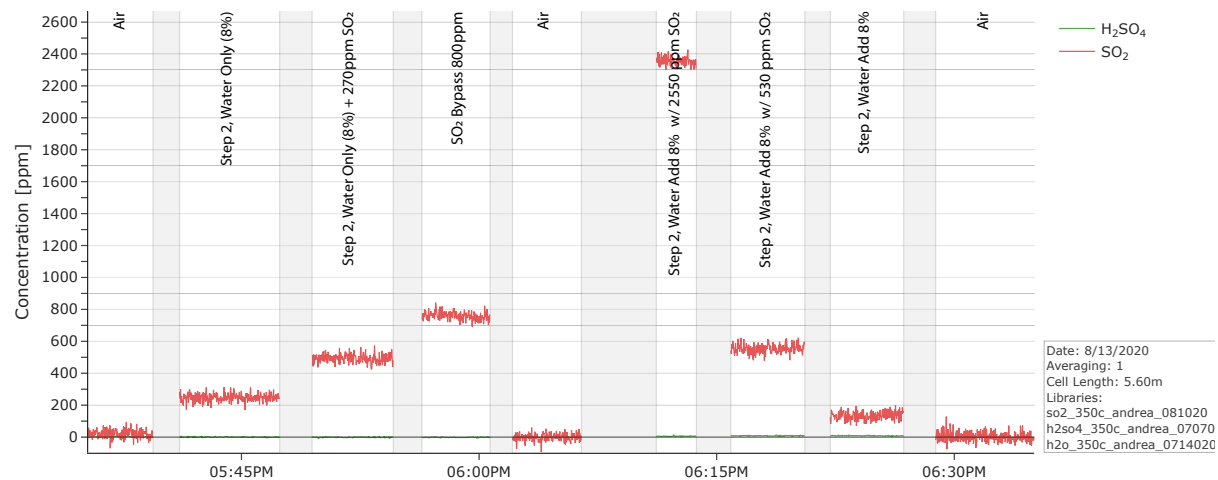
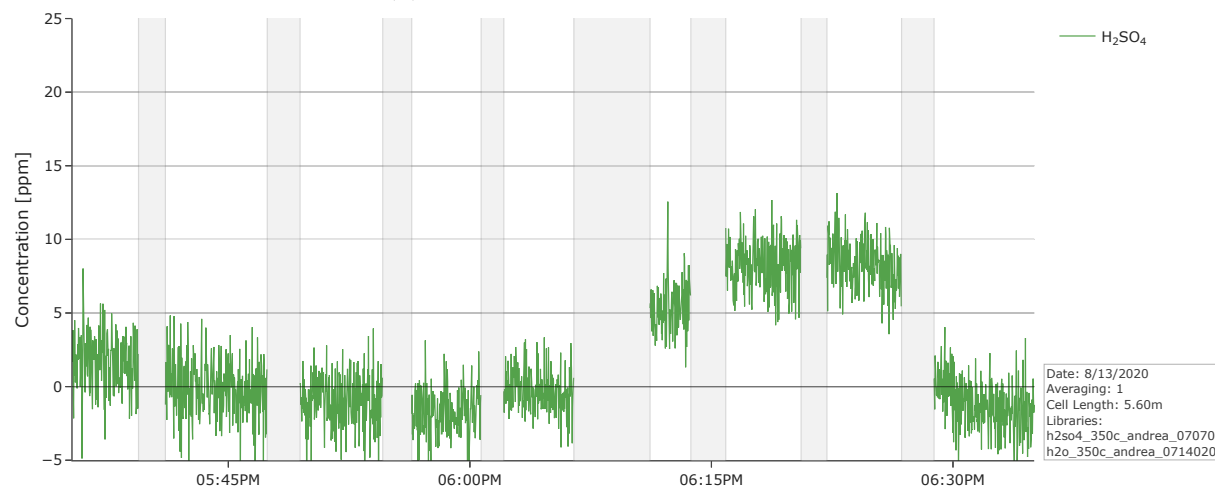
The current ECQCL 7 test configuration does not appear to be a promising technique for the accurate determination of SO_2 and SO_3 in realistic flue gas conditions typical of high-sulfur coal firing (8% water, around 2500ppm of SO_2 , and 40 to 60ppm of $\text{SO}_3/\text{H}_2\text{SO}_4$). The main obstacle is the very high SO_2 concentration, which completely saturates the absorbance. The presence of water creates additional issues, but at a level that could be managed. Sulfur trioxide readings do not create issues. The measurement could still be possible at 8% H_2O only if the levels of SO_2 were lower than about 500ppm, typical of low-sulfur coal firing. A possible solution to measure higher sulfur concentrations is in the dilution of the flue-gas with air inside the measurement cell, but clean and dry air at the power plant testing site is not always available. A second option is the reduction of the path length, however the solution would have drawbacks in terms of limits of detection and accuracy of the measurement.

Operations at high water vapor and high sulfur dioxide levels needs the definition of additional spectral libraries, as Beer-Lambert's law (using low concentrations libraries) does

not appear to predict well the concentration values when the absorbance levels are large.

ECQCL 8 in realistic conditions

The data set for this section is for Step 2 ECQCL 8 08/13/2020 experiment, with $T = 350C$ and 8% water vapor. As in Section 6.2.10, no H_2SO_4 concentration short-term catalyst transient is present, since the high-temperature valve was installed in the experimental rig. Figure 6.38 represents the SO_2 and H_2SO_4 concentrations along the experiment timeline. A close-up is provided for H_2SO_4 concentrations, since it is present at much lower levels than SO_2 .

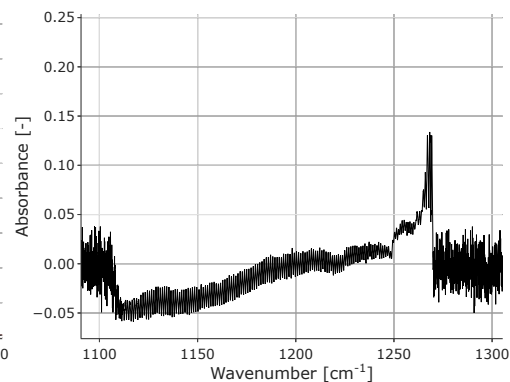
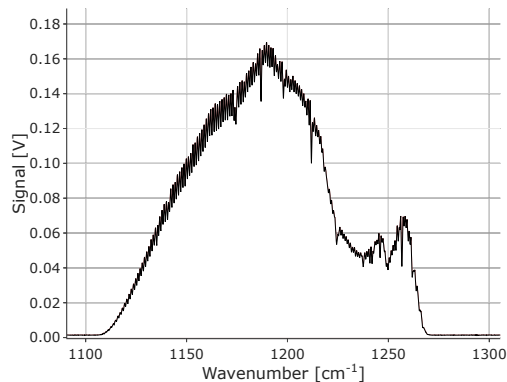
(a) SO_2 and H_2SO_4 concentrations.(b) Closeup of H_2SO_4 concentrations.Figure 6.38: SO_2 and H_2SO_4 concentrations for Step 2 ECQCL 8 08/13/2020 $T = 350\text{C}$ experiment timeline.

Description**Raw detector signal [V]****Absorbance spectrum [-]**

Air

05:37:43 PM

For this test, the air background was captured at the 06:02:38 PM. The difference between the current *Air* condition and the background *Air* condition is not related to window damage, as no strongly corrosive gases have been present in the cell between the two conditions. This absorbance behavior has been noticed in all ECQCL 8 data sets and it is attributed to a drift in the laser signal generation (see Section 6.19).

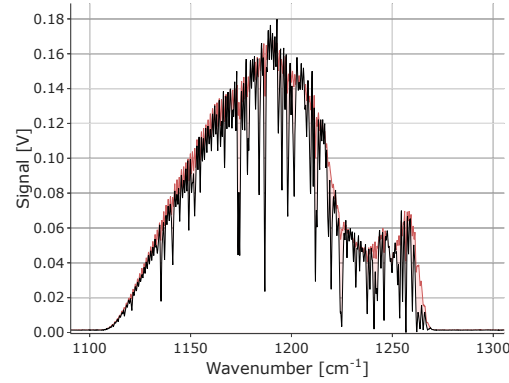
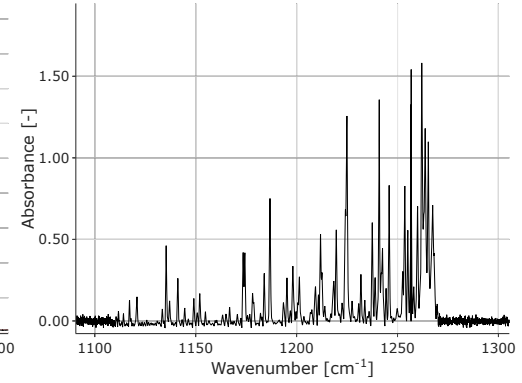


Description

Step 2, Water Only 8%

05:47:15 PM

High levels of water vapor (8%) create sharp dips in the detector signal, even if water is a weak absorber at this wavelength. The detector is yet not saturated at any wavelength, and the laser does not experience any measurement issues under these conditions. Notably, the fitting algorithm is providing an incorrect SO₂ measurement (see Figure 6.38), possibly interpreting some sharp water features as SO₂.

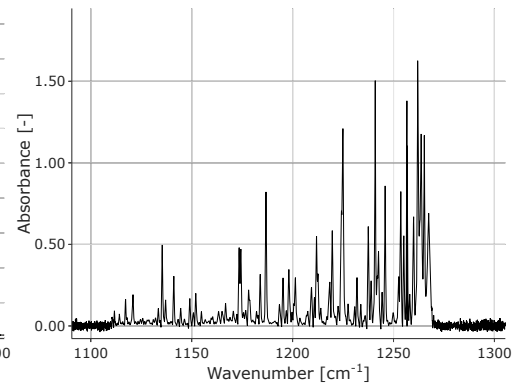
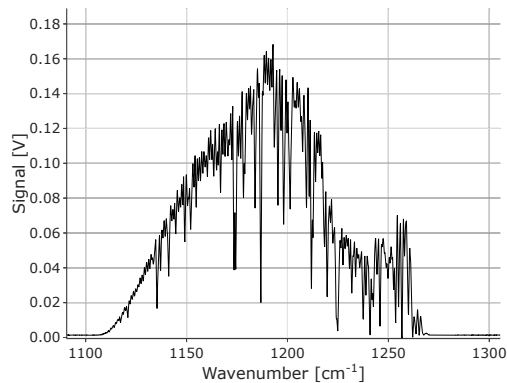
Raw detector signal [V]**Absorbance spectrum [-]**

Description**Raw detector signal [V]****Absorbance spectrum [-]**

Step 2, Water Only 8% with 270ppm SO₂

05:52:40 PM

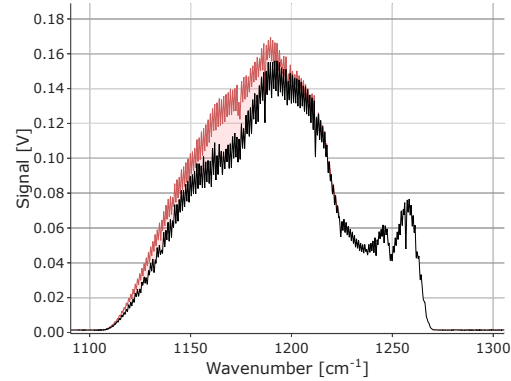
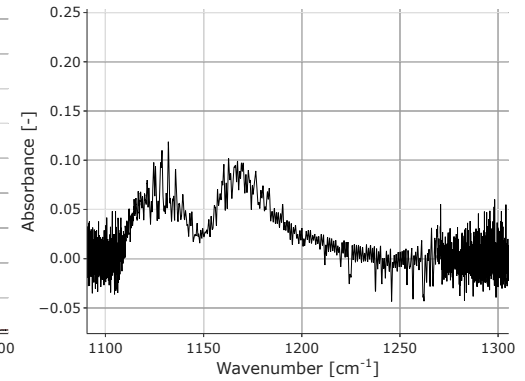
SO₂ is added to the measurement cell. The raw detector signal does not present any issues under these conditions. The fitting algorithm predicts quantitatively well the SO₂ addition, albeit with an offset from the 8% water vapor of the previous case. The SO₂ absorbance spectrum is too weak to be visually noticed in the overall absorbance spectrum, that is dominated by the water vapor spectrum.



Description
800ppm SO₂ Bypass

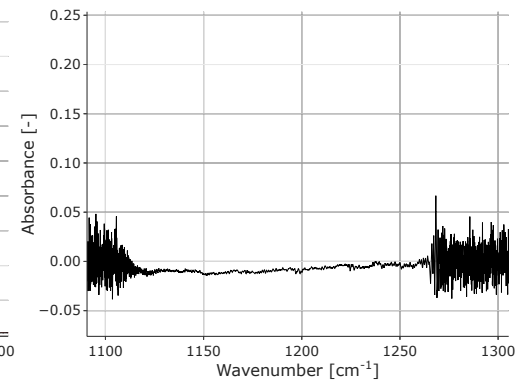
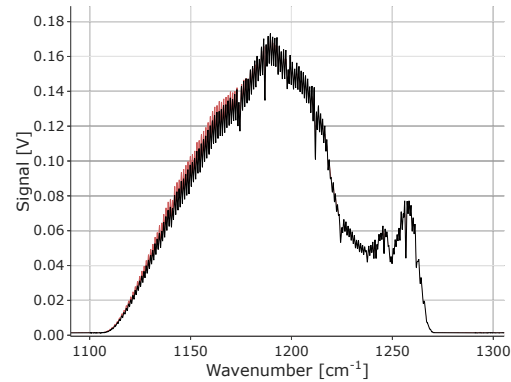
05:57:52 PM

The sensor does not have any issues dealing with 800ppm SO₂. The SO₂ absorbance is directly visible from the absorbance spectrum frame. The fitting algorithm output estimated the presence of 759ppm SO₂, with a standard deviation of 25ppm (3.4%).

Raw detector signal [V]

Absorbance spectrum [-]

Air

06:02:38 PM

The raw detector signal in this test conditions constitutes the background signal for the whole tests. Up to this point, no strongly corrosive SO₃ or H₂SO₄ has been present in the cell.



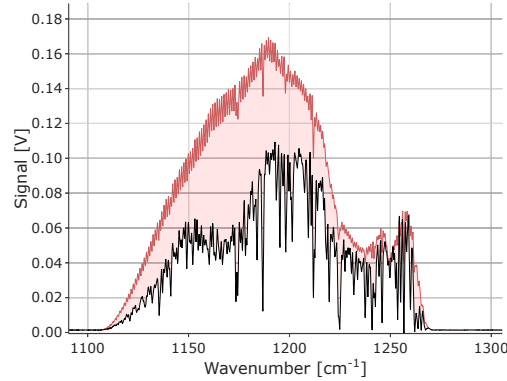
Description

Step 2, Water Add 8% with 2550ppm SO_2

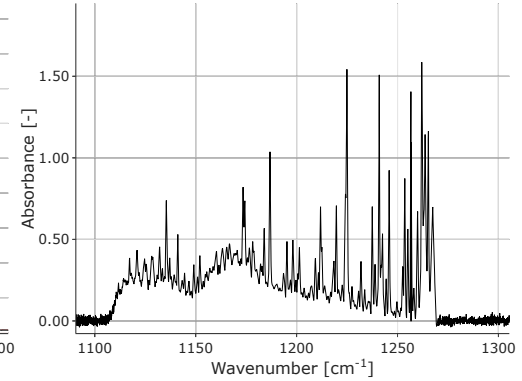
06:13:28 PM

This is the nominal power-plant condition. The sensor is not saturated at any wavelength, so it is possible to apply a properly fit the absorbance spectrum. The SO_2 reading is $2350\text{ppm} \pm 25\text{ppm}$ (1.1% standard deviation), while the H_2SO_4 reading is $5.5\text{ppm} \pm 1.6\text{ppm}$ (30% s.d.). As seen in Figure 6.38, the H_2SO_4 measurement presents significant noise and manifests a large standard deviation. At high concentration, SO_2 absorbance spectrum is visible from the absorbance frame, while H_2SO_4 spectral contribution is not.

Raw detector signal [V]



Absorbance spectrum [-]

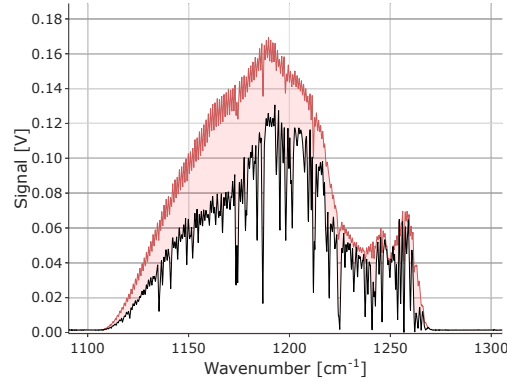


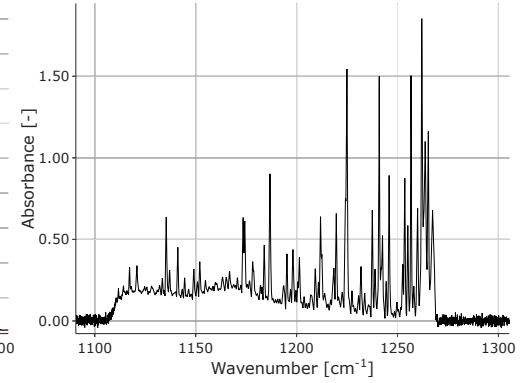
Description

Step 2, Water Add 8% with 530ppm SO₂

06:18:41 PM

SO₂ is reduced to around 530ppm. The SO₂ reading is 553ppm±27ppm (5.0% s.d.), while the H₂SO₄ reading is 8.2ppm±1.7ppm (20.6% s.d.). Sulfuric acid concentration levels should be the same as the previous case, but the estimated value increased instead. Possibly at very high SO₂ concentration the SO₂ absorbance starts to impact the accuracy of H₂SO₄, when H₂SO₄ is present at very low concentration levels.

Raw detector signal [V]

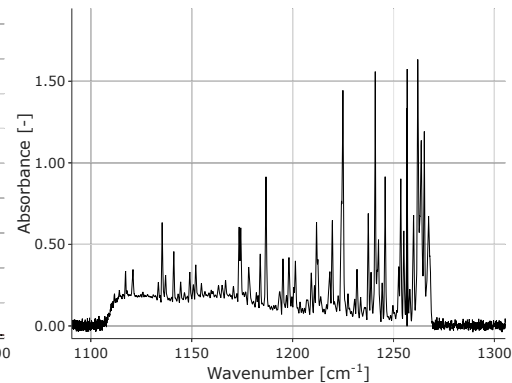
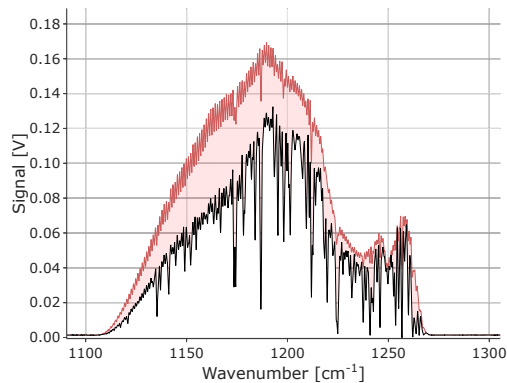
Absorbance spectrum [-]

Description**Raw detector signal [V]****Absorbance spectrum [-]**

Step 2, Water Add 8%

06:23:40 PM

No additional SO₂ is injected in this case, and the SO₂ presence is uniquely due to unconverted SO₂ from the catalytic oxidation. From the data fit, SO₂ concentration is quantified at 134ppm±26ppm (19.6%), while the H₂SO₄ concentration is unaltered with respect to the previous case.



Description

Raw detector signal [V]

Absorbance spectrum [-]

Air

06:28:52 PM

Air is flowing in the measurement cell. The window damage (in the form of a layer of BaSO_4) is clearly visible, even if H_2SO_4 has been present in the cell for only about 15min. Moreover, the current test temperature of 350C minimizes H_2SO_4 and the consequent BaSO_4 formation on the windows.

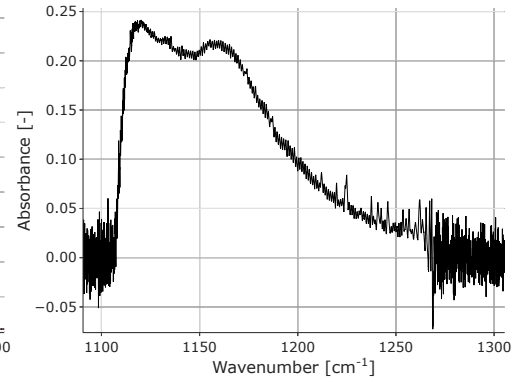
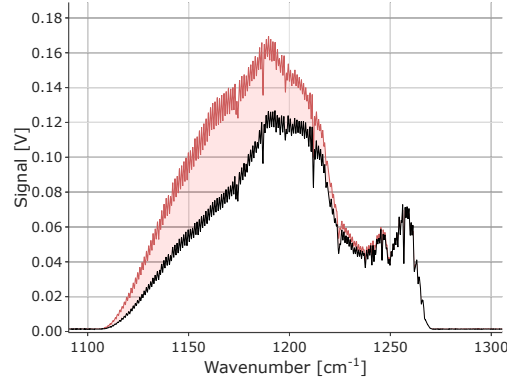


Table 6.11: Description, raw detector signal, and absorbance for each test condition, for Step 2 ECQCL 8 08/13/2020 $T = 350C$ experiment, represented in temporal order.

Some conclusions can be extracted from the data presented in Table 6.11, strictly related to the current multi-pass laser configuration. SO_2 can be sufficiently well characterized at concentrations between 500ppm and 2500ppm. However, low concentrations of SO_2 (<300ppm) present very large measurement uncertainties. It may be possible to improve the fitting performance by defining different spectral libraries correspondent to different concentrations, as the absorbance dependence on concentration over broad ranges might not be linear.

The presence of water can alter the prediction from the data fit. The phenomenon can depend on the fitting of the sharp features characterizing both water and SO_2 , but also from window damage. For example, a 250C test case is represented in Figure 6.39. For that case, the SO_2 concentration are correctly predicted up to about 3:20 PM, when H_2SO_4 is added to the cell. At 250C, almost all SO_3 is in the form of H_2SO_4 , so the window damage occurs rapidly. The SO_2 concentrations start to misrepresent the physical conditions, possibly because the absorbance spectrum of BaSO_4 is very similar to the one of SO_2 .

H_2O vapor concentration of up to 8% does not constitute a problem for the ECQCL 8 laser in this configuration. Low H_2SO_4 concentration is extracted successfully from the absorbance spectrum, since H_2SO_4 is a strong absorber. The standard deviation for the 350C case was around 20%, that was less than 2ppm for the analyzed case. For the 250C test of Figure 6.39, the standard deviation was 5%, (2.6ppm) with respect to the 56ppm mean H_2SO_4 concentration value in *Water Add* conditions. It would be ideal to operate the measurement at low temperatures, where all the SO_3 is in the form of H_2SO_4 , and the H_2SO_4 absorbance spectrum is strong and more reliable. However, at low temperature conditions the H_2SO_4 attack on the window is very swift, and it would rapidly invalidate not only SO_2 measurements but the full data set in minutes. The preliminary analysis of Figure 6.38 shows that the data fit for low H_2SO_4 concentrations and very large SO_2 concentration lacks in accuracy. The reason is unclear. The variation between the two cases (*Step 2, Water Add 8% with 2550ppm SO_2* and *Step 2, Water Add 8% with 530ppm SO_2*) is larger than the

standard deviation of the measurement. It is possibly due to a difference in the experimental condition, but it could also mean that at very large SO_2 concentrations its absorbance is so strong that the H_2SO_4 contribution is hindered and cannot be properly accounted for.

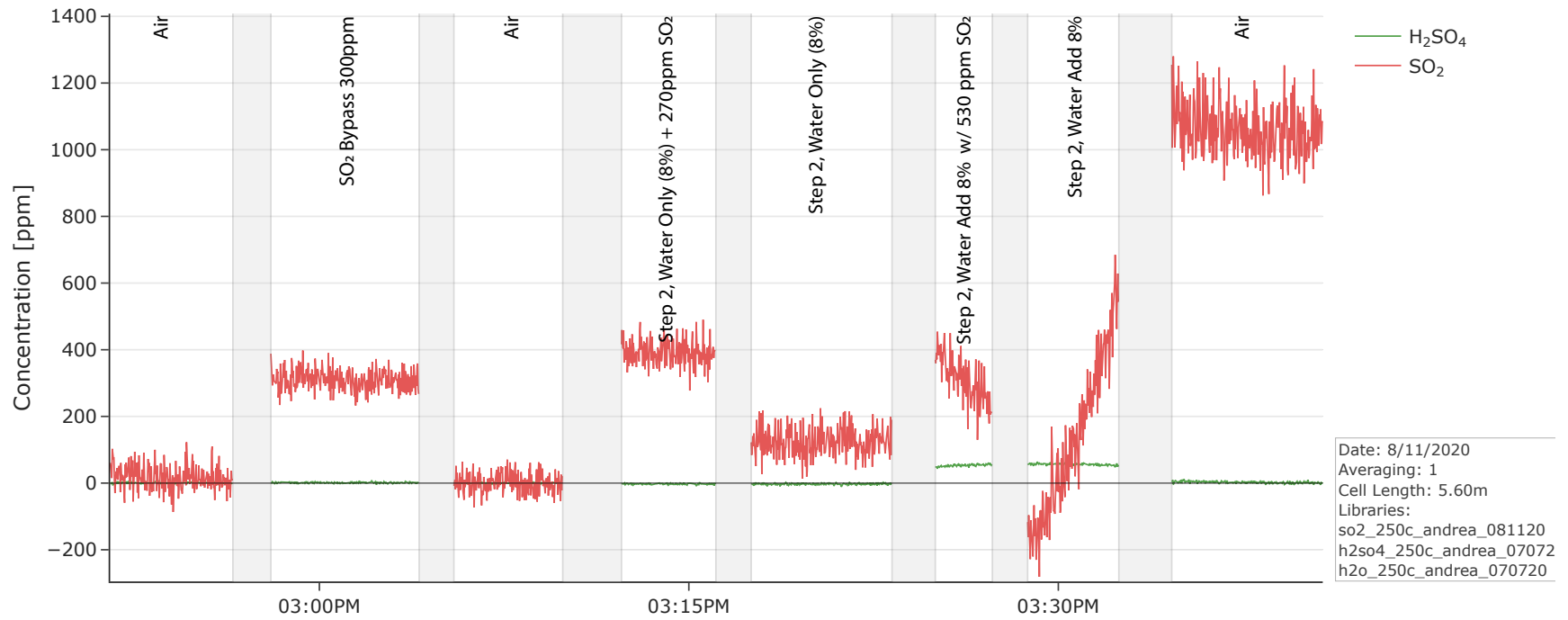


Figure 6.39: SO₂ and SO₃ concentrations in the Step 2 ECQCL 8 08/11/2020 $T = 250^{\circ}\text{C}$ experiment timeline

The ECQCL 8 techniques does not present spectroscopic problems in realistic flue gas conditions (8% water, around 2500ppm of SO₂, and 40 to 60ppm of SO₃/H₂SO₄), as the issues related to SO₂ estimation uncertainty and noisy measures could likely be solved. The very important problem in the use of ECQCL 8 is the window material. This laser relies on the measurement of H₂SO₄, but H₂SO₄ is directly responsible for the extremely fast window damage process that can easily invalidate the measurements. To fully realize the potential of this technique, a window material that has high transmissivity in the Mid-IR and does not react with SO₂, SO₃, H₂O, and most importantly H₂SO₄ is needed.

Chapter 7

Summary

This chapter summarizes the efforts described in this dissertation and provides the key conclusions resulting from the work. Recommendations for further work complete the chapter.

The objectives of this experimental study were the investigation of the feasibility of using spectroscopic techniques for continuous measurements of SO_3 , SO_2 , and H_2SO_4 , and the direct verification of chemical equilibrium between SO_3 and H_2SO_4 in flue-gas conditions. A continuous and direct measurement of the specified sulfur species would allow the fine tuning of sorbents used for flue-gas desulfurization (FGD), thereby reducing operational costs and emissions, particularly considering the increasingly common power-plant flexible operations, where power-plants load and emissions vary in time. If the chemical equilibrium between SO_3 and H_2SO_4 is verified, the optical measurement of only one species would suffice to determine the concentration of the other, assuming that temperature and water vapor concentration are known. Two distinct techniques were used for optical measurements, one targeting the UV wavelength region (Differential Optical Absorption Spectroscopy, DOAS) and the other focused on the mid-IR region (External Cavity Quantum Cascade Laser, ECQCL).

An experimental facility able to replicate temperature and sulfur species composition of typical flue-gas was hence built. The setup includes a high-temperature measurement cell carefully designed and characterized, with an accurate thermal control system. The system

was used to generate an array of measurement conditions at ambient pressure over the range of temperature from 250 to 350C (523K to 623K) and over the key species ranges from 0-100ppm SO₃/H₂SO₄ and 0-2500ppm SO₂, with up to 8% water vapor. Operations proved stable, reliable, accurate, and repeatable.

7.1 Conclusions

The experimental results combined with the use of chemical kinetics and equilibrium analysis for the conditions simulating coal-combustion flue-gas have led to the following significant conclusions:

1. The SO₃ desorption using VK59 and VK48 vanadia catalysts permitted unadulterated SO₃ mid-IR library spectra capture at ambient pressure and temperatures of 250C, 300C, and 350C. The contribution of this work is that it does not rely on the spectral subtraction of other species such as SO₂. Moreover, the species concentrations based on optical absorption from the recorded SO₃ spectra were validated by the industry-standard EPA Method 8A sampling technique to avoid relying on a sulfur balance.
2. For the first time, the expectation of chemical equilibrium between SO₃ and H₂SO₄ at flue-gas temperatures has been investigated experimentally with spectroscopic measurements at 3% water vapor concentration. The equilibrium between the two species has been verified within a 12% uncertainty level, which is in line with the uncertainty related to the cell temperature readings and flow generation. Since the approach to chemical equilibrium is favored as water vapor is added, the assumption that SO₃ and H₂SO₄ are in mutual equilibrium is a good one even for the higher water vapor conditions of flue gas.
3. A high-temperature spectral library for H₂SO₄ in the mid-IR region near 8 micron was also recorded. The detection of a sulfuric acid spectral fingerprint using ECQCL

between $\sim 250\text{-}350$ degree C is novel. There remains a level of uncertainty of the absorbance magnitude at 300C but the spectral signature is clear.

4. BaF₂ windows installed on the measurement cell rapidly degraded in transmission performance when sulfuric acid was present. The degradation is attributed to the formation of a BaSO₄ layer on the windows. The recorded H₂SO₄ and SO₂ spectra have been processed to eliminate the BaSO₄ interference effectively.
5. The DOAS technique is found to be unsuitable to measure SO₃. It was experimentally verified that the absorbance of sulfur trioxide in the UV consists of a broadband contribution. There were no detectable narrowband features as would be essential for DOAS measurements.
6. The ECQCL 7, sensing SO₂ and SO₃ at 7 micron, in conjunction with a multi-pass configuration (16-pass, 5.6m path length) has the capability of detecting flue-gas conditions up to 8% water vapor when SO₂ concentration is below 500ppm.
7. With the same multi-pass cell configuration, the ECQCL 8 can measure SO₂ and H₂SO₄ in the 8 μ m spectral region in flue-gas conditions up to 8% water vapor, albeit the SO₂ measurement is affected by a large uncertainty margin.

7.2 Recommendations and future work

A further expansion on the techniques used in this work, together with some recommendations, is provided in this section. The DOAS technique is not promising under flue-gas conditions. Aside from the broadband absorbance of SO₃ mentioned previously, another possibly insurmountable issue is the overlap of SO₃ spectrum with the SO₂ spectrum, with the latter being up to ten times as strong for equal concentrations. Under flue-gas conditions, not only is SO₂ a much stronger absorber, but it is also present in flue-gas at more than ten times the concentration of SO₃.

The ECQCL 7 technique is promising. It provided stable and reliable measurements, and it was able to meet the requirements on detectability and accuracy in the specific configuration that was analyzed (16-pass, 5.6m path length). In order to additionally improve the measurement readings from the instrument, especially at higher absorbance levels, the spectral fit algorithm needs to be improved, possibly to include piece-wise libraries for different concentration of absorbers and/or account for non-linearity effects. In the current configuration, the system operations were bound by SO_2 levels. The measurements are successful at SO_2 levels below 500ppm, typical of low-sulfur coal flue gas. However, moderate to high SO_2 concentrations ($>500\text{ppm}$) – a regular occurrence for high-sulfur coal flue-gas – would saturate the absorption so that no light would reach the detector and no measurement would be possible. Two different solutions can be the addition of an air dilution flow to the flue-gas or the reduction of the path length. The former would decrease the negative influence of high SO_2 and water concentrations, but it is difficult to implement in the field, where the access to dry and clean air is limited. It would also require very high sensitivity for SO_3 measurements, as its levels would decrease with dilution as well. The latter is easier to implement, but it would sensibly decrease the measurement accuracy and limits of detection. Both solutions should be investigated to determine the best trade-off. Another strategy could be an increase in lasing power, even if the repercussions would likely extend to the performance and capabilities of each component of the laser system, possibly generating a different set of problems. Water is a strong absorber at 7 micron, and while water vapor concentrations have been limited to 8% in this work, it is expected that concentrations higher than 8% would saturate the absorbance and yield unsatisfactory measurement performances.

The ECQCL 8 technique offers some advantages over ECQCL 7. For example the detection of SO_2 and H_2SO_4 was not spectroscopically limited by the saturation of the absorption and was successful in all the analyzed flue-gas conditions. Water is a weak absorber in this spectral region, therefore water vapor should not be an issue even at concentrations larger than 8%. More work is needed to increase the lasing stability (eliminating the signal genera-

tion drift). In turn, the laser will provide more accurate measurement of SO_2 concentrations, that are currently offered with large margin of uncertainty. The engineering challenge associated with the ECQCL 8 laser is the mitigation of window damage. New strategies to avoid sulfuric acid attack on windows are needed to operate this laser successfully. While operating at high-temperature decreases the extent of the damage, it also decreases the concentrations of H_2SO_4 , which is the target molecule for this laser and this study.

The Lasers, Flames, and Aerosol (LFA) Laboratory at UCI is now equipped with a state-of-the-art facility for the generation of SO_2 , SO_3 , and H_2SO_4 at simulated-flue gas conditions in a stable and controlled environment. While the data collected in this work is already of scientific importance, the facility has the potential of further investigating issues associated with the measurement of flue gas species by current and future techniques.

Bibliography

- [1] Chen-Lin Chou. Sulfur in coals: A review of geochemistry and origins. *International Journal of Coal Geology*, 100:1–13, 2012. ISSN 0166-5162. doi: <https://doi.org/10.1016/j.coal.2012.05.009>. URL <https://www.sciencedirect.com/science/article/pii/S0166516212001516>.
- [2] Wencheng Xia and Guangyuan Xie. A technological review of developments in chemical-related desulfurization of coal in the past decade. *International Journal of Mineral Processing*, 161:65–71, 2017. ISSN 0301-7516. doi: <https://doi.org/10.1016/j.minpro.2017.02.013>. URL <https://www.sciencedirect.com/science/article/pii/S0301751617300480>.
- [3] A. L. Moretti and C.S. Jones. *Advanced Emissions Control Technologies for Coal-Fired Power Plants*, 2012.
- [4] WD Halstead and JRW Talbot. Sulphuric acid dewpoint in power station flue gases. *Journal of the Institute of Energy*, 53:142–5, 1980.
- [5] David J. Bayless, Alan R. Schroeder, Michael G. Olsen, David C. Johnson, James E. Peters, Herman Krier, and Richard O. Buckius. The effects of cofiring natural gas and coal on sulfur retention in ash. *Combustion and Flame*, 106(3):231–240, 1996. ISSN 00102180. doi: 10.1016/0010-2180(95)00187-5.
- [6] Stephen F. Mueller and Robert E. Imhoff. Estimates of particle formation and growth in coal-fired boiler exhaust-II. Theory and model simulations. *Atmospheric Environment*, 28(4):603–610, 1994. ISSN 13522310. doi: 10.1016/1352-2310(94)90036-1.
- [7] Jack Bionda. Flue Gas SO₃ Determination-Importance of Accurate Measurements in Light of Recent SCR Market Growth. *Poweplant Chemistry*, 4:582–589, 2002.
- [8] K.R. Parker and A. Sanyal. Effective capture of respirable sized particulates using electrostatic precipitator technology. *Proceedings of the American Power Conference*, editor A.E. McBride, 61:174–179, 1999.
- [9] Arideep Mukherjee and Madhoolika Agrawal. *A Global Perspective of Fine Particulate Matter Pollution and Its Health Effects*, pages 5–51. Springer International Publishing, 2018. ISBN 978-3-319-66875-8. doi: 10.1007/398_2017_3. URL https://doi.org/10.1007/398_2017_3.

- [10] C Arden Pope, Michael J Thun, Mohan M Namboodiri, Douglas W Dockery, John S Evans, Frank E Speizer, Clark W Heath, et al. Particulate air pollution as a predictor of mortality in a prospective study of us adults. *American journal of respiratory and critical care medicine*, 151(3):669–674, 1995.
- [11] George D Thurston, Richard T Burnett, Michelle C Turner, Yuanli Shi, Daniel Krewski, Ramona Lall, Kazuhiko Ito, Michael Jerrett, Susan M Gapstur, W Ryan Diver, et al. Ischemic heart disease mortality and long-term exposure to source-related components of us fine particle air pollution. *Environmental health perspectives*, 124(6):785–794, 2016.
- [12] Oyewale Mayowa Morakinyo, Matlou Ingrid Mokgobu, Murembiwa Stanley Mukhola, and Raymond Paul Hunter. Health outcomes of exposure to biological and chemical components of inhalable and respirable particulate matter. *International journal of environmental research and public health*, 13(6):592, 2016.
- [13] Richard Reiss, Elizabeth L Anderson, Carroll E Cross, George Hidy, David Hoel, Roger McClellan, and Suresh Moolgavkar. Evidence of health impacts of sulfate-and nitrate-containing particles in ambient air. *Inhalation toxicology*, 19(5):419–449, 2007.
- [14] Colin Henderson. Increasing the flexibility of coal-fired power plants. *IEA Clean Coal Centre*, 15, 2014.
- [15] IEA. Coal 2020 - analysis and forecast to 2025. Technical report, IEA, December 2020. All rights reserved.
- [16] US Energy Information Administration. Short-term energy outlook. Technical report, EIA, February 2021.
- [17] C-L Chou. Geochemistry of sulfur in coal. In Wilson L Orr and Curt M White, editors, *Geochemistry of Sulfur in Fossil Fuels*, chapter 2, pages 30–52. ACS Publications, 1990.
- [18] Nujhat N. Choudhury and Bihter Padak. A comprehensive experimental and modeling study of sulfur trioxide formation in oxy-fuel combustion. *International Journal of Greenhouse Gas Control*, 51:165–175, 2016. ISSN 17505836. doi: 10.1016/j.ijggc.2016.05.016. URL <http://dx.doi.org/10.1016/j.ijggc.2016.05.016>.
- [19] Daniel Fleig, Emil Vainio, Klas Andersson, Anders Brink, Filip Johnsson, and Mikko Hupa. Evaluation of SO₃ measurement techniques in air and oxy-fuel combustion. *Energy and Fuels*, 26(9):5537–5549, 2012. ISSN 08870624. doi: 10.1021/ef301127x.
- [20] Toby Lockwood. Techno-economic analysis of pc versus cfb combustion technology. *IEA Clean Coal Centre, Report CCC/226, London, UK*, 2013.
- [21] Jiyoung Ahn, Ryan Okerlund, Andrew Fry, and Eric G. Eddings. Sulfur trioxide formation during oxy-coal combustion. *International Journal of Greenhouse Gas Control*, 5(SUPPL. 1):S127–S135, 2011. ISSN 17505836. doi: 10.1016/j.ijggc.2011.05.009. URL <http://dx.doi.org/10.1016/j.ijggc.2011.05.009>.

- [22] Carlo Orsenigo, Alessandra Beretta, Pio Forzatti, Jiri Svachula, Enrico Tronconi, Fiorenzo Bregani, and Aldo Baldacci. Theoretical and experimental study of the interaction between NO_x reduction and SO₂ oxidation over DeNO_x-SCR catalysts. *Catalysis Today*, 27(1-2):15–21, 1996. ISSN 09205861. doi: 10.1016/0920-5861(95)00168-9.
- [23] Hiroyuki Kamata, Hiroaki Ohara, Katsumi Takahashi, Akinori Yukimura, and Yori-masa Seo. SO₂ oxidation over the V₂O₅/TiO₂ SCR catalyst. *Catalysis Letters*, 73(1):79–83, 2001. ISSN 1011372X. doi: 10.1023/A:1009065030750.
- [24] A. W. Castleman Jr., Richard E. Davis, H. R. Munkelwitz, I. N. Tang, and William P. Wood. Kinetics of association reactions pertaining to H₂SO₄ aerosol formation. *Int. J. Chem. Kinet., Symp. No. 1*, pages 629–640, 1975. URL www.scopus.com. Cited By :61.
- [25] R. Hofmann-Sievert and A. W. Castleman. Reaction of SO₃ with water clusters and the formation of H₂SO₄. *Journal of Physical Chemistry*, 88(15):3329–3333, 1984. ISSN 00223654. doi: 10.1021/j150659a038.
- [26] T. S. Chen and P. L. Moore Plummer. Ab initio MO investigation of the gas-phase reaction SO₃ + H₂O → H₂SO₄. *Journal of Physical Chemistry*, 89(17):3689–3693, 1985. ISSN 00223654. doi: 10.1021/j100263a023.
- [27] C. E. Kolb, J. T. Jayne, D. R. Worsnop, M. J. Molina, R. F. Meads, and A. A. Viggiano. Gas Phase Reaction of Sulfur Trioxide with Water Vapor. *Journal of the American Chemical Society*, 116(22):10314–10315, 1994. ISSN 15205126. doi: 10.1021/ja00101a067.
- [28] J. A. Phillips, M. Canagaratna, H. Goodfriend, and K. R. Leopold. Microwave detection of a key intermediate in the formation of atmospheric sulfuric acid: The structure of H₂O-SO₃. *Journal of Physical Chemistry*, 99(2):501–504, 1995. ISSN 00223654. doi: 10.1021/j100002a008.
- [29] Barbara J.; Finlayson-Pitts and Jr. James N. Pitts. *Chemistry of the Upper and Lower Atmosphere*. Elsevier, 2000. ISBN 9780122570605. doi: 10.1016/B978-0-12-257060-5.X5000-X. URL <https://linkinghub.elsevier.com/retrieve/pii/B9780122570605X5000X>.
- [30] Thomas Reiner and Frank Arnold. Laboratory investigations of gaseous sulfuric acid formation via SO₃+H₂O+M→H₂SO₄+M: Measurement of the rate constant and product identification. *The Journal of Chemical Physics*, 101(9):7399–7407, 1994. ISSN 00219606. doi: 10.1063/1.468298.
- [31] Xiuyan Wang, Y. G. Jin, Masako Suto, L. C. Lee, and H. E. O’Neal. Rate constant of the gas phase reaction of SO₃ with H₂O. *The Journal of Chemical Physics*, 89(8):4853–4860, 1988. ISSN 00219606. doi: 10.1063/1.455680.
- [32] John T. Jayne, Ulrich Pöschl, Yu Min Chen, David Dai, Luisa T. Molina, Douglas R. Worsnop, Charles E. Kolb, and Mario J. Molina. Pressure and temperature dependence

- of the gas-phase reaction of SO₃ with H₂O and the heterogeneous reaction of SO₃ with H₂O/H₂SO₄ surfaces. *Journal of Physical Chemistry A*, 101(51):10000–10011, 1997. ISSN 10895639. doi: 10.1021/jp972549z.
- [33] Matthias Hofmann and Paul von Rague Schleyer. Acid Rain: Ab Initio Investigation of the H₂OSO₃ Complex and Its Conversion into H₂SO₄. *Journal of the American Chemical Society*, 116(11):4947–4952, 1994. ISSN 15205126. doi: 10.1021/ja00090a045.
- [34] Zachary R. Lee, Shengjie Zhang, Luis A. Flores, and David A. Dixon. Predicting the Formation of Sulfur-Based Brønsted Acids from the Reactions of SO_x with H₂O and H₂S. *Journal of Physical Chemistry A*, 123(46):10169–10183, 2019. ISSN 15205215. doi: 10.1021/acs.jpca.9b08433.
- [35] Laura J. Larson, Mayuso Kuno, and Fu Ming Tao. Hydrolysis of sulfur trioxide to form sulfuric acid in small water clusters. *Journal of Chemical Physics*, 112(20):8830–8838, 2000. ISSN 00219606. doi: 10.1063/1.481532.
- [36] Thomas Loerting and Klaus R. Liedl. Toward elimination of discrepancies between theory and experiment: The rate constant of the atmospheric conversion of SO₃ to H₂SO₄. *Proceedings of the National Academy of Sciences of the United States of America*, 97(16):8874–8878, 2000. ISSN 00278424. doi: 10.1073/pnas.97.16.8874.
- [37] Miquel Torrent-Sucarrat, Joseph S. Francisco, and Josep M. Anglada. Sulfuric acid as autocatalyst in the formation of sulfuric acid. *Journal of the American Chemical Society*, 134(51):20632–20644, 2012. ISSN 00027863. doi: 10.1021/ja307523b.
- [38] J. Menasha. *Characterization of ammonium bisulfate formation in a bench-scale single-channel air preheater*. PhD thesis, University of California, Irvine, 2010.
- [39] Hannah Chalmers, Jon Gibbins, and Matt Leach. Valuing power plant flexibility with ccs: the case of post-combustion capture retrofits. *Mitigation and Adaptation Strategies for Global Change*, 17(6):621–649, 2012.
- [40] Peizhi Liao, Yiguo Li, Xiao Wu, Meihong Wang, and Eni Oko. Flexible operation of large-scale coal-fired power plant integrated with solvent-based post-combustion CO₂ capture based on neural network inverse control. *International Journal of Greenhouse Gas Control*, 95:102985, 2020.
- [41] Mathieu Lucquiaud, Hannah Chalmers, and Jon Gibbins. Potential for flexible operation of pulverised coal power plants with CO₂ capture. *Energy materials*, 2(3):175–180, 2007.
- [42] Yuliang Dong, Xu Jiang, Zhihong Liang, and Jiahai Yuan. Coal power flexibility, energy efficiency and pollutant emissions implications in china: A plant-level analysis based on case units. *Resources, Conservation and Recycling*, 134:184–195, 2018. ISSN 0921-3449. doi: <https://doi.org/10.1016/j.resconrec.2018.03.012>. URL <https://www.sciencedirect.com/science/article/pii/S0921344918301137>.

- [43] MR Haines and JE Davison. Designing carbon capture power plants to assist in meeting peak power demand. *Energy Procedia*, 1(1):1457–1464, 2009.
- [44] Debra Lew and Greg Brinkman. The western wind and solar integration study phase 2. Technical report, National Renewable Energy Lab.(NREL), Golden, CO (United States), 2013.
- [45] ”EPRI, - Himes R.”. Assessment of SCR Temperature Variation vs Load. Personal communication, 2019.
- [46] Prabir Basu. *Circulating fluidized bed boilers: Design, operation and maintenance*. Springer, 2015. ISBN 9783319061733. doi: 10.1007/978-3-319-06173-3.
- [47] R Cai, X Ke, Y Huang, S Zhu, Y Li, J Cai, H Yang, J Lyu, and M Zhang. Applications of ultrafine limestone sorbents for the desulfurization process in cfb boilers. *Environmental science & technology*, 53(22):13514–13523, 2019.
- [48] E.J. Anthony and D.L. Granatstein. Sulfation phenomena in fluidized bed combustion systems. *Progress in Energy and Combustion Science*, 27(2):215–236, 2001. ISSN 0360-1285. doi: [https://doi.org/10.1016/S0360-1285\(00\)00021-6](https://doi.org/10.1016/S0360-1285(00)00021-6). URL <https://www.sciencedirect.com/science/article/pii/S0360128500000216>.
- [49] Guangxi Yue, Runxia Cai, Junfu Lu, and Hai Zhang. From a cfb reactor to a cfb boiler. the review of r&d progress of cfb coal combustion technology in china. *Powder Technology*, 316:18–28, 2017. ISSN 0032-5910. doi: <https://doi.org/10.1016/j.powtec.2016.10.062>. URL <https://www.sciencedirect.com/science/article/pii/S0032591016307550>. Fluidization for Emerging Green Technologies.
- [50] Penghao Ye, Senmao Xia, Yu Xiong, Chaoyang Liu, Fei Li, Jiamin Liang, and Huarong Zhang. Did an ultra-low emissions policy on coal-fueled thermal power reduce the harmful emissions? evidence from three typical air pollutants abatement in china. *International Journal of Environmental Research and Public Health*, 17(22):8555, 2020.
- [51] Shiyan Chang, Jiankun Zhuo, Shuo Meng, Shiyue Qin, and Qiang Yao. Clean coal technologies in china: Current status and future perspectives. *Engineering*, 2(4):447–459, 2016. ISSN 2095-8099. doi: <https://doi.org/10.1016/J.ENG.2016.04.015>. URL <https://www.sciencedirect.com/science/article/pii/S2095809917300814>.
- [52] Fan Zhang, Yali Xue, Donghai Li, Zhenlong Wu, and Ting He. On the flexible operation of supercritical circulating fluidized bed: Burning carbon based decentralized active disturbance rejection control. *Energies*, 12(6):1132, 2019.
- [53] LJ Muzio, GC Quartucy, and JE Cichanowicz. Overview and status of post-combustion nox control: Sncr, scr and hybrid technologies. *International Journal of Environment and Pollution*, 17(1-2):4–30, 2002.
- [54] J. Menasha, D. Dunn-Rankin, L. Muzio, and J. Stallings. Ammonium bisulfate formation temperature in a bench-scale single-channel air preheater. *Fuel*, 90(7):

- 2445–2453, 2011. ISSN 00162361. doi: 10.1016/j.fuel.2011.03.006. URL <http://dx.doi.org/10.1016/j.fuel.2011.03.006>.
- [55] Lawrence Muzio, Sean Bogseth, Richard Himes, Yu Chien Chien, and Derek Dunn-Rankin. Ammonium bisulfate formation and reduced load SCR operation. *Fuel*, 206(x):180–189, 2017. ISSN 00162361. doi: 10.1016/j.fuel.2017.05.081. URL <http://dx.doi.org/10.1016/j.fuel.2017.05.081>.
- [56] Shunwei Chen, Yanling Zhao, and Ruiqin Zhang. Formation mechanism of atmospheric ammonium bisulfate: Hydrogen-bond-promoted nearly barrierless reactions of SO_3 with NH_3 and H_2O . *ChemPhysChem*, 19(8):967–972, 2018. doi: <https://doi.org/10.1002/cphc.201701333>. URL <https://chemistry-europe.onlinelibrary.wiley.com/doi/abs/10.1002/cphc.201701333>.
- [57] Gehui Wang, Renyi Zhang, Mario E. Gomez, Lingxiao Yang, Misti Levy Zamora, Min Hu, Yun Lin, Jianfei Peng, Song Guo, Jingjing Meng, Jianjun Li, Chunlei Cheng, Tafeng Hu, Yanqin Ren, Yuesi Wang, Jian Gao, Junji Cao, Zhisheng An, Weijian Zhou, Guohui Li, Jiayuan Wang, Pengfei Tian, Wilmarie Marrero-Ortiz, Jeremiah Secrest, Zhuofei Du, Jing Zheng, Dongjie Shang, Limin Zeng, Min Shao, Weigang Wang, Yao Huang, Yuan Wang, Yujiao Zhu, Yixin Li, Jiayi Hu, Bowen Pan, Li Cai, Yuting Cheng, Yuemeng Ji, Fang Zhang, Daniel Rosenfeld, Peter S. Liss, Robert A. Duce, Charles E. Kolb, and Mario J. Molina. Persistent sulfate formation from London fog to Chinese haze. *Proceedings of the National Academy of Sciences*, 113(48):13630–13635, 2016. ISSN 0027-8424. doi: 10.1073/pnas.1616540113. URL <https://www.pnas.org/content/113/48/13630>.
- [58] SO₃ Measurement - MCSO₃. <https://multi-instruments.nl/wp-content/uploads/2018/07/SO3-analyser-.pdf>, 2013. retrieved March 14, 2021.
- [59] ProCeas[®] - SO₂/SO₃ analyzer. <https://www.ap2e.com/wp-content/uploads/ProCeas-SO2-SO3-analyzer.pdf>, 2010. retrieved March 14, 2021.
- [60] Arke SO₃ System - Instruction Manual. <http://tools.thermofisher.com/content/sfs/manuals/EPM-manual-Arke.pdf>, 2013. retrieved March 14, 2021.
- [61] J. Kriesel, C. Makarem, R. Himes, D. Dunn-Rankin, A. Biasioli, Y.C. Chien, and L. Muzio. Mid IR Laser Sensor for Continuous SO₃ Monitoring to Improve Coal-Fired Power Plant Performance during Flexible Operations. https://www.optoknowledge.com/documents/publications/OKSI_SO3monitor_NETLmeeting2019.pdf, 2019. 2019 Proceedings DOE/NETL Project Review Meeting for Crosscutting Research. Retrieved March 14, 2021.
- [62] Unisearch DOAS Stack Systems - Industrial monitors. <https://ektimo.com.au/wp-content/uploads/2021/02/P02-DOAS-gas-analyser.pdf>, 2021. retrieved March 14, 2021.

- [63] Ashok K. Jain. Method 8A - Determination of sulfuric acid vapor or mist and sulfur dioxide emissions from kraft recovery furnaces. Technical Report December, NCASI, 1996. URL <https://www3.epa.gov/ttnemc01/ctm/ctm-013.pdf>.
- [64] Breen Probe - SO₃/ABS/ADM. <https://breenes.com/wp-content/uploads/breen-probe-so3-12-2020.pdf>, 2020. retrieved March 14, 2021.
- [65] U. Platt and J. Stutz. *Differential Optical Absorption Spectroscopy Principles & Applications*. Springer, 2008. ISBN 9783540211938.
- [66] Thomas Durbin and John T Pisano. Construction of a DOAS Instrument for Installation at CARB for Low Level Measurement of SO₂ to Investigate the Relation between SO₂ and Sulfate ARB Contract No. 10-312. Technical report, University of California, Riverside, 2014.
- [67] R. Volkamer, T. Etzkorn, A. Geyer, and U. Platt. Correction of the oxygen interference with UV spectroscopic (DOAS) measurements of monocyclic aromatic hydrocarbons in the atmosphere. *Atmospheric Environment*, 32(21):3731–3747, nov 1998. ISSN 1352-2310. doi: 10.1016/S1352-2310(98)00095-8. URL <https://www.sciencedirect.com/science/article/pii/S1352231098000958>.
- [68] J B Burkholder, M Millis, and S McKeen. Upper limit for the UV absorption cross section of H₂SO₄. *Geophys. Res. Lett.*, 27(16):2493–2496, 2000.
- [69] Paul E. Hintze, Henrik G. Kjaergaard, Veronica Vaida, and James B. Burkholder. Vibrational and electronic spectroscopy of sulfuric acid vapor. *Journal of Physical Chemistry A*, 107(8):1112–1118, 2003. ISSN 10895639. doi: 10.1021/jp0263626.
- [70] James B. Burkholder and Stuart McKeen. UV absorption cross sections for SO₃. *Geophysical Research Letters*, 24(24):3201–3204, dec 1997. ISSN 00948276. doi: 10.1029/97GL03255. URL <http://doi.wiley.com/10.1029/97GL03255>.
- [71] Hannelore Keller-Rudek, GK Moortgat, Rolf Sander, and R Sørensen. The mpi-mainz uv/vis spectral atlas of gaseous molecules of atmospheric interest. *Earth System Science Data*, 5(2):365–373, 2013.
- [72] A. C. Vandaele, P. C. Simon, J. M. Guilmot, M. Carleer, and R. Colin. SO₂ absorption cross section measurement in the UV using a Fourier transform spectrometer. *Journal of Geophysical Research*, 99(D12):25599–25605, 2004. ISSN 0148-0227. doi: 10.1029/94jd02187.
- [73] Kouhei Kurata, Takao; Izawa, Jun; Kusama, Shigeru; Suzuki. Development of so₃ concentration measurement system. *Ishikawajima-Harima Giho/IHI Engineering Review*, 36(3):135–140, 2003.
- [74] E Fajans and CF Goodeve. The absorption spectrum of sulphur trioxide. *Transactions of the Faraday Society*, 32:511–514, 1936.

- [75] Federico Capasso. High-performance midinfrared quantum cascade lasers. *Optical Engineering*, 49(11):111102, 2010.
- [76] Peter Geiser. New opportunities in mid-infrared emission control. *Sensors*, 15(9):22724–22736, 2015. ISSN 1424-8220. doi: 10.3390/s150922724. URL <https://www.mdpi.com/1424-8220/15/9/22724>.
- [77] Andreas Hugi, Richard Maulini, and Jérôme Faist. External cavity quantum cascade laser. *Semiconductor Science and Technology*, 25(8):083001, 2010.
- [78] Brian E. Brumfield, Matthew S. Taubman, Jonathan D. Suter, and Mark C. Phillips. Characterization of a swept external cavity quantum cascade laser for rapid broad-band spectroscopy and sensing. *Opt. Express*, 23(20):25553–25569, Oct 2015. doi: 10.1364/OE.23.025553. URL <http://www.opticsexpress.org/abstract.cfm?URI=oe-23-20-25553>.
- [79] Petros Kotidis, Erik R Deutsch, and Anish Goyal. Standoff detection of chemical and biological threats using miniature widely tunable qcls. In *Micro-and Nanotechnology Sensors, Systems, and Applications VII*, volume 9467, page 94672S. International Society for Optics and Photonics, 2015.
- [80] Katharina Wörle, Felicia Seichter, Andreas Wilk, Chris Armacost, Tim Day, Matthias Godejohann, Ulrich Wachter, Josef Vogt, Peter Radermacher, and Boris Mizaikoff. Breath analysis with broadly tunable quantum cascade lasers. *Analytical Chemistry*, 85(5):2697–2702, 2013. doi: 10.1021/ac3030703. URL <https://doi.org/10.1021/ac3030703>. PMID: 23320383.
- [81] HITRANonline. <https://hitran.org/>, 2020.
- [82] Laurence S Rothman, Iouli E Gordon, Alain Barbe, D Chris Benner, Peter F Bernath, Manfred Birk, Vincent Boudon, Linda R Brown, Alain Campargue, J-P Champion, et al. The hitran 2008 molecular spectroscopic database. *Journal of Quantitative Spectroscopy and Radiative Transfer*, 110(9-10):533–572, 2009.
- [83] David M Sonnenfroh, Mark G Allen, W Terry Rawlins, Claire Gmachl, Federico Capasso, Albert Hutchinson, Deborah Sivco, A Y Cho, Bell Laboratories, Lucent Technologies, Mountain Ave, and Murray Hill. Pollutant emission monitoring using QC laser-based mid-IR sensors. *Proceedings of SPIE*, 4199, 2001. ISSN 0277786X. doi: 10.1117/12.417364.
- [84] SpectralCalc. <https://www.spectralcalc.com>, 2018.
- [85] N.F. Henfrey and B.A. Thrush. The ν_3 band of SO₃ at high resolution. *Chemical Physics Letters*, 102(2-3):135–138, nov 1983. ISSN 00092614. doi: 10.1016/0009-2614(83)87379-5. URL <https://linkinghub.elsevier.com/retrieve/pii/0009261483873795>.

- [86] Arthur Maki, Thomas A. Blake, Robert L. Sams, Nicolae Vulpanovici, Jeffrey Barber, Engeline T.H. Chrysostom, Tony Masiello, Joseph W. Nibler, and Alfons Weber. High-Resolution Infrared Spectra of the ν_2 , ν_3 , ν_4 , and $2\nu_3$ Bands of 32S16O₃, 2003. ISSN 00222852.
- [87] Wilson T. Rawlins, Joel M. Hensley, David M. Sonnenfroh, David B. Oakes, and Mark G. Allen. Quantum cascade laser sensor for SO₂ and SO₃ for application to combustor exhaust streams. *Applied Optics*, 44(31):6635, 2005. ISSN 0003-6935. doi: 10.1364/ao.44.006635.
- [88] Tuomas Hieta and M Merimaa. Simultaneous detection of so₂, so₃ and h₂o using qcl spectrometer for combustion applications. *Applied Physics B*, 117(3):847–854, 2014.
- [89] Alexander Fateev and Sønnik Clausen. Sulfur trioxide measurement technique for SCR units. Technical Report 1885, The Danish Environmental Protection Agency, Oct 2016. URL <https://www2.mst.dk/Udgiv/publications/2016/10/978-87-93529-18-2.pdf>.
- [90] Tom Durbin and John T Pisano. Laboratory Testing of the Equilibrium between H₂SO₄ and SO₃ at Temperatures Reflective of Coal Fired Power Plant Environments Using FTIR Spectroscopy Table of Contents. Technical report, University of California, Riverside, 2008.
- [91] Christopher S. Goldenstein, Victor A. Miller, R. Mitchell Spearrin, and Christopher L. Strand. Spectraplot.com: Integrated spectroscopic modeling of atomic and molecular gases. *Journal of Quantitative Spectroscopy and Radiative Transfer*, 200:249–257, 2017. ISSN 0022-4073. doi: <https://doi.org/10.1016/j.jqsrt.2017.06.007>. URL <https://www.sciencedirect.com/science/article/pii/S0022407317302996>.
- [92] Antonios Christodoulakis and Soghomon Boghosian. Molecular structure of supported molten salt catalysts for so₂ oxidation. *Journal of Catalysis*, 215(1):139–150, 2003.
- [93] "Haldor Topsøe". VK series - Sulphuric acid catalysts, "2008".
- [94] Jiri Svachula, Louis J. Alemany, Natale Ferlazzo, Pio Forzatti, Enrico Tronconi, and Fiorenzo Bregani. Oxidation of sulfur dioxide to sulfur trioxide over honeycomb denoxing catalysts. *Industrial & Engineering Chemistry Research*, 32(5):826–834, 1993. doi: 10.1021/ie00017a009.
- [95] Christopher Bertole. Sox and the scr-how sulfur influences catalyst operation. *CORMETECH – 2019 Reinhold NOx-Combustion-CCR Round Table*, 2019.
- [96] Daniel Fleig, Klas Andersson, Fredrik Normann, and Filip Johnsson. SO₃ Formation under oxyfuel combustion conditions. *Industrial and Engineering Chemistry Research*, 50(14):8505–8514, 2011. ISSN 08885885. doi: 10.1021/ie2005274.

- [97] J. S. Jayakumar, S. M. Mahajani, J. C. Mandal, Kannan N. Iyer, and P. K. Vijayan. CFD analysis of single-phase flows inside helically coiled tubes. *Computers and Chemical Engineering*, 34(4):430–446, 2010. ISSN 00981354. doi: 10.1016/j.compchemeng.2009.11.008. URL <http://dx.doi.org/10.1016/j.compchemeng.2009.11.008>.
- [98] R. C. Xin and M. A. Ebadian. Natural convection heat transfer from helicoidal pipes. *Journal of Thermophysics and Heat Transfer*, 10(2):297–302, 2008. ISSN 0887-8722. doi: 10.2514/3.787.
- [99] Yasuo Mori and Wataru Nakayama. Study on forced convective heat transfer in curved pipes. (3rd report, theoretical analysis under the condition of uniform wall temperature and practical formulae). *International Journal of Heat and Mass Transfer*, 10(5):681–695, 1967. ISSN 00179310. doi: 10.1016/0017-9310(67)90113-5.
- [100] Guillaume Coden. Relationship between so₃ and h₂so₄ in power plant flue gas. *ENSMA – Promotion 2019*, 2018.
- [101] "ANSYS, Inc.". *ANSYS Fluent User's Guide 2020 R2*, 2020.
- [102] Peter Glarborg, Dorte Kubel, Kim Dam-Johansen, Hong Ming Chiang, and Joseph W. Bozzelli. Impact of SO₂ and NO on CO oxidation under post-flame conditions. *International Journal of Chemical Kinetics*, 28(10):773–790, 1996. ISSN 05388066. doi: 10.1002/(SICI)1097-4601(1996)28:10<773::AID-KIN8>3.0.CO;2-K.
- [103] Maria U. Alzueta, Rafael Bilbao, and Peter Glarborg. Inhibition and sensitization of fuel oxidation by SO₂. *Combustion and Flame*, 127(4):2234–2251, 2001. ISSN 00102180. doi: 10.1016/S0010-2180(01)00325-X.
- [104] Lusi Hindiyarti, Peter Glarborg, and Paul Marshall. Reactions of so₃ with the O/H radical pool under combustion conditions. *Journal of Physical Chemistry A*, 111(19):3984–3991, 2007. ISSN 10895639. doi: 10.1021/jp067499p.
- [105] J. Giménez-López, M. Martínez, A. Millera, R. Bilbao, and M. U. Alzueta. SO₂ effects on CO oxidation in a CO₂ atmosphere, characteristic of oxy-fuel conditions. *Combustion and Flame*, 158(1):48–56, 2011. ISSN 00102180. doi: 10.1016/j.combustflame.2010.07.017.
- [106] Sander Gersen, Martijn Van Essen, Harry Darneveil, Hamid Hashemi, Christian Tihic Rasmussen, Jakob Munkholdt Christensen, Peter Glarborg, and Howard Levinsky. Experimental and Modeling Investigation of the Effect of H₂S Addition to Methane on the Ignition and Oxidation at High Pressures. *Energy and Fuels*, 31(3):2175–2182, 2017. ISSN 15205029. doi: 10.1021/acs.energyfuels.6b02140.
- [107] Ayten Yilmaz, Lusi Hindiyarti, Anker D. Jensen, Peter Glarborg, and Paul Marshall. Thermal dissociation of so₃ at 1000–1400 K. *Journal of Physical Chemistry A*, 110(21):6654–6659, 2006. ISSN 10895639. doi: 10.1021/jp0557215.

- [108] Yanwei Zhang, Hui Yang, Junhu Zhou, Zhihua Wang, Jianzhong Liu, and Kefa Cen. Detailed kinetic modeling of homogeneous H₂SO₄ decomposition in the sulfur-iodine cycle for hydrogen production. *Applied Energy*, 130:396–402, 2014. ISSN 03062619. doi: 10.1016/j.apenergy.2014.05.017. URL <http://dx.doi.org/10.1016/j.apenergy.2014.05.017>.
- [109] Daniel Fleig, María U. Alzueta, Fredrik Normann, María Abián, Klas Andersson, and Filip Johnsson. Measurement and modeling of sulfur trioxide formation in a flow reactor under post-flame conditions. *Combustion and Flame*, 160(6):1142–1151, 2013. ISSN 00102180. doi: 10.1016/j.combustflame.2013.02.002. URL <http://dx.doi.org/10.1016/j.combustflame.2013.02.002>.
- [110] F. G. Cerru, A. Kronenburg, and R. P. Lindstedt. A systematically reduced reaction mechanism for sulphur oxidation. *Proceedings of the Combustion Institute*, 30(1):1227–1235, 2005. ISSN 15407489. doi: 10.1016/j.proci.2004.08.083.
- [111] "ANSYS, Inc.". *ANSYS Fluent Theory Guide 2020 R2*, 2020.
- [112] HITRAN on the web. <https://hitran.iao.ru/>, 2021.
- [113] Angela Sifontes, Edgar Cañizales, Jhoan Toro-Mendoza, Edward Ávila, Petra Hernández, Blas Delgado, Brenda Gutiérrez, Y. Diaz, and Eliandreina Cruz-Barrios. Obtaining highly crystalline barium sulphate nanoparticles via chemical precipitation and quenching in absence of polymer stabilizers. *Journal of Nanomaterials*, 2015, 02 2015. doi: 10.1155/2015/510376.
- [114] David E Chasan and George Norwitz. Infrared determination of inorganic sulfates and carbonates by the pellet technique. Technical report, FRANKFORD ARSENAL PHILADELPHIA PA, 1969.
- [115] Inc. Coblentz Society. *NIST Chemistry WebBook, NIST Standard Reference Database Number 69*, chapter The Coblentz Society Desk Book of Infrared Spectra. Eds. P.J. Lindstrom and W.G. Mallard, National Institute of Standards and Technology, Gaithersburg MD, 20899, (retrieved January 14, 2021). URL <https://doi.org/10.18434/T4D303>.

Appendix A

ECQCL experiment log

The experiment log details the chronological sequence of ECQCL tests and the parameters that characterize them. The following tables include also notes and comments on each experiment set. Table 6.9 collects the data set for Step 1 tests, while Table A.2 and Table A.3 detail the Step 2 tests for ECQCL 7 and ECQCL 8 respectively.

A.1 Step 1

Day	SO_x [ppm]	β [%]	T [C]	Path length [m]	ECQCL	Notes
05/12/2020	300	8	350	2.14	7	CaF ₂ Siliconert windows installed Path length shorter than expected
05/15/2020	300	8	300	2.14	7	Software problems. Only partial experiment completed
05/18/2020	300	8	250	2.14	7	
05/19/2020	150	8	250	2.14	7	
05/25/2020	150	8	250	5.60	7	Laser re-aligned. Window polished
05/25/2020	150	8	300	5.60	7	
05/26/2020	150	3	350	5.60	7	Window polished. One window broke. One CaF ₂ and one BaF ₂ window installed. Switched to 3% H ₂ O
05/27/2020	50	3	250	5.60	7	SO ₂ and SO ₃ larger than expected. Catalyst is possibly not yet equilibrated
05/27/2020	50	3	300	5.60	7	As 05/27/2020
05/28/2020	50	3	350	5.60	7	As 05/27/2020
05/29/2020	100	3	250	5.60	7	

Day	SO_x [ppm]	β [%]	T [C]	Path length [m]	ECQCL	Notes
06/09/2020	100	3	300	5.60	7	
06/13/2020	100	3	350	5.60	7	
06/16/2020	50	3	250	5.60	7	
06/18/2020	50	3	300	5.60	7	
06/29/2020	50	3	350	5.60	7-8	Replaced and polished windows. Two BaF ₂ windows installed for ECQCL 8
06/30/2020	50	3	300	5.60	7-8	
06/30/2020	50	3	250	5.60	7-8	
07/02/2020	50	3	350	5.60	7-8	
07/06/2020	100	3	350	5.60	7-8	
07/07/2020	100	3	350	5.60	7-8	
07/07/2020	100	3	300	5.60	7-8	
07/07/2020	100	3	250	5.60	7-8	
07/09/2020	100	3	300	5.60	7-8	Polished windows
07/13/2020	100	3	250	5.60	7-8	Polished windows
07/14/2020	150	3	350	5.60	7-8	

Day	SO_x [ppm]	β [%]	T [C]	Path length [m]	ECQCL	Notes
07/14/2020	150	3	300	5.60	7-8	
08/06/2020	150	3	250	5.60	7-8	New cell insulation installed (improved temperature uniformity). Main flow high-temperature valve installed. One new window installed. Polished windows. Strong etaloning.
08/09/2020	150	3	350	3.65	7-8	Polished windows. Lost laser alignment. Re-aligned to lower path length. Strong etaloning

Table A.1: Step 1 Experiment runs

A.2 Step 2

Day	SO ₂ [ppm]	SO ₃ [ppm]	β [%]	T [C]	PathLength[m]	Notes
08/10/2020	50 - 530	50	8	350	5.40	Laser re-aligned
08/11/2020	50 - 530	50	8	300	5.40	
08/11/2020	50 - 530	50	8	250	5.40	
08/13/2020	50 - 530 - 2550	30 - 50	8	350	5.40	Windows polished
08/15/2020	30 - 40 - 510 - 520 - 530	10 - 2030 - 40	1.6 - 8	350	5.40 8	
08/15/2020	30 - 40 - 510 - 520 - 530	10 - 2030 - 40	1.6 - 8	350	5.40	

Table A.2: Step 2 ECQCL7 Experiment runs

Day	SO ₂ [ppm]	H ₂ SO ₄ [ppm]	β [%]	T [C]	PathLength[m]	Notes
08/10/2020	50	25	8	350	5.40	Laser re-aligned
08/11/2020	50 - 530	40	8	300	5.40	
08/11/2020	50 - 530	47	8	250	5.40	

08/13/2020	50 - 530 - 2550	25	8	350	5.40	Windows polished
08/18/2020	20 - 1010	10	8	350	5.40	
08/18/2020	20 - 1010	15	8	300	5.40	
08/18/2020	20 - 1010	20	8	250	5.40	
08/22/2020	100 - 1100	50	8	350	5.40	Windows polished
08/22/2020	100 - 1100	80	8	300	5.40	

Table A.3: Step 2 ECQCL8 Experiment runs